Implementing Diode-Pumped Solid-State Lasers into Instrumental Analytics

D I S S E R T A T I O N

zur Erlangung des akademischen Grades

d o c t o r r e r u m n a t u r a l i u m
(Dr. rer. nat.)

im Fach: Chemie

Spezialisierung: Angewandte Analytik und Umweltchemie

eingereicht an der
Mathematisch-Naturwissenschaftlichen Fakultät
der Humboldt-Universität zu Berlin

von
Dipl.-Chem. Andreas Bierstedt

Präsidentin der Humboldt-Universität zu Berlin:
Prof. Dr.-Ing. Dr. Sabine Kunst

Dekan der Mathematisch-Naturwissenschaftlichen Fakultät:
Prof. Dr. Elmar Kulke

Gutachter/innen:
1. Prof. Dr. Ulrich Panne
2. Prof. Dr. Michael W. Linscheid
3. Prof. Dr. Ilko Bald

Tag der mündlichen Prüfung: 19.10.2018

Abstract

Without any doubt, one of the most momentous technical achievements of the last century has been the invention of the laser. Today, merely some decades after its first technical realization, the laser has established a leading role in such broad application fields as sensing and control engineering, consumer electronics, as well as industrial production and materials processing. Analytical chemistry does not make an exception. The possibility of both spatially and temporally well-confined introduction of precisely dosed and defined energy into any material is nowadays widely exploited in a plethora of analytical techniques. A milestone in the field of laser technology was the advent of diode-pumped solid-state (DPSS) lasers. This new generation of laser systems combines the benefits of an advantageous energy balance, caused by resonant excitation of the laser medium, with an enhancement in flexibility in terms of modulation of the laser output. While DPSS lasers already account for half of the devices used in materials processing, the dissemination in the analytical sciences has so far hardly occurred. Also here, the inherent advantages of DPSS lasers regarding efficiency, reliability, flexibility, and beam profile could greatly contribute in a multitude of analytically relevant sub-steps. This thesis closes this gap by studying the applicability of a current state-of-the-art DPSS laser for as different tasks as laser ablation, Raman spectroscopy, atomic and molecular emission spectroscopy, all the way to generating a generally new quasi-continuous airborne plasma for ambient ionization. In all cases studied, the improvement of the respective analytical techniques could be ascribed to the intrinsic properties of the used laser.

Zusammenfassung

Eine der bedeutendsten technischen Errungenschaften des letzten Jahrhunderts beinhaltet zweifelsfrei die Erfindung des Lasers. Bereits wenige Jahrzehnte nach seiner ersten technischen Umsetzung ist er heute aus so unterschiedlichen Anwendungsbereichen wie der Mess- und Regeltechnik, der Unterhaltungselektronik, sowie der industriellen Fertigung und Materialbearbeitung nicht mehr wegzudenken. Die analytische Chemie bildet hier keine Ausnahme. Die Möglichkeit mittels Laserstrahlung sowohl räumlich als auch zeitlich definiert einen maßgeschneiderten Energieeintrag in Materialsysteme vorzunehmen, wird heute umfangreich in diversen Analyseverfahren eingesetzt. Ein Meilenstein auf dem Gebiet der Laserentwicklung stellt die Einführung diodengepumpter Festkörperlaser (DPSS) dar. Diese neuartige Lasergeneration vereint die Vorteile einer begünstigten Energiebilanz durch resonante Anregung im Lasermedium mit einer erhöhten Flexibilität der zeitlichen Modulation der Laserausgangsleistung. Während DPSS Laser auf dem Gebiet der Materialbearbeitung bereits die Hälfte des Marktanteils ausmachen, finden sie bislang in den analytischen Wissenschaften nur wenig Verbreitung. Auch hier könnten die inhärenten Vorteile von DPSS Lasern bezüglich Konversionseffizienz, Stabilität, Flexibilität und Strahlprofil maßgeblich zu einer Optimierung relevanter Teilschritte beitragen. Die vorliegende Arbeit schließt diese Lücke, indem sie die Anwendbarkeit eines modernen DPSS Lasers für solch unterschiedliche Aufgaben wie der Laserablation, der Raman-Spektroskopie, der atomaren und molekularen Emissionsspektroskopie, bis hin zur Erzeugung eines neuartigen quasi-kontinuierlichen, luftgetragenen Plasmas für die Atmosphärendruck-Ionisation untersucht. In allen Studien konnten die Verbesserungen der jeweiligen analytischen Verfahren auf die Eigenschaften des verwendeten Lasers zurückgeführt werden.

Table of Contents

List of Abbreviations

APCI	atmospheric pressure chemical ionization
APGD	atmospheric pressure glow discharge
API	atmospheric pressure interface
APPI	atmospheric pressure photoionization
CI	chemical ionization
DAPCI	desorption atmospheric pressure chemical ionization
DAPPI	desorption atmospheric pressure photoionization
DART	direct analysis in real time
DBD	dielectric barrier discharge
DESI	desorption electrospray ionization
DPSS	diode-pumped solid-state
EI	electron ionization
EL-API-HTOF MS	einzel lens atmospheric pressure interface high resolution time-of-flight mass spectrometer
ESI	electrospray ionization
FAPA	flowing atmospheric-pressure afterglow

ICP	inductively coupled plasma
LA DBD MS	laser ablation dielectric barrier discharge mass spectrometry
LA ESI MS	laser ablation electrospray ionization mass spectrometry
LA ICP MS	laser ablation inductively coupled plasma mass spectrometry
LAMMA	laser microprobe mass analyzer
LDI	laser desorption / ionization
LIBS	laser-induced breakdown spectroscopy
LIMS	laser ionization mass spectrometry
LIP	laser-induced plasma
LTP	low-temperature plasma
MALDI	matrix-assisted laser desorption / ionization
MCP	multichannel plate
MIPI	microwave-induced plasma ionization
Nd:YAG	neodymium-doped yttrium aluminum garnet
Nd:YVO_4	neodymium-doped yttrium orthovanadate
OES	optical emission spectroscopy
PADI	plasma-assisted desorption / ionization
Q-API-HTOF MS	quadrupole atmospheric pressure interface high resolution time-of-flight mass spectrometer
SIMS	secondary ion mass spectrometry
TIC	total ion current
TOF MS	time-of-flight mass spectrometer

List of Figures

1 Introduction

The work described in this thesis outlines several promising applications of a diode-pumped solid-state (DPSS) laser, including (1) a laser ablation system coupled with plasma post-ionization, (2) a hybrid setup combining ambient mass spectrometry and Raman spectroscopy in a single instrument, and (3) a novel ionization technique based on an airborne laser-spark ion source. Within the scope of this introductory chapter, first, an overview of the projects realized within this thesis is given, followed by a brief review of important scientific concepts relevant to this work. Particular focus will be put on the DPSS laser, the fields of ambient mass spectrometry and Raman spectroscopy, as well as the characterization of plasmas. Specific and more detailed overviews of the scope of each individual study are enclosed within the respective chapters.

1.1 Scope of the Presented Work

The physical properties of lasers, such as coherence, monochromatism, collinearity, and brilliance allow for unrivaled focusing conditions of their optical output. The resulting small dimensions of a tightly focused laser spot provide unique spatial resolution, while the resulting high energy densities allow for the controlled formation of highly energetic, as well as temporally and spatially well-confined plasmas. Both features show great potential for analytical applications. DPSS lasers combine these typical advantages of lasers with unprecedented portability, duty cycles, lifetime, and applicability in harsh environments at favorable energy conversion rates.[1] The design and set-up of analytical instrumentation that can potentially benefit from this enabling technology has until now only been scarcely reported.

This thesis focuses on the development of novel analytical applications that exploit the exceptional characteristics of DPSS lasers. Different setups have been designed, built, and tested, including (1) a laser ablation system coupled to dielectric barrier discharge (DBD) post-ionization for ambient mass spectrometry, (2) a hyphenated setup combining ambient mass spectrometry and Raman spectroscopy in a single instrument, and (3) a novel ambient ionization source based on a quasi-continuous airborne laser-spark. The thesis is structured as follows:

The remainder of this introductory chapter provides a brief review of important scientific concepts relevant to this work. In particular, the operation principle and advantages of the DPSS laser are described, followed by an introduction to the analytical methods of ambient mass spectrometry and Raman spectroscopy. Since each of the above-named experimental arrangements (1–3) involves a plasma for the generation of charged particles, the evaluation of their performance and fundamental characteristics is another essential part of this thesis. Consequently, also a brief introduction to the characterization of plasmas is given here.

In Chapter 2, a custom-made electrically driven plasma probe based on the working principle of a DBD is described and characterized by its transient current / voltage consumption, optical emission spectroscopy, and nascent species mass spectrometry. The herein obtained results reveal the presence of two distinct charge moieties, which significantly affect the formation of reactant species for mass spectrometry applications.

While electrically driven plasmas are capable of ionizing a wide range of low molecular weight compounds, they are mainly applied for producing ions out of highly volatile molecules. Therefore, the presented setup of Chapter 2 was extended by a DPSS laser for an efficient conversion of low vapor pressure samples into the gas phase, followed by a subsequent ionization of the ablated neutrals in the intercepting DBD exhaust. The construction, optimization, and application of this prototype is presented in Chapter 3.

Though mass spectrometry ranges among the most informative analytical techniques available, it is not the ultimate solution to every complex analytical problem. Hence, today's research aims at the combination of different analytical techniques. Within Chapter 4, such a hyphenated setup, based on the instrumental integration of the laser ablation post-ionization technique and Raman spectroscopy into one experimental setup, is presented. The characteristic feature of this system is the single DPSS laser unit and optical beam path, shared by both individual experiments. The variable repetition rate of the DPSS laser enables the user to perform either the spectrometric or the spectroscopic experiment. The final design allows for the observation of complementary information from the same sample spot, thereby facilitating the unambiguous identification of analytes.

While the experiments presented in Chapters 2–4 utilize an electrically driven plasma for the ion formation from neutral gas phase analytes, an alternative approach for the non-targeted spectrometric analysis of samples can be realized using an airborne laser-spark ion source. Instrumental details on this novel ionization scheme, as well as a comprehensive feasibility study to evaluate its performance as an ion source for ambient desorp-

tion / ionization mass spectrometry, can be found in Chapter 5. Though such plasmas are typically applied for the atomization / ionization of sample material, simple and uncluttered mass spectra out of different gaseous, liquid, and solid phase test samples are observed displaying almost exclusively intact molecular ions.

In order to understand this process on a fundamental level, in the first part of Chapter 6, the gas phase, fluid-dynamic, and chemical processes in and around the plasma are elucidated by means of time-integrated and time-resolved optical emission spectroscopy, shadowgraph imaging, and mass spectrometry. In the second part of Chapter 6, the laser-spark technique is applied for the detection of different low molecular weight volatile organic compounds. Therefore, a gas phase sampling unit is added to the experimental arrangement presented in Chapter 5. After successful optimization, analytical figures of merit are determined. Moreover, for a rough classification among existing atmospheric pressure ionization techniques, real life samples are analyzed and the results are directly compared to an atmospheric pressure chemical ionization (APCI) setup.

Chapter 6 reveals that, in contrast to electrically driven plasma approaches, in the laser-induced analogue a shock wave is formed that results in a dynamic matter transport. The latter causes a rarefied density regime in the former plasma core, thus leading to a decrease in plasma density and analyte number density, both of which are detrimental for analytical purposes. To compensate for this effect, in Chapter 7, the implementation of an ultrasonic acoustic resonator into the experimental setup shown in Chapter 6 is realized. The beneficial effect of an acoustic standing wave inside the resonator on the performance of the airborne laser-spark is visualized by a spectrally dispersed analysis of the emitted radiation, as well as by measuring the positive mode reagent-ion population *via* ambient mass spectrometry.

Finally, a concluding overview about the overall results is given in Chapter 8.

1.2 Diode-Pumped Solid-State Laser

Following the first introduction of the laser,[2] a widespread variety of instruments have been presented, covering a spectral range from the far infrared to the soft X-ray region.[3] Typically, lasers can be categorized according to their gain medium. The most common media include solid-state materials, gases, and liquids. Among these, solid-state gain media are most widely used since they are easily produced without the need of complex capsulation, as compared to gases or liquids, while they typically exhibit a strong gain factor.[4]

Solid-state media are commonly crystalline or glass rods, to which a dopant is added to efficiently absorb the pump light and generate gain. Besides a number of transition metal ions, especially the lanthanide series has proven to be promising candidates as active ions with demonstrated laser transitions in 12 of the 14 elements.[5] Due to their numerous metastable energy levels, the maintenance of population inversion is facilitated. While lanthanides can store absorbed energy on a timescale of milliseconds, transition metal ions, such as chromium, titanium, and cobalt store energy for no more than a microsecond.[6] Furthermore, rare earth elements are used because their excited states are not strongly coupled to thermal vibrations of the crystalline lattice and the lasing threshold can be reached at relatively low pump power. Out of the hundreds of solid-state media in which laser action has been achieved, the most commonly used is the neodymium-doped yttrium aluminum garnet (Nd:YAG). In this case, typically 1% of the yttrium ions in the host crystal structure are replaced by the trivalent neodymium ion.[7]

The most frequently used excitation sources to optically pump conventional solid-state media are flashlamps or noble gas arc lamps. While the lamp pumping benefits from very high pump powers and is accepted as a robust technology, conversion of the pump to laser radiation is typically low, caused by the insufficient overlap of the broad emission spectrum of the excitation source and the narrow absorption lines of Nd:YAG. Typically, less than

3% of the overall electrical input power is converted into laser radiation.[8] Since optical absorption of Nd:YAG is only efficient in relatively narrow wavelength bands, most of the broadband radiation provided by the flashlamp is converted into heat.

Alternatively, laser diodes have shown potential to efficiently pump the gain medium.[9] Laser diodes are semiconductor lasers in which the active medium is a p–n junction and gain is achieved through electrical pumping. In these devices, the recombination of electrons and holes produces a stimulated emission, with the wavelength being determined by the band gap of the semiconductor material. The significant advantages of semiconductor light sources were first recognized by Newman in the early 1960s,[10] only one year after the discovery of the diode laser itself.[11] In this proof of principle, Newman stated that the spectral overlap of a GaAs diode together with the pump absorption band of the trivalent neodymium ion could lead to an efficient, compact, and simplified all solid-state laser. Only one year later, in 1964, Keyes and Quist set up the first DPSS laser. The latter was constructed out of GaAs semiconductor material to pump uranium doped CaF_2 at 4 K.[12] However, early progress was tremendously slowed by the need for cryogenic cooling and the low power levels of the laser diodes. It took again nearly a decade after the first pioneering experiment until DPSS lasers became practical, when efficient high-power and reliable laser diodes that could be operated at room temperature became widely available.[13]

Diode pumping offers certain advantages in terms of optical efficiency, thermal handling, compactness, robustness, lifetime, and beam quality. Because these advantages become relevant throughout this thesis, they are shortly explained in the following:

(1) *Optical efficiency*: By using narrow band emitting laser diodes (optical bandwidth is typically 1 nm) the efficiency of the resonant pump process is dramatically increased. Direct excitation of the absorption band of the active medium minimizes the unwanted losses in the lasing crystal with an optical to optical conversion efficiency of up to 70%.

As compared to the values for conventional flashlamp pumping of 3–5%, the electrical to optical efficiency of a DPSS laser typically ranges between 25–50%.[5]

(2) *Thermal handling*: Since the pump source resonantly pumps a single absorption band of the active dopant, in contrast to conventional broadband flashlamps which pump over most of the visible spectrum, the heat loading in the diode-pumped system, with respect to the available laser power, is dramatically reduced. Consequently, thermal effects, such as stress birefringence, thermal lensing, and thermal fracture of the gain medium, are significantly reduced, which reflects in an increased quality of the lasers' temporal and spatial beam profile. Likewise, the reduced amount of heat enables current state-of-the-art instruments to use solely air-cooling systems instead of an active liquid cooling. This feature allows to construct compact and portable devices for in-field applications.

(3) *Long lifetime*: The use of laser diodes to pump solid-state lasers was further driven from applications that require efficient, reliable, and especially long-lived optical sources, such as remote sensing from satellites or space-based communication, where routine service is not possible.[14] The operational lifetime of laser diodes at room temperature is much larger than that of conventional arc or filament lamps. While commercial laser diodes operate without significant degradation for more than 30 000 hours in continuous wave mode or around 10^9 shots in pulsed operation, arc lamps for continuous wave pumping are typically replaced after 200–400 hours of operation and flashlamps for pulsed pumping after approximately 10^7 pulses.[14,15]

(4) *Compactness and robustness*: The most straightforward reduction in the DPSS lasers' size stems from the fact that diodes are smaller than arc lamps. Due to the lower thermal restraints, the optical gain medium can be built smaller. Often crystals of only several millimeter in size are used.[16] On top of that, the redundant liquid cooling offers another possibility to shrink the diode-pumped laser in size. Since the pumping radiation can be also delivered *via* optical fibers,[17] an even more compact and additionally more

robust geometry can be achieved. The absence of moving parts and the redundant service access for lamp exchange make these lasers ideally suited for an integrated design.

(5) *Beam quality*: In flashlamp-pumped lasers, the heat is deposited in the total volume of the active gain material. However, the cooling is only performed at the edges of the laser crystal, which induces a temperature gradient inside the gain medium. This leads to a gradient in index of refraction, and thus allows for a stable coexistence of multiple lasing modes inside the resonator. In contrast, DPSS media are more isotropically thermalized, and a single mode operation is favored. Single mode lasers have a better quality, expressed by the so called M^2 factor. The latter quantifies the real deviations from an ideal Gaussian beam and reflects how well the laser beam can be focused. As a consequence, the output of a DPSS laser can be focused onto a smaller spot, resulting in higher photon densities and better spatial resolution in laser spot interrogation experiments.

(6) *Flexible repetition rates*: In contrast to flashlamps, optical pumping *via* diode lasers occurs continuously. The high brilliance of the diodes' output realizes a steady population inversion inside the gain medium. This inversion can be depopulated randomly, which ensures a maximum flexibility in repetition rates of DPSS lasers. In principle, all rates between single shot and continuous wave operation can be achieved with one single resonator setup, whereas in traditional lasers the optical beam path and the cooling need to be adjusted to the operation rate. Thus, flashlamp-pumped lasers are commonly restricted to lower repetition rates of 1–100 Hz.

In case of the DPSS analogue, the repetition rate flexibility once more greatly benefits from the little thermal heating of the gain medium, independent on its excitation / depletion equilibrium and the high quality beam profile. Consequently, DPSS lasers can be operated at repetition rates of several (up to hundreds) kHz. At comparable temporal pulse widths, this corresponds to duty cycles of 10^{-5}–10^{-3}, *i.e.*, 2–4 orders of magnitude higher than that of conventional lasers.

In summary, DPSS lasers are attractive sources of coherent light for many different scientific applications. The plethora of advantages given above highlight the technological potential and indicate the full potential of this novel technique still being far from exhaustively exploited. Compared to its lamp-pumped predecessor, the inherent advantages of the DPSS laser regarding efficiency and reliability, compactness and ruggedness, as well as flexibility and versatility are outstanding. Ideally, these advantages can be directly transferred to the analytical instruments deploying laser radiation.

1.3 Ambient Mass Spectrometry

In 1912, Thomson and Ashton visualized the deflection of neon ions in an electrical field and discovered that neon is composed of the two isotopes ^{20}Ne and ^{22}Ne.[18] Their device was the first setup in which ions were separated at reduced pressure according to their mass-to-charge ratio (m/z), later known as mass spectrometry. Since the first discovery, the field of mass spectrometry was extended by a number of groundbreaking, sometimes Nobel Price rewarded experiments and has become one of the most powerful analytical techniques for chemical identification and quantitative analysis.

In principle, every mass spectrometer comprises three fundamental components: An ionization source is required to transfer the target molecules / atoms from the condensed phase to the gas phase, and subsequently forms ions out of the former neutral species. Due to their charge, these ions can be effectively manipulated in an electric or magnetic field, and thus separated based on their m/z in the mass analyzer. Eventually, the ions are observed with a detector. Taking into account the high demands on collision-free ion flight paths, it is essential to provide vacuum conditions. Thus, for a long time, mass spectrometry experiments were performed directly inside the high vacuum housing of the mass spectrometer.

Certain technical developments had a dramatic impetus on the entire field of mass spectrometry by making it possible to ionize and investigate new classes of compounds. For instance, initially, samples could be only ionized in vacuum, which imposed many limitations on the analyte. While volatile samples could be successfully studied, the fundamental problem in analyzing non-vacuum compatible compounds, such as liquids or liquid-containing solid samples, was the high gas load that would be generated from the evaporating system. As the mass analyzer and the detector require a low pressure environment, the applied pumping ensemble needs to cope with the large gas volumes generated. For instance, a liquid flow of 1 mL min^{-1} water results in a gas load of more than 1 L min^{-1} upon evaporation.[19]

During that early stage of mass spectrometry, electron ionization (EI)[20] and later on also chemical ionization (CI)[21] were most commonly applied for ion generation. Besides the fact that both techniques were still restricted to vacuum, which tremendeously limited the range of applicable target analytes, the development of CI made soft ionization of volatile compounds practical that otherwise suffer from extensive fragmentation under the high energetic EI conditions. Early notable efforts to decouple the ionization process from the high vacuum region of the mass analyzer *via* atmospheric pressure interfaces were presented in the 1960s. The implementation of the pinhole orifice by Knewstubb *et al.*[22] and Shahin,[23] the usage of multipole ion guides,[24] and the technological progress in turbomolecular pump techniques, paved the way for the subsequent development of atmospheric pressure ion sources, started by Horning and co-workers in the 1970s. Initially, their design of an external ionization source employed a ^{63}Ni foil as a source of electrons to induce the ionization of reagent gas,[25] but was replaced later on by a corona discharge electrode. The latter was successfully coupled to gas chromatography mass spectrometry and liquid chromatography mass spectrometry.[26,27] Moreover, for the first time, the term atmospheric pressure ionization was coined, which since then became established as a collective term comprising different ionization schemes that share the common denominator of ion formation at atmospheric pressure.[25]

Albeit functional, these ionization schemes could not cope with the analytical demand for high sample throughput in liquid chromatography applications, as well as sensitivity for high molecular weight compounds. For samples in the liquid phase, these issues were solved with the introduction of electrospray ionization (ESI),[28] based on the preliminary research of Dole and co-workers.[29,30] For the spectrometric analysis of condensed phase samples, matrix-assisted laser desorption / ionization (MALDI)[31,32] was introduced, which was later on transposed to atmospheric conditions by Laiko *et al.*[33] Even though ESI and MALDI have simplified the spectrometric analysis and range upon the standard ionization methods in mass spectrometry, still complex and time-consuming sample treatment steps are required that may introduce chemical interferences, as well as perturbation of the analyte environment and its spatial distribution in the matrix.[34] Furthermore, classical ESI and MALDI are incapable of directly volatilizing analytes from the untreated sample, which makes complex sample introduction approaches mandatory.

The latest contemporary revolution in the history of mass spectrometry was launched in the early 2000s with the introduction of desorption electrospray ionization (DESI)[35] and direct analysis in real time (DART).[36] Compared to ESI and MALDI, these ionization schemes already enclose the sampling into the evaporation / ionization step, and thus generate analyte ions out of the unpreprocessed sample at atmospheric pressure. Inspired by the advent of these two techniques, a new subfield of mass spectrometry emerged, later referred to as ambient mass spectrometry[37] and ambient desorption / ionization mass spectrometry.[38]

A conceptual diagram of an ambient desorption / ionization mass spectrometry experiment is shown in Fig. 1.1. The sample is placed within the desorption / ionization beam. Primary reactants are carried from the ion generation region to the sample with a sweep gas and / or a liquid, resulting in the release of analyte molecules into the gas phase, followed by the subsequent ionization step. *Via* the atmospheric pressure interface, ions are drawn into the mass spectrometer, separated with respect to their m/z, and detected.

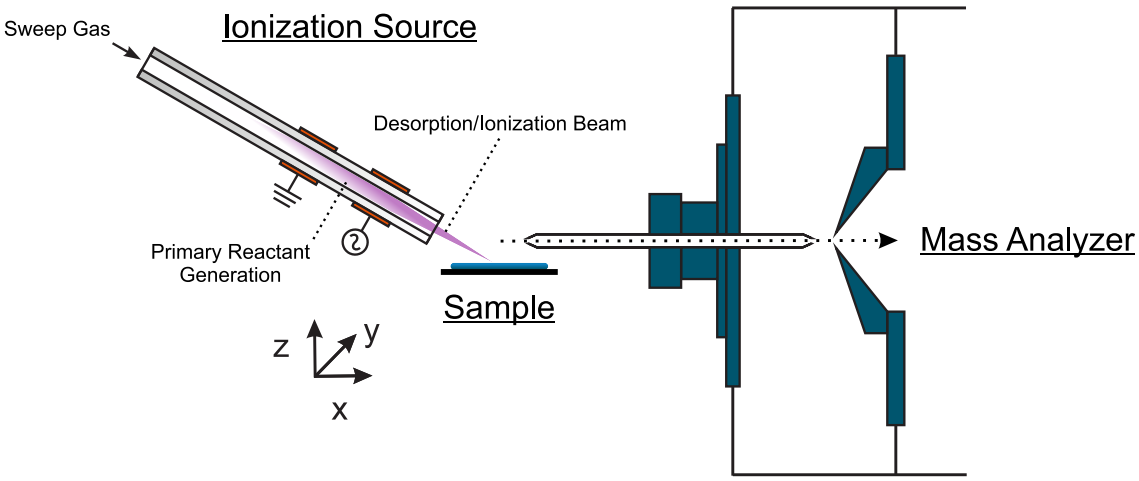

Figure 1.1: Conceptual diagram of an ambient desorption / ionization mass spectrometry experiment comprising an ionization source operated under ambient conditions, the sample, and an atmospheric pressure mass spectrometer.

Ambient mass spectrometry combines the benefits of recent advances in vacuum and ion source technology with the high selectivity and sensitivity inherent to the spectrometric analysis. Each of these techniques shares the following main features:

(1) *Simplicity*: Ions are generated and maintained under atmospheric conditions, which allows unique experiments to be performed on a variety of samples in their native state, [39,40] a process which previously required significant sample preparation.

(2) *Sensitivity and chemical specificity*: Ambient ionization mass spectrometry is well-suited for trace analysis. Detection limits into the low femtomole range have been observed for DART [36] and DESI. [40–42] Moreover, these methods have been shown to display a comparably low matrix and salt sensitivity, one of the typical drawbacks of ESI. [43]

(3) *Minimal sample pretreatment*: Additional and time-consuming sample preparation steps, such as preconcentration, extraction, derivatization, or dissolution, are no longer needed (except the addition of internal standards for quantitative analysis). As a re-

sult, ambient mass spectrometry has been greatly acknowledged by different scientific disciplines for *in-situ* chemical analysis, spatially resolved interrogations, non-destructive surface analysis, or even *in-vivo* investigations.[34,44,45]

(4) *High-throughput and real-time capability*: Transferring the ion generation outside the mass spectrometer minimizes the total analysis time for a single measurement and allows for the rapid screening and simultaneous identification of different compounds in complex matrices. Usually, the total analysis time per sample can be reduced to less than 5 s.[46] Thus, ambient mass spectrometry has become more and more associated with as diverse applications as drug discovery, doping control, forensics, food safety, and quality control.[37,45,47]

(5) *Portability*: Without substantial modifications, each desorption / ionization technique is interfaceable to nearly any current state-of-the-art atmospheric pressure mass spectrometer, including commercially available benchtop systems, as well as portable miniature mass spectrometers.[48,49]

(6) *Soft ionization*: Ambient ionization is commonly referred to as a soft ionization technique.[50] Since the excess energy can be easily dissipated among the ubiquitous air molecules *via* collisional cooling, often, but not necessarily, simple and uncluttered mass spectra with little or no fragment-ion content are obtained. The spectral simplicity can be rationalized by the involved ionization processes. The latter mostly occur by analogy with ESI or CI mechanisms, which are known to produce few fragment-ions.[38]

With the development of new variants, combinations, and hybrids, a plethora of terminologies and acronyms have been introduced since 2004. As a consequence, distinguishing the ambient desorption / ionization techniques from the more conventional atmospheric pressure ionization sources can help to delineate the different applications that are best paired with each method.[50] The classification into subsets varies in between the avail-

able review articles, with a certain degree of overlap.[38,51–55] The following classification proposed by Monge *et al.*[44] is based on the underlying intrinsic desorption / ionization mechanisms.

- One-step techniques where desorption occurs by solid-liquid extraction followed by coventional atmospheric pressure ionization-based ion production mechanisms.
- One-step plasma-based techniques involving thermal or chemical sputtering neutral desorption followed by gas phase chemical ionization.
- Two-step techniques involving thermal desorption or mechanical ablation in the first step followed by a second, separate step where secondary ionization occurs.
- Two-step techniques involving laser desorption / ablation followed by an independent secondary ionization step.
- Two-step methods involving acoustic desorption approaches.
- Multimode techniques combining two or more ambient mass spectrometry techniques.
- One-of-a-kind techniques that make use of other principles for desorption or ionization that do not belong to any of the previous categories.

While these subsets are sometimes debatable, they should help to range the introduced ionization techniques within this thesis among the existing ionization schemes for ambient mass spectrometry.

1.4 Raman Spectroscopy

The phenomenon of Raman scattering was first observed by Raman and Krishnan,[56] and independently by Landsberg and Mandelstam in 1928.[57] Their results confirmed the earlier theoretical predictions of Smekal about the inelastic scattering of light.[58] Since these early days, Raman spectroscopy has become an established and practical method of chemical analysis and characterization.[59,60] The mechanism that leads to a Raman spectrum is a nonresonant scattering process. Thus, for a fundamental understanding, a short consideration of inelastic light-matter interaction is helpful.

Photons can be described as a wave vector with a momentum p corresponding to an energy E that is represented by its time-dependent electromagnetic field. When molecules are subjected to radiation, each molecule experiences this energy as an oscillating electric field, which can be expressed as

$$\mathrm{E} = \mathrm{E}_0 \cos(2\,\pi\,\nu_0\,\mathrm{t})\,, \tag{1.1}$$

where E_0 is the amplitude and ν_0 the frequency of the electric field component of the incident radiation. Caused by the electrons movement along the molecular orbitals around the nucleii, the molecules themselves also feature transient electromagnetic fields. When light is scattered by a molecule, the time-dependent electric field component of the incoming radiation can interact with the electron cloud of the molecules, inducing an electric dipole moment μ, which is given by

$$\mu = \alpha\,\mathrm{E} = \alpha\,\mathrm{E}_0 \cos(2\,\pi\,\nu_0\,\mathrm{t})\,, \tag{1.2}$$

with the molecule specific polarizability tensor α, quantifying the extent of the linear perturbation. In an elastic scattering process, no energy conversion occurs and the induced dipole will emit radiation of its own oscillating frequency, *i.e.*, the excitation frequency. This process is known as Rayleigh scattering. If the molecule is treated to posess different

vibrational energy states, inelastic scattering, including a transformation from kinetic to potential energy, can occur. In the simplest case of a harmonic diatomic molecule with a ladder of vibrational eigenstates, energetically separated by the frequency ν_{vib}, the nuclear displacement Q is described as

$$\mathrm{Q} = \mathrm{Q}_0 \cos\left(2\ \pi\ \nu_{vib}\ \mathrm{t}\right), \tag{1.3}$$

where Q_0 is the amplitude (maximal displacement) of the molecular vibration. For small displacements, the polarizability as a function of this displacement α can be approximated by a Taylor series expansion, namely,

$$\alpha = \alpha_0 + \frac{\delta\alpha}{\delta\mathrm{Q}}\,\mathrm{dQ}\,. \tag{1.4}$$

In this equation α_0 represents the polarizability at the equilibrium position and $\frac{\delta\alpha}{\delta\mathrm{Q}}$ is the derivative of α with respect to the change in Q. Eventually, substitution of Eq. 1.4 into Eq. 1.2 yields

$$\begin{aligned}\mu = {} & \alpha_0\ \mathrm{E}_0 \cos\left(2\ \pi\ \nu_0\ \mathrm{t}\right) \\ & + \frac{1}{2}\left(\frac{\delta\alpha}{\delta\mathrm{Q}}\right)\mathrm{Q}_0\ \mathrm{E}_0 \cos\left[2\ \pi\ \left(\nu_0 - \nu_{vib}\right)\ \mathrm{t}\right] \\ & + \frac{1}{2}\left(\frac{\delta\alpha}{\delta\mathrm{Q}}\right)\mathrm{Q}_0\ \mathrm{E}_0 \cos\left[2\ \pi\ \left(\nu_0 + \nu_{vib}\right)\ \mathrm{t}\right].\end{aligned} \tag{1.5}$$

In addition to the elastic Rayleigh scattering in which the frequency of the light ν_0 does not change by definition, two frequencies, namely, $\nu_0 \pm \nu_{vib}$, arise. Here, the scattered light has a different frequency than the incident light, differing by the energetic equivalent of the molecular frequency ν_{vib}. By analogy with the redshift observed in fluorescence experiments, this shift is referred to as Stokes shift. Consequently, the inelastic scattering processes are called Stokes and anti-Stokes scattering, referring to a red and blueshift, respectively. In the practical application of Raman scattering, a spectral analysis of the scattered light reveals spectral lines that are displaced with respect to the central Rayleigh

peak by the vibrational energy of the individual vibrations in the scattering molecules. In this way, a vibrational spectrum can be obtained without the necessity of resonant absorption spectroscopy, as in IR spectroscopy. Accordingly, Raman spectroscopy yields information specific for the sample under investigation and provides a structural fingerprint by which molecules can be identified.[61] Further, Eq. 1.5 also indicates that if the polarizability does not change during a vibration, the corresponding transition is not Raman active. Compared to IR spectroscopy in which vibrational transitions only become visible if the vibration goes along with a change in the molecules total dipole moment, this results in two different selection rules for the two vibrational spectroscopy techniques. Considering an oscillating dipole as the source of radiation, the intensity of the scattered light I can be given by the proportionality formula[62]

$$\mathrm{I} \propto \left(\frac{\delta\alpha}{\delta \mathrm{Q}}\right)^2 \mathrm{I}_0 \, \mathrm{N} \, (\nu_0 \pm \nu_{vib})^4 \,. \tag{1.6}$$

According to Eq. 1.6, the scattered radiation depends on the derivative of the polarizability, the intensity of the incident radiation I_0, the number of scattering molecules N, and the frequency of the scattered light. Regarding these dependencies, Raman spectroscopy can be used quantitatively and the signal strength (and thus the sensitivity of the method) scales with the intensity and the wavelength of the used excitation light. This scaling with the properties of the incident light, together with the fact that Raman scattering does not require resonant light (*i.e.*, of a specific wavelength), make lasers ideal excitation sources for Raman experiments.

Fig. 1.2 depicts an energy diagram of the three principal scattering processes and the corresponding theoretical Raman spectrum. The most intense type of scattering is the Rayleigh scattering. In this process, after an excitation into a virtual energy state, the excited molecule returns back into its original vibrational state. Since the release of energy during the relaxation process equals the energy initially absorbed, no net change in energy is involved. Consequently, the incident photon is re-emitted with the same wavelength.

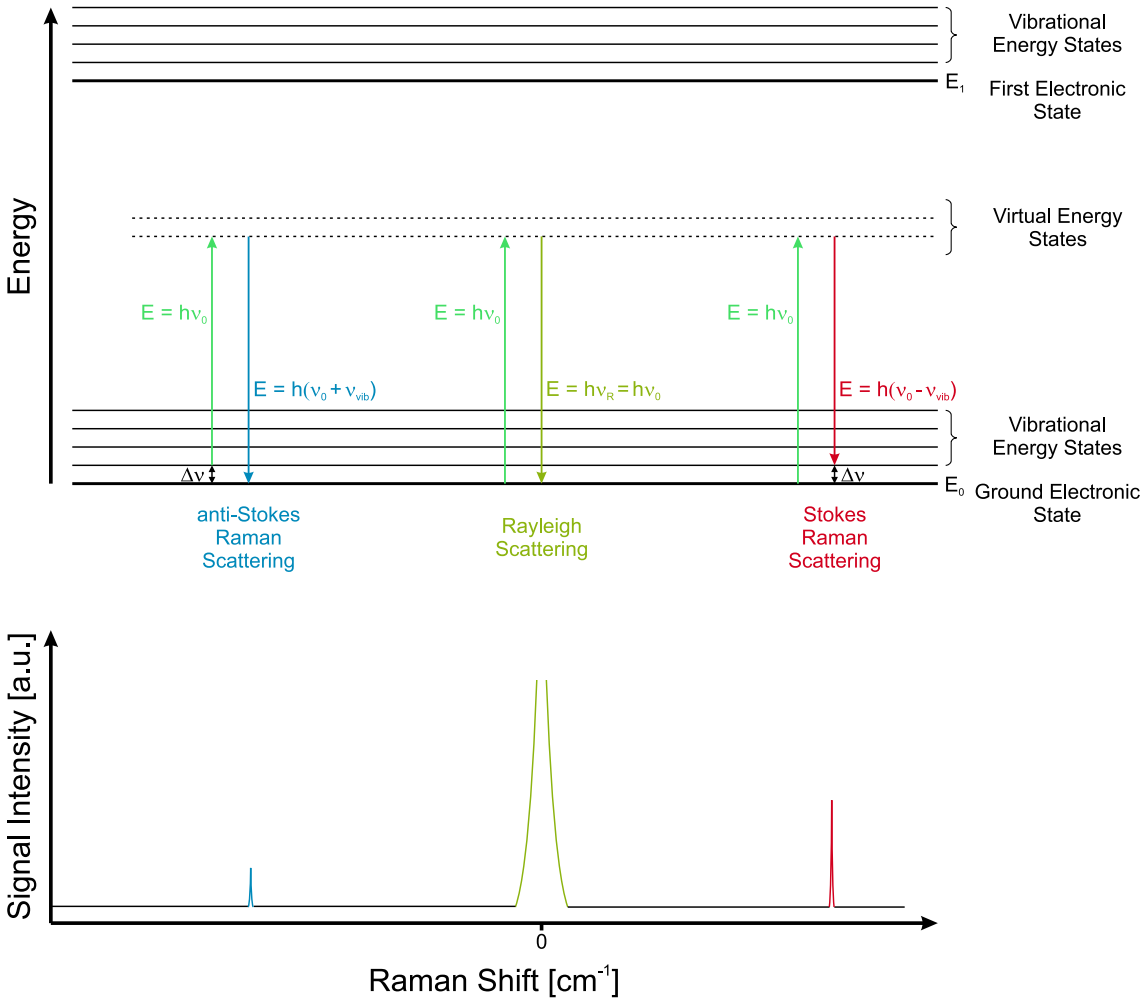

Figure 1.2: Energy diagram (top) displaying the principal energy transfers related to Raman spectroscopy: anti-Stokes Raman scattering (scattered photon has higher energy than the incident photon), Rayleigh scattering (incident and scattered photon have the same energy), Stokes Raman scattering (scattered photon loses energy compared to the incident photon). Theoretical Raman spectrum (bottom).

In contrast, only ≈ 1 in 10^8 photons is scattered at optical frequencies different from the incident photons.[63] The process leading to this inelastic scatter is termed the Raman effect: The molecule changes its vibrational or rotational state upon the interaction with the incoming photon and the energy of the scattered photon differs by an amount cor-

responding to a vibrational transition. In Stokes scattering, a molecule that is excited from its vibrational ground state to a virtual energy level does not return to the ground state, but to the first excited vibrational state. In this case, the vibrational energy of the molecule is increased and a photon with a red-shifted frequency, and thus lower energy is emitted. Simultaneously, in the anti-Stokes case, the interaction of photons with a molecule already present in the first vibrational level results in the subsequent population and relaxation from a high-lying virtual energy level back to the ground state. Since the final energy level is lower than the primary one, the vibrational energy of the molecule is decreased and blue-shifted photons with a higher energy are emitted.

In the corresponding Raman spectrum, the intensity of the scattered radiation is plotted as a function of the Raman shift (frequency difference to the incident photons). By analogy with IR spectra, the commonly used unit for the latter uses wavenumbers (cm^{-1}). Since the same vibration is involved in both Stokes and anti-Stokes shift, the spectral features are symmetrically distributed around $\Delta\,\nu = 0$. Because according to the Maxwell-Boltzmann distribution at room temperature the majority of molecules exist in the ground state, the respective signal intensities of the Stokes and anti-Stokes lines typically differ by approximately one order of magnitude.[64]

In principle, monochromatic light of any wavelength can be used to obtain a Raman spectrum. Nonetheless, the selection of the excitation wavelength depends on several factors: Considering Eq. 1.6, it becomes clear that the excitation wavelength drastically affects the detection of the scattering process. If the wavelength of the excitation laser is reduced by factor two (*e.g.*, from 1064 nm to 532 nm), the Stokes (and anti-Stokes) bands are 16 times more intense due to the increased Raman scattering cross section. For strong pulsed lasers, the nonlinear efficiency for a frequency doubling process (as the exemplary frequency conversion from 1064 nm to 532 nm) is high and a conversion yield close to 0.5 can be achieved. This implies that it is feasible to include nonlinear higher order frequency generation processes to obtain shorter wavelength laser sources. As a tradeoff,

if the excitation energies reach the visible and ultraviolet wavelength range, fluorescence becomes more pronounced. In contrast to the Raman scattering effect, fluorescence is a resonant phenomenon. As a result, even trace amounts of highly fluorescent impurities or weakly fluorescent samples often mask the Raman bands. To minimize the competetive fluorescence contribution, it is possible to shift the excitation wavelength to the IR region. The explanation is that at a longer wavelength, the energy transitions responsible for the fluorescence are no longer possible. Besides fluorescence quenching, also time-resolved Raman scattering or enhancement techniques, such as Resonance Raman spectroscopy [65] and surface enhanced Raman scattering, [66] are commonly used to enhance the intensity of the Raman scattering, which facilitates the study of compounds present at low concentations. [67–69] Alternatively, UV lasers can be used to improve the spectral quality of the Raman data. [70] In many cases, UV Raman spectroscopy has the advantage of being insensitive to autofluorescence. Though this insensitivity seems counterintuitive in the first place, given that many fluorophores are efficiently excited in this wavelength range, in the deep UV ($\lambda < 250$ nm), the Stokes shift of fluorescence is often much larger than the Raman shift of the bands of interest, and thus autofluorescence does not interfere with the Raman spectrum. [71] The disadvantage, however, is that photochemical processes may lead to undesired side-reactions. In addition, laser heating can also be a problem during such measurements. Especially blue and black samples are capable of absorbing light strongly, and thus blackbody radiation may occur in the spectra, accompanied by thermal damaging of the original structure. [72]

1.5 Plasma Characterization

The term plasma describes a gas which is at least partially ionized and contains particles of various types, such as electrons, radicals, atoms, molecules, and (molecular) ions. [73] It was first introduced by Langmuir in the 1920s. He described his observation as follows: ”Except near electrodes, where there are sheaths containing very few electrons, the ionized gas contains ions and electrons in about equal numbers so that the resultant space charge

is very small. We shall use the name plasma to describe this region containing balanced charges of ions and electrons." [74]

By providing sufficient energy into a neutral gas, positively charged ions can be formed by stripping away electrons from the present atoms and molecules. Both charged and uncharged heavy species (those with nuclei, *i.e.*, all but electrons) carry a high level of internal excitation. For atoms and elemental ions, this means a partial population of excited electronic states, while molecules and molecular ions populate various electronic, vibrational, or rotational excited states. This, eventually, leads to a quasi-stationary thermalization inside the plasma. The deactivation channel of this dynamic equilibrium is dominated by inelastic collisions with cold neutrals, recombination events, radiation, and Bremsstrahlung. Once the activation overcomes this relaxation, a stable plasma can subsist. As a result, positive and negative charges coexist and move relatively independently in the plasma. The behavior of a plasma is largely determined by the charged particles, resulting in unique properties that are not encountered in the three traditional states of matter (solid, liquid, and gas). Accordingly, the plasma is often referred to as the fourth state of matter. Though it is closely related to the gas phase, it differs in a number of ways. Despite the existence of localized charge concentrations, resulting in electrical conductivity, another feature of plasmas is maintaining electroneutrality, because in a microcanonical ansatz there are approximately equal numbers of positively and negatively charged species.

Besides naturally occuring plasmas, as in stars, lightnings, or polar aurorae, plasmas can be produced artificially and operated in a wide range of conditions. [75] Despite the different number densities inside the partially charged gas, a major criterion for classification is the dwell time of the plasma. In a transient plasma (such as lightning), the gas is excited in a temporally singular event and the plasma lifetime is merely determined by the relaxation kinetics. In contrast, in a continuous plasma (such as flames, stars, or the aurora borealis), the excitation occurs on a longer timescale, building up a steady state equilibrium between excitation and relaxation channels. In an artificial plasma, the re-

quired energy for the formation of a plasma medium can be provided by different external sources of energy, including electrical discharges, electromagnetic fields, or the electromagnetic field of a laser. Throughout the remainder of this thesis, two different plasma sources are investigated, namely, a DBD and a laser-induced plasma (LIP), which are commonly used representatives of steady and transient plasmas, respectively.

The physics involved in a gaseous breakdown is complex and the physical properties change significantly with space and time. Hence, it is important to characterize the plume properties with high spatial and temporal precision. A wide range of plasma diagnostic tools has been employed in order to comprehensively characterize and determine the decisive properties of atmospheric pressure plasma sources. The applied techniques can be categorized to be either active or passive tools.

Active methods utilize additional sensing devices that "actively" probe the plasma, such as physical sensors or radiation that interact with the plasma. Among these, optical absorption spectroscopy can be applied as a reliable tool for absolute density determination in optically thin media,[76] whereas laser-induced fluorescence[77] allows for the detection of ground states and long-lived metastables.[78] Light scattering, inlcuding Rayleigh[79] and Thomson scattering[80] can be used to determine the electron temperature, while imaging experiments, such as shadowgraphy[81] and Schlieren,[82] are well-known experimental approaches to elucidate the plasma expansion behavior. They provide valuable information about the morphology, shock wave propagation, plasma decoupling, and turbulence formation. Despite the growing contribution of optical techniques, still a classical approach to the diagnostic workflow is represented by electrostatic probes (often associated with the Langmuir probe).[83] In its simplest form, it consists of a metallic electrode, inserted into the plasma. By measuring the current flowing through the probe as a function of the applied voltage, the electron temperature and the electron density can be determined. However, all these active approaches are less often used, because they potentially perturb the plasma, are often expensive, and experimentally demanding.

In contrast, passive interrogation approaches exploit the intrinsic properties of the plasma. Due to the high degree of electronic excitation of the plasma species, a large number of radiative relaxation processes occur. The latter offer the route of plasma characterization by monitoring the optical spectrum, typically in the UV / Vis range, emitted by the plasma. This method can be applied by remote inspection, which is not affecting the plasma in any way and can be realized with robust and inexpensive setups. Optical spectroscopy methods are ideal for determining the spatial and temporal distribution of both ions and neutrals in the plasma discharge, because of their distinct emission. It is one of the oldest and most established diagnostic tools in plasma processing, technology, and fundamental research,[84] and can be traced back to the early 1800s, when scientists first realized that elements emitted specific colors of light.[85] In the presented experiments, characteristic light emitted from the species within the plasma is recorded. This radiation is the result of a specific transition from an excited high lying energy state into an energetically lower state or the electronic ground state, thereby emitting photons. While atoms exhibit discrete well-known energy levels, molecules exhibit further sub-electronic states, arising from the relative movement af the atoms nuclei with respect to each other, which are vibrational and rotational energy levels. Accordingly, every electronic transition may be accompanied by vibrational or rotational transitions that cause a blue or redshift of the energy of the emitted photons, respectively. Hence, atoms typically yield single emission lines for specific transitions, while molecules display a series of spectral lines, so-called progressions.

Optical emission spectra are informationally rich and several physical properties of the plasma can be indirectly derived *via* simple physicochemical treatment of the spectra: The obtained number densities of the individual species allow for an accurate determination of the degree of dissociation. Assuming a local thermodynamic equilibrium, *i.e.*, a population of excited states according to the Boltzmann distribution, the electronic temperature can be obtained by determining the state distribution. Moreover, since the homogenous line broadening in the recorded spectra is dominated by the Stark-effect, the line width of

known transitions is a measure for the electron density. However, the main disadvantage of this technique is that the measurements are integrated over a line of sight, yielding only averaged information along a certain plasma region, and that the processing of data is often indirect.[76] Additionally, a number of species exist that are not well suited for the spectroscopic detection, *e.g.*, protonated water cluster ions, which do not absorb or emit light in the UV / Vis range.[86]

Besides the spectral analysis of the emitted plasma radiation, the group of passive characterization tools also includes electrical measurements, such as recording the current / voltage profiles on the plasma electrodes.[87–89] The temporal behavior of the electrical power uptake can help to classify the discharge type (corona, glow, or spark) for electrically driven plasmas. Furthermore, spectrometric studies can be conducted to examine the population of positively and negatively charged atomic and molecular species in a plasma discharge. Besides the possibility to perform quantitative analysis, mass spectrometry further benefits from its high sensitivity and time resolution capabilities. On the downside, the reagent-ion spectra only depict those ions that survive the transfer to the detector, which is not necessarily representative of what occurs in the discharge itself. For these reasons, the theoretical characterization of plasmas using simulations and numerical models offers an alternative route to gain insight into the large number of plasma processes.[90]

Recapitulating, it has to be mentioned that each of the above-mentioned plasma diagnostic tools is only useful for evaluating certain information about the plasma. Thus, to obtain a detailed picture of the underlying fundamental processes within the respective plasma, this thesis focuses on a comprehensive combination of passive measurements, supplemented by an active visualization.

2 Characterization of a Dielectric Barrier Discharge for Post-ionization

Among the plethora of techniques that have been proposed for ambient desorption / ionization mass spectrometry, the application of a DBD has attracted much attention in different fields of life science. Typically, a nonequilibrium discharge excites a gas stream that subsequently desorbs and ionizes sample matter. To achieve a reasonable sensitivity of these systems, this process has to be located in the immediate vicinity of the MS inlet due to the very short mean-free path and the high collision rates at atmospheric pressure. To circumvent these hindrances and enhance the sampling efficiency, a combination of a laser ablation setup and a versatile DBD probe for post-ionization is proposed. Due to the absence of commercially available DBD ion sources and the fact that the incorporated processes of the desorption / ionization step are not fully understood in detail yet, this chapter focuses first on the characterization of a custom-made DBD ion source, prior to the above-mentioned combination.

Based on:
Bierstedt, A.; Pannne, U.; Rurack, K.; Riedel, J. *Journal of Analytical Atomic Spectrometry* **2015**, *30*, 2496–2506.

2.1 Dielectric Barrier Discharge

The term "dielectric barrier discharge" describes the formation of a nonequilibrium gas discharge under ambient conditions between two electrodes that are powered by modulated high voltage and separated by one or two insulating dielectric barriers. It was first reported by Siemens as a device used to generate ozone from atmospheric pressure oxygen or air.[91] Intensive research, originally oriented toward an improved ozone formation, resulted in diverse applications in many areas of science. Besides widespread biomedical[92] and industrial applications,[93] such as nonthermal decontamination,[94] gas treatment,[95] and materials processing,[87] DBDs are also finding use in analytical research.[96]

Depending on their operation parameters, DBDs can be either used to efficiently dissociate analytes, which promoted their use as atomizers for the elemental detection performed by optical emission spectroscopy[97,98], or they can be applied as ionization sources for ambient mass spectrometry.[45,99–103] For the latter, different configurations have been described wherein the DBD is either utilized for subsequent desorption / ionization of sample matter or applied solely as a source of reagent-ions. In the case of desorption / ionization, the most commonly used configurations are the DBD ion source,[104] the low-temperature plasma (LTP),[105] and the plasma-assisted desorption / ionization (PADI) probe.[106] In contrast, a DBD-based ion source that has been used only for the production of reagent-ions was developed by Hiraoka and co-workers,[107–110] also known as the atmospheric pressure chemi / chemical ionization source. In general, these plasma-driven techniques benefit most from their simplicity, flexibility, portability, the absence of additional solvents, a low power consumption, the possibility to operate at atmospheric pressure with different discharge gases, and their high chemical activity.[93,96,99,101]

The first experimental arrangement for ambient desorption / ionization mass spectrometry originally employed a capacitively coupled discharge between a pin and a copper sheet electrode with the sample positioned on a glass slide placed between the electrodes.[104]

This direct exposure of the analyte to the nascent plasma, however, resulted in a pronounced formation of fragmentation products. In consequence, instrumental development resulted in several indirect sample introduction approaches wherein the sample deposition on the dielectric was discarded. Instead, insulating capillaries that transport the discharge gas were simultaneously used as the dielectric barrier. Two basic configurations have been reported to either construct a plasma jet which is departing the capillary or staying inside the capillary (see Fig. 2.1).[101] A DBD with one dielectric barrier can be constructed by the pin-ring design or the tube-ring design. In both arrangements, modulated high voltage is applied to the ring electrode wrapped around the capillary, while the inner electrode (pin or tube) is grounded. The second configuration comprises the application of two dielectric barriers (ring-ring design). While a dielectric tube is used to guide the discharge gas, two ring electrodes, fixed at a certain distance, are wrapped around the insulator. The application of appropriate high voltage enables the plasma ignition in the airgap between these electrodes.

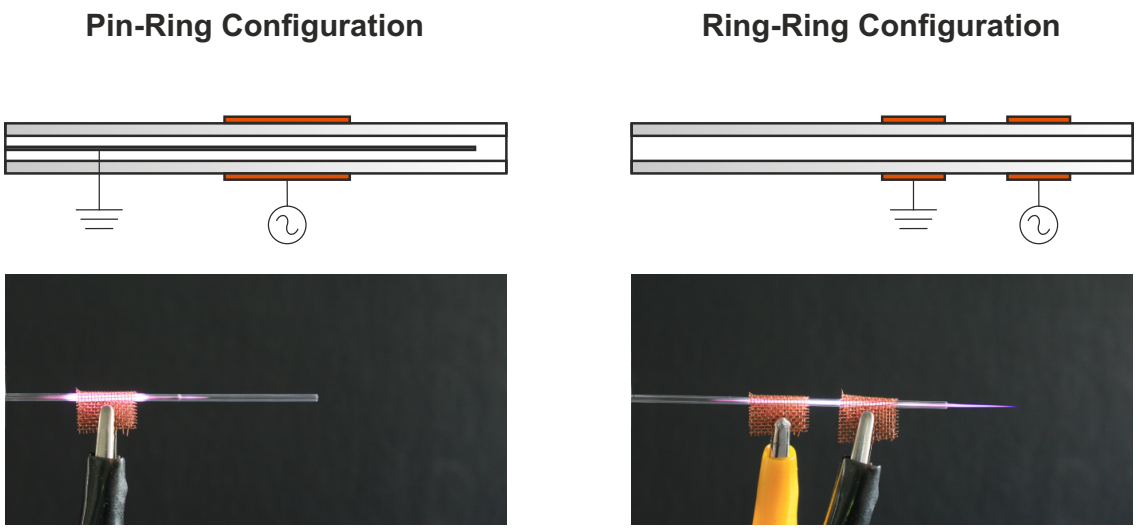

Figure 2.1: Schematic representations of a DBD probe in pin-ring (left) and ring-ring configuration (right), as well as corresponding side-view photographs of the electrical discharges ignited in helium.

In 2010, Almasian *et al.*[111] combined both configurations in a single setup, and thus obtained selectable fragmentation patterns from the same sample. These results demonstrated that tuning the chemical activity of the ion source is possible. In contrast to the steady growing number of publications, the number of fundamental studies elucidating how the probe characteristics affect the ionization performance still lags behind. Without this knowledge, the entire range of compounds, the DBD may be suitable for, cannot be exhaustively utilized and improved. What is known is the following: The discharge region is dominated by a large number of microdischarges. Thus, the breakdown is strongly heterogenous, resulting in a rather low ambient gas temperature of ≈ 30 °C.[112] Highly reactive species, including high-energy electrons, metastable neutrals, and radical ions / neutrals are generated, which potentially transfer charge onto the analyte.

In the indirect sample introduction scheme, the plasma provides the energy for both the sample desorption and the charge transfer for an effective analyte ion formation. A more thorough look onto the two processes and their individual demands should therefore be provided: As in other ambient plasma-based desorption / ionization techniques, the mere sample pick up is favored even by mildly elevated gas temperatures.[113] Thus, the desorption mechanism for most plasma-based ion sources is claimed to be essentially thermal.[105] *Nota bene* the thermal influence refers to the kinetic rotational and vibrational temperatures, under which nuclei are displaced since they carry the main momentum. In strong contrast are the electronic temperatures that can be evaluated *via* Boltzmann analysis of the optical emission spectra. Despite the mild conditions and the low overall heat, the observed electronic state populations in DBDs easily correspond to electronic temperatures of several thousand Kelvin. Though thermal effects certainly influence the desorption process, also other factors, such as chemical sputtering or a photo-induced desorption could contribute and therefore cannot be fully neglected.[114] Opposing the sample desorption, the electronic excitation is commonly accepted to be the driving force for ion formation. Optical spectroscopy experiments showed the state distributions inside the plasma, and therefore also the ionization efficiency, to strongly depend on external parameters of the

plasma source.[78,115,116] Over the years, the main influences were identified to be briefly: (1) the probe geometry, including the material and arrangement of the electrodes and the dielectric,[105,111,117–119] (2) the identity and flow rate of the discharge gas,[104,120] including also the use of additives,[121–123] and (3) the high voltage pulse characteristics.[88]

Based on a comprehensive study on the influence of the applied voltage, Franzke and co-workers[87] reported on the presence of two operational modes in which current flows: a homogenous moiety and a filamentary moiety that can be selectively discriminated against by altering the driving voltage.[124,125] These modes were classified to go along with a soft ionization in the homogenous mode (at low voltages) and a more harsh ionization that leads to considerable dissociation of the target compound for the filamentary operation (driven by higher voltages). Shelley *et al.*[88] demonstrated that the waveform shape also has an influence on the plasma mode. Filamentary discharges that appear to be capacitively driven occur at times when the temporal derivative of the voltage is large, while homogenous discharges are driven by a steep change in the voltage. Furthermore, they also observed a dependence of the type of preferential discharge behavior on the formation of charge transfer and proton transfer products. Most recently, spatiotemporal measurements of the optical emission from a helium-sustained capillary-DBD indicated the ring-ring-shaped plasma to consist of several individual components: the plasma jet, the inner early plasma, and the coincident plasma which is capable of dissociating molecules in the interelectrode region.[126,127]

One subgoal of this thesis is to demonstrate the potential of DPSS lasers in laser ablation / post-ionization applications. For the reasons given above, a DBD was chosen as the (versatile) post-ionization source. However, as can be seen from the vast number of different terminologies and acronyms within the family of plasma-based ion sources, the comparability between the individual instrumental designs is not automatically given. Consequently, this chapter encloses several experiments to evaluate the analytical performance and fundamental characteristics of the custom-made ion source.

2.2 Experimental

2.2.1 Chemical Reagents

Helium (99.999%, Linde, Berlin, Germany), argon ($\geq$ 99.999%, Linde, Berlin, Germany), and nitrogen (99.99%, Air Liquide, Berlin, Germany) were used as plasma gases. Aqueous ammonia solution (20 / 22%) was purchased from Fisher Scientific UK (Loughborough, UK). Acetone (synthesis grade, AppliChem, Darmstadt, Germany) and ferrocene (98%, Acros Organics, Geel, Belgium) were used as target compounds without further purification.

2.2.2 Configuration of the Dielectric Barrier Discharge Ion Source

A schematic of the in-house fabricated DBD ion source is shown in Fig. 2.2a. Briefly, its design is based on the above-mentioned pin-ring configuration. Since the individual components are commercially available mass products, an efficient, low-cost ($<$ 250 €) ion source has been constructed.

Copper mesh (mesh size: 1 mm $\times$ 1 mm, electrode width: 1.0 cm) wrapped around a borosilicate quartz capillary (GB 150-8P, o.d. 1.50 mm, i.d. 0.86 mm, Science Products GmbH, Hofheim, Germany) served as the high voltage electrode. A stainless steel acupuncture needle (NSP 3070 Premium Silver Handle, length: 10 cm, Akupunkturnadeln-Wandrey GmbH, Berlin, Germany) was placed inside the capillary and served as the counter electrode. A 1/16 in. Swagelok Tee-piece was used to fix the position of the grounded electrode, the borosilicate quartz capillary, and the discharge gas feed line. The gas flow was controlled using a GFC17 mass flow meter (0.0–2.0 L min^{-1}, Analyt-MTC GmbH, Müllheim, Germany). Unless stated otherwise, a flow rate of 1.0 L min^{-1} was used. No additional heating of the discharge gas was applied. High voltage was provided by a low-cost flyback transformer (PLASMSP_v2, Voltagezone Electronics e.U., Graz, Austria) fed by using a standard laboratory power supply (Voltcraft PS 2403 Pro, Conrad Electronic, Hirschau, Germany). This generator setup was capable of producing up to

15 kV_{pp} at a sine waveform and a frequency of 120 kHz. The applied voltage was monitored with a high voltage probe (Voltcraft H 40, Conrad Electronic, Hirschau, Germany) coupled to a digital oscilloscope (TDS 2024B, Tektronix, Beaverton, U.S.A.). Current waveforms were recorded by measuring the voltage drop across a 1 kΩ resistor connected between the powered electrode and the ground.

The DBD was mounted onto a manual 3D translation stage (M-UMR5.25, M-UMR8.25, Newport, Irvine, U.S.A. and MT1, Thorlabs, Dachau, Germany) and centered on axis with the inlet capillary, where the population of reagent-ions was found to be at their maximum intensities. The free space distance was set to 2.0 cm, and thus facilitates the sample handling and additional instrumentation. Note further that the dielectric glass tube itself protrudes 3.0 cm from the actual discharge region. In contrast to the widely used ring-ring configuration which yields a considerable afterglow of the plasma (as can be seen on the right in Fig. 2.1), the chosen pin-ring approach (depicted on the left in Fig. 2.1) allowed for an effective spatial separation between the plasma itself and the final sampling region. This arrangement ensured that only the excited gas stream interacted with the sample. Qualitative measurements were conducted by coating the wooden handle of cotton swabs with the neat target samples and exposing them directly at the midpoint between the ion source and the MS inlet.

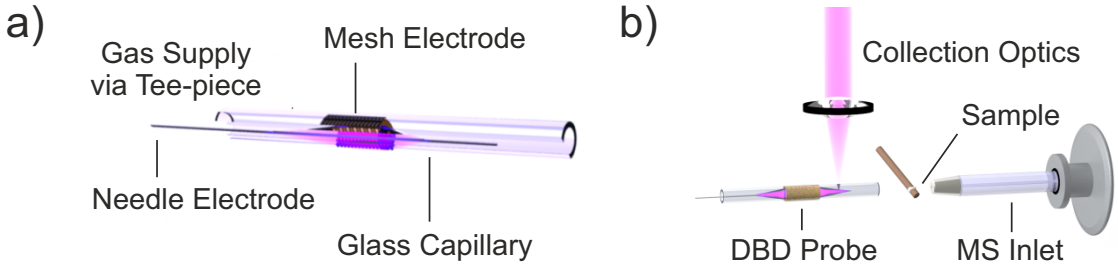

Figure 2.2: (a) DBD probe based on the pin-ring configuration. (b) DBD probe in front of the MS inlet. Collection optics above the plasma probe were installed to characterize the optical plasma emission.

2.2.3 Mass Spectrometer

Mass spectra were recorded with two custom-designed versions of the API-HTOF MS, manufactured by Tofwerk AG (Thun, Switzerland). Both instruments are set up in a similar fashion consisting of a high resolution, orthogonal extraction, reflectron time-of-flight mass spectrometer (TOF MS) and an atmospheric pressure interface (API). The latter is separated into a series of differentially pumped stages, equipped with different ion optics that guide the sampled ions from atmospheric pressure toward the high vacuum region of the mass analyzer, while withdrawing excessive gas and solvent vapor.[128,129] Along the ion travel path downstream of the initial pressure reduction, electrical field strength can be optionally established, which determines the extent of electrical-field-driven chemistry on the acquired ion population.

The expansion of gas into the first stage of differential pumping, as well as the implementation of different ion optics mark the major difference between both instruments. In version 1, ions are drawn into the mass spectrometer through a capillary inlet, followed by a skimmer / einzel lens (EL) assembly to capture and focus the primary ion beam toward the low pressure region of the TOF MS. In contrast, version 2 utilizes a protruding inlet orifice, followed by a combination of two radio frequency-only quadrupoles (Q). The latter result in a better confinement of the primary ion beam, and thus higher ion transmission efficiencies. At the same time, the collisions inside these multipoles can be used to induce an effective collisional dissociation of weakly-bound cluster species, while the skimmer / einzel lens combination of version 1 typically yields a substantial amount of non-thermalized ion / solvent cluster distributions. To denote explicitly each of the above-named instruments, the terminologies "EL-API-HTOF MS" and "Q-API-HTOF MS" are introduced for version 1 and version 2, respectively. Detailed instrumental descriptions of both instruments are attached in Fig. A-1 and Fig. A-3. Unless stated otherwise, both instruments were operated in single reflectron geometry, using the positive ion mode. Integrated mass spectra were recorded with a total acquisition time of 10 s and an extraction rate of 20 kHz.

2.2.4 Time-integrated UV / Vis Emission Spectroscopy

The optical emission of the DBD was investigated in two different configurations: (1) Time-integrated UV / Vis emission spectra were recorded perpendicular to the discharge region *via* a fiber coupling fixed at a distance of 2.0 cm from the powered electrode (refer to Fig. 2.2b). The optical fiber was connected to a Czerny-Turner spectrograph (Shamrock SR-303i-B, 1800 grooves / mm grating, ANDOR Technology Ltd., Belfast, UK), equipped with a CCD camera (iDus, −65 °C, Andor Technology Ltd., Belfast, UK). The entrance slit width was 150 µm and the acquisition time per spectrum was set to 2 s. (2) Additional spectrally and spatially resolved measurements were conducted with a second optical setup that has been described previously for the characterization of LIPs.[130] Therefore, the DBD probe was fixed in a top-down position on a micrometer stage (M-UMR8.25, Newport, Irvine, U.S.A.). The optical emission was collected with a 75 mm focal length lens orthogonal to the dielectric glass tube. The collimated light was guided by three broad band mirrors and focused by a 200 mm focal length lens onto the entrance slit of a Czerny-Turner spectrograph (Acton 500, 2400 grooves / mm grating, Princeton Instruments, Trenton, U.S.A.) coupled to an iCCD camera (PI-MAX, Princeton Instruments, Trenton, U.S.A.). The entrance slit width was adjusted to 50 µm and the wavelength of interest was recorded, yielding 2D images that were obtained slice-by-slice using a step size of 250 µm. For this set of experiments, the acquisition time was increased to 4 s.

2.3 Results and Discussion

The combination of a flyback transformer and a laboratory power supply enables the performance of the DBD to be examined with varying output voltages. Thus, without the necessity of geometrical changes the plasma can be operated either in a homogenous discharge mode at lower output voltages (5 kV_{pp}) or a filamentary discharge mode at higher output voltages (15 kV_{pp}). The chosen power supply generates a sinusoidal waveform with a frequency of 120 kHz. In most earlier studies DBD ion sources were typically limited to a maximum output voltage of about 6 kV_{pp} and lower frequencies.[104,105,111]

2.3.1 Temporally Resolved Current / Voltage Profiles

A simple and universally applicable method to distinguish between the individual discharge regimes is to measure the plasma current. Therefore, transient current / voltage profiles were recorded for the DBD ion source operated with helium. The results are shown in Fig. 2.3. Waveform (a) and (b) represent the homogenous discharge mode at 5 kV_{pp} and the filamentary discharge mode at 15 kV_{pp}, respectively.

As can be seen, both modes produce stable discharges with very reproducible events. However, each regime exhibits a different discharge pattern of current waveforms which are highly dependent on the provided input voltage. Furthermore, the individual waveforms indicate that each half cycle produces short-lived discharges at each transition between positive and negative voltage. Using the homogenous mode (0.9 W, 5 kV_{pp}) only isolated, but regularly distributed discharge events occur. A similar behavior has been observed previously for a squarewave- and sawtooth-driven LTP.[88] These consistent current pulses may indicate the formation of plasma bullets, which are high-velocity ionization waves known to occur within DBDs.[131,132] In contrast, as the applied voltage rises, an increasing number of erratic microdischarges are observed. The detailed process of switching between both discharge moieties can be followed in Fig. A-4 in the appendix. In the filamentary mode (5.6 W, 15 kV_{pp}) the current spikes become more frequent due to the increasing voltage change. The current waveform is dominated by a variety of many short sporadic plasma pulses, accompanied by a minor number of prominent stronger discharges. Compared to the current pulses observed in Fig. 2.3a, here, even the smaller microdischarges carry higher current. In addition, the exact temporal position of the discharge spikes is shifted toward the voltage extrema. While the homogenous discharges occur at a maximum of the first derivative of the current flow, *i.e.*, at the time of the highest capacitive stress, now the absolute value of current leads to discharges. Consequently, the two plasmas can be also described as capacitively driven versus charge-driven. On top of that, at higher voltages the discharge occurs over a longer period of the cycle; hence, results in the production of a higher number of reagent-ions.

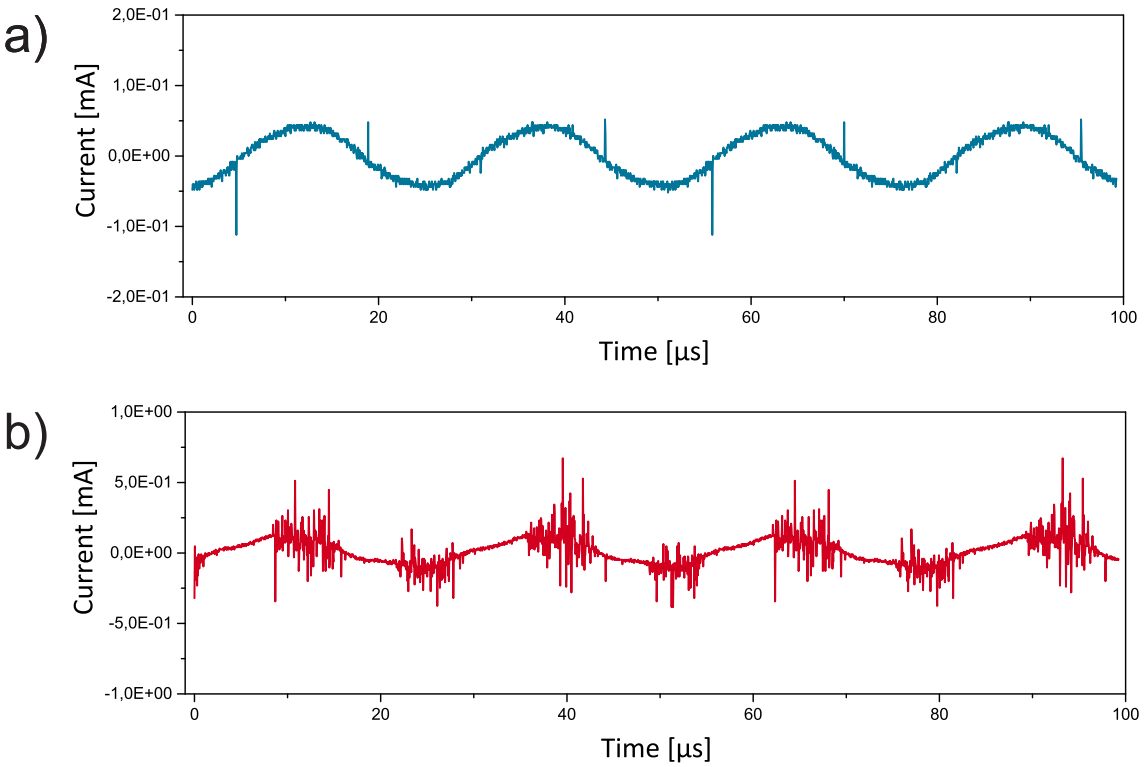

Figure 2.3: Temporally resolved current / voltage profiles for the DBD ion source fed with helium. (a) DBD in homogenous mode (5 kV_{pp}). (b) DBD in filamentary mode (15 kV_{pp}).

2.3.2 Reagent-Ion Formation

A question of fundamental interest in plasma-based ambient mass spectrometry concerns the origin and subsequent reaction pathways of the charging species. Though a wealth of knowledge on the fundamental properties and characteristics of plasmas already exists within the atomic spectroscopy community, the ionization mechanisms of plasma-based ambient desorption / ionization sources are mainly suggested on the basis of the detected background and analyte ions in the mass spectra,[36,105,133] and mechanisms believed to exist in APCI.[25,134] To gain further insight into the subsequent desorption / ionization process, several research groups have initiated work over the last decade.[75,78,115,119,123,135–141] Each of these studies has contributed significant insight and demonstrated the ionization process to be rather complex.

Though all these ion sources operate with fundamentally different discharge settings, they often perform similarly in many aspects of ambient desorption / ionization analysis.[142] For instance, the identity of the plasma gas has been shown to affect the sensitivity and reagent-ion formation, with helium providing the best performance for all sources.[115] Another similarity includes the reactant species they produce: Protonated water clusters $[(H_2O)_nH]^+$ are the predominant positively charged reactants formed in air, accompanied by further ionic species originating from the surrounding atmosphere, such as $N_2{}^+$ and $O_2{}^+$.[36,133,138,143,144] Accordingly, major analyte ions produced are protonated molecular ions $[M+H]^+$, formed *via* proton transfer ionization, and molecular cations $M^{\cdot+}$, generated either by electron, charge transfer, or Penning ionization.[138]

Based on the mechanistic description of DART,[36] the formation of positively charged analyte ions is commonly attributed to the helium metastable atoms $He_m{}^*$. Given their long lifetimes and high internal energies (19.8 eV and 20.9 eV for the $^3S_1$ and $^1S_0$ state, respectively),[1] these species virtually ionize any molecule (M) directly through Penning ionization (Reaction 2.1).[2]

$$He_m{}^* + M \longrightarrow He + M^{\cdot+} + e^- \tag{2.1}$$

Apart from this reaction channel, alternative pathways involving the Penning ionization of atmospheric gases, such as water vapor, nitrogen, or oxygen, are conceivable, resulting in a subsequent generation of reagent-ions.

$$He_m{}^* + N_2 \longrightarrow He + N_2{}^+ + e^- \tag{2.2}$$

$$He_m{}^* + O_2 \longrightarrow He + O_2{}^+ + e^- \tag{2.3}$$

$$He_m{}^* + H_2O \longrightarrow He + H_2O^+ + e^- \tag{2.4}$$

[1] Throughout this thesis, all physical constants of atoms and small molecules have been taken from the NIST standard reference data repository.[145]

[2] To emphasize the radical character of a molecular cation, the nomenclature $M^{\cdot+}$ is used throughout the remainder of this thesis. For smaller reagent-ions, such as $H_2O^{\cdot+}$, $O_2{}^{\cdot+}$, or $N_2{}^{\cdot+}$, the dot is typically omitted.

Though each of these species has been assigned in the literature,[143] the ionization of moist air results in the predominant formation of proton-bound water clusters *via* the following sequence of ion / molecule reactions:[25,146]

$$N_2 + e^{-*} \longrightarrow {N_2}^+ + 2\,e^- \tag{2.5}$$

$${N_2}^+ + 2\,N_2 \longrightarrow {N_4}^+ + N_2 \tag{2.6}$$

$${N_4}^+ + H_2O \longrightarrow {H_2O}^+ + 2\,N_2 \tag{2.7}$$

$${H_2O}^+ + H_2O \longrightarrow {H_3O}^+ + OH \tag{2.8}$$

$${H_3O}^+ + (n\,-\,1)\,H_2O + N_2 \longrightarrow [(H_2O)_nH]^+ + N_2 \tag{2.9}$$

Upon the presence of neutral analyte, charge can be transferred *via* interactions with the above-named reagent-ions. Depending on the nature of the analyte, molecules that possess higher proton affinities than the bare water molecule (691 $kJ\,mol^{-1}$) undergo a proton transfer ionization, whereas the formation of molecular cations can be rationalized by a charge transfer ionization, as shown in Reaction 2.10 and 2.11, respectively.

$$[(H_2O)_nH]^+ + M \longrightarrow n\,H_2O + [M + H]^+ \tag{2.10}$$

$${O_2}^+ + M \longrightarrow {M^{\cdot}}^+ + O_2 \tag{2.11}$$

This set of reactions, however, only holds true for ion sources that remove charged species ahead of the sampling region. In fact, this mechanism has been adopted for most plasma-based techniques, even those that do not filter ions.[105,106,133] Thus, further studies were conducted to elucidate the ionization mechanism. As a result, the studies published by Heywood *et al.*[78] and Chan *et al.*[115,119] indicated that ${He_m}^*$ is not essential for a plasma-based ion source to perform well. Unlike previously thought, the key intermediate ${N_2}^+$ was not found to be solely formed by Penning ionization or high-energy electrons, but to be the result of a charge transfer reaction with ${He_2}^+$, generating at least 30% of ${N_2}^+$.[115,119]

$${He_2}^+ + N_2 \longrightarrow 2\,He + {N_2}^+ \tag{2.12}$$

Recapitulating, a prerequisite for any succesful coupling with laser ablation mass spectrometry is to determine the diverse reaction pathways of the custom-built ion source that lead to the formation of positively charged analyte ions. Therefore, the identity and the distribution of reagent-ions were investigated with respect to the discussed operational modes. Fig. 2.4 depicts the reagent-ion mass spectra for the helium-sustained DBD operated in the homogenous discharge mode (5 kV_{pp}) and the filamentary discharge mode (15 kV_{pp}), respectively. The ion detection was performed with the EL-API-HTOF MS.

The positive mode reagent-ion population of the homogenous discharge mode is depicted in Fig. 2.4a. The spectrum is dominated by a progression of ion peaks representing protonated water clusters of the type $[(H_2O)_nH]^+$. The cluster size distribution can be differentiated into two structural elements: a gaussian-shaped signal pattern at smaller n, with the maximum signal intensity peaking around $n = 4$, and an elongated tail comprising aggregates with a strongly increased number of water molecules ($n > 9$). While the narrow spectral feature between $n = 2$–6 is similar to the thermally equilibrated cluster distribution of $[(H_2O)_nH]^+$ described by Sunner *et al.*[147] for a corona discharge at room temperature conditions, the widely distributed proton-bound water clusters with $n > 9$ have been ascribed earlier in the literature[148–151] as aggregates originating from jet cooling.[3] In contrast to previous characterization studies,[88,143] charge transfer promoting ions, including NO^+ (m/z 30), $O_2{}^+$ (m/z 32), $NO_2{}^+$ (m/z 46), and $O_3{}^+$ (m/z 48), are not detected with the described experimental arrangement. Instead, additional ion peaks at m/z 36 and 54 are observed representing unidentified ions. A review of the literature reveals this reagent-ion spectrum to resemble those previously detected for other ambient plasma-based ion source / orthogonal TOF MS couplings, including DART[143] and the microplasma ionization source.[152] Furthermore, it is identical to the reagent-ion spectra observed for a corona discharge coupled to the same TOF MS.

[3] Within the first stage of pressure reduction, the nascent ions undergo multiple collisions with coexisting ambient neutral molecules, followed by the formation of a supersonic gas jet which expanding into the first evacuated chamber of the mass spectrometer. During this expansion, energy from internal degrees of freedom of the embedded ion-neutral aggregates is converted into translational energy. This leads to a rapid adiabatic cooling; hence, a stabilization of the preformed clusters.

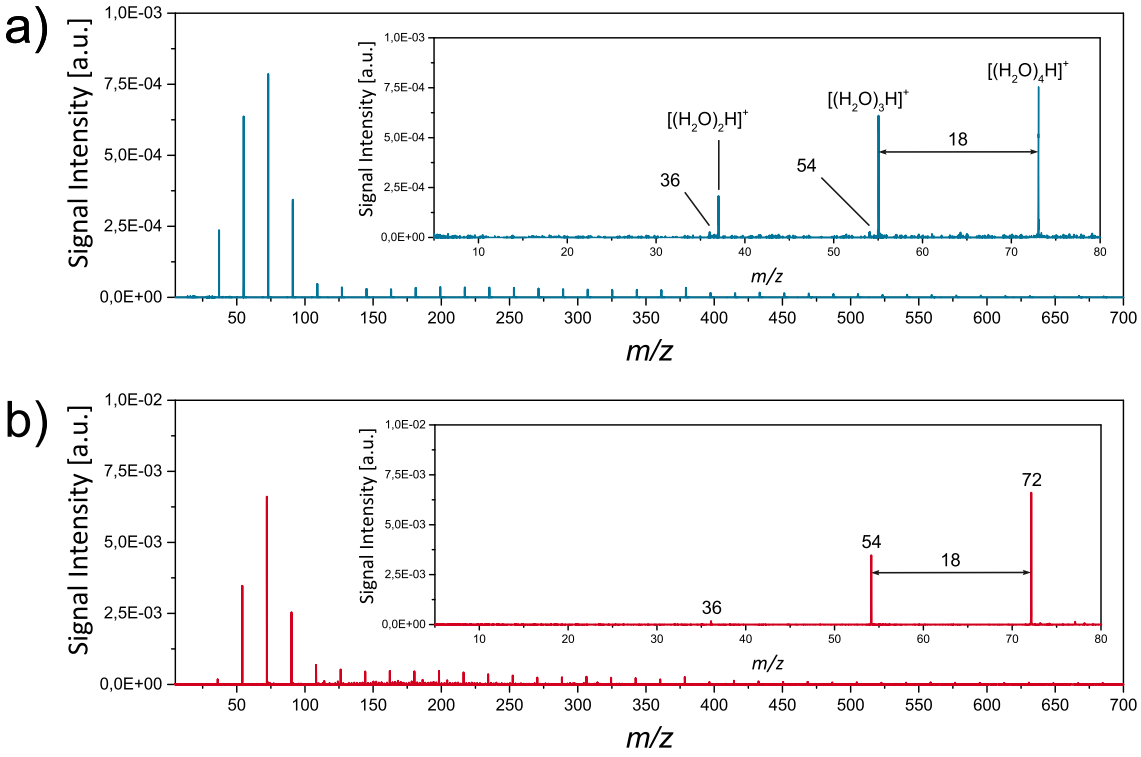

Figure 2.4: Positive mode reagent-ion population recorded with the EL-API-HTOF MS. (a) DBD in homogenous mode (5 kV_{pp}). (b) DBD in filamentary mode (15 kV_{pp}).

As has been reported in the literature,[153] the cluster size n dictates how charge is transferred from $[(H_2O)_nH]^+$ onto the neutral gas phase analyte to yield singly charged protonated molecules of the type $[M+H]^+$. While for smaller aggregates with n = 1–3 a direct proton transfer ionization according to Kebarle's water displacement mechanism (see Reaction 2.13 and 2.14) is feasible,[147,154,155] for n = 3–9, a microenvironment interaction is discussed in which the analyte enters the proton-bound solvent cluster by ligand switching / ligand association.[156–159] Upon cluster activation, either by an electrical field or by other means, a collisional decomposition of the ion-bound solvent cluster further downstream in the intermediate pressure regions is achieved (see Reaction 2.15–2.17). Ion clusters with n > 9 are known to be essentially unreactive.[160] Accordingly, throughout the remainder of this chapter, a high abundance of proton-bound water cluster ions with n = 2–6 is considered advantageous to yield analyte ions of the type $[M+H]^+$.

The reagent-ion background spectrum of the filamentary discharge mode is displayed in Fig. 2.4b. Similar to the homogenous discharge operation, a progression of equidistant ion peaks with a bimodal signal intensity distribution is observed. However, a closer inspection of the signal pattern reveals that, now, this series consists of the above-mentioned even-numbered ion peaks, while ion peaks associated with $[(H_2O)_nH]^+$ usually exhibit a quite low abundance or are completely absent. Furthermore, a striking change is the increase in the detected total ion current (TIC) by a factor of three, which can be attributed to the higher number of formed species over which the induced charge is distributed (refer to Fig. 2.3b). Thus, the single ion species signal (*e.g.*, *m/z* 72 in Fig. 2.4b compared to *m/z* 73 in Fig. 2.4a) experiences a gain in signal intensity by approximately one order of magnitude. This finding suggests a significant increase in sensitivity by simply applying a higher driving potential. The tenfold signal increase can be rationalized by the sixfold increase in electrical power consumption (0.9 W for recording the mass spectrum shown in Fig. 2.4a, and 5.6 W for recording the mass spectrum given in Fig. 2.4b).

$$[(H_2O)_{n=1-3}H]^+ + M \longrightarrow [M+H]^+ + n\ H_2O \tag{2.13}$$

$$[(H_2O)_{n=1-3}H]^+ + M + k\ N_2 \longrightarrow [M+H]^+ + n\ H_2O + k\ N_2 \tag{2.14}$$

$$[(H_2O)_{n>3}H]^+ + M \longrightarrow [M + (H_2O)_{n-m}H]^+ + m\ H_2O \tag{2.15}$$

$$[(H_2O)_{n>3}H]^+ + M + N_2 \longrightarrow [M + (H_2O)_{n>3}H]^+ + N_2 \tag{2.16}$$

$$[M + (H_2O)_{n>3}H]^+ + k\ N_2 \longrightarrow [M+H]^+ + n\ (H_2O) + k\ N_2 \tag{2.17}$$

The diverse interactions of the helium plasma jet with the surroundings produce a variety of reagent-ions. Most of these carry enough internal energy to ionize atmospheric H_2O (IE = 12.6 eV) and form H_2O^+. The water radical cation and its unprotonated ionized clusters $[(H_2O)_n]^+$ therefore provide a feasible rationalization of the signal progression depicted in Fig. 2.4b. However, experimental observations of these ions are scarcely reported since they are formed in a highly vibrationally excited state.[161–163] Without sufficient dissipation of the excess energy in these clusters, a fast barrierless autoprotonation process is initiated under atmospheric conditions resulting in the formation of the

well-known proton-bound water clusters.[161] Consequently, it stands to reason that the observed even-numbered ion peaks shown in Fig. 2.4 rather stem from a dissociation of atmospheric N_2, followed by the formation of N-containing reactive species. Since the mass spectra recorded with the EL-API-HTOF MS showed no spectral contributions from any charge transfer species in both of the investigated operational modes, reference measurements were conducted with the DBD probe placed in front of a second time-of-flight mass spectrometer (Q-API-HTOF MS).

Fig. 2.5a shows the reference background spectrum of the DBD operated in the homogenous discharge mode (5 kV_{pp}). As observed for the previous measurement, the mass spectral pattern is characterized by a progression of protonated water clusters of the type $[(H_2O)_nH]^+$. However, due to the presence of suitable electric fields in the ion transfer region, a significant shift in the cluster size distribution toward smaller clusters with $n = 1$–3 is induced. Furthermore, the lower number of collisions in the protruding inlet orifice of the Q-API-HTOF MS allows for a higher survival of reactants: High abundant ion peaks associated with NO^+ and $O_2{}^+$ are detected at m/z 30 and 32, while minor abundant ionic species, including N_2H^+, $NO_2{}^+$, and $O_3{}^+$, are observed at m/z 29, 46, and 48, respectively. In accordance with Reaction 2.11, these charge transfer carriers are known to yield molecular cations of the type $M^{\cdot+}$.

The reference background spectrum of the helium plasma jet operated in the filamentary discharge mode (15 kV_{pp}) is depicted in Fig. 2.5b. Upon increasing the discharge voltage, the spectral pattern undergoes two fundamental changes: First, as observed before, the increasing input voltage directly translates into a gain in signal intensity for all ionic species by approximately one order of magnitude. Second, similar to the previous interrogation experiment, the additional progression of even-numbered ion peaks, starting at m/z 18, becomes apparent in the mass spectrum when a higher discharge voltage is applied. Additionally, the ionic species N_2H^+ (m/z 29), NO^+ (m/z 30), $O_2{}^+$ (m/z 32), and $NO_2{}^+$ (m/z 46) are still present in the spectrum.

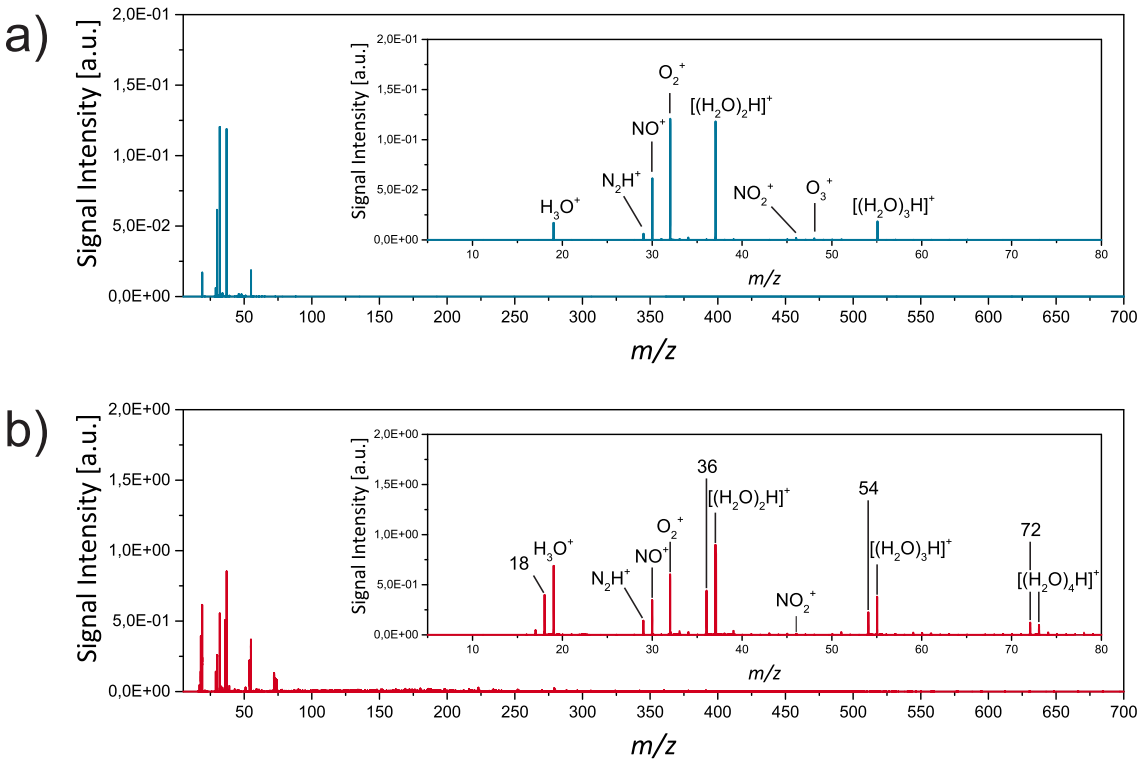

Figure 2.5: Positive mode reagent-ion population recorded with the Q-API-HTOF MS. (a) DBD in homogenous mode (5 kV_{pp}). (b) DBD in filamentary mode (15 kV_{pp}).

A literature review of different plasma-based ion sources revealed the mass spectral response of the filamentary discharge mode shown in Fig. 2.5b to be most consistent with the data for a microwave-induced plasma ionization (MIPI) source.[164] Although MIPI utilizes even harsher operating conditions in terms of its power consumption and applied frequency (30 W and 2450 MHz for the MIPI source compared to 5.6 W and 120 kHz for the DBD probe in filamentary mode), most of the detected reagent-ion peaks for the DBD are also present in the background spectrum of the MIPI source. In this case, the even-numbered ion peaks at *m/z* 36, 54, and 72 were associated with the following hydrated ammonia clusters: $[(NH_3)(H_2O)H]^+$, $[(NH_3)(H_2O)_2H]^+$, and $[(NH_3)(H_2O)_3H]^+$.[164] This spectral assignment was made based on an earlier publication on the *in-situ* formation of ammonia using a gas mixture of N_2/H_2 in a microwave plasma.[165] Depending on the plasma parameters and the experimental arrangement, the following ionic products were produced:

NH_3^+, NH_4^+, H_3O^+, N_2H^+, NO^+, $[(NH_3)_2H]^+$, and $[(NH_3)(H_2O)H]^+$ at *m/z* 17, 18, 19, 29, 30, 35, and 36, respectively. Accordingly, it is proposed that the progression of even-numbered ions present in the DBD reagent-ion background spectra originates from proton-bound ammonia NH_4^+ and its hydrated clusters of the type $[(NH_3)(H_2O)_nH]^+$.

Since the observation of NH_4^+ is mechanistically of huge importance, a potential misinterpretation by an isobaric interference with the unprotonated water radical cation H_2O^+ needs to be ruled out. To corroborate the hypothesis of a gas phase initiated dissociation / ionization mechanism resulting in the formation of NH_4^+, three experiments were conducted: (1) a remeasurement of the reagent-ion background spectra using the EL-API-HTOF MS in high resolution triple reflectron geometry, (2) a replacement of helium by alternative plasma gases, and (3) a spectrometric study examining the effect of an increased ammonia concentration in the gas phase on the reagent-ion population.

(1) Using the EL-API-HTOF MS in high resolution mode, mass differences of selected ion pairs were determined and compared to the theoretical values for the formation of either proton-bound ammonia water clusters of the type $[(NH_3)(H_2O)_nH]^+$ or unprotonated $[(H_2O)_n]^+$ cluster ions. The TOF mass analyzer used within these studies provides a mass resolution of over 3000 across the 50–500 Da range. The experimental mass difference was 0.985 Da for $[(NH_3)(H_2O)_4H]^+$ and $[(H_2O)_5H]^+$ in the lower mass region, and 0.981 Da for $[(NH_3)(H_2O)_{24}H]^+$ and $[(H_2O)_{25}H]^+$ in the higher mass region. The calculated mass difference for NH_4^+ and H_3O^+ is 0.984 Da, which is in good agreement with the experimental data. In contrast, the mass difference for H_2O^+ and H_3O^+ is 1.008 Da. This result corroborates the above-made assumption of NH_4^+ being the source of the even-numbered progression of ion peaks.

(2) Though helium has been employed in most plasma-based ionization schemes, a rationale for the detection of NH_4^+ was sought by feeding alternative plasma gases to the DBD ion source. In this set of experiments, helium was replaced by either pure argon or

pure nitrogen. In accordance with the literature,[166] the power requirements to sustain an equivalent discharge with these plasma gases were found to be larger than those needed for the helium-sustained plasma. Thus, the DBD ion source had to be operated in the filamentary discharge mode (15 kV_{pp}).

Using pure argon to sustain the plasma (spectrum not shown), hardly any formation of reagent-ions was traceable, which is likely to be caused by the lower internal energies of the argon metastable states (11.6 eV or 11.7 eV),[167,168] as compared to the higher ionization energies of H_2O (12.6 eV) and N_2 (15.6 eV). These findings correlate well with earlier results obtained for Ar-DBD[116] and Ar-DART.[169–171]

In contrast, when pure nitrogen was used as the discharge gas, the reagent-ion background spectrum depicted in Fig. 2.6 reveals a similar signal pattern to that shown for the helium-sustained plasma operated at 15 kV_{pp} (Fig. 2.4b). However, a comparable performance was only observed upon increasing the gas flux to 2.0 $L\,min^{-1}$ while decreasing the distance to the inlet capillary of the EL-API-HTOF MS to 1.0 cm. The spectrum shows a predominant formation of the proposed proton-bound ammonia water clusters $[(NH_3)(H_2O)_nH]^+$, while odd-numbered ion peaks representing the formation of $[(H_2O)_nH]^+$ are only present in low abundance. This change in the spectral pattern is consistent with the results published by Pérez *et al.*,[172] investigating the performance of a DART ion source operated with either helium or nitrogen. In addition, a novel series of equidistant ion peaks becomes apparent in the mass spectrum, starting at *m/z* 35. The presence of these species has been observed earlier for the N_2 / H_2 microwave plasma,[165] as well as for a hollow cathode ion source fed with pure H_2O vapor and N_2.[173,174] Thus, in accordance with the above, these ion peaks are assigned to $[(NH_3)_2(H_2O)_nH]^+$.

(3) In contrast, the signal progression of $[(NH_3)_2(H_2O)_nH]^+$ can be only detected with the helium-sustained plasma upon the artificial enrichment of ammonia in the sampling region of the DBD. Figure 2.7 depicts the online monitoring of the *m/z* traces of $[(NH_3)_2H]^+$

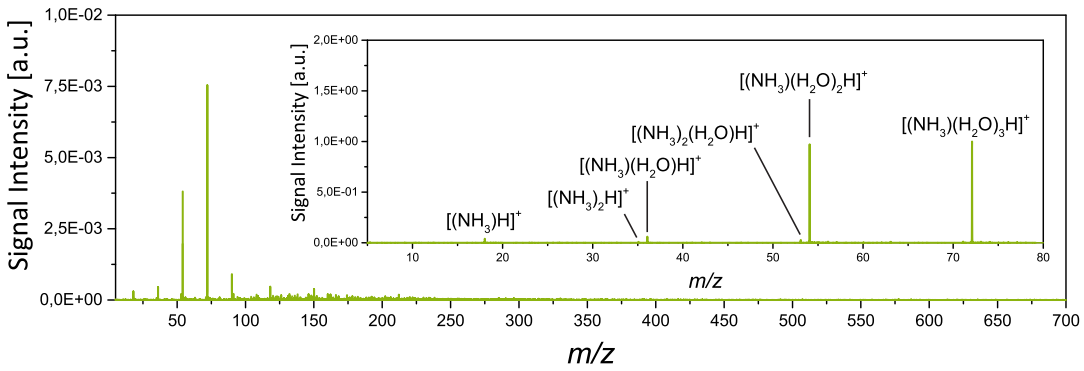

Figure 2.6: Positive mode reagent-ion spectrum of the DBD operated in filamentary mode (15 kV_{pp}). Pure nitrogen was used as the plasma gas.

at *m/z* 35, $[(NH_3)(H_2O)H]^+$ at *m/z* 36, and $[(H_2O)_2H]^+$ at *m/z* 37 upon this reversible addition. At the given time intervals t_1 = 180–240 s and t_2 = 450–510 s (grey-shaded areas), the increased gas phase concentration of ammonia causes the signals for *m/z* 36 and 37 to decrease significantly, whereas the signal for *m/z* 35 increases. This clustering behaviour can be rationalized by a temporarily increased concentration of ammonia and the individual proton affinities of water (691 $kJmol^{-1}$) and ammonia (854 $kJmol^{-1}$).

Recapitulating, the acquired spectrometric data corroborate the presence of the two discharge modes. As for the transient current / voltage profiles, both regimes appear to be superimposed and coexist as competetive ion formation channels. At lower input voltages, the DBD produces predominantly protonated water clusters and charge transfer species, whereas at higher voltages the additional reagent-ion NH_4^+ is detected. The latter potentially serves as an additional ionization agent or forms clusters. Moreover, the conducted experiments suggest an *in-situ* formation of ammonia out of ambient H_2O and N_2 by the filamentary driven plasma. Thus far, this reaction has not been considered for DBD-based plasma sources. Going into more detail, those ion peaks have been observed earlier for many other plasma-based atmospheric pressure ionization schemes, including corona discharge,[23,146] LTP,[112] flowing atmospheric-pressure afterglow (FAPA),[143] microplasma ion source,[152] and PADI,[175] but have not been assigned.

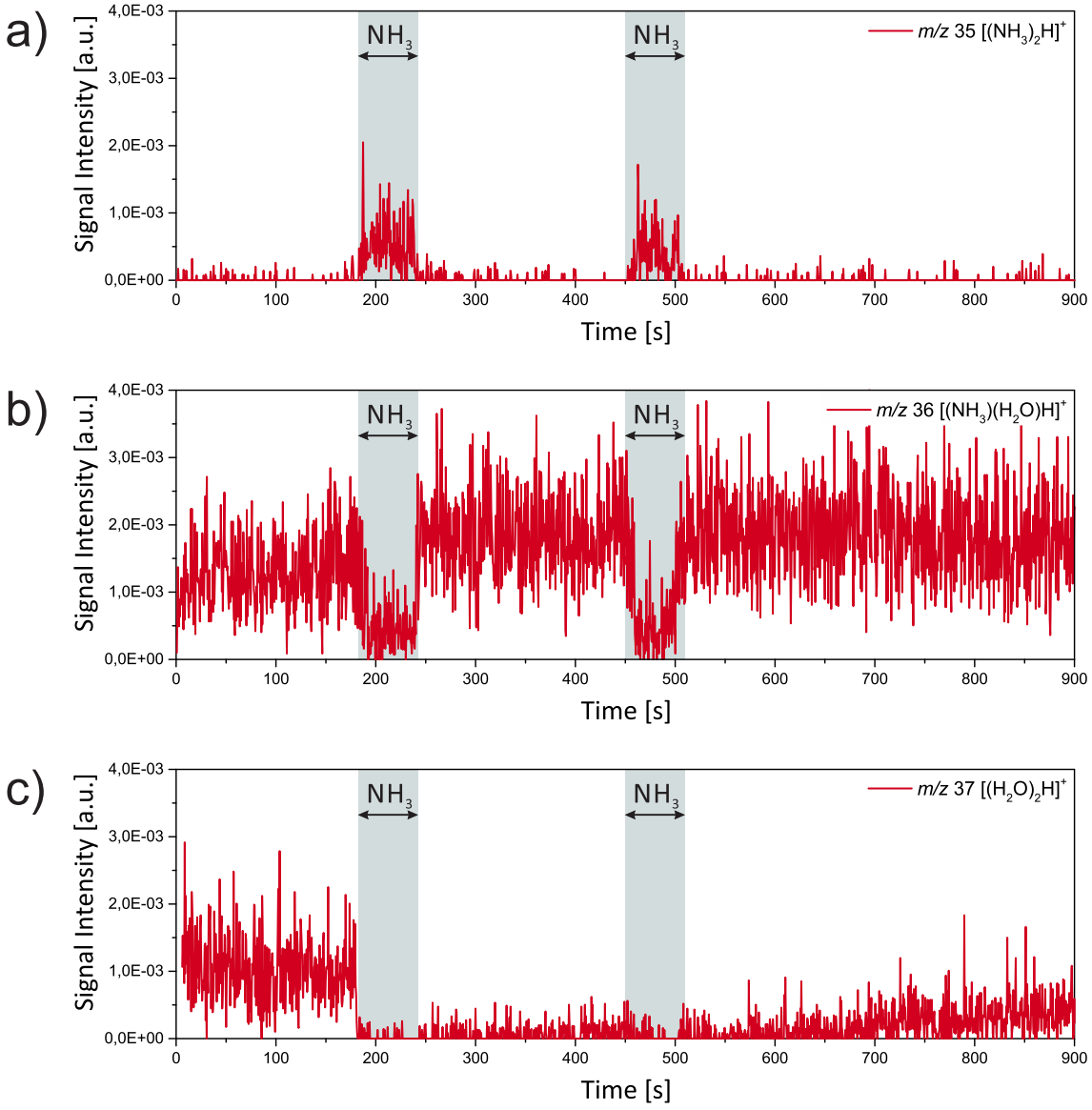

Figure 2.7: Extracted ion chronograms of (a) $[(NH_3)_2H]^+$, (b) $[(NH_3)(H_2O)H]^+$, and (c) $[(H_2O)_2H]^+$ using the helium-sustained DBD in filamentary mode (15 kV_{pp}). Aqueous ammonia solution was introduced into the gap between the ion source and the MS inlet at t_1 = 180–240 s and t_2 = 450–510 s (grey-shaded areas).

2.3.3 Spectroscopic Characterization of the Dielectric Barrier Discharge

The optical characterization of plasma-based ambient desorption / ionization sources has brought forth further insights into the relevant excitation energy processes in the plasma and the afterglow region.[78,115,116,119,120,125] Therefore, additional emission studies were conducted to envision the differences between the two discharge regimes by which the custom-made DBD operates.

Optical Emission Spectroscopy of the He-DBD

Fig. 2.8 depicts time-averaged optical emission spectra integrated along the vertical axis of the helium-sustained discharge operated in either homogenous (5 kV_{pp}) or filamentary mode (15 kV_{pp}).

Though different operational parameters are applied in the present study, the emission spectra shown in Fig. 2.8, resemble the spectral composition of most other helium-sustained discharges at atmospheric pressure (*e.g.*, APGD,[176] DBD,[116,177], LTP,[119] FAPA,[135] and DART[178]). For both operational modes a number of molecular spectral contributions are observed in the shorter wavelength region of the electromagnetic spectrum, including emission associated with OH ($A^2\Sigma^+ \rightarrow X^2\Pi$) at 306–309 nm, excited neutral N_2 ($C^3\Pi_u \rightarrow B^3\Pi_g$) between 313–434 nm, and ${N_2}^+$ (${B^2\Sigma_u}^+ \rightarrow {X^2\Sigma_g}^+$) ranging from 387–471 nm. Spectral contributions from other reactive molecular species, which have been occasionally reported, including NO[176,179,180] and CN,[181] are not observed in the presented experiments. In addition, the spectrum shows major atomic emission lines between 500–850 nm which can be readily attributed to H I, He I, and O I. The unassigned spectral features between 600–750 nm stem from first order Bragg artefacts of the emitted plasma radiation which are detected in the second blazing order of the spectrograph. For all practical purposes, the individually recorded spectra result to be equivalent, except for the absolute emission intensities. The latter are found to be much stronger if a higher input voltage is applied. As has been described in the literature,[119,179] the presence of non-helium species in the discharge region can be most likely attributed to the diffusion of

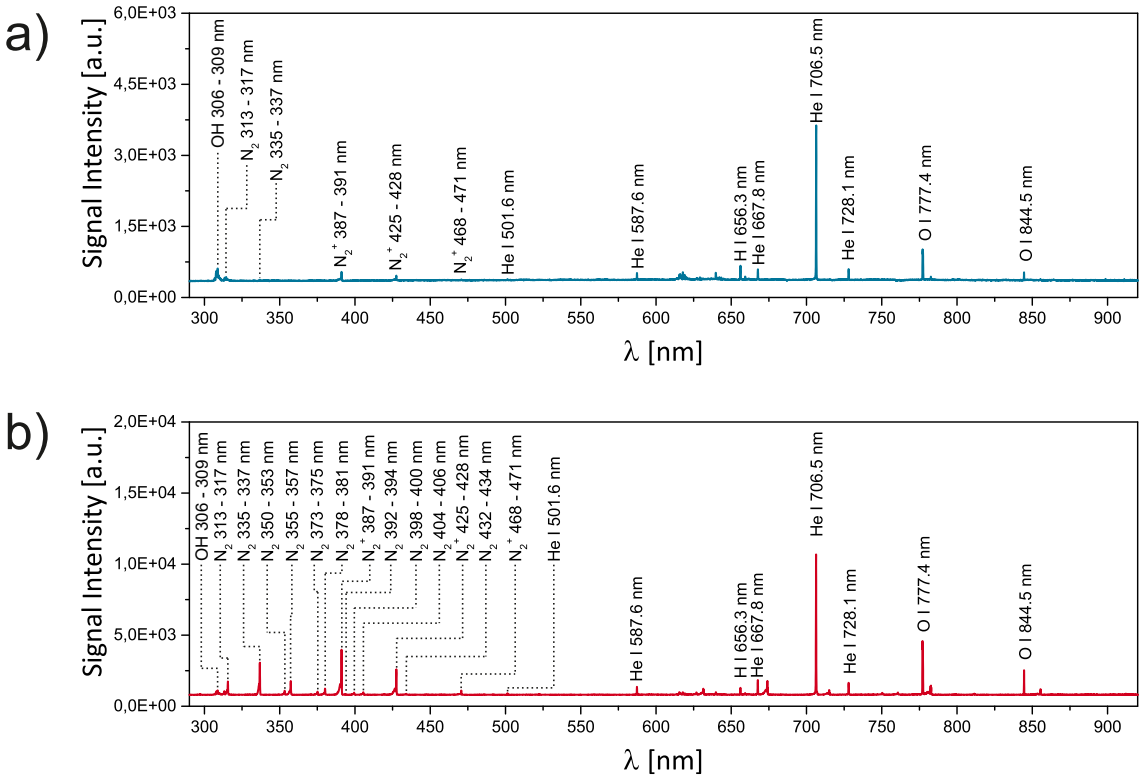

Figure 2.8: Time-integrated optical emission spectra obtained from the helium-sustained DBD. (a) Homogenous discharge mode (5 kV_{pp}). (b) Filamentary discharge mode (15 kV_{pp}).

surrounding air into the borosilicate glass capillary since all these probes are built without air-tight housings.

Optical Emission Spectroscopy of alternative Discharge Gases

For an estimation of the thermal plasma conditions, the discharge gas was permutated. In these experiments, the plasma gas serves as a probe for the excitation conditions which rely on the individual ionization energies of the different gases. Furthermore, the use of alternative plasma gases can lead to a deeper understanding of the pronounced differences observed in the nascent ion distributions. Fig. 2.9 exhibits the optical emission spectra of the DBD operated in the filamentary mode (15 kV_{pp}) and fed with (a) argon and (b) nitrogen.

Compared to the presented emission spectra of the helium-driven plasma, the spectrum obtained with argon, depicted in Fig. 2.9a, produces an almost entirely different spectral pattern. In particular, the spectrum resembles that of the neutral argon atom, except for weak bandheads of the second positive system of N_2 ($C^3\Pi_u \rightarrow B^3\Pi_g$) and molecular emission associated with the (0,0) band of OH ($A^2\Sigma^+ \rightarrow X^2\Pi$) at 306–309 nm. Additional molecular emission attributed to $N_2{}^+$ (${B^2\Sigma_u}^+ \rightarrow {X^2\Sigma_g}^+$) is not detected from the argon-driven discharge. Likewise, spectral contributions originating from H I and O I are not distinguishable from the background. The observed lack of reactive nitrogen species, commonly considered as the key intermediates for the production of $[(H_2O)_nH]^+$, accompanied by the intensive emission from the plasma gas, coincides well with the unsatisfactory spectrometric performance of the Ar-DBD. Again, the distinct gas phase chemistry of the plasma can be rationalized by the fact that the metastable argon atom carries less energy than the helium analogue (either 11.6 eV or 11.7 eV). In consequence, the system is only capable of exciting the second positive system of N_2, which requires 11.1 eV of energy. To detect molecular emission from $N_2{}^+$ (${B^2\Sigma_u}^+ \rightarrow {X^2\Sigma_g}^+$), 15.6 eV are required. Hence, argon was discarded as the plasma gas of choice for a preferably non-selective post-ionization source.

The effect of a complete replacement of helium with pure nitrogen as the plasma gas is displayed in Fig. 2.9b. Compared to the helium-sustained plasma, the only shared feature is emission obtained from the second positive system of N_2 ($C^3\Pi_u \rightarrow B^3\Pi_g$), whereas spectral contributions from $N_2{}^+$ (${B^2\Sigma_u}^+ \rightarrow {X^2\Sigma_g}^+$), OH ($A^2\Sigma^+ \rightarrow X^2\Pi$), H I, and O I are not distinguishable from the background. This spectral appearance stands in contrast to the helium-DBD case. Among the observed molecular emitting species in the helium-sustained plasma, emission lines associated with $N_2{}^+$ are the most prominent, regardless of the discussed operational mode. However, the relative signal intensities of $N_2{}^+$ (${B^2\Sigma_u}^+ \rightarrow {X^2\Sigma_g}^+$) and N_2 ($C^3\Pi_u \rightarrow B^3\Pi_g$) can be seen to reverse in Fig. 2.9b in comparison to the helium-sustained discharge in Fig. 2.8b. This behavior can be explained as follows: In principle, the $C^3\Pi_u$ state of N_2 can either be populated directly

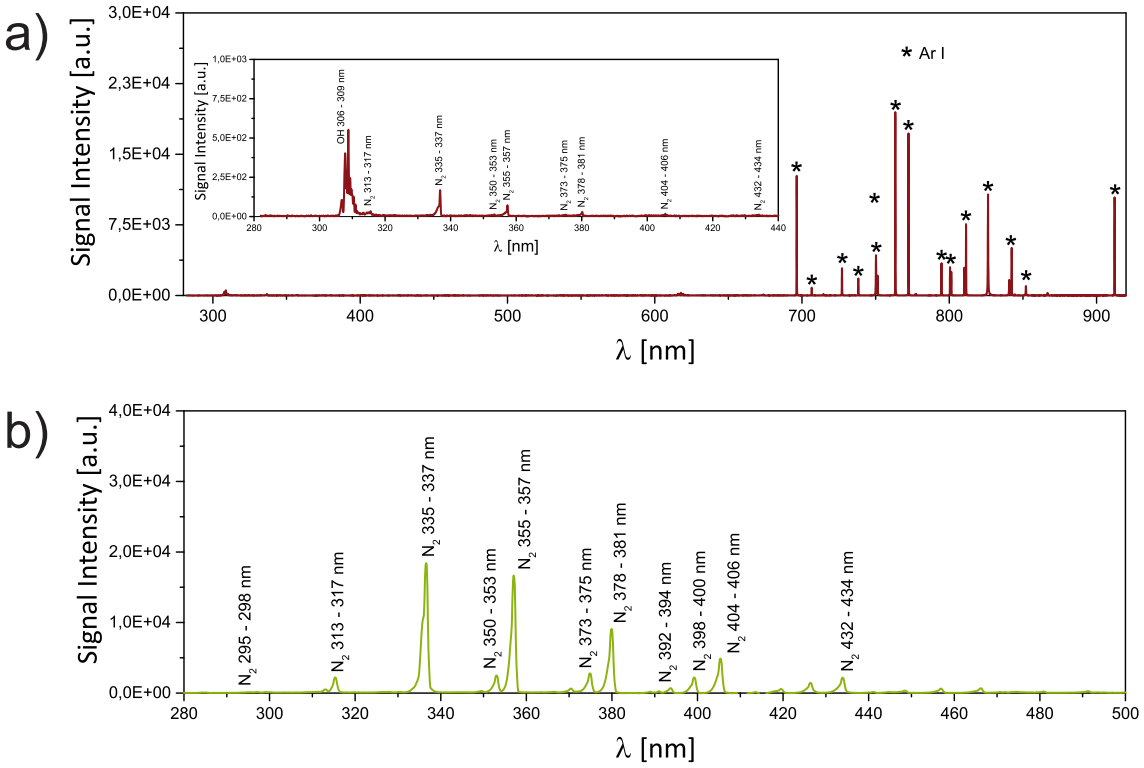

Figure 2.9: Time-integrated optical emission spectra obtained from the DBD fed with (a) pure argon and (b) pure nitrogen.

from the $X^1\Sigma_g$ ground state *via* electron-impact excitation or by electron capture relaxation of the N_2^+ $X^2\Sigma_g^+$ ionic state. However, according to earlier publications,[182–184] the formation of N_2^+ $X^2\Sigma_g^+$ cannot be initiated in plasmas operated in pure nitrogen and at atmospheric pressure. Accordingly, the direct excitation of ground state molecular nitrogen remains the only viable reaction pathway inside a N_2-driven DBD. In the case of the helium-sustained DBD, the spatially resolved emission studies published by Chan *et al.* could rule out electron impact as the major source for either excited N_2 species. Here, the formation of N_2^+ was found to be formed *via* collision with He_m^* and He_2^+. The nascent N_2^+, however, could be shown to further undergo recombination processes either with any electrons present or *via* capturing an electron from other molecules with a lower ionization energy (12.1 eV, 12.6 eV, and 15.6 eV for O_2, H_2O, and N_2, respectively).

Recapitulating, a correlation of the individual spetrometric and spectroscopic performance of the investigated discharge gases showed that the excited state chemistry of helium is crucial for the efficient formation of reagent-ions for ambient mass spectrometry applications. The energetically high lying electronic and Rydberg states open a plethora of additional energetically accessible states of involved species, making helium the carrier and discharge gas of choice. This finding is at first somewhat counterintuitive since the involvement of more reactive species, many of them with a huge oxidative potential, might result in unwanted fragmentation. However, throughout the literature, helium-driven discharges are discussed to form the chemically "cleaner" mass spectra.

2.3.4 Controlled Formation of Reagent-Ions

The results obtained thus far suggest the neutral excited N_2 to open an additional product channel for the *in-situ* formation of ammonia. The latter possesses a much higher proton affinty than the bare water molecule, and thus should be able to ionize a narrower set of analytes *via* direct proton transfer ionization.[153] As described in the literature,[185] this selectivity can be utilized to differentiate isobaric species, when only one is able to accept a proton from $NH_4{}^+$. Accordingly, it is favorable to investigate if the reagent-ion formation of the helium-sustained plasma can be controlled to produce either $[(H_2O)_nH]^+$ or $[(NH_3)(H_2O)_nH]^+$ in high abundance. Significant parameters that were found to alter the reagent-ion population include the discharge voltage and the gas flux.

Effect of the Discharge Voltage

Fig. 2.10a displays the signal intensities of $[(H_2O)_4H]^+$ (*m/z* 73) and $[(NH_3)(H_2O)_4H]^+$ (*m/z* 90) as a function of the applied discharge voltage. Reagent-ion spectra were recorded at a fixed helium flow rate of 1.0 L min^{-1}, while the voltage was varied between 4–15 kV_{pp}. The left part of the graph, covering the lower voltage region (4–7 kV_{pp}), is in accordance with the most common spectral appearance of other plasma-based desorption / ionization sources. Most abundant background signals arise from proton-bound water clusters, promoting the formation of $[n\mathrm{M}{+}\mathrm{H}]^+$, while ammonium species are usually present in lower

abundance or are completely absent. Further increase of the voltage leads to an inversion of the reactive species concentrations. Starting at about 7 kV_{pp}, an excess of ammonia containing reactants is observed. Now, proton donation from NH_4^+ leads to the formation of positively charged product ions containing the analyte molecule.

Effect of the Gas Flow Rate

A correlation between the plasma gas flow and the optical emission of a helium-sustained LTP has been reported earlier by Chan *et al.*[119] Their results imply that an increased concentration of high-energetic helium species, and as a consequence a higher concentration of reagent-ions, is produced by simply increasing the gas flux. To examine this effect with respect to the discussed product channels, *i.e.*, the predominant formation of $[(H_2O)_nH]^+$ or $[(NH_3)_2(H_2O)_nH]^+$ in the homogenous and the filamentary discharge mode, reagent-ion background spectra were acquired with varying helium flow rates between 0.1–2.0 $L\,min^{-1}$. For each data point shown in Fig. 2.10b, the signal intensity ratio between the protonated water tetramer $[(H_2O)_4H]^+$ at *m/z* 73 and its corresponding ammonia cluster $[(NH_3)(H_2O)_4H]^+$ at *m/z* 90 was calculated and plotted as a function of the gas flux. For this set of experiments, the acquisition time per spectrum was increased to 60 s. Moreover, in filamentary operation, the distance between the DBD ion source and the MS inlet was held at 2.0 cm, while in the homogenous discharge mode a decrease to 1.0 cm was necessary due to an overall lower ion count.

Regarding the calculated ratios, both operational modes show similar trends. While the formation of hydrated ammonia clusters clearly benefits from lower flow rates; thus, longer dwell times, proton-bound water cluster ions are preferably formed at higher flow rates and shorter dwell times. Most likely, this result goes along with a more effective energy transfer into the present plasma gas, eventually sufficing for a cleavage of the N_2 triple bond. According to the literature,[126] this fragmentation / atomization predominantly occurs in the close vicinity of the electrodes, for spatially resolved spectroscopy mapping experiments suggest the electron density and the energy to be highest (Fig. 2.11).

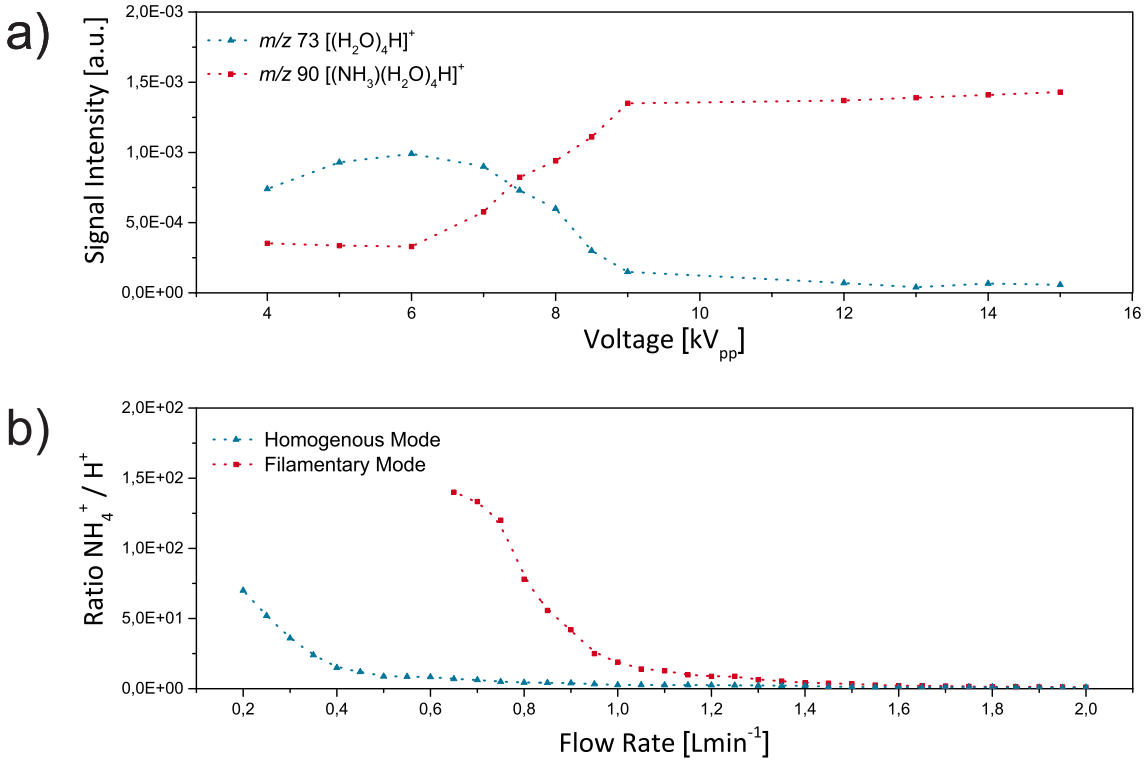

Figure 2.10: Effect of (a) the discharge voltage and (b) the gas flux on the reagent-ion population of the helium-sustained DBD.

Nonetheless, it should be noted that even at higher flow rates, for both operational modes, ion peaks originating from hydrated ammonium aggregates are present, but to a significantly lower extent. The operational voltage difference merely affects the individual graphs for each mode to be shifted along the x-axis. The formation of $[(NH_3)(H_2O)_nH]^+$ starts to become more dominant below 0.5 L min^{-1} in the homogenous discharge mode, while in the filamentary discharge mode the same trend already becomes apparent at about 1.2 L min^{-1}. In addition, both modes are restricted to a minimal gas flux to avoid a capillary meltdown and direct arc formation. The ignition of stable discharges starts at 0.2 L min^{-1} and 0.6 L min^{-1} in the homogenous and the filamentary discharge mode, respectively.

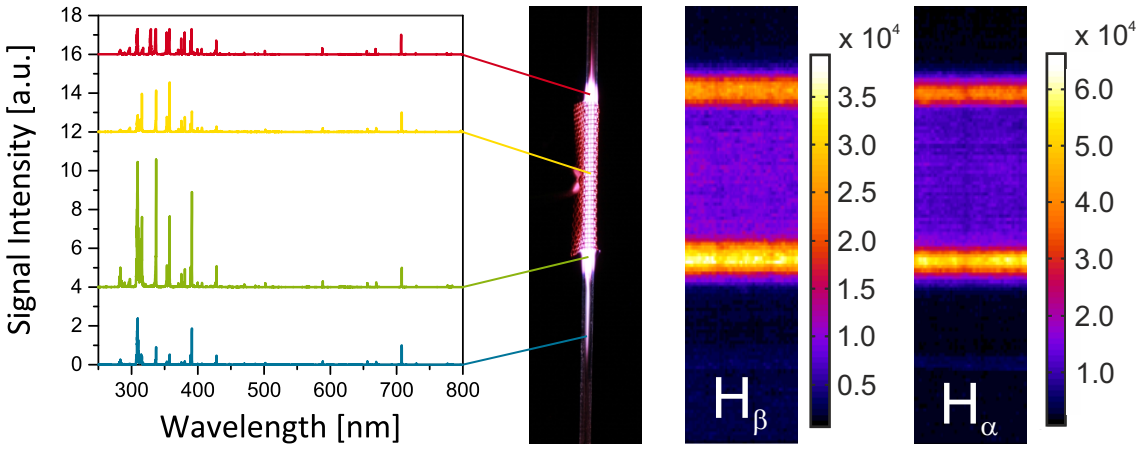

Figure 2.11: Spatial imaging of the helium-sustained discharge in filamentary mode. A photograph of the DBD, fixed in a top-down position, is given for better orientation of the spatial position. The gas flow rate was set to 1.0 L min^{-1} and the discharge voltage was 15 kV$_{pp}$. On the left side, four selected emission spectra showcase a significant dependence of the optical emission on the spatial position inside the plasma probe. The spectra are normalized to the He I signal at 706.5 nm and vertically offset from each other for a clear representation. On the right side, exemplary spatial mappings of the optical emission originating from H_α and H_β transitions of the Balmer series are plotted.

2.3.5 Mass Spectrometric Analysis of Test Compounds

Thus far, a good understanding of the individual processes inside the plasma was achieved. The results indicate that, depending on the chosen experimental paramaters, a distinct chemical environment can be defined in which the analyte is ultimately ionized. In the next step, the effect of these plasma conditions on the ionization pathways of two model analytes was examined. Out of the vast number of samples reported in the literature, acetone and ferrocene were chosen as test compounds due to their vapor pressure and well-known ionization properties.[166,186] In addition, the organometallic compound ferrocene has been used earlier as a standard sample for plasma-based ionization techniques since the presence / absence of characteristic fragmentation products allows for a rough estimation of the plasma conditions.[143,187] The recorded spectral data are summarized in Fig. 2.12.

Introducing acetone into the sampling region, *i.e.*, the midpoint between the ion source and the MS inlet, the mass spectrum for the DBD operated in the homogenous discharge mode exhibits the formation of singly charged monomers $[M+H]^+$ at *m/z* 59 and $[M+NH_4]^+$ at *m/z* 76, dimers $[2M+H]^+$ at *m/z* 117 and $[2M+NH_4]^+$ at *m/z* 134, and trimers $[3M+H]^+$ at *m/z* 175 and $[3M+NH_4]^+$ at *m/z* 192. Further spectral contributions include three analyte-containing cluster series that originate from $[M+(H_2O)_nH]^+$ with $n = 1$–5 (*m/z* 77, 95, 113, 131, 149), $[2M+(H_2O)_nH]^+$ with $n = 1$–3 (*m/z* 135, 153, 171), and $[3M+(H_2O)_nH]^+$ with $n = 1$ (*m/z* 193), in descending order of intensity. In addition, the minor abundant ion peaks below *m/z* 100 stem from residual protonated water clusters not consumed in the sample charging mechanism.

In contrast, when the DBD was operated in filamentary mode, the spectral pattern of the mass spectrum changes significantly. Except for the ion peak at *m/z* 59, representing the protonated acetone monomer $[M+H]^+$, the predominant ion peaks are assigned to association products of the type $[nM+NH_4]^+$ at *m/z* 76, 134, and 192, with $n = 1$–3, respectively. Further product ions in lower abundance stem from $[M+(NH)_3(H_2O)H]^+$ at *m/z* 94, $[M+(NH)_3(H_2O)_2H]^+$ at *m/z* 112, and $[2M+(NH)_3(H_2O)H]^+$ at *m/z* 152. The equidistant ion peaks at *m/z* 18, 36, 54, 72, and 90 originate from $NH_4{}^+$ and its hydrated cluster ions of the type $[(NH_3)(H_2O)_nH]^+$ with $n = 1$–4, respectively.

The high abundance of mostly clustered ions can be explained by the high vapor pressure of acetone, the neat concentrations sampled, and the applied instrumental settings (non-heated inlet capillary, weak declustering potential, non-heated discharge gas). Referring to Section 2.3.2, the only conceivable reaction pathways to yield bare protonated analyte molecules $[nM+H]^+$ are a proton transfer ionization, and a ligand switching / association process, followed by a collision-induced dissociation of the ion-bound solvent cluster. Taking into consideration that the proton affinities of $[(H_2O)_nH]^+$ are 832, 888, and 919 kJmol^{-1} for $n = 2$, 3, and 4,[154] a direct proton transfer from these species onto the neutral acetone molecule with a proton affinity of 812 kJmol^{-1} is less favorable than

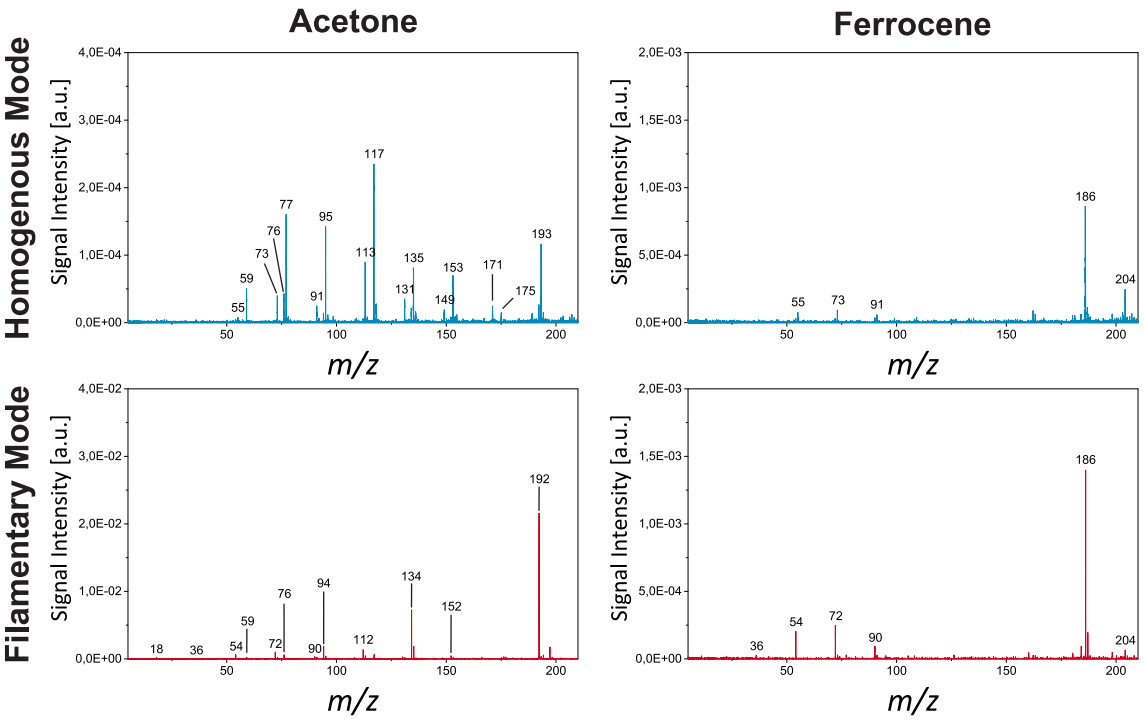

Figure 2.12: Effects of the discussed discharge modes on the analyte ionization chemistry of the test compounds acetone and ferrocene.

the formation of proton-bound solvent / analyte clusters. The detection of partially hydrated cluster ions $[n\mathrm{M}+(\mathrm{H_2O})_m\mathrm{H}]^+$ that have not yet undergone complete decomposition strongly corroborates the presence of this intracluster protonation reaction. In contrast, in the filamentary operation mode, a direct proton transfer from $\mathrm{NH_4}^+$ or $[(\mathrm{NH_3})(\mathrm{H_2O})_n\mathrm{H}]^+$ onto the neutral acetone molecule was not observed. These results can be rationalized by the corresponding proton affinities of water, acetone, and ammonia, which increase in the order of 691, 812, and 854 kJmol^{-1}, respectively. Instead, it was found that, where a reaction occured, ion association products of the type $[n\mathrm{M}+\mathrm{NH_4}]^+$, formed either by a three-body ion-molecule association or by ligand switching processes,[153,174] tended to dominate the recorded mass spectra. The latter reaction mechanism further provides a feasible explanation for the presence of $[n\mathrm{M}+(\mathrm{NH})_3(\mathrm{H_2O})_m\mathrm{H}]^+$. The predominant detection of these ammoniated analyte containing product ions is further corroborated by a recent publication by Sugimura *et al.*[188] They reported on trends toward the selec-

tive formation of $[M+NH_4]^+$ using a commercially available DART source. Based on the screening of over 600 samples, this adduct selectivity has been attributed to the presence of oxygen atoms in the sample compound, stabilizing the ammoniated molecular ions.

The introduction of the second test compound ferrocene into the sampling region did not result in any substantial difference in spectral abundance between the two investigated discharge modes. Product ions containing the analyte are immediately observed at *m/z* 186 and *m/z* 204, representing the intact ferrocenium cation $M^{\cdot+}$ and its water adduct $[M+H_2O]^{\cdot+}$, respectively. While the filamentary regime has been discussed throughout the literature to induce fragmentation processes,[124] no evidence for such pronounced effects was observed, most probably due to the separation of the actual discharge and sampling region.

2.4 Conclusion

A versatile helium-driven DBD ion source has been constructed and characterized by its current / voltage consumption, optical emission spectroscopy, and ambient mass spectrometry. Direct comparison of these data indicated the presence of two distinct charge moieties. The first is driven by rapid transient discharges through the dielectric barrier, denoted homogenous mode, while the second is caused by high static potential differences that result in filamentary discharges. Both regimes are superimposed and coexist as competitive ion formation channels, but could be altered by the discharge gas, the gas flux, and the operational voltage of the discharge setup, to significantly affect the formation of secondary reagent-ions for ambient mass spectrometry applications.

Proton transfer reagents $[(H_2O)_nH]^+$ were preferentially at their highest abundance when the DBD was operated in the homogenous discharge mode (lower output voltages) and fed with higher helium flow rates, whereas the formation of $NH_4{}^+$ and its corresponding cluster ions $[(NH_3)(H_2O)_nH]^+$ was found in the opposite conditions. Unlike most liter-

ature on plasma-based ambient desorption / ionization sources, the conducted experiments strongly suggest the formation of the latter reactant species to be caused by a gas phase initiated dissociation / ionization mechanism in the presence of atmospheric N_2 and H_2O. In consequence, the spectrometric analysis of the organic test compound acetone yielded in the detection of either proton-bound analyte ions $[n\mathrm{M}+\mathrm{H}]^+$ or association products $[n\mathrm{M}+\mathrm{NH_4}]^+$ in the homogenous and the filamentary discharge mode, respectively. In case of the second test compound ferrocene, the difference in spectral abundance between the two discharge modes was almost negligible, which could be rationalized by an independent analyte charging mechanism. Though the filamentary operation has been discussed in the literature to induce fragmentation processes, no evidence for such pronounced effects was observed for the test compounds used.

Eventually, the presented setup exhibited lower geometrical restrictions compared to a wide number of ionization schemes for ambient desorption / ionization mass spectrometry. As shown above, the filamentary operation of the helium-sustained DBD ion source yielded satisfactory results even at higher distances between the actual discharge region and the capillary inlet of the mass spectrometer. The air gap of 2.0 cm enables the present system to be extended by a laser for an improved conversion of condensed matter into the gas phase and a subsequent ionization in the DBD exhaust.

3 Laser Ablation Dielectric Barrier Discharge Ambient Mass Spectrometry

Laser ablation mass spectrometry provides high spatial resolution analysis capabilities that have not been matched so far by other desorption / ionization techniques for ambient mass spectrometry. Laser light exposure of the sample surface enables a well-confined energy introduction that produces an abundance of neutral molecules and small particles in the gas phase. Since only a minor class of compounds can be directly ionized by exposing them to laser irradiation, the implementation of a post-ionization source is often necessary to result in a competetive analytial method. In return, the separation of the ablation / desorption and the ionization in two consecutive and independent steps introduces a vaster flexibility in problem-specific instrumentation. In this chapter, a novel experimental arrangement for plasma-based ambient mass spectrometry is presented, combining laser ablation by a pulsed DPSS laser and the custom-made DBD ion source that has been characterized in Chapter 2.

Based on:
Bierstedt, A.; Riedel, J. *Methods* **2016**, *104*, 3–10.

3.1 Toward the Separation of the Desorption / Ionization Process

In ambient mass spectrometry, ion sources are employed for direct surface analysis, including the desorption and ionization of molecules in a single mechanistic step. Among the multitude of ionization techniques, the individual designs mostly rely on well-established ionization schemes that can be roughly categorized by the underlying physical processes driving the desired charge separation within the molecules.[38] Promising concepts include DESI,[40] desorption atmospheric pressure chemical ionization (DAPCI),[42] desorption sonic spray ionization (DeSSI),[189] and desorption atmospheric pressure photoionization (DAPPI).[190] Likewise, the family of electrically driven plasmas, including DART,[36] FAPA,[133] and DBD / LTP,[104,105] has proven potential for the analysis of compounds directly from untreated surfaces.

However, a shortcoming of most plasma-based ion sources is their restriction to analyze mainly highly volatile compounds. Except for DART, plasma-based ion sources are typically operated with working gas temperatures of < 100 °C,[105] which favors the analysis of heat-sensitive materials. In contrast, gas temperatures of up to several hundred degrees are typically applied in DART,[36] accelerating the analyte desorption rates, and thus increasing the sensitivity of detection. Accordingly, besides momentum transfer and photo-induced desorption, thermal desorption is claimed to be the predominant mechanism for plasma-based ion sources to convert condensed phase sample matter into the gas phase. This assertion is further corroborated by the fact that throughout the literature elevated plasma gas temperatures were found to result in a gain in analyte signal.[105,115] For instance, Martinez-Jarquin *et al.*[113] investigated the influence of the electrode voltage on the plasma gas temperature of a LTP probe to address the analysis of nonvolatile species. The temperature, and thus the extent of desorption, could be controlled by simple regulation of the input voltage, yielding an extended applicability toward less volatile analytes, however, yet not sufficient for low vapor pressure solids.

Another approach to increase the concentration of analyte molecules in the gas phase involves the dissolution of sample into ricocheting droplets by means of a (hot) solvent jet. However, in the case of DAPCI and DAPPI, this combination was found unsuitable for large molecules and thermolabile compounds.[190] As the applied temperature increased, higher signal intensities were observed due to an enrichment of analyte in the gas phase, but also the tendency toward unwanted fragmentation processes grew.[191]

While each of the above-mentioned techniques has found important applications in different fields of life science, their sensitivity is ultimately limited to the combined efficiency of the desorption / ionization process. Since most target molecules are either nonvolatile or thermally labile, an obvious solution to achieve higher sensitivity while maintaining soft ionization is the separation of the desorption / volatilization from the ionization into two independent steps. This movement yielded in a new family of ionization schemes combining laser ablation and secondary post-ionization.[192]

Providing laser light on the sample surface enables a well-dosed energy input, both spatially and temporally confined. This energy transfer leads into fast coupling of heat and mechanical stress into the sample, resulting in an immediate ejection of neutral molecules and small particles into the surrounding gas phase. However, since only a minor class of compounds can be directly ionized by exposing them to laser radiation,[193] the use of a secondary ionization source is often necessary to result in a competetive analytical method. Following this approach, the radiation absorption efficiency and ablation plume expansion remain the limiting factors determining the abundance of aerosolized sample, while the post-ionization source dictates the ion generation and transmission efficiencies. By now, several combinations have been proposed using either continuous wave or pulsed laser systems. Especially a pulsed laser can provide gentle desorption of sample matter from the surface, although the laser fluence of pulsed systems is large compared to continuous wave lasers. Soft heating of the sample surface and, ultimately, volatilization of molecules into the gas phase is obtained due to an effective energy dissipation between

individual consecutive lasing events. As a consequence, the extent of unwanted fragmentation can be held on a minimum level. In contrast to simple thermal desorption, laser ablation post-ionization has a fourfold benefit: (1) The acquisition time can be drastically shortened.[194] (2) The sample consumption can be reduced yielding similar or even higher sensitivity.[191] (3) The use of a pulsed laser adds the advantage of a snychronization between the release of analyte and the interrogation capacity (analyte on demand).[195] (4) High spatial resolution both in plane and in depth can be achieved, thereby enabling access to mass spectrometry imaging applications.[196]

The spatial distribution of molecules within complex samples is of great interest in different subfields of bioanalytical chemistry since it provides valuable information about the relative position and the potential interplay between neighboring analytes, which would be clearly lost in a standard analysis of the homogenized bulk material.[197] Especially the mapping of low molecular weight compounds has emerged as a challenging task for the well-established spectrometric imaging techniques MALDI,[31] laser desorption / ionization (LDI),[198] and secondary ion mass spectrometry (SIMS),[199] as they require vacuum compatibility of the sample and additional sample preparation steps that are mandatory to obtain interpretable data. Moreover, while MALDI suffers from ion suppression effects and overlapping isobaric effects (since most of the conventional matrices form cluster ions of the same or comparable m/z as the analyte), matrix-free LDI and SIMS potentially exhibit significant fragmentation, which limits their application range.[197,200]

To circumvent these hindrances, ambient mass spectrometry offers an excellent alternative. Prior to the implementation of laser ablation units, several feasibility studies have been conducted using solely the combined desorption / ionization techniques for fast imaging experiments. While the range of accessible molecules could be dramatically extended, the lateral resolution was limited by dispersive gas-flow dynamics and the presence of solvents, which might spread to neighboring areas, resulting in a lateral cross talk of individual pixels in case of all fluid-dynamic desorption techniques. Typical values

were achieved in the upper µm to mm regime, *e.g.*, 200 µm for DESI,[35] 0.5–1.0 mm for FAPA,[133] 1.0 mm for DAPPI and LTP,[190,201] and 2.0–4.0 mm for DART.[202] In the case of DBD and DESI, further improvements have been reported minimizing the interrogation spot size to a competetive level with laser-based methods. Liu *et al.*[203] reported on a DBD probe producing a plasma jet in the 100 µm regime, while Laskin *et al.*[204] presented spectrometric images obtained by a nano DESI source with a lateral resolution of ≈ 12 µm.

Until now, the lateral resolution of laser-based instruments has been scarcely matched by other ambient mass spectrometry techniques. Spatial resolutions of down to a few micrometers and less can nowadays be routinely achieved by commercial instruments. Starting in 1986, Kolaitis and Lubman[205] pioneered the separation of desorption and ionization as two individual mechanistic steps. In their case, a Nd:YAG laser operating at $\lambda = 532$ nm was used to desorb neutral molecules and post-ionization was realized *via* a ^{63}Ni β ion source. In 2002, Coon *et al.*[206] revisited the topic and presented an improved setup combining laser desorption and CI *via* a corona discharge. The by far most popular combination of laser ablation and ESI (LA ESI MS) was proposed by Nemes *et al.*[207] in 2007, implementing a mid-IR laser working at 2.94 µm wavelength, but with a comparably low lateral resolution (350–400 µm). LA ESI MS is capable of detecting a variety of molecular classes with a mass of up to 66 kDa at low detection limits (fmol). In 2008, Shelley *et al.*[208] were the first to investigate the coupling of laser ablation and a plasma-based ionization technique: the FAPA. In their enclosed system, compounds were limited to a lower mass range of < 1 kDa, but the lateral resolution reached 20 µm. In contrast, Galhena *et al.*[209] reported on an open-air configuration using infrared laser ablation metastable-induced chemical ionization to avoid the contamination of enclosure walls. Another tool for the concurrent observation of compounds was presented with the introduction of infrared laser ablation atmospheric pressure photoionization.[210] More recent publications, however, again refocused on plasma-based strategies for post-ionization, including either electrically-driven plasmas, such as DBD,[191] DART,[211] and the vacuum-assisted plasma ion source[212] or post-ionization by radiation from a laserplasma.[213]

In this chapter, the potential of combining a laser ablation sample introduction approach and a custom-designed DBD probe for the ambient spectrometric interrogation of low molecular weight compounds, henceforth referred to as LA DBD MS, is investigated. The subsequent ionization by a helium plasma jet is chosen due to its unique properties, such as the absence of solvents and its high chemical activity. The latter has been previously investigated by Albert *et al.*[214] and demonstrated these plasmas to be an attractive method for the ionization of diverse low molecular weight compounds over a wide polarity range when compared to conventional ESI and APCI.

For the first time in this thesis, a frequency-doubled high repetition rate DPSS laser is used to achieve the ablation process for this specific combination. This proof of principle experiment paves the way around an intrinsic shortcoming of pulsed laser ablation imaging experiments: the analysis time. While most instruments rely on discharge-driven gas lasers or flashlamp-pumped solid-state lasers whose repetition rates are commonly limited to lower values of 1–100 Hz, with the recent advances in laser technology the analysis time is typically no longer limited by the laser repetition rate, but rather by the instrument configuration, the acquistion mode, and the type of mass analyzer. Taking into account the high spatial resolution for laser ablation mass spectrometry imaging experiments and the resulting number of sample spots that need to be mapped to arrive at a full image, the overall acquisition time for one image can easily grow into the dimension of many hours up to days.[215] Thus, as has been demonstrated for MALDI imaging experiments, the high repetition rates of modern DPSS lasers bear the potential to drastically accelerate the throughput, specificity, and sensitivity for high-speed ion image acquisition when compared to current commercially available instrumentation.[194,215–218]

3.2 Experimental

3.2.1 Chemical Reagents

Helium (99.999%, Linde, Berlin, Germany) was used as the discharge gas for the DBD probe. L-lysine ($\geq$ 98%, Sigma Aldrich, Steinheim, Germany), L-arginine (98%, Sigma Aldrich, Steinheim, Germany), urea (99%, Acros Organics, Geel, Belgium), polyethylene glycol (PEG) 200 ($\geq$ 98%, AppliChem, Darmstadt, Germany) and ferrocene (98%, Acros Organics, Geel, Belgium) were used directly without further purification. The nonsteroidal anti-inflammatory drug ibuprofen (Ratiopharm GmbH, Ulm, Germany) and the pharmaceutical extract wild mint oil (*Mentha arvensis*, *ext.*) were bought at a domestic pharmacy. Dried chili pepper pods were obtained from a local supermarket.

3.2.2 Instrumentation

A schematic of the experimental arrangement is given in Fig. 3.1a. In addition, Fig. 3.1b depicts a close-up photograph of the laser ablation process of an ibuprofen tablet followed by DBD post-ionization in front of the MS inlet. Note that the plasma source geometry resulting in a visible afterglow was chosen for visualization purposes of the used helium jet only. This "guide for the eye" was achieved by using the DBD in the ring-ring configuration, as shown on the right in Fig. 2.1. Throughout all experiments in this chapter, however, the pin-ring arrangement depicted on the left side of Fig. 2.1 was utilized.

Coherent radiation at $\lambda = 532$ nm was generated by a DPSS laser (Conqueror 3-LAMBDA, Nd:YVO_4, 1 Hz–500 kHz, average output power: 12 W at 50 kHz, max. 300 µJ / pulse, pulse width: $<$ 10 ns, Compact Laser Solutions GmbH, Berlin, Germany) with an internal second harmonic generation, placed on an optical breadboard above the drift tube of the used TOF mass analyzer. For versatile alignment of the laser light, the laser beam passed three laser mirrors, consecutively. Two second harmonic Nd:YAG laser mirrors were used as a dichroic harmonic separation after which the fundamental ($\lambda = 1064$ nm) and the 808 nm pump-laser light were diverged onto a laser beam dump.

The second harmonic was focused on the sample surface using a high power microspot focusing objective (LMH-5x-532, Thorlabs, Dachau, Germany) with a working distance of $f = 35$ mm and a numerical aperture of $N_A = 0.13$.

For additional control, a beam shutter (SH05, Thorlabs, Dachau, Germany) driven by a shutter controller (SC10, Thorlabs, Dachau, Germany) was used to block the laser beam, if necessary. The laser pulse energy was measured at the position of the sample holder using a NOVA II laser power meter (Ophir Photonics, Darmstadt, Germany), to be 30–100 µJ / pulse, corresponding to a laser fluence of 0.6–2.0 J / cm^2 at 20 kHz. The laser spot size was determined by exposing thermal paper to the focused laser beam. Afterwards, the photosensitized spots were investigated with a confocal microscope (LabRAM HR800, magnification: 10x, HORIBA Jobin Yvon GmbH, Bensheim, Germany). The setup produced circular craters of approximately 0.005 mm^2 on the paper, 40 µm in diameter. While the main objective of this work was not to conduct high resolution imaging experiments, these 40 µm were chosen to be on the order of a typical lateral resolution of a comparable mass spectrometry mapping device.

Subsequent desorption / ionization of the analyte-containing aerosol was achieved by the excited gas stream of a DBD probe. The design and operational parameters of this probe have been discussed in detail in the preceding chapter; thus, merely a brief description is given here: A nonequilibrium plasma was ignited between an internal grounded stainless steel electrode and an outer powered copper mesh electrode, separated by a borosilicate glass tube serving as the dielectric barrier (Fig. 3.1c). Modulated high voltage was provided by a flyback transformer fed by a laboratory power supply. The setup provided an output voltage between 4–15 kV_{pp} at a sine waveform and a frequency of 120 kHz. To sustain the discharge and fluid-dynamically support the ion transmission into the high vacuum of the mass spectrometer, helium was streamed through the glass tube at a moderate flow rate of 0.4 L min^{-1}, adjusted by a mass flow controller (GFC17, Analyt-MTC GmbH, Müllheim, Germany). The plasma probe was co-axially placed in front of the MS inlet on

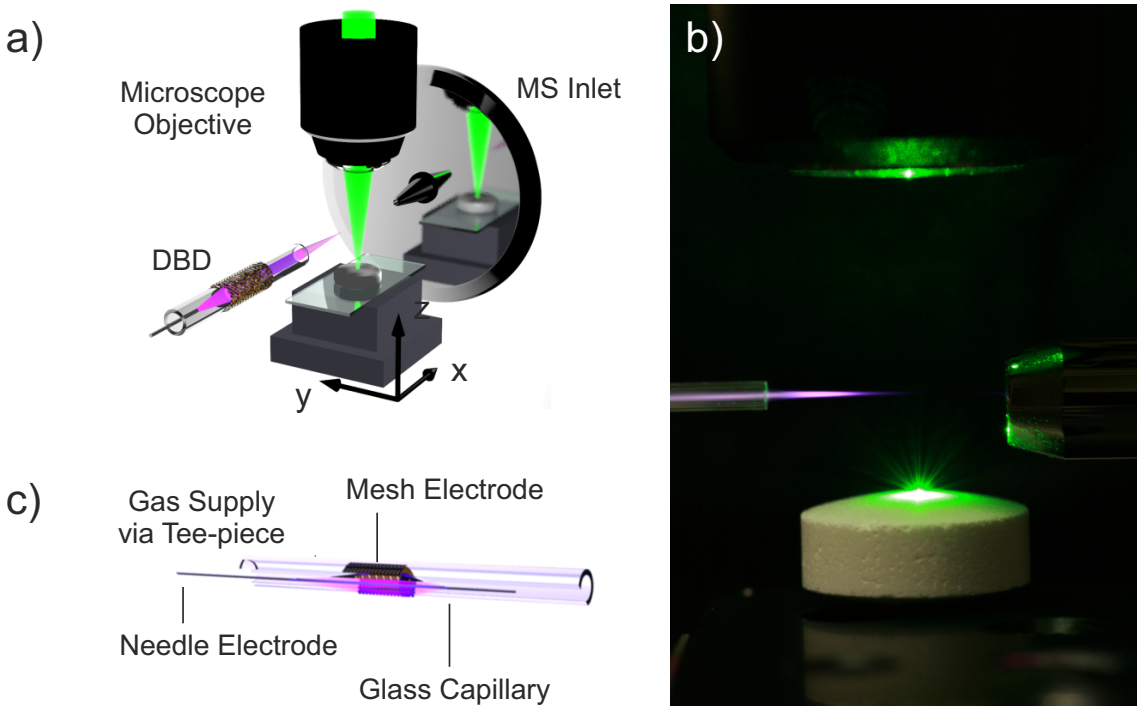

Figure 3.1: (a) Schematic of the experimental arrangement. 532 nm laser light is focused through a microscope objective on the sample surface, inducing sample ablation. Subsequently, the resulting aerosol collides with reagent-ions produced *via* the DBD ion source. (b) Side-view photograph of the laser ablation process of an ibuprofen tablet followed by DBD post-ionization. The plasma geometry has been adjusted for visualization purposes only. (c) Schematic representation of the DBD ion source.

a multidimensional translation stage (M-UMR5.25, M-UMR8.25, Newport, Irvine, U.S.A. and MT1, Thorlabs, Dachau, Germany). The free space distance between the DBD and the MS inlet was set to 1.5 cm. Moreover, it should be noted that the DBD capillary end itself protrudes ≈ 3.0 cm from the actual discharge region. This configuration ensures only pre-excited gas and not the plasma itself to interact with the generated aerosol.

Mass spectrometric studies were conducted using an orthogonal TOF mass analyzer coupled to an atmospheric pressure interface (EL-API-HTOF MS, Tofwerk AG, Thun, Switzerland). The instrument was operated in single reflectron geometry and positive ion mode. Unless stated otherwise, integrated mass spectra were obtained by choosing an

acquisition time of 5 s and an extraction rate of 12.5 kHz. Throughout this study, two different approaches for the initial pressure reduction were tested: (1) a 150 mm resistive glass capillary (i.d. 0.6 mm) fixed in a KF40 pinch screw connection and (2) a home-built conical shaped inlet (i.d. 150 µm). A schematic and detailed description of each configuration is given in Fig. A-1 and Fig. A-2, respectively. The exact positioning of the post-ionization source along x, y, and z (see Fig. 3.1a) was optimized to result in maximum ion yield of the reagent-ion background, discussed in Chapter 2.

Samples were put on a circular sample plate, 2.0 cm in diameter, placed ≈ 5.0 mm below the inlet of the mass spectrometer. Motorized translation stages (MT3-Z8, Thorlabs, Dachau, Germany) allowed for optimal positioning of the sample surface in the focus of the laser light. To minimize the effect of air flow, the sample was shielded by a simple chamber. It consists of a hollow cylinder machined of teflon (i.d. 2.5 cm, height: 1.5 cm) with two drilled holes (i.d. 1.0 cm) for the MS inlet, as well as the glass capillary of the DBD and a microscope glass slide (neoLab, Heidelberg, Germany) on top.

3.3 Results and Discussion

3.3.1 Working Principle

LA DBD MS is supposed to follow a two-step mechanism with subsequent ablation and ionization of molecules directly out of the untreated sample. Fig. 3.2 depicts intermediate results during the arrangement of the experimental workflow and reveals the individual contributions of the promoted ablation process induced by the irradiation of the sample with 532 nm laser light and the ionization *via* the excited gas stream generated by the DBD probe, respectively. As the test compound an intact ibuprofen tablet was used.

Fig. 3.2a depicts a blank spectrum recorded with laser exposure, but without the DBD. To ensure a comparable fluid-dynamic behavior, the helium stream from the DBD probe toward the inlet was switched on (but without the high voltage for achieving the discharge).

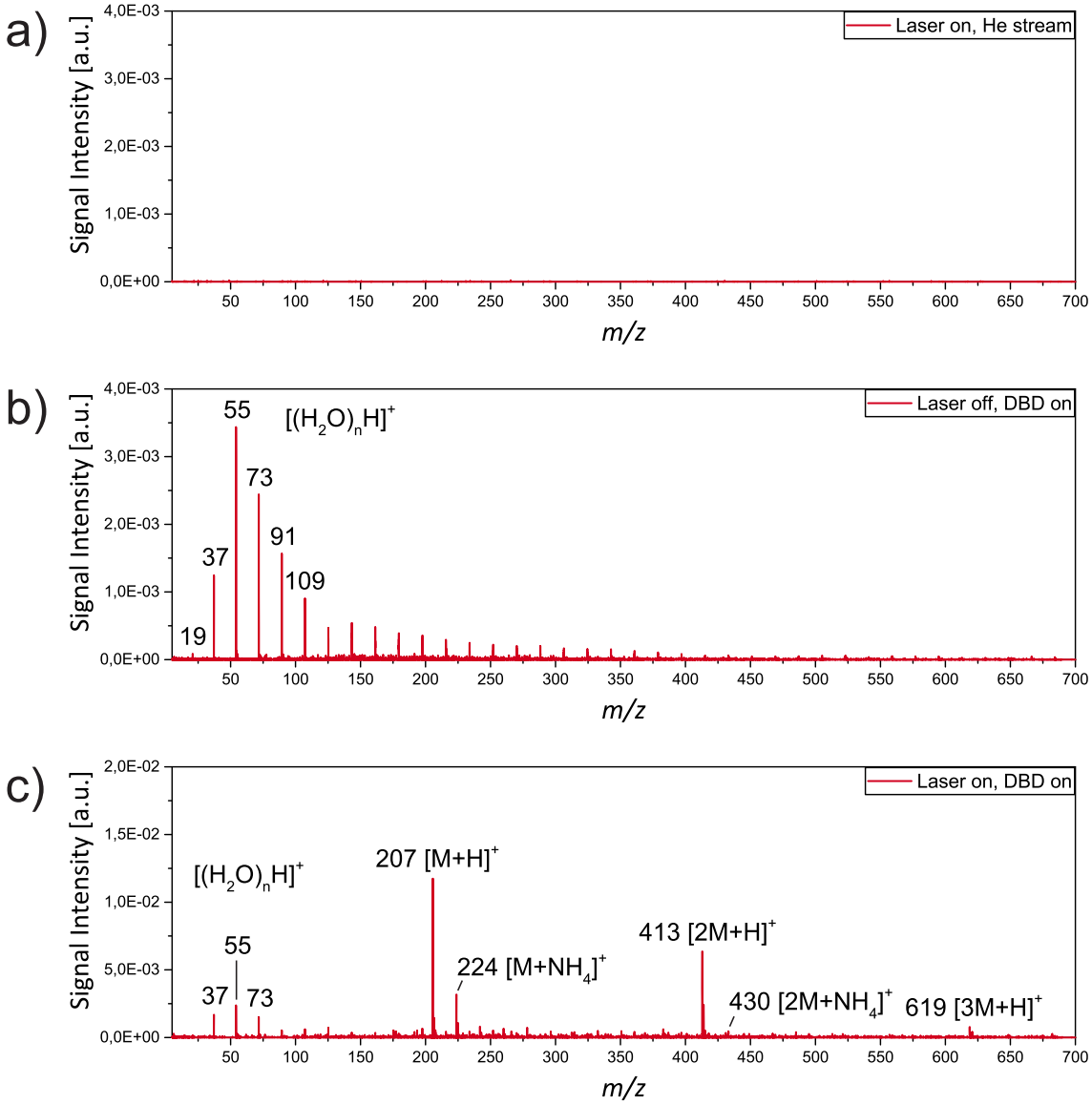

Figure 3.2: LA DBD MS of an intact ibuprofen tablet. (a) Mass spectrum using laser irradiation, supported by a helium gas stream for enhanced ion transmission toward the inlet orifice. (b) Characteristic mass spectral pattern of protonated water clusters produced by the ignited helium-driven DBD probe, while the laser beam is blocked. (c) Mass spectrum of an ibuprofen tablet *via* combined laser irradiation and powered DBD probe.

Hardly any ion signal is detected, indicating that a mere irradiation of the sample does not result in ionized analyte molecules.

When, in contrast, the laser was turned off and the DBD ion source was switched on, solely signals of different reagent-ions (*i.e.*, precursor ions that transfer their charge onto introduced analyte molecules consecutively) dominate the mass spectral pattern in Fig. 3.2b. As discussed in the preceding chapter, these potentially include protonated water cluster ions of the type $[(H_2O)_nH]^+$, proton-bound ammonia water clusters $[(NH_3)(H_2O)_nH]^+$, and charge transfer carriers, such as NO^+, $O_2{}^+$, $NO_2{}^+$, and $O_3{}^+$, opening a number of conceivable pathways for the ionization of sample matter upon its introduction.

Fig. 3.2c, finally, depicts the acquired mass spectrum of a generic ibuprofen tablet upon laser irradiation and the generation of an excited gas stream by DBD post-ionization. An immediate signal response was observed without breaching or preprocessing the tablet in any way. Analyte signals are assigned to the protonated monomer $[M+H]^+$, dimer $[2M+H]^+$, and trimer $[3M+H]^+$ of ibuprofen at *m/z* 207, 413, and 619, respectively. Furthermore, a second series of minor abundant analyte-containing association products is obtained at *m/z* 224 and 430 representing the ammoniated monomer $[M+NH_4]^+$ and dimer $[2M+NH_4]^+$, respectively. In addition, at the low mass region of the mass spectrum, still a substantial amount of residual reagent-ions that can be identified as $[(H_2O)_nH]^+$ with $n = 2$–4 are observed. Their detection assures that the charge introduction into the ionization region occured in abundance.

3.3.2 Effect of the Atmospheric Pressure Interface

In contrast to conventional *in-vacuo* ionization techniques, such as MALDI, SIMS, or LDI, a prerequisite of ambient ionization mass spectrometry is the efficient transfer of analyte ions from atmospheric pressure into the high vacuum region of the mass analyzer to obtain meaningful data.

The initial pressure reduction of most current API MS instruments (typical values for the first vacuum chamber range between ∼1–10 mbar) is achieved by either one of the two basic designs for interfacing a mass spectrometer: Either a pinhole orifice at the tip of a converging or diverging electrode, with opening angles between 10–340°,[219–221] or a connection by means of an inlet capillary[221–223] is installed to restrict the gas flow. Between these two designs, the reported ion transmission efficiencies vary significantly. Best reported values range between 0.02–5% for orifice-based inlet systems,[224–226] while inlet capillaries may transmit up to 30% of the generated ions.[222,227–230] These findings are usually attributed to the presence of a laminar flow[1] inside the capillary.

Besides high ion transmission efficiency, it is of utmost importance for future ablation experiments that the temporal response function is short, yielding representative mass spectra in a minimum time frame. At the same time cross talk between subsequent sample positions in spatially resolved measurements has to be avoided. Therefore, during the assembly of this setup, the performance of two different atmospheric pressure inlets for direct sampling in an open-air configuration was tested, including a commercially available 150 mm resistive glass capillary and a custom-made diverging skimmer interface. The latter is inspired by the so-called ConDuct approach that has been reported by Krutchinsky *et al.*[232,233] According to their observations, electrodes containing a conical channel with a small angular divergence produce narrow, slowly expanding ion beams and exhibit superior ion transmission efficiencies of almost 100%.

Fig. 3.3 depicts transient signal traces for the singly charged ibuprofen monomer following 5 s of laser irradiation and their corresponding integrated LA DBD MS spectra for the capillary inlet and the conical skimmer inlet, respectively. A closer inspection of these data indicates significant differences and reveals the high complexity of the gas flow dynamics between the two approaches. Three fundamental changes are apparent:

[1] The fluid moves in parallel layers along continuous and well-defined trajectories. The flow has no significant velocity components perpendicular to the flow axis and random disturbances in the flow dissipate quickly due to the viscosity of the flowing fluid.[231]

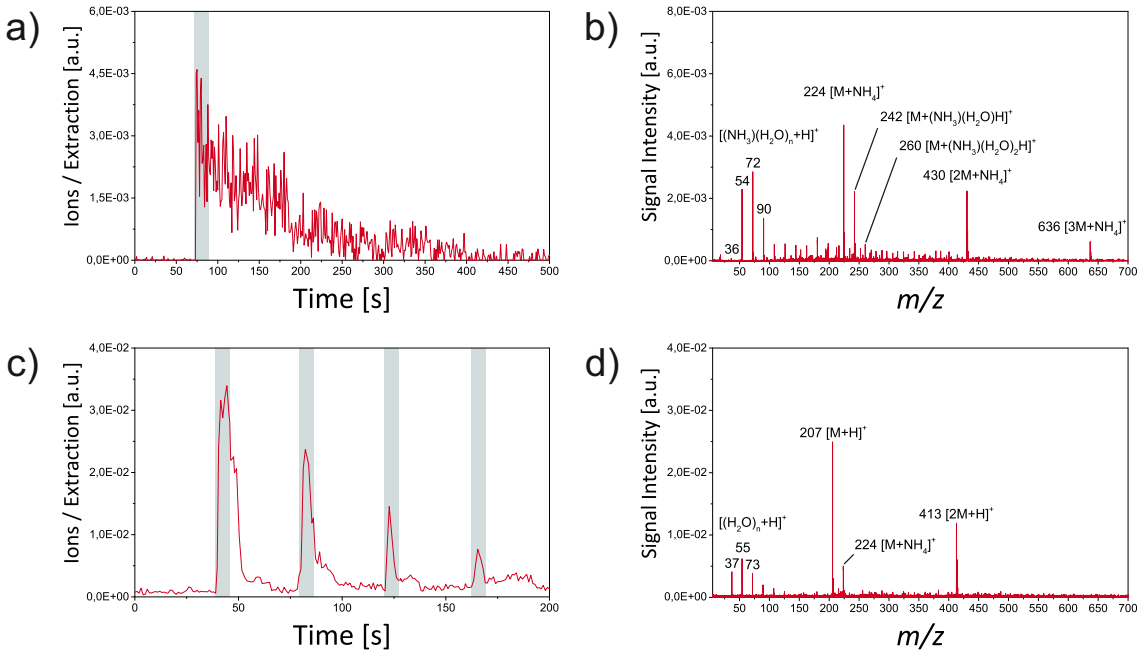

Figure 3.3: Effect of different atmospheric pressure interfaces on the spectrometric performance. (a) Extracted ion trace of the ammoniated ibuprofen monomer $[M+NH_4]^+$ (m/z 224), applying laser irradiation of 5 s at t = 70 s, and (b) corresponding mass spectrum using the inlet capillary. Analyte ions are exclusively observed as ammonium adducts. In contrast, the temporal response of the instrument is drastically accelerated using the conical skimmer interface. (c) Extracted ion trace of the protonated ibuprofen monomer $[M+H]^+$ (m/z 207), applying laser irradiation of 5 s at the indicated time intervals (grey-shaded areas), and (d) corresponding mass spectrum using the conical skimmer inlet. Now, the analyte is preferably detected as $[nM+H]^+$

.

(1) The original concept for the reduction of the temporal response is successfully achieved. Using the inlet capillary (Fig. 3.3a), the transient signal for the ammoniated ibuprofen monomer $[M+NH_4]^+$ at m/z 224 instantly increases upon laser irradiation, but decays over a period of approximately six minutes, after only 5 s of sample irradiation. In contrast, when the mass spectrometer was equipped with the conical inlet, the ion trace for the protonated ibuprofen $[M+H]^+$ at m/z 207 nicely follows the boxcar shape (grey-shaded area) for the laser irradiation (Fig. 3.3c). In consecutive measurements, the temporally resolved character of the ion response remains, only the overall analyte signal

intensity is reduced. This finding can be rationalized by the defocusing of the laser beam on the sample surface after sample depletion since all four subsequent ablation cycles were performed on the same sample spot. A second outcome of this arrangement is the negligible variation of the signal-to-noise ratio toward shorter acquisition times.

(2) Though the conical inlet only comprises a 150 µm orifice compared to the 0.6 mm orifice of the resistive glass capillary, its implementation yields an overall tenfold higher signal intensity (comparing the most abundant ibuprofen containing signals $[M+NH_4]^+$ in Fig. 3.3b and $[M+H]^+$ in Fig. 3.3d).

(3) The exchange of the atmosphere-to-vacuum interface can be seen to drastically affect the observed mass spectral pattern. In case of the capillary duct, the reagent-ion formation is shifted toward a preferred formation of proton-bound ammonia water clusters $[(NH_3)(H_2O)_nH]^+$ which subsequently form association products upon the collision with neutral analyte molecules. Accordingly, the corresponding mass spectrum shown in Fig. 3.3b exhibits the ammoniated ibuprofen monomer $[M+NH_4]^+$ at *m/z* 224 as the base peak. Additional signals in minor abundance are attributed to the following species: $[M+(NH_3)(H_2O)H]^+$ at*m/z* 242, $[2M+NH_4]^+$ at *m/z* 430, and $[3M+NH_4]^+$ at *m/z* 636. Further investigations showed that an unfavorable cluster growth can be followed up to the formation of heptamers. In strong contrast, the skimmer interface reveals not only the preferred formation of protonated water cluster species $[(H_2O)_nH]^+$, but also a decrease in cluster formation. The corresponding mass spectrum shown in Fig. 3.3d depicts the protonated molecular ion $[M+H]^+$ at *m/z* 207, the stabilized ammonium adduct $[M+NH_4]^+$ at *m/z* 224, and the protonated dimer $[2M+H]^+$ at *m/z* 413.

The rather different performances can be rationalized on the basis of the individual gas flow dynamics of each inlet system: In most modern API MS instruments, the bridging between atmospheric pressure and the high vacuum region of the mass analyzer ($< 10^{-5}$ mbar) is commonly achieved by an iterative multi-step differential pumping.

Following this approach, the exhaust of the primary transmission geometry is usually sampled by a second coaxial skimmer interface.[234,235] This configuration is also used in the EL-API-HTOF MS (see Fig. A-2).

Ion beams that expand through a capillary into the background pressure of the first pumping stage are known to be quite divergent.[221,232] Thus, only the central part of the emerging gas stream can be captured. In contrast, the use of conical skimmers results in more narrowly distributed, unidirectional ion beams.[221] Based on the assumption that the conical inlet behaves in a similar manner, the sampling process of the second skimmer would be much more efficient, which could account for the currently observed signal enhancement. Despite this fact, the different inlet geometries further determine the interaction time with the boundaries of each interface. For orifice-based inlets, ion residence and reaction times within microseconds have been reported,[236,237] while the gas flow through a capillary can take up to several milliseconds.[232] Thus, in the case of the non-heated capillary passage, the condensation of analyte-containing particles becomes more likely and leads to an unwanted lengthening of the instrument response function. The latter is reflected by the temporal behavior of the extracted ion chronogram given in Fig. 3.3a. More Recently, Wißdorf *et al.*[227] examined the gas flow dynamics in different inlet capillaries. In contrast to the general assumption that the gas flow inside capillaries is of a laminar state, they observed the transport to be of at least transitional,[2] if not turbulent flow conditions.[3] Therefore, it is proposed that ions are not generally discharged upon collision with the capillary wall,[222] but rather participate in a complex surface / gas phase exchange chemistry. Based on the results presented in Chapter 2 and 3, the latter could play an important role for the observed *in-situ* formation of ammonia. For the remainder of the experiments, the diverging conical inlet was used.

[2] Turbulences are observed in the center, while a laminar flow exists near the boundaries. The flow is considered unstable and potentially shifts rapidly to a turbulent state.[231]

[3] The flow exhibits erratic velocity components perpendicular to its main flow axis. Chaotic vortices are transported with the flow and interact with each other, inducing considerable diffusion of heat and dispersed substances in the bulk gas flow.[231]

3.3.3 LA DBD MS of Test Compounds

Selected representatives of different low molecular weight compounds have been chosen to demonstrate the performance of LA DBD MS, including substances of different physical state, polarity, and volatility. Mass spectra were obtained from urea, the amino acids L-lysine and L-arginine, the liquid polymer polyethylene glycol (PEG) 200, the metal-organic compound ferrocene, and the pharmaceutical extract wild mint oil (*Mentha arvensis*, *ext.*). Pure samples were deposited directly on the sample holder and exposed to laser radiation. As shown before in Section 3.3.1, the ionization of the neutral analyte is mainly attributed to an interaction with the reagent-ions generated in the helium-driven discharge, instead of an ionization *via* laser radiation. Therefore, intact and singly charged molecules are expected as the most abundant species, accompanied by the presence of clustered ions.

As shown in Fig. 3.4a, three different signal series of interest are present in the mass spectrum of urea. Single ion formation $[M+H]^+$ (m/z 61) and $[M+NH_4]^+$ (m/z 78) and dimerization $[2M+H]^+$ (m/z 121) and $[2M+NH_4]^+$ (m/z 138) are observed as the most abundant signals. Further ion peaks stem from residual protonated water cluster species $[(H_2O)_nH]^+$ with $n = 2$ (m/z 37) and $n = 3$ (m/z 55).

The feasibility of the LA DBD MS setup to detect amino acids was demonstrated using L-lysine and L-arginine. Due to their basic character, both compounds are well known preferably yield protonated species. In case of L-lysine, the recorded mass spectrum (Fig. 3.4b) exhibits the protonated monomer ion $[M+H]^+$ at m/z 147, accompanied by the ammonium adduct $[M+NH_4]^+$ at m/z 164.

Fig. 3.4c depicts the mass spectrum of L-arginine. The predominant ion peaks at m/z 175 and 349 indicate the formation of the protonated L-arginine monomer $[M+H]^+$ and the protonated dimer $[2M+H]^+$, respectively. In addition, further spectral contributions in minor abundance are assigned to the ammonium adducts $[M+NH_4]^+$ at m/z 192 and $[M+(NH_3)(H_2O)H]^+$ at m/z 210.

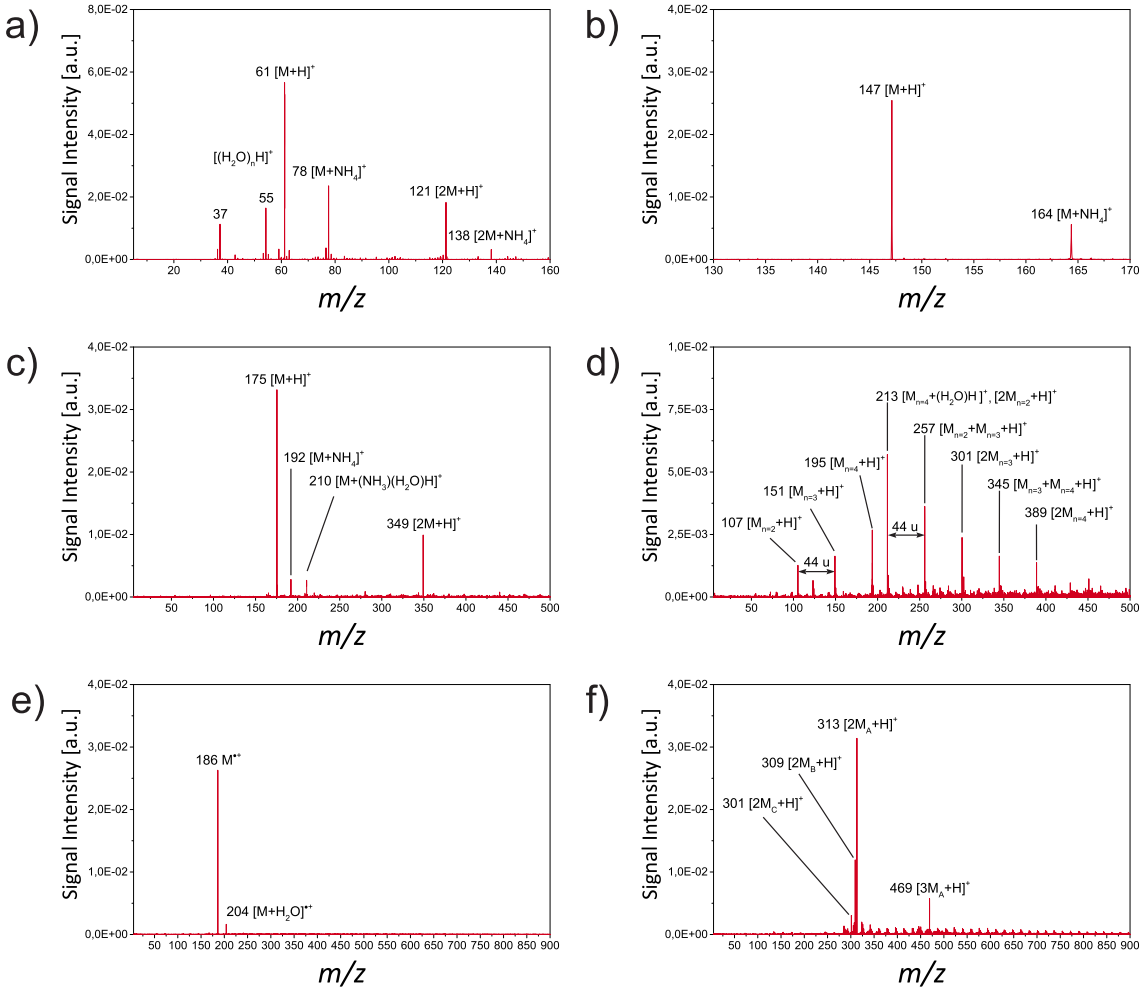

Figure 3.4: Mass spectra of selected target analytes: (a) urea, (b) L-lysine, (c) L-arginine, (d) polyethylene glycol (PEG) 200, (e) ferrocene, and (f) wild mint oil (*Mentha arvensis, ext.*).

The mass spectrum of ferrocene is given in Fig. 3.4d. As discussed in the preceding chapter, the metal-organic compound was specifically chosen to evaluate the operating conditions of the two-step LA DBD MS combination. In recent publications, ferrocene has been used as a precursor to produce iron-based nanoparticles, either *via* a laser-driven pyrolysis [238,239] or a photolytic decomposition using a DBD. [187] Thus, the spectrometric detection of the intact ferrocenium cation corroborates the underlying assumption that neither the applied laser ablation step nor the subsequent DBD post-ionization deteriorates

the molecular information of the probed species. The introduction of a few crystals of ferrocene into the sampling region while the laser beam was blocked, but the post-ionization source was powered, resulted in a pronounced detection of the intact ferrocenium cation $M^{\cdot+}$ at *m/z* 186 and a minor abundant ion peak at *m/z* 204 associated with the water adduct $[M+H_2O]^{\cdot+}$. Upon the additional irradiation of the target sample with 532 nm laser light, the combination of LA DBD MS yields an augmented population of neutrals in the surrounding atmosphere, and thus a gain in signal by a factor of 5 is observed.

LA DBD MS was also applied for the analysis of liquid samples. As a test compound the polymer polyethylene glycol (PEG) 200 was chosen. The given nominal molecular weight, in this case 200, refers to the most abundant oligomer in the polydisperse mixture, containing a broad distribution of molecular weights. A simplified chemical formula can be given as $HO(CH_2CH_2O)_nH$. The obtained mass spectrum in Fig. 3.4e is mainly composed of different analyte-containing signal progressions. The latter include several spectral contributions assigned to the singly charged protonated ions $[M_n+H]^+$ and $[M_n+(H_2O)H]^+$, with $n = 2$–4, and a number of cluster species in higher abundance that represent either the pure dimeric species $[2M_n+H]^+$ with $n = 2$–4 or mixed cluster ions. Nonetheless, due to the characteristic mass difference of 44 Da, corresponding to one subunit of ethylene oxide, a spectral assignment of the individual signal propagations was possible.

Fig. 3.4f depicts the acquired mass spectrum of the pharmaceutical extract wild mint oil, containing a mixture of mainly menthol, menthone, isomenthone, and menthofuran in descending extents, respectively. Preferably, the singly charged protonated dimers $[2M+H]^+$ of menthol (*m/z* 313), menthone (*m/z* 309), and menthofuran (*m/z* 301) are observed. Furthermore, the ion peak at *m/z* 469 can be assigned to the protonated menthol trimer $[3M+H]^+$. Similar to the analysis of ferrocene, a $\approx$7.5-fold signal enhancement is obtained upon laser irradiation, compared to the pure DBD mass spectrum.

3.3.4 LA DBD MS of Chili Pepper

After LA DBD MS was successfully applied for the analysis of pure samples, a feasibility study evaluating the direct analysis of biological samples was conducted by studying a dried chili pod. The latter is known to contain the naturally abundant capsaicin. This alkaloid is produced as a secondary metabolite by addition of a branched fatty acid to vanillylamine and can be found in different quantities throughout the individual parts of the fruit: in the placental tissue holding the seeds, the membranes, and the flesh. Individual measurements were carried out, using the inner part of the pod holding the seeds, the outer membrane and flesh, and the seeds, consecutively. Upon the exposure with laser light and the subsequent ionization *via* the DBD probe, mass spectra were detected, indicating the presence of capsaicin. Throughout the consecutive experiments the signal pattern stayed the same. However, as expected, the signal intensities for the capsaicin originating ions varied and decreased according to the known distribution of the alkaloid.

An exemplary mass spectrum is depicted in Fig. 3.5. LA DBD MS was performed on the central part of a capsicum fruit. The intact capsaicin is detected as a protonated molecular ion $[M+H]^+$, but in rather low abundance. Earlier mass spectrometric studies using a plasma-based ion source already demonstrated that capsaicin tends to decompose.[36] The inset in Fig. 3.5 depicts the individual fragment-ions of the known fragmentation pathway. Previous observations using the LTP showed the highest abundance for m/z 137, a characteristic signal for the vanillyl moiety resulting from the cleavage of the C–N-bond and a subsequent rearrangement of the aromatic ring structure, and an ion peak at m/z 306 representing the intact protonated capsaicin.[201]

A comparison with the literature spectrum suggests that the degree of primary analyte fragmentation here is merely caused by the analyte being susceptible to oxidative stress rather than a harsh ablation / ionization method itself. However, the obtained mass spectral pattern only partially resembles the recent findings. As observed before, the single ion formation for capsaicin is observed. However, the signal intensity for the vanillyl fragment

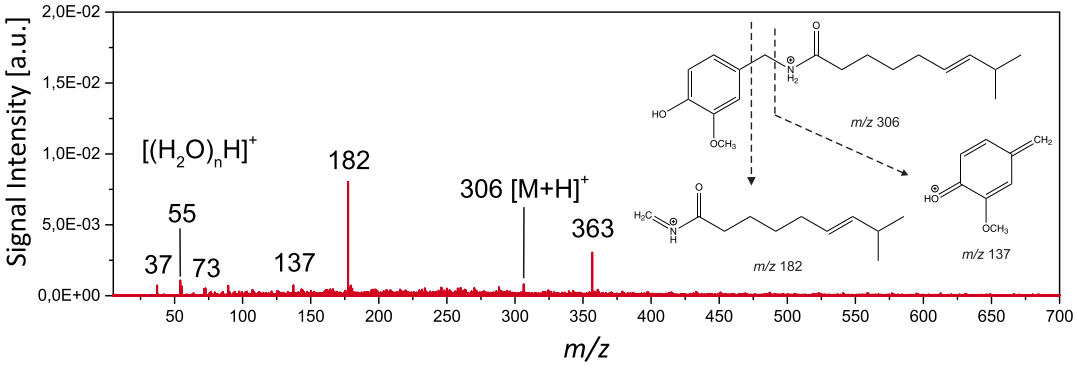

Figure 3.5: Mass spectrum obtained from a dried chili fruit. The signal at m/z 306 is assigned to the intact protonated capsaicin molecule $[M+H]^+$. Ion peaks in higher abundance represent the formation of fragmentation products, indicating either the cleavage of the benzylic C–C bond yielding the dominant signal at m/z 182 and its dimer m/z 363, or cleavage of the C–N bond resulting in a subsequent rearrangement of the aromatic ring structure and formation of the vanillyl moiety at m/z 137.

is found to be drastically different, yielding only small signal intensities. In contrast, the signal at m/z 182 and its belonging dimer at m/z 363 dominate the mass spectrum. The presence of these ions indicates that the reaction pathway for the cleavage of the benzylic carbon bond is facilitated under these experimental conditions.

3.4 Conclusion

A prototype for plasma-based ambient mass spectrometry analysis has been constructed that comprises a laser ablation sample introduction approach and a DBD for post-ionization. Effective ablation was achieved by the second harmonic output ($\lambda = 532$ nm) of a DPSS laser operating at a repetition rate of 20 kHz, pulse energies below 100 µJ, and a spot diameter of 40 µm. In contrast to former ambient desorption / ionization setups, the lateral resolution was only determined by the focal spot size of the laser and not limited by the dimensions of a plasma or the lateral resolution provided by a diverging solvent jet. Though the mass range was restricted to lower m/z values of up to 1 kDa (characteristic for most ambient desorption / ionization techniques), this combination suffers less from matrix effects in the lower mass region compared to the well-established MALDI approach.

Upon laser irradiation, the ejected neutral analyte-containing aerosol was transported by the intercepting exhaust of the DBD probe toward an in-house designed atmospheric pressure inlet. Depending on the nature of the analyte, subsequent vaporization and ionization yielded mainly singly charged protonated molecular ions $[n\mathrm{M}+\mathrm{H}]^+$, stabilized ammonium adducts $[n\mathrm{M}+\mathrm{NH_4}]^+$, or radical cations $n\mathrm{M}^{\cdot+}$, while the degree of primary analyte fragmentation was usually low. The versatility of this technique was demonstrated by recording mass spectra of several test compounds of different polarity, ionization energy, and vapor pressure. Eventually, the analytical capabilities of LA DBD MS were examined by detecting several coexisting analytes in an unpreprocessed mint oil sample and the naturally abundant alkaloid capsaicin in its native matrix of a chili pepper fruit.

4 Hyphenated Setup for Laser Ablation Dielectric Barrier Discharge Ambient Mass Spectrometry and Raman Spectroscopy

The approach of combining different complementary characterization techniques to solve complex analytical problems has a distinguished history. By now, mass spectrometry and Raman spectroscopy have been scarcely applied as complementary methods, although a combination of both would result in a highly beneficial and powerful analytical tool: While Raman spectroscopy displays structural information, mass spectrometry allows for an accurate determination of molecular mass. Within this chapter, a setup based on the instrumental integration of the LA DBD MS setup, introduced in Chapter 3, and an optical compartment for Raman spectroscopy into a single instrument is presented. The core of this system is a shared DPSS laser with a variable repetition rate of up to 200 kHz. By adjusting the repetition rate of the laser, and thus controlling the pulse energy, the operational conditions are set to either experiment to perform spectrometric or spectroscopic measurements. The final design allows for the acquisition of complementary data sets from the identical sample volume and provides the opportunity for an unambiguous identification of target analytes.

Based on:
Bierstedt, A.; Schmid, T., Panne, U.; Riedel, J. manuscript in preparation.

4.1 The Complementarity of Mass Spectrometry and Raman Spectroscopy

In recent years, the approach to use multiple combined analytical techniques for spectrochemical analysis has received increasing attention to account for the complex analytical problems that arise from the chemical and physical diversity of most anthropogenic and natural samples.[240–245] To obtain a comprehensive understanding of their individual properties and functions, a simultaneous observation of complementary information, denoted as "hyphenation", is highly desirable. Historically, the term "hyphenation" was first phrased by Hirschfeld to describe the positive synergy of two or more different analytical techniques with the aim to acquire comprehensive and informative data sets of analytes, compared to those obtained from a standalone technique.[246]

The hyphenation of different characterization techniques has brought forth some memorable breakthrough, *e.g.*, the combination of an in-house fabricated gas chromatograph and a TOF MS, first described in the late 1950s,[247] has matured to a cornerstone of modern mass spectrometry.[248] Surprisingly, spectroscopic and spectrometric methods have rarely been hyphenated. However, recent technical advancements indicate one of the most promising future directions of mass spectrometry is toward the instrumental integration with non-destructive, non-spectrometric techniques.[55,249] To achieve a simple yet powerful hyphenation, laser-based ambient mass spectrometry and Raman spectroscopy are promising candidates. Both techniques can be applied for the rapid online and *in-situ* analysis of samples without extensive sample preparation. Though both methods yield characteristic fingerprints, each technique for itself exhibits distinct strengths and weaknesses in its standalone applicability.

Laser-based ambient mass spectrometry uses short laser pulses to ablate and convert condensed phase material into the gas phase, which is then post-ionized, transferred into the mass analyzer, separated with respect to its m/z, and detected. Usually, a TOF MS is

employed as the mass analyzer of choice due to its ability to acquire an entire mass spectrum from each ablation event.[192] Without chemical labeling or the application of an additional light-harvesting matrix (which would clearly distort the corresponding Raman spectra in the hyphenation approach), an accurate determination of the exact molecular mass, and thus a molecular formula, can be provided. Moreover, current state-of-the-art instruments are also able to provide structural information by tandem mass spectrometry experiments (MS / MS). The latter is based on the selective fragmentation of a precursor ion of a particular *m/z* to produce characteristic secondary fragments. However, while a sufficient amount of primary ions is mandatory to run this technique, at the same time also only a limited acquisition window is available in most imaging or high-throughput scenarios, which sometimes restricts MS / MS experiments.

A complementary approach to obtain structural information involves the application of Raman spectroscopy, which is capable of providing molecular fingerprints and functional group information.[61] While in the spectrometric experiments the molecules are consumed throughout the analysis procedure, *i.e.*, mass spectrometry is intrinsically a destructive technique, Raman spectroscopy could be performed prior to the spectrometric analysis without altering or depleting the sample. However, especially in the case of complex samples, Raman signals become often unspecific since the resulting vibrational spectrum will be a superposition of the spectra of each of the components in the mixture. Thus, typically a library searching or post-processing of the data has to be conducted to interpret the spectral information and allow for qualitative analysis. Consequently, a combination of Raman spectroscopy and mass spectrometry could be highly beneficial to alleviate those drawbacks.

Earlier work in combining these two techniques in a sequential fashion was conducted in the areas of biology,[250–253] cultural heritage,[254] forensics,[255] and surface analysis.[256,257] These endeavors already state the relevance and roughly sketch the potential of a successful online combination. Though all these studies yielded complementary infor-

mation, the correlation of the individual data sets is hampered with respect to the spatial resolution of each individual instrument. According to Hirschfeld,[246] hyphenation encompasses more than just the use of two different analytical techniques on a single sample for the same purpose. Instead, it is considered to be an instrument or a method, in which both instruments are mould into a single integrated unit. Another aspect of true hyphenation is the shared use of instrumental components in a way that the combined system is more compact and more affordable than two standalone instruments. This approach has been scarcely attempted by now.

In 1998, Williams *et al.*[258,259] investigated heterogeneous catalytic systems placed inside a gas-tight reaction chamber by coupling surface enhanced Raman spectroscopy along with the parallel option to examine the gas phase composition by means of a residual gas analyzer. Likewise, in the following years, Nijhuis *et al.*[260] and Valero-Pedraza *et al.*[261] performed experiments on catalytic metal oxides in a similar manner. Another instrumental design was patented in 2014, termed a dual-spectroscopy detection apparatus for gas phase samples.[262] Its layout differs mainly by its sample introduction, using a pyrotube with a heater coil for sample evaporation. As stated, Raman measurements can be either performed directly within the inlet capillary or the pyrotube. Throughout, all these experimental arrangements focused mainly on the analysis of readily available gas phase analytes. In contrast, hyphenated instruments for the analysis of condensed phase samples in their native state were still lacking.

While Raman spectroscopy can be readily applied for the analysis of solid, liquid, and gaseous samples, a prerequisite of mass spectrometry is the efficient conversion of sample matter into the gas phase. With the introduction of ambient mass spectrometry, the transformation of samples was dramatically simplified.[263] Out of the variety of different ambient ionization schemes reported by now, in 2016, Meher *et al.*[264] combined the simplicity of paper spray ionization mass spectrometry[265] and a Raman spectroscope. The overall effectiveness of this approach became especially apparent since even MS / MS

experiments were unable to differentiate positional isomers that have been used as test compounds. In contrast, the spectroscopic measurements yielded meaningful vibrational spectra and served as the basis for an unambiguous identification of target analytes.

For the comprehensive study of (bio)chemical systems, often the identification of the included constituents in terms of their net-concentrations is not enough, but the additional information of the spatial distribution is pivotal for the sample's functionality. Accordingly, in many experiments the lateral defintion of the interrogation spot is realized by employing a spatially confined laser beam. In terms of mass spectrometry, laser ablation / desorption is most commonly known from MALDI,[31,32] even though also various laser ablation post-ionization couplings have been demonstrated to be promising tools for chemical imaging applications.[192,197]

Throughout, these techniques rely on the capability of a laser to deliver a high density of light onto a spatially well-defined area. In addition to this spatial resolution, the majority of spectroscopic techniques exploits laser light's other intrinsic properties, such as coherence, monochromaticity, and polarization. Only in the proposed hyphenated spectroscopy / ablation experiments, all the favorable properties of laser radiation are fully exploited. By now, this combination has been hampered by instrumental compromises: Most laser-based setups employ pulsed flashlamp-pumped solid-state lasers with typical pulse lengths in the ns-range and low repetition rates up to 100 Hz, but sufficient pulse energies to convert condensed matter into the gas phase. For Raman Spectroscopy, these lasers are poorly suited having excessive energies and low duty cycles, leading to unfavorable signal-to-noise ratios and long integration times. In addition, the high peak intensities of a flashlamp-pumped laser potentially induce surface alteration. Thus, continuous wave lasers are commonly used as an excitation source instead.[67]

In accordance with the main objective of this thesis, a viable alternative to the flashlamp-pumped laser has been applied in different fields of analytical chemistry,[194,218,266–268] the

pulsed DPSS laser. Compared to a flashlamp-pumped system, the latter is more compact, entirely air-cooled, and characterized by its exceptional output characteristics, such as an excellent beam quality, single mode lasing, and low pulse-to-pulse fluctuations.[5,14,15] Moreover, their flexible repetition rates of up to hundreds of kHz make them suitable candidates for Raman experiments.[268] At the same time, the current generation of commercially available DPSS lasers is capable of providing pulse energies that are sufficient to ablate every material by focusing the laser beam with conventional optics.

In this chapter, a novel instrumental design is presented in which a shared DPSS laser is subsequently applied as the excitation laser for Raman spectroscopy and laser-based ambient mass spectrometry. Due to the shared optical beam path, signals from the identical sample volume are obtained. The new approach of the instrumental integration of the DPSS laser delivers a performance for both techniques that is competitive to most conventional laser systems.

4.2 Experimental

4.2.1 Chemical Reagents

Polyethylene glycol (PEG) 200 ($\geq 98\%$) and methanol ($> 99.9\%$) were purchased from AppliChem (Darmstadt, Germany), ferrocene (98%) and *tert*-butylbenzene (99%) from Acros Organics (Geel, Belgium), *N*-acetyl-*para*-aminophenol (98%) and ibuprofen ($\geq 98\%$) from Sigma Aldrich (Steinheim, Germany), *N*-acetyl-*meta*-aminophenol (99%) from J&K Scientific GmbH (Pforzheim, Germany), and rhodamine B from Lambda Physik AG (Goettingen, Germany). The pain relievers ibuprofen and paracetamol (both Ratiopharm GmbH, Ulm, Germany) were obtained from a domestic pharmacy. Ultra-high purity helium (99.999%, Linde, Germany) was used as the discharge gas for the post-ionization source. All chemicals were used directly without further purification.

4.2.2 Instrumentation

To achieve an optimal spatial overlap of the interrogation volume while minimizing the total cost of the proposed experimental setup, it is highly desirable to implement a shared laser system for both Raman spectroscopy and laser-based ambient mass spectrometry. The experimental arrangement shown in Fig. 4.1 comprises three main components: (1) the shared DPSS excitation laser, (2) the spectrometric component, including a TOF MS with an atmospheric pressure interface and an electrically driven plasma probe for post-ionization, as well as (3) an optical spectroscopy compartment, consisting of suitable collection optics and a detection system for spectral recordings. Note that the results presented in this chapter have been conducted with a predecessor laser model and a preliminary experimental setup for the mass spectrometric detection. As a result, slight deviations in the experimental details and in the obtained results can be found, when directly compared to those shown in Chapter 3.

A compact DPSS laser (Blade YVO_4 IR_25, Nd:YVO_4, 1 Hz–200 kHz, Compact Laser Solutions GmbH, Berlin, Germany) was employed, which is capable of generating 25 ns laser pulses at its fundamental wavelength ($\lambda = 1064$ nm). A reduction of the total irradiance can be achieved by adjusting either the diode pump power (which scales with the laser output), a defocusing of the laser beam while conducting the Raman experiment, or by operating the laser system at even higher Q-switch repetition rates. Scenario one and two have switching times on the order of several seconds. Therefore, a faster alternative to alter the irradiance properties was achieved by keeping the continuous laser power constant (no change in the voltage applied to the pump-diodes), but to only alter the repetition rate, thereby distributing the overall energy over a higher number of laser pulses. This option maintains the steady irradiance and only affects the pulsed laser fluence since the two desired operational modes can be commuted within microseconds. Consequently, the switching between the spectroscopic and spectrometric mode can be performed with only an electronic change in the pulse repetition rate.

For the combined Raman / LA DBD MS experiments, the visual second harmonic of the output of the DPSS laser (λ = 532 nm) was used. To generate this frequency doubled coherent light, the near-IR fundamental of the Nd:YVO_4 laser (λ = 1064 nm) was fed through a beta barium borate (BBO) crystal under the phase matching angle, resulting in a maximum pulse energy of 50 µJ / pulse at a repetition rate of 2 kHz. This setting was used for the laser ablation experiment. Toward higher repetition rates, the frequency conversion efficiency dropped, and at the maximum repetition rate of 100 kHz no green light could be generated. The optimum compromise between high repetition rate and pulse energy was found to be 2.7 µJ / pulse at 15 kHz. This setting was used for the quasi-continuous Raman excitation. To prevent leakage of intense 1064 nm infrared light and 808 nm pump-laser light into the beam, a polarizing harmonic separation was used. Subsequently, by an ultrasteep laser-flat beamsplitter (LPD02-532RU-25, Semrock, Rochester, U.S.A.), mounted in a 45° angle, the laser beam was directed into a high power microspot focusing objective (LMH-5x-532, f = 35 mm, N_A = 0.13, Thorlabs, Dachau, Germany). The irradiated spot size was empirically determined to be 40 µm in diameter.

Raman spectra were recorded in an interrogation geometry antiparallel to the excitation light path. Back-scattered light was collected and recollimated by the same microscope objective, passed the dichroic laser-flat beamsplitter, a 532 nm single-notch filter (NF01-532U-25, Semrock, Rochester, U.S.A.), and a plano-convex lens (LA4306, f = 40 mm, Thorlabs, Dachau, Germany), focusing the light into an optical fiber. The other end of the fiber was connected to the entrance slit of a Czerny-Turner spectrograph (SR-303i-B, triple grating torret: 600, 1200, 1800 grooves / mm, Andor Technology Ltd., Belfast, UK), equipped with a CCD camera (iDus, −65 °C, Andor Technology Ltd., Belfast, UK). Unless stated otherwise, the entrance slit width was 150 µm and the acquisition time per spectrum was set to 2 s.

To perform UV Raman experiments, a current state-of-the-art DPSS laser was used (Conqueror 3-LAMBDA, Nd:YVO_4, 1 Hz–500 kHz, average output power: 12 W at 50 kHz,

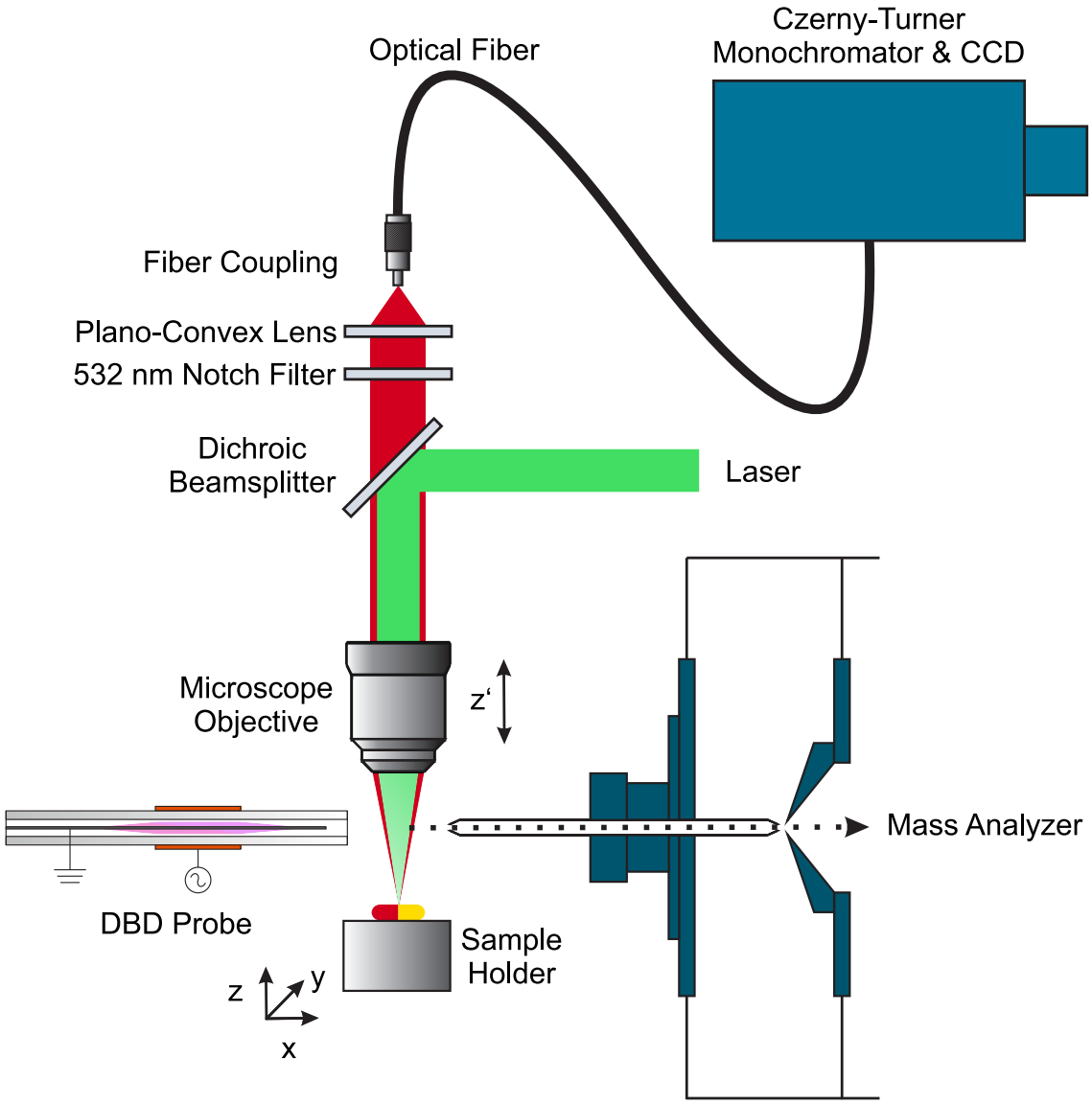

Figure 4.1: Schematic diagram for hyphenated laser spectroscopy and LA DBD MS. Coherent radiation for both techniques was provided by a shared DPSS laser placed on an optical breadboard above the drift region of the mass analyzer.

pulse width: <10 ns, Compact Laser Solutions GmbH, Berlin, Germany) with an internal second and third harmonic generation. The resulting pulse energies were 300 µJ and 100 µJ for the wavelengths 532 nm and 355 nm, respectively. For better comparison, this laser was also operated at a repetition rate of 15 kHz. Moreover, due to the change in wavelength, the ultra-steep laser-flat beamsplitter was exchanged to match the 355 nm laser light (LPD01-355RU-25, Semrock, Rochester, U.S.A.).

A detailed description of the mass spectrometric component has been given in Chapter 3. Briefly, it consists of the DPSS laser system, generating an analyte-containing aerosol out of the irradiated sample, which is then post-ionized in the excited helium plasma jet of a custom-made DBD probe, introduced in Chapter 2. Ion detection was carried out with the EL-API-HTOF MS, manufactured by Tofwerk AG (Thun, Switzerland). In contrast to the conical inlet used throughout the remainder of this thesis, the ion transfer into the first chamber of differential pumping was still realized with the 150 mm resistive glass capillary. A detailed description of this specific setup is given in the appendix (Fig. A-1). Unless stated otherwise, the mass analyzer was operated in single reflectron geometry and positive ion mode to record integrated mass spectra with an extraction rate of 20 kHz, at an overall acquisition time per spectrum of 2 s.

4.3 Results and Discussion

4.3.1 Laser Spectroscopy

As has been discussed in the introductory chapter, Raman scattering is a low light application. As a consequence, the huge contrast between the bright excitation light and the comparably by several orders of magnitude weaker Stokes signal hampered the visual alignment of the collection beam path. Since the detected signal was extremely sensitive to the exact fine tuning of the optical elements, prior to the Raman measurements, laser-induced fluorescence experiments with a 0.4 µM methanolic solution of rhodamine B were conducted. Upon irradiation with the focused laser beam, the emitted fluorescence light

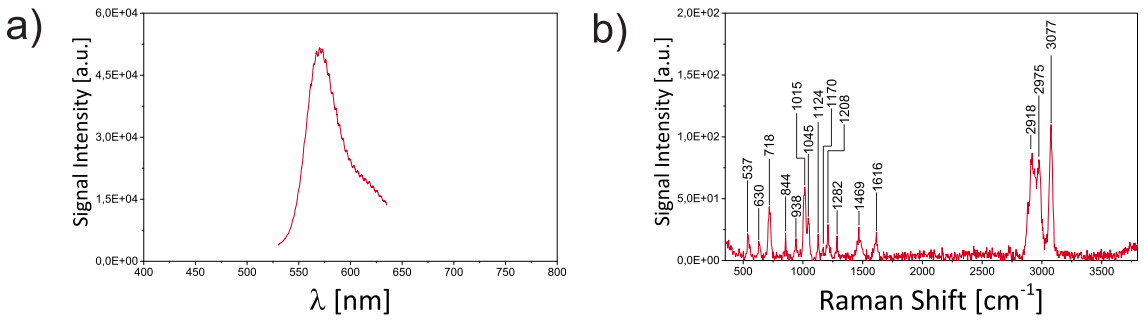

Figure 4.2: (a) Fluorescence microscopy spectrum of a 0.4 µM methanolic solution of rhodamine B. The fringes in the recorded spectral intensity are artifacts from the collection beam path geometry. (b) Raman spectrum of *tert*-butylbenzene.

was several orders of magnitude more intense than Raman signal and could be easily seen by the bare eye. Thus, the visual alignment of the experimental setup could be facilitated and resulted the fluorescence to end in a tightly focused spot on the entrance end of the optical fiber. Afterwards, the fine-tuning of the collection optics was undertaken to result in maximum absolute fluorescence intensity. An example of a fluorescence microscopy spectrum can be seen in Fig. 4.2a. Even though the acquisition time was reduced to the shortest acquisition window possible ($t = 0.001$ s), the excitation of the fluorophore rhodamine B yielded a strong signal response with an emission maximum at $\lambda = 570$ nm.

4.3.2 Hyphenation

After geometrical optimization of the optical elements, the collection efficiency of the setup was high enough to obtain meaningful Raman spectra. An example is given in Fig. 4.2b, depicting the Raman spectrum of *tert*-butylbenzene. By directly comparing the experimental spectrum and previously published data,[269] the same band positions with only minor band shifts can be observed. Following this step, the hyphenated experiments could be performed. The typical working procedure was as follows: First, the non-destructive spectroscopic method was applied at high repetition rates, but lower pulse energies, preventing sample removal or sample damage. Afterwards, this interrogation step was followed by the sample-consuming laser ablation post-ionization experiment, which requires lower repetition rates, but higher pulse energies, to ensure ablative sampling.

Ferrocene

For the first hyphenation experiment, the metal-organic compound ferrocene was investigated as the sample of choice. Given its high symmetry, the molecule exhibits a well-known vibrational spectrum, whereas previously conducted ambient mass spectrometry experiments, *e.g.*, shown in Reference [143] or in the preceding Chapters 2 and 3, readily yielded simple and easy-to-interpret mass spectra.

The recorded Raman spectrum of ferrocene is depicted in Fig. 4.3a. The individual peak positions were assigned by comparing the experimentally obtained vibrational modes with previously published data.[270–272] At lower wavenumbers, characteristic spectral features arise due to the symmetric ring-metal stretching modes of ferrocene at 301, 309, and 319 cm^{-1}. Another Raman band in the same vibrational energy range is detected at 390 cm^{-1} and originates from the symmetric ring tilting vibrations of the cyclopentadienyl ligand. Going to higher wavenumbers, further spectral contributions are observed that can be either associated with the ring breathing mode of the cyclopentadienyl anion at 1098 and 1106 cm^{-1} or the bending mode of C–H perpendicular to the ring system at 1059 cm^{-1}. Moreover, additional Raman bands are observed in the C–H stretching region of the spectrum (depicted in the inset in Fig. 4.3a) at 3090, 3103, and 3116 cm^{-1}. They represent the stretching vibration of C–H in different intramolecular positions.

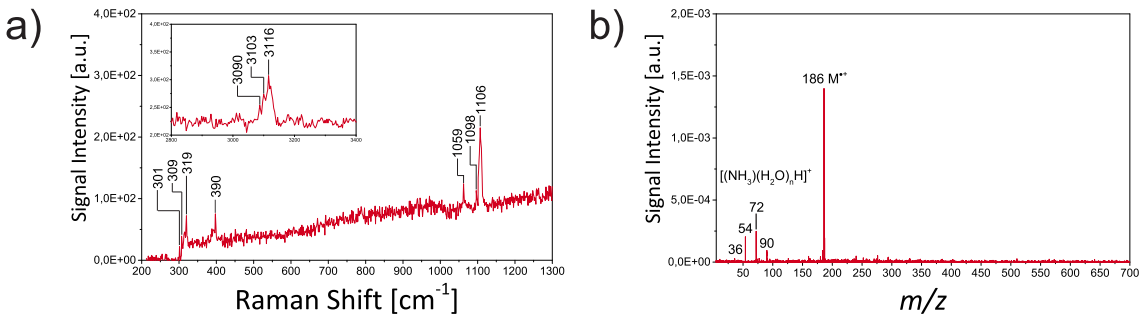

Figure 4.3: Complementary data set of the metal-organic compound ferrocene: (a) Raman spectrum. (b) Mass spectrum obtained by LA DBD MS.

The complementary LA DBD MS spectrum is depicted in Fig. 4.3b. As can be seen, it bears a striking similarity with the previously recorded mass spectra: The predominant ion peak derives from the detection of the intact ferrocenium cation $M^{\cdot+}$ at m/z 186. In addition, minor spectral contributions at lower m/z values stem from residual reagent-ions of the type $[(NH_3)(H_2O)_nH]^+$, which are not consumed in the sample charging mechanism of ferrocene. Throughout this interrogation step, no evidence for any pronounced fragmentation was observed.

As has been described in Chapter 2, the high resolution mode of the used TOF mass analyzer allows for an unambiguous spectral assignment. In this fashion, the analytical power of the spectrometric experiment is demonstrated since in case of an unknown sample the mass spectrum provides the possibility to determine the analyte's molecular formula.

Polyethylene glycol (PEG) 200

To further emphasize the flexible applicability of the hyphenated approach, a combined Raman / LA DBD MS experiment of the liquid polymer PEG 200 was conducted.

According to the routine described above, at first, the liquid sample was illuminated at higher repetition rates, yielding the Raman spectrum shown in Fig. 4.4a. By comparison with earlier Raman studies,[273–275] a good correlation between the experimentally obtained Raman spectrum and the literature was observed. In the next step, the individual spectral bands were assigned according to the Raman studies and DFT calculations reported by Samuel and Umapathy.[276] In general, the recorded Raman spectrum can be divided into four regions of interest. Each of these represents a characteristic combination of CH_2 - related vibrations, which are typically accompanied by considerable contributions originating from the C–O and C–C stretching vibrations of the backbone. In the first spectral region (800–1200 cm^{-1}), vibrations associated with the rocking mode of CH_2 at different intramolecular positions (either in the middle of the polymer chain or near the OH terminus) are observed. Similarly, the second region of interest, ranging from

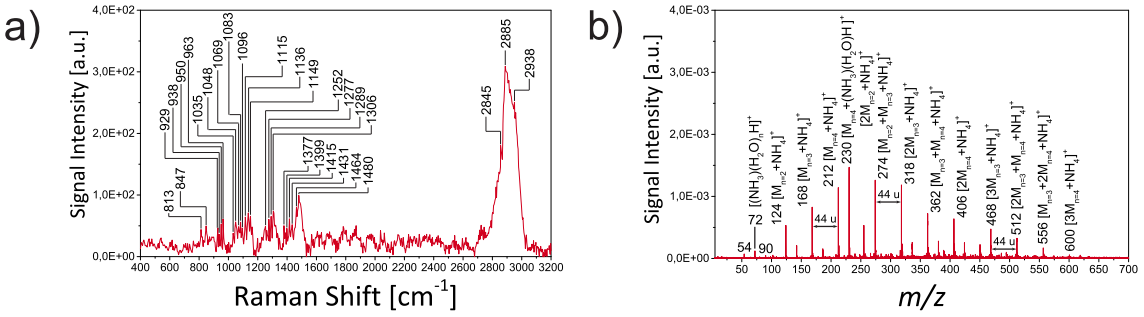

Figure 4.4: Complementary data set of PEG 200: (a) Raman spectrum. (b) Mass spectrum obtained by LA DBD MS.

1250–1450 cm^{-1}, comprises a number of signals that exhibit a mixed character of CH_2 wagging and backbone (C–O and C–C) stretching vibrations. In addition, a third group of Raman bands, present in between approximately 1450–1500 cm^{-1}, can be assigned to the scissoring modes of CH_2. The most prominent spectral feature can be found in the C–H stretching region of the optical spectrum. Regarding the asymmetry of the broad band, the signal is assumed to be a convolution of at least three superimposed vibrational modes with the local maxima at 2845, 2885, and 2938 cm^{-1}. These Raman bands are associated with the symmetric and antisymmetric stretching vibrations of C–H.

Fig. 4.4b shows the complementary mass spectrum of PEG 200. In general, it is comparable to the one shown in the preceding chapter, with the only striking difference being the primary charge carrier. As has been discussed in Chapter 2, the experimental arrangement of the spectrometric compartment results in the predominant formation of even-numbered reagent-ions of the type $[(NH_3)(H_2O)_nH]^+$, whose unused residuals can be observed in the spectrum at *m/z* 54, 72, and 90. Accordingly, all labeled analyte-containing ion peaks are assigned to be ammonium adducts. Given the characteristic mass intervals of 44 Da, representing one ethylene oxide subunit, the following signal progressions of equally spaced ion peaks can be distinguished: $[M_n{+}NH_4]^+$, $[M_n{+}(NH_3)(H_2O)H]^+$, $[2M_n{+}NH_4]^+$, and $[3M_n{+}NH_4]^+$, with n = 2–4, as well as clustered ions of a mixed oligomer composition.

Ibuprofen

Following the sample library in Chapter 3, as the next sample, an unpreprocessed tablet containing the nonsteroidal anti-inflammatory drug ibuprofen was analyzed.

The Raman spectrum shown in Fig. 4.5a depicts the characteristic fingerprint region for ibuprofen ranging from 700–1700 cm^{-1}. It is composed of several intramolecular vibrations distinctive of the atomic bonds, the molecular conformations, and the close molecular neighboring. For an unambiguous spectral identification, first, the optical spectrum of the pharmaceutical formulation was correlated to a prerecorded reference spectrum of pure crystalline ibuprofen (depicted in blue in Fig. 4.5a). Afterwards, the experimental band positions were assigned by direct comparison to earlier Raman studies.[277–279]

A closer inspection reveals the obtained vibrational frequencies to correlate well with the published data by Jubert *et al.*[278] Within the investigated fingerprint region, the assembled DPSS laser-based setup allowed for the spectral assignment of at least 27 Raman bands out of 34 that have been recorded with a commercial Raman spectrometer (Bruker IFS66 adapted with a FRA 106 FT-Raman accessory).[278] Characteristic spectral features for aromatic systems can be found in form of the Raman band at 744 cm^{-1}, associated with the out-of-plane C–C ring deformation of the aromatic ring, and the Raman bands at 853, 1010, 1281, 1453, 1575, and 1608 cm^{-1}, all attributed to the vibrations of aromatic C–C bonds (in-plane C–C ring deformation and C–C ring stretching). Further aromatic C–H bond specific features (in order of ascending vibrational energy) can be identified as follows: The Raman bands at 782, 820, 833, 866, and 882 cm^{-1} correspond to the out-of-plane C–H bending, while the signals at 1114, 1169, 1206, 1305, 1321, and 1462 cm^{-1} originate from in-plane C–H bending. In addition, the following vibrational frequencies are of non-aromatic origin: 941 cm^{-1} (CH_3 rocking), 961 cm^{-1} (CH_2 rocking), 1072 cm^{-1} (CH_2 twisting), 1093, 1181, 1268, and 1339 cm^{-1} (all C–H bending), 1432 cm^{-1} (symmetric CH_3 deformation and C=O–H bending), and 1441 cm^{-1} (CH_2 deformation and antisymmetric CH_3 deformation).

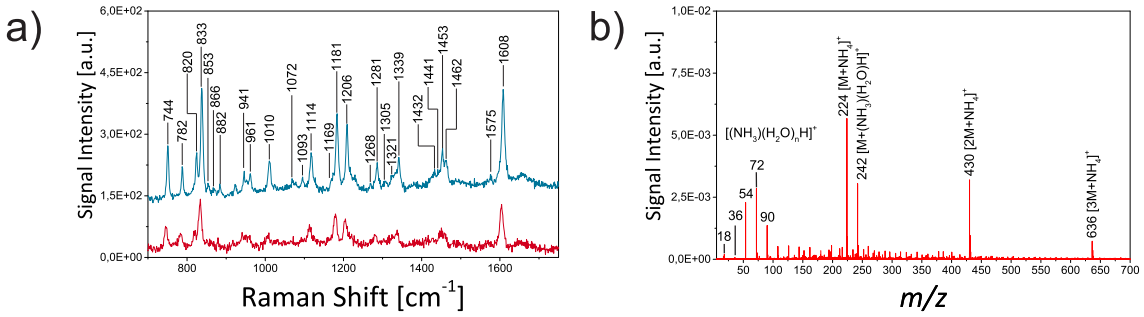

Figure 4.5: (a) Raman spectrum of an unpreprocessed ibuprofen tablet (red) and reference spectrum of pure crystalline ibuprofen (blue). (b) Corresponding mass spectrum of the pharmaceutical formulation obtained by LA DBD MS.

After switching to the spectrometric operation mode, the complementary LA DBD MS spectrum could be recorded and analyzed. An exemplary spectrum of the pharmaceutical formulation is shown in Fig. 4.5b. In addition to the remaining unused reagent-ions of the type $[(NH_3)(H_2O)_nH]^+$ at the usual even-numbered *m/z* positions, the ion peaks that are detected at *m/z* 224, 430, and 636 refer to the appearance of the ammoniated monomer $[M+NH_4]^+$, dimer $[2M+NH_4]^+$, and trimer $[3M+NH_4]^+$ of the active ingredient ibuprofen, respectively. Further, the analyte-containing signal at *m/z* 242 contributes to the spectrum in the form of the $[M+(NH_3)(H_2O)H]^+$ ion. Once more, LA DBD MS exhibits a comparably low degree of fragmentation. Characteristic fragments that are typically observed under high energetic conditions,[280,281] such as the primary fragmentation products $[C_{12}H_{17}]^+$ at *m/z* 161 (representing the loss of the carboxyl group) and $[C_{10}H_{11}O_2]^+$ at *m/z* 163 (indicating the loss of the propyl radical), as well as the secondary tropylium fragment ion $[C_7H_7]^+$ at *m/z* 91 are not prominent in the acquired mass spectra.

Compared to ferrocene and polyethylene glycol, the potential of hyphenating mass spectrometry and Raman spectroscopy becomes even more apparent in the case of ibuprofen. The multitude of vibrational bands that can be assigned corroborates the informational richness of Raman spectra. Even slight changes in the analyte's structure go along with a shift of the corresponding band positions. Consequently, the acquired Raman spectrum can be directly correlated to a molecular geometry.

Paracetamol

To further demonstrate the feasibility of the hyphenated technique in differentiating molecular structures, the pain reliever paracetamol (*N*-acetyl-*para*-aminophenol) and its positional isomer metacetamol (*N*-acetyl-*meta*-aminophenol) were studied. Paracetamol is a long-established over-the-counter pharmaceutical and ranges among the most commonly used analgesics.[282] Though it is regarded as a very safe drug, toxic effects are not only associated with the use of high doses, but can be rather encountered with chronic use at lower doses.[283] Consequently, the leading cause of drug-induced liver injury in the developed world is an overdose with paracetamol.[284] In contrast, the isomeric compound metacetamol is recently being considered as a promising alternative because of its lower toxicity.[285]

Since the above-named positional isomers share the same molecular formula, and thus molecular weight, those compounds are non-distinguishable in a fast screening MS analysis and may also show a similar behavior in fragmentation experiments. To circumvent these problems and achieve a structural discrimination, Raman spectroscopy experiments can be performed to provide compound-specific fingerprint spectra. Accordingly, this experiment serves as another testbed to evaluate the hyphenated Raman / LA DBD MS approach for an unambiguous identification of an active ingredient in the presence of pharmaceutical excipients. The strategy for this proof of principle was as follows: After the acquisition of a Raman and a LA DBD MS fingerprint of a store-bought paracetamol tablet, the complementary data set was used to confirm the identity of acetylaminophenol (spectrometrically), as well as its isomeric "para" form (spectroscopically).

Fig. 4.6b displays the acquired LA DBD MS spectrum of a generic paracetamol tablet. Besides the detection of omnipresent proton-bound ammonia water adducts at *m/z* 36, 54, 72, and 90, the predominant ion peaks at *m/z* 152, 169, and 320 reveal the presence of $[C_8H_{10}NO_2]^+$, $[C_8H_{13}N_2O_2]^+$, and $[C_{16}H_{22}N_3O_4]^+$ or $[M+H]^+$, $[M+NH_4]^+$, and $[2M+NH_4]^+$, with M being the active ingredient acetylaminophenol, respectively. An ad-

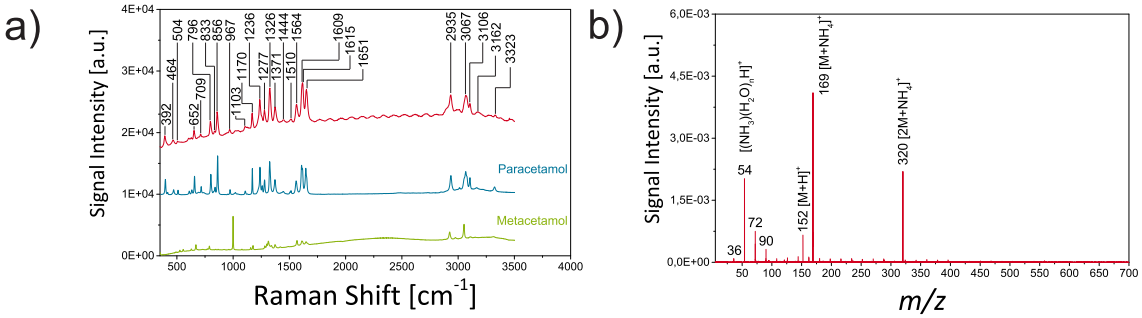

Figure 4.6: (a) Raman spectrum of an unpreprocessed paracetamol tablet (red), and reference spectra of the pure crystalline compounds paracetamol (blue) and metacetamol (green). (b) Mass spectrum of the pharmaceutical formulation using LA DBD MS.

ditional verification of this spectral assignment has been successfully established by using the high resolution acquisition mode of the TOF MS. As expected, identical results were obtained for the isomer metacetamol (spectrum not shown). Likewise, high energetic EI-MS experiments could not yield a difference in the spectra of isomers, as reported in the literature.[286] Thus, a structural discrimination between the two positional isomers based solely on the acquired spectrometric data cannot be achieved.

Irradiation of the neat paracetamol tablet with laser light of a higher repetition rate yielded the vibrational spectrum plotted in red in Fig. 4.6a. To highlight the spectral differences between the discussed positional isomers, in-house measured reference spectra of the pure crystalline compounds paracetamol and metacetamol are also included in the figure in blue and green, respectively. For the latter measurements, corresponding metadata are attached in Fig. A-5 and Fig. A-6. A direct comparison between the vibrational spectrum of the pharmaceutical formulation and the reference spectrum of pure paracetamol reveals the same band positions and relative signal intensities with only minor band shifts (< 5 cm^{-1}). Within the investigated spectral window, paracetamol exhibits at least 26 Raman bands which can be described in terms of 11 bond stretching modes, 9 in-plane and 4 out-of-plane deformation modes, as well as 2 bending modes associated to the CH_3 group of the acetylamino substituent.[287]

In detail, characteristic vibrational frequencies for the aromatic system can be assigned as follows: The signals observed at 652 and 796 cm^{-1} can be related to in-plane C–C ring deformation modes, the Raman band at 709 cm^{-1} to an out-of-plane C–C ring deformation mode, and the spectral contributions at 856, 1326, 1510, 1609, and 1615 cm^{-1} to ring breathing and C–C stretching vibrations. Moreover, the spectral features at 392, 464, 1236, and 1277 cm^{-1} originate from in-plane deformation modes and stretching modes of the C–R bond, with R being the acetylamino or hydroxyl substituent, respectively. Additional C–H bond specific features are observed at 833 and 967 cm^{-1} (out-of-plane C–H bending), 1103 and 1170 cm^{-1} (in-plane C–H bending), as well as 3067 and 3162 cm^{-1} (C–H stretching). Signals of non-aromatic origin contribute to the spectrum in form of the following vibrational frequencies: 504 cm^{-1} (in-plane deformation of C=O), 1371 cm^{-1} (symmetric CH_3 deformation), 1444 cm^{-1} (antisymmetric CH_3 deformation), 1564 cm^{-1} (in-plane N–H bending, amide II), 1651 cm^{-1} (C=O stretching), 2935 cm^{-1} (symmetric CH_3 stretching), 3016 cm^{-1} (overtone of the amide II band), and 3323 cm^{-1} (N–H stretching).

Despite its structural similarity, only a poor correlation between the recorded vibrational spectra of paracetamol and metacetamol can be found, which is in good agreement with earlier observations by McGregor *et al.*[288] and Agnew *et al.*[289] The Raman spectrum of metacetamol shows easily discernible differences with the vibrational band at 998 cm^{-1}, corresponding to vibrational modes of the aromatic ring, being the strongest. Another difference in the fingerprint region of the metacetamol spectrum includes the absence of the paracetamol-specific vibrational frequencies at 392, 464, 504, and 856 cm^{-1}, whereas new vibrational modes become readily apparent at 524, 555, 627, and 1154 cm^{-1}. Hence, these results prove the desired biunique assignment of the analyzed sample to the molecular formula and structure of *N*-acetyl-*para*-aminophenol.

4.3.3 Wavelength Dependence on the Raman intensity

As has been discussed in the introductory chapter, the amount of light which is scattered throughout the Raman process is inversely proportional to the fourth power of the excitation wavelength. Consequently, the use of pulsed ultraviolet lasers for Raman excitation is considered favorable.[70,71] Nonetheless, UV Raman experiments are still scarcely conducted, which is mainly due to two reasons: First, the main spectral competition of Raman scattering is fluorescence and the probability of an electronic excitation, which can consecutively lead to fluorescent relaxation, is also often increased toward shorter wavelengths. The second reason is a mere technical problem. Typically, most Raman experiments are operated using continuous laser illumination. Since UV light is most commonly generated *via* non-linear optical conversion processes like frequency doubling, the optical power is critical. Because the conversion of energy to power is inversely proportional to the temporal duration, continuous laser sources intrinsically have lower power densities and therefore cannot be frequency converted efficiently.

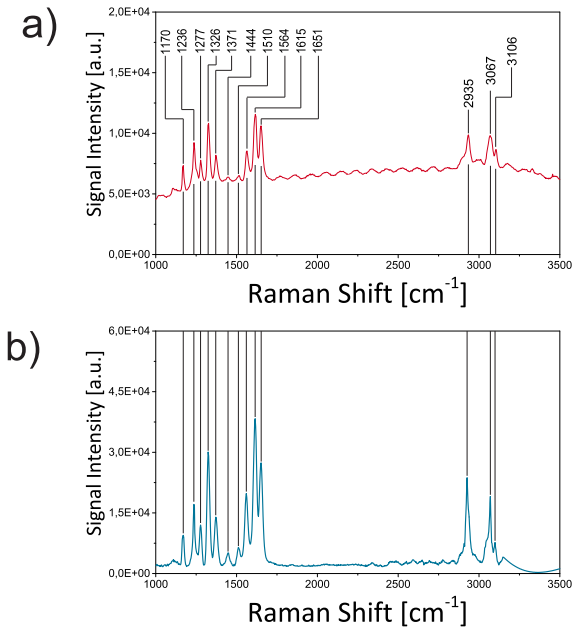

Figure 4.7: (a) Raman spectrum of paracetamol excited with the Blade YVO_4 IR_25 laser operating at 532 nm. (b) UV Raman spectrum excited with the Conqueror 3-LAMBDA operating at 355 nm.

This technical hindrance can be circumvented by using short laser pulses with high repetition rates. This *modus operandi* provides a suitable compromise between high peak powers of the individual pulses and a relatively high optical duty cycle. Accordingly, independent of the presented hyphenation with laser-based ambient mass spectrometry, DPSS lasers further bear the potential to become a powerful new light source for UV Raman setups. To follow this idea, in a short trial, the general applicability of a current state-of-the art DPSS laser (Conqueror 3-LAMBDA) as a coherent light source for Raman scattering of light of $\lambda = 355$ nm was evaluated. 355 nm corresponds to the third harmonic of the Nd:VVO_4 fundamental wavelength of 1064 nm and is generated by mixing one photon of 1064 nm and one photon of 532 nm, respectively. At a pulse length of ≤ 10 ns and a pulse energy of 300 µJ / pulse at 532 nm, the frequency tripling results in a pulse energy of ≈ 100 µJ / pulse at $\lambda = 355$ nm.

In two subsequent experiments, the same sample was irradiated with the second and third harmonic of the laser output. The spectral analysis of the Stokes scattered light resulted in the spectra depicted in Fig. 4.7a and Fig. 4.7b, respectively. As the common assignment of the two individual spectra shows, identical Raman profiles were obtained, independent of the used excitation wavelength. Despite small variations in relative signal intensity, the spectra are qualitatively equivalent to each other. A quantitative comparison, however, reveals an improved absolute signal intensity and a resulting improvement in signal-to-noise ratio in the case of the 355 nm excitation. Taking into account the lower power of the UV laser, this finding is in accordance with the wavelength dependency derived from Eq. 1.6. Though the acquisition and collection of UV Raman spectra was not the scope of this thesis, this small experiment could further demonstrate the potential of DPSS lasers for the generation of high repetition rate pulsed (quasi-continuous) laser light for UV Raman experiments.

4.4 Conclusion

Within this chapter, an instrumental combination of two standalone analytical methods, namely, laser-based ambient mass spectrometry and Raman spectroscopy, into a single instrument was realized. The core of this setup is a shared DPSS laser, serving as a cost-effective component. By adjusting its repetition rate, and thus the pulse energy, either the spectrometric or the spectroscopic experiments were conducted. In addition, the use of a shared excitation light source and optical beam path for both orthogonal techniques always granted a spatial overlap of the interrogated sample volume. The latter is a characteristic feature of true hyphenation and has not been achieved earlier for this specific combination of techniques. By investigating several test compounds, differing in both their chemical structures and properties, the applicability of this approach was evaluated. Complementary data sets which allow for an unambiguous compound identification were obtained in a single run, comprising the molecular weight, and thus molecular formula, as well as analyte-specific structural fingerprints and functional group information. Eventually, the full potential of the proposed setup became apparent upon analyzing the positional isomers paracetamol and metacetamol. The results clearly demonstrated that only the synergetic superposition of comprehensive chemical information allowed for a rapid biunique assignment of the identity and structure of paracetamol.

In addition, to explore the potential of DPSS lasers for UV Raman spectroscopy, the Raman scattering of paracetamol, excited either with the Blade YVO_4 IR_25 operating at 532 nm or its successor laser model Conqueror 3-LAMBDA operating at 355 nm, was examined. Shifting the excitation laser light from the visible region to the UV resulted in a threefold benefit: Besides an improved absolute signal intensity and signal-to-noise ratio, a fluorescence ”suppression” could be achieved using the UV laser since the Raman spectrum lies close to the excitation laser line, while the fluorescence is shifted to longer wavelengths. Thus, the results show a promising future of this novel application of an established technique.

5 Airborne Laser-Spark for Ambient Desorption / Ionization Mass Spectrometry

In this chapter, a novel laser-based ionization scheme for ambient desorption / ionization mass spectrometry is introduced. The concept is based on a robust, easy-to-operate, and sensitive quasi-continuous LIP ignited in front of the atmospheric pressure interface of a TOF mass analyzer. To ensure a sufficient duty cycle of the presented system, a high repetition rate DPSS laser is used as the excitation source. To evaluate the initial performance of the laser-based ionization scheme, a comprehensive feasibility study is presented. A vast ensemble of different gaseous, liquid, and solid phase analytes, including polar and non-polar hydrocarbons, sugars, low-mass active ingredients of pharmaceuticals, as well as biomolecules in food samples directly out of their complex matrices, is shown to entirely yield easily accessible yet meaningful mass spectra. Although LIPs are commonly known to have temperatures above 10 000 K and therefore efficiently atomize any sample material, mass spectra of intact molecular ions are recorded that exhibit a surprisingly low fragment-ion content.

Based on:
Bierstedt, A.; Riedel J. *European Journal of Mass Spectrometry* **2016**, *22*, 105–114. Copyright © [2016] (SAGE Publications). Reprinted by permission of SAGE Publications.
and:
Bierstedt, A.; Kersten, H.; Glaus, R.; Gornushkin, I.; Panne, U.; Riedel J. *Analytical Chemistry* **2017**, *89*, 3437–3444. Copyright © [2017] (ACS Publications). Reprinted by permission of ACS Publications.

5.1 Laser Ionization Mass Spectrometry

Throughout the years, mass spectrometry has become a powerful technique for many analytical and bioanalytical applications.[34] Its ever-growing analytical performance is entangled with the development of novel instruments and ionization sources, constantly addressing the fundamental goals of mass spectrometry: minimizing the demands on sample preparation, while maximizing the ionization efficiency.[263] Among the myriad of ionization schemes for mass spectrometry, the concept of using a laser as an ionization tool perfectly fulfills the above-mentioned purpose, and thus has played an exceptional role in the history of mass spectrometry.

Laser ionization mass spectrometry (LIMS) dates back to the early 1960s and was initiated by the unsatisfactory results obtained from the trace analysis of dielectric samples with the spark-ionization technique.[290] In 1963, only three years after the successful demonstration of the first laser,[2] Honig and Woolston[291,292] were the first to investigate the interaction of a focused laser and a target surface by means of mass spectrometry. In these first experimental studies, a pulsed ruby laser with a single pulse lasting 50 µs was focused on the surface of metals, semiconductors, and insulators, igniting a microplasma in which subsequent vaporization, atomization, excitation, and ionization of the bulk material occurred. Following this approach, atoms at different excitation levels, electrons, ions, and clusters were detected within the plasma plume. Driven by the potential of LIMS, developments in both laser and mass spectrometer technology have seen laser-based mass spectrometry flourish into one of the most widely used analytical techniques available. In subsequent years, the versatile character of the novel ion source provided access to a variety of samples ranging from pure inorganic and organic substances to complex mixtures in different real life applications.[293–298]

In general, any mass analyzer can be used in conjunction with a laser ion source. Accordingly, different designs were developed, including mass separation of the laser-induced

ion beam by magnetic sector analyzers (single or double focusing mass spectrometer) or dynamic systems (quadrupole or TOF mass analyzer).[195] Although the first TOF instruments exhibited a rather poor performance, the time-gated ion formation of LIMS was ideally suited to be used in conjunction with these devices.[295,299] The most striking advantage over the competing magnetic sector instruments was the superior acquisition rate of several full mass spectra per second they delivered. From each individual lasing event, a complete mass spectrum could be recorded and allowed for direct *in situ* multi-elemental analysis.

The first instruments were constructed using the same ion extraction strategy: Samples are typically placed in the same high vacuum chamber housing the mass analyzer. Thus, prior to each measurement, the sample needs to be transferred into the high vacuum, which is not only time-consuming, but also restricts the technique to vacuum-compatible samples. Upon laser irradiation, the produced ions are ejected from the surface and directly accelerated into the drift region of the TOF mass analyzer, resulting in a straightforward and inexpensive design with high ion transmission efficiencies.[300]

Nevertheless, the first experiments already revealed the main limitations of LIMS. To perform quantitative analysis and resolve the elemental composition of the sample, high irradiance is necessary to completely desorb, dissociate, and ionize the sample. Unfortunately, high-irradiance conditions (long pulse duration and large spot diameter) come along with the unavoidable formation of multiple charged ions which may result in severe spectral interferences. Furthermore, large microplasmas are formed, generating nascent ions with a broad temporal spread and a wide kinetic energy distribution in the order of several tens to hundreds of eV.[301] In contrast, normal static mass analyzers only have an acceptance of ions with a velocity spread corresponding to a kinetic energy of 10–20 eV. Therefore, most of the fast ions cannot be confined onto detectable ion trajectories. The resulting peak broadening and limited mass resolution significantly restricted the analytical capabilities of LIMS.

Consecutive research focused on improving the sensitivity and mass resolution, parameters that could be mostly affected by the excitation laser and modifications of the TOF mass analyzer. Important progress included the introduction of Q-switched lasers to allow for reduced pulsed length: Fenner *et al.*[295] reported on the first prototype of a laser microprobe mass spectrometer using a laser pulse with 30 ns pulse duration, focused onto an area of 2×10^{-5} cm^2 by means of a microscope objective. Meanwhile, problems that arose from the broad kinetic energy range of the laser-induced ions were alleviated upon the implementation of electrostatic energy filters (time-of-flight discriminator in reflectron geometry) and other focusing devices.[195] This development reached its preliminary climax with the appearance of the first commercially available instruments: the laser microprobe mass analyzer (LAMMA)[198] and the laser ionization mass analyzer (LIMA).[302] Depending on the chosen experimental conditions, these instruments provided either information on the elemental composition of the sample, or allowed for a detailed speciation of inorganic compounds and a structural characterization of organic compounds through fingerprints of fragment-ions.

While the availability of these instruments led to a rapid expansion of different applications of LIMS, at the same time, it paved a way for a dawning paradigm change in laser-based mass spectrometry. LIMS exploited a non-resonantly driven laser-induced microplasma as the primary ion source. This approach yielded in high sensitivity with almost no selectivity. The complete opposite behavior was achieved in the first resonant ionization schemes. In the late 1970s, resonant laser ionization was invented for high resolution gas spectroscopy experiments coupled to MS detection,[303–305] but was soon after employed on the LAMMA instruments. By admixing light absorbing compounds with the sample, a resonant excitation of the matrix ensured an economic light harvesting to produce molecular ions with minimal fragmentation, termed MALDI.[31,32] The advent of MALDI overcast the microplasma-based approaches by far and has ever since evolved as one of the most successful spectrometric techniques for a wide variety of high molecular weight compounds, including peptides, proteins, oligosaccharides, and synthetic

polymers.[197,306] However, *in vacuo* LIMS experiments were still conducted to analyze inorganic samples.[195] The imbalance in the kinetic energy release was overcome by even better ion optics, such as the quadrupole ion trap / time-of-flight hybrid mass spectrometer[307,308] or the implementation of orthogonal extraction TOF analysis.[309] Nowadays, most inorganic MS is performed by laser ablation inductively coupled plasma mass spectrometry (LA ICP MS), supplanting non-resonant LIMS, which is primarily due to the fact that LA ICP MS allows for quantitative major, minor, and trace element analysis of a wide variety of solid and liquid samples, along with the ability to determine isotope ratios with high accuracy and high precision.[310]

The latest innovation in laser-based mass spectrometry is the ability to record mass spectra of ordinary samples in their native environment outside the mass spectrometer and without additional sample preparation. Several promising variants based on the combination of a laser desorption / ablation unit and a secondary ionization source have been reported by now.[55] Surprisingly, this development also led to a resurgence of laser-induced microplasma approaches. For the latter, relocating the ion generation to atmospheric pressure conditions, followed by a subsequent ion transfer into the vacuum part of the mass analyzer, would have a twofold benefit: (1) a simplified sample introduction and (2) a collisional cooling of the formed nascent ions inside the laser plume by ambient buffer gas, prior to the spectrometric analysis.

By now, only four publications reported on a LIP as an ion source for ambient mass spectrometry.[211,213,311,312] All these techniques are based on the plasma ignition on metal surfaces. In 2012, He *et al.*[311] combined the exhaust of a commercially available DART source and a LIP, obtained by focusing a frequency doubled Nd:YAG laser (10 Hz, pulse energy: 50–200 mJ / pulse, pulse width: 6 ns) onto a metal sample for trace element analysis. However, this method yielded a relatively poor sensitivity, but could be improved later on by magnetic confinement and the use of a femtosecond laser (150 kHz, pulse energy: 150 µJ / pulse, pulse width: 600 fs).[211] The most striking shortcoming of the preceding

experiment, namely, the low duty cycle of the flashlamp-pumped solid-state laser, was overcome by the high repetition rate femtosecond laser and yielded limits of detection in the lower ppm range. Another experiment for the analysis of organic compounds was presented by Alimpiev and co-workers.[213,312] By means of laser ablation or a microflow controller, organic molecules were introduced into a reaction chamber and subsequently ionized by the emitted radiation of a LIP, ignited on a metal target. However, besides the introduction of metallic reactive species that can generate chemical interferences, this approach further introduces undesired erratic pulse-to-pulse fluctuations caused by target surface inhomogeneities.

To avoid any chemical interferences, a simple alternative to achieve the ambient desorption / ionization of target analytes by means of a LIP is presented in this chapter. The design is based on a quasi-continuous airborne plasma, which is ignited in front of the first differential pumping stage of an orthogonal TOF MS. The approach of igniting the plasma in ubiquitous air minimizes interferences and instabilities caused by the plasma generation. Because the duty cycle has been shown to be a critical parameter,[311] a pulsed DPSS laser with a controllable repetition rate up to several hundred kHz is used.

5.2 Experimental

5.2.1 Chemical Reagents

Anthracene (97%), L-phenylalanine ethyl ester hydrochloride (99%), methyl salicylate ($\geq$ 99%), and *n*-(tert-Butoxycarbonyl)-L-cysteine methyl ester (97%) were purchased from Sigma Aldrich (Steinheim, Germany), polyethylene glycol (PEG) 200 ($\geq$ 98%) and *n*-butanol (99.5%) from AppliChem (Darmstadt, Germany), and ferrocene (98%), toluene (99.9%) and *tert*-butylbenzene (99%) from Acros Organics (Geel, Belgium). Anisole ($\geq$ 99%) was obtained from Carl Roth (Karlsruhe, Germany), *o*-xylole ($\geq$ 98%) from Fisher Scientific UK (Loughborough, UK), and anhydrous D(+)-glucose from Merck (Darmstadt, Germany). The analgesics ibuprofen, paracetamol (both Ratiopharm GmbH, Ulm, Ger-

many), and diclofenac (Hexal AG, Holzkirchen, Deutschland) were obtained from a domestic pharmacy. Garlic cloves, lemon grass, and apples were bought in a local supermarket. All chemicals and samples were used without further purification.

5.2.2 Instrumentation

A close-up photograph of the airborne laser-spark in front of the atmospheric pressure interface of a TOF MS and a schematic of the experimental arrangement are given in Fig. 5.1. Briefly, this simple approach consists of two major components: (1) the optical system including the laser and the beampath and (2) the TOF MS.

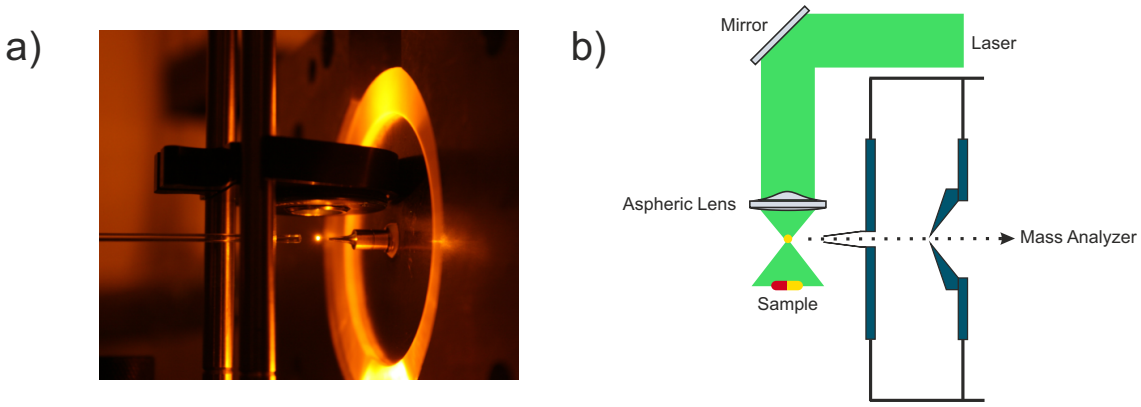

Figure 5.1: (a) Side-view photograph of the airborne laser-spark in front of the atmospheric pressure interface of the mass spectrometer. The photo is taken through a bandline filter for $\lambda = 532$ nm. (b) Schematic diagram of the used setup for ambient desorption / ionization mass spectrometry.

532 nm laser light was provided by a high repetition rate DPSS laser (Conqueror 3-LAMBDA, Nd:YVO_4, 1 Hz–500 kHz, average output power: 12 W at 50 kHz, max. pulse energy: 300 µJ / pulse , pulse width: <10 ns, Compact Laser Solutions GmbH, Berlin, Germany) with internal second harmonic generation. The DPSS laser and the corresponding optomechanical system were installed on an optical breadboard above the drift region of the employed mass spectrometer. To ensure a versatile alignment, three Nd:YAG laser mirrors (NB1-K13, Thorlabs, Dachau, Germany) were passed consecutively by the incident laser light. Eventually, the laser beam was guided through an aspheric lens with a

short focal length of $f = 8$ mm and a high numerical aperture of $N_A = 0.50$ (C240TME-A, Thorlabs, Dachau, Germany) yielding a stable quasi-continuous LIP, ignited in the open laboratory environment. To monitor the power consumption of the LIP, a pyroelectric laser power meter (NOVA II, Ophir Photonics, Darmstadt, Germany) was used.

Following the approach established in Chapter 2, two custom-designed versions of the API-HTOF MS (Tofwerk AG, Thun, Switzerland), namely, the EL-API-HTOF MS and the Q-API-HTOF MS, were used to investigate the positive mode reagent-ion population. A detailed description of both instruments is given in Fig. A-2 and Fig. A-3, respectively. For both arrangements, the airborne laser-spark was ignited on-axis with the MS inlet, at a free space distance of 2.0 mm. Both instruments were operated in single reflectron geometry, using the positive ion mode. Integrated mass spectra were recorded with an acquisition time of 5 s and an extraction rate of 12.5 kHz. Unless explicitly stated, all remaining experiments were conducted using the EL-API-HTOF MS.

5.2.3 Sample Analysis

Qualitative spectrometric analyses of each of the selected test compounds were performed by placing the samples ≈ 2 cm below the focus point of the aspheric lens. Since the incident laser beam propagates downwards in the laboratory frame, the fraction of laser light, which was not consumed in maintaining the plasma, exits the plasma downwards and enables the thermal desorption of molecules directly from the untreated sample surface, followed by the subsequent ionization in the plasma vicinity. While this proof-of-concept study focuses first on this straightforward introduction of thermal desorption, alternative ways for the sample introduction, such as thermal desorption by plasma-induced convection[130] or a gas-carried sample introduction through a capillary from a spatially separated desorption unit (shown in Fig. 5.1a) will be adressed in the following chapter. Solid phase test compounds were deposited on a spatula. For the analysis of liquids, the wooden handles of disposible cotton swabs were coated with neat sample solutions. Pharmaceutical tablets were held by tweezers and used without breaching or opening the tablets in any way.

Fresh garlic and lemon grass slices were cut and immediately analyzed to avoid oxidative degradation of the samples. Apple peel was directly exposed to the laser beam.

5.3 Results and Discussion

5.3.1 Characteristics of the Airborne Laser-Spark Ion Source

Concurrently to the development and application of laser-based techniques for the spectrometric analysis, the formation of a dielectric breakdown caused by optical radiation at ambient conditions was exploited for atomic emission spectroscopy under the name of laser-induced breakdown spectroscopy (LIBS).[313]

In LIBS, a highly energetic pulsed laser is focused onto the target surface to ablate a small portion of material, which subsequently interacts with the tailing laser pulse to form a localized microplasma. Inside the plasma, further vaporization, atomization, ionization, and excitation processes occur, causing the plasma to emit characteristic light of the elemental composition within the plume. The overall ionization efficiency of a LIP scales with the electron number density n_e and the electron temperature T. Characteristic values are $n_e = 10^{16}$–10^{18} cm^{-3} and $T = 6\,000$–$23\,000$ K (after 1–5 µs at atmospheric pressure).[314]

Among the number of electrically driven plasmas, the most comparable equivalent is the inductively coupled plasma (ICP) with $n_e = 10^{14}$–10^{15} cm^{-3} and $T = 5\,000$–$12\,000$ K.[315] For comparison, the plasma probes discussed in Chapter 2 exhibit reference values of $n_e = 10^{11}$–10^{12} cm^{-3} [119,316] and gas temperatures between 30–500 °C (since these plasma are optically dark at the region of interest, no electron temperature can be given).[105,138] Accordingly, it was expected that the laser-spark ion source involves a unique ionization chemistry that is inaccessible to most electrical discharges, making it a promising alternative to the ICP for direct elemental analysis, rather than an ion source for molecular mass spectrometry.

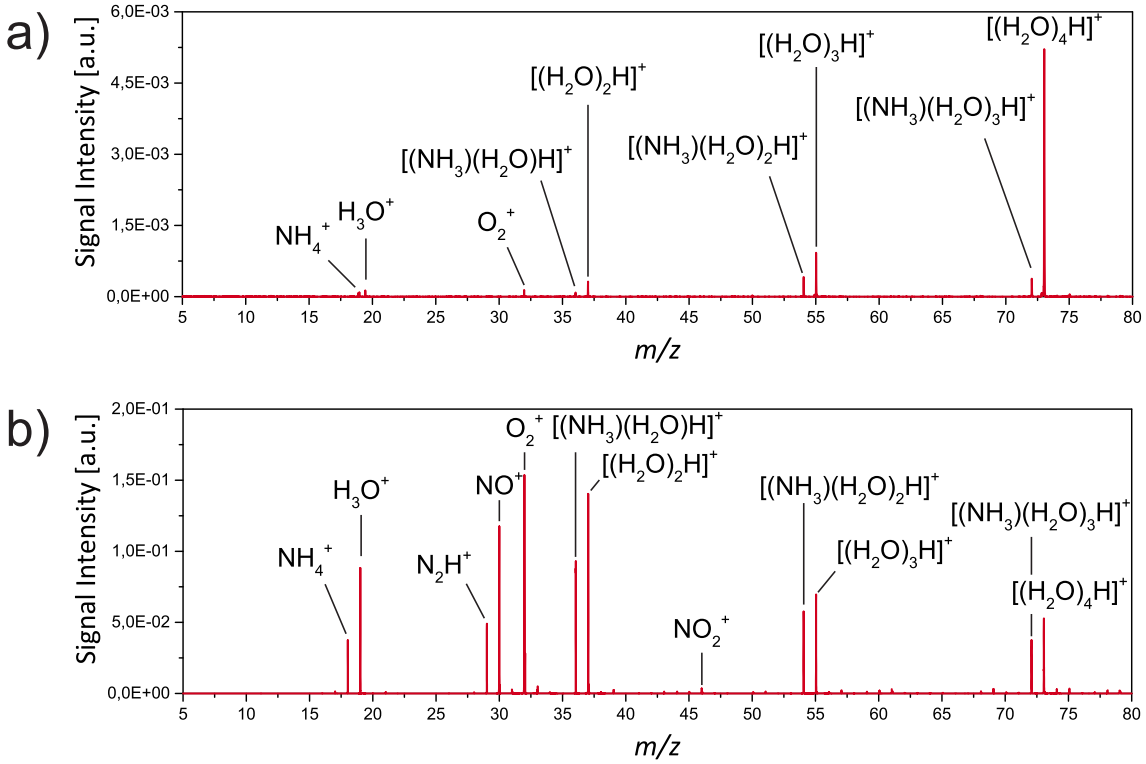

Figure 5.2: (a) Positive mode reagent-ion population produced out of ambient air using the EL-API-HTOF MS. Characteristic reagent-ions include protonated water clusters, $[(H_2O)_nH]^+$, ammoniated water clusters, $[(NH_3)(H_2O)_nH]^+$, and the charge transfer carrier $O_2{}^+$. (b) Positive mode reagent-ion population produced out of ambient air using the Q-API-HTOF MS. Additional ion peaks were identified to be N_2H^+ at m/z 29, NO^+ at m/z 30, and $NO_2{}^+$ at m/z 46.

Fig. 5.2 depicts the positive mode reagent-ion population for the airborne laser-spark ion source coupled either to the EL-API-HTOF MS or the Q-API-HTOF MS. In both cases, the LIP was ignited directly in the open laboratory environment. The steady-state ion signal recorded with the EL-API-HTOF MS, shown in Fig. 5.2a, comprises a dominating series of protonated water clusters $[(H_2O)_nH]^+$ with maximum signal intensities centering around $n = 4$, accompanied by proton-bound ammonia water adducts of the type $[(NH_3)(H_2O)_nH]^+$, as well as the charge transfer promoting ion $O_2{}^+$ in minor abundance. Although not shown here, clustered ions with masses up to $\sim$1 kDa were observed. These higher mass water clusters are not stable under ambient conditions. Instead, they are more likely the result of an effective clustering process of smaller conglomerates dur-

ing the transition from the atmospheric pressure region into the high vacuum of the mass spectrometer. Since the inlet system in this configuration is followed by a cylindrical einzel lens instead of a multipole (for comparison see Fig. A-1 and Fig. A-3), no subsequent collisions occur and the clusters once formed remain intact.

This assumption is further corroborated by the reagent-ion background spectrum acquired with the multipole containing Q-API-HTOF MS. For better comparison, the atmospheric pressure inlet, described in Fig. A-3, was replaced by the conical-shaped inlet used for the EL-API-HTOF MS. As can be seen in Fig. 5.2b, the reagent-ion population remains basically the same, including the presence of $[(H_2O)_nH]^+$, $[(NH_3)(H_2O)_nH]^+$, and different charge transfer carriers. Nonetheless, the two quadrupole ion guides can be seen to significantly affect the mass spectral pattern: (1) The signal intensity is found to be increased by two orders of magnitude, most likely caused by a better overall ion transmission, compared to the cylindrical einzel lens of the EL-API-HTOF MS. (2) Since the high pressure quadrupole serves as an efficient collision-induced dissociation chamber, the progression of $[(H_2O)_nH]^+$ and $[(NH_3)(H_2O)_nH]^+$ clusters is shifted along the x-axis toward lower m/z values. Highest signal intensities are observed for $[(NH_3)(H_2O)H]^+$ at m/z 36 and $[(H_2O)_2H]^+$ at m/z 37. Moreover, a number of additional reactants is detected, namely, N_2H^+, NO^+, and $NO_2{}^+$ at m/z 29, 30, and 46, respectively. The presence of these species in plasma-based ambient mass spectrometry has already been demonstrated in Chapter 2.

Surprisingly, the observed reagent-ion population for the airborne laser-spark ion source was almost identical to the data that have been reported previously for a number of atmospheric pressure discharges, including the DBD (see Chapter 2), the LTP,[88] DART,[143] and the microplasma discharge ionization souce[152], but showed no similarity with a typical spectrum observed in ICP MS, where molecular structures are not represented in the generated ions.

In the next step, the temporal stability and switching capabilities of the ion source were evaluated. Fig. 5.3a depicts the extracted ion chronograms of the protonated water tetramer $[(H_2O)_4H]^+$ at *m/z* 73) and the ammonium adduct $[(NH_3)(H_2O)_3H]^+$ at *m/z* 72, produced by the LIP ion source. The progression nicely resembles the presence of reagent-ions for a distinct period of time when the plasma is ignited. Immediately after the laser is turned on (grey-shaded areas), the plasma is ignited producing nascent reagent-ions, which can be followed by the sharp increasing signal of both ion traces. Likewise, when the laser is turned off and the irradiation stops, the time-resolved ion signals decline instantly. In between two individual lasing events no ions are detected, suggesting that the generation of reactants is solely based on the discharge chemistry in the gas phase. In contrast to many other plasma-driven ionization schemes, no noteworthy decay time after switching events is observed.

To assess the long-term stability of the airborne laser-spark ion source, the reagent-ion formation was monitored over a prolonged operation time. The plasma was centrally positioned in front of the atmospheric pressure inlet and sampled the ambient laboratory air. In total, 400 000 single mass spectra were acquired over a timescale of 100 minutes. Within this timeframe, the laser-spark ion source exhibited an exceptionally stable ion yield for each of the above-mentioned reactant species. As an example, the time-resolved signal intensities of $[(H_2O)_3H]^+$ (*m/z* 55), $[(NH_3)(H_2O)_2H]^+$ (*m/z* 54), and $O_2{}^+$ (*m/z* 32) are plotted in Fig. 5.3b.

Further, the repetition rate of the excitation laser and the power consumption to maintain the active plasma were correlated for maximum intensity of the plasma-derived reactants (Fig. 5.3c). The blue squares depict the dependency between the detected ion trace of the protonated water tetramer $[(H_2O)_4H]^+$ (*m/z* 73) and the applied repetition rate of the DPSS laser. A mass spectral response of the protonated water tetramer was obtained for repetition rates ranging from 25–40 000 Hz. Toward these extremes the plasma formation was found to become unstable and barely visible. At a repetition rate of 26 kHz, the

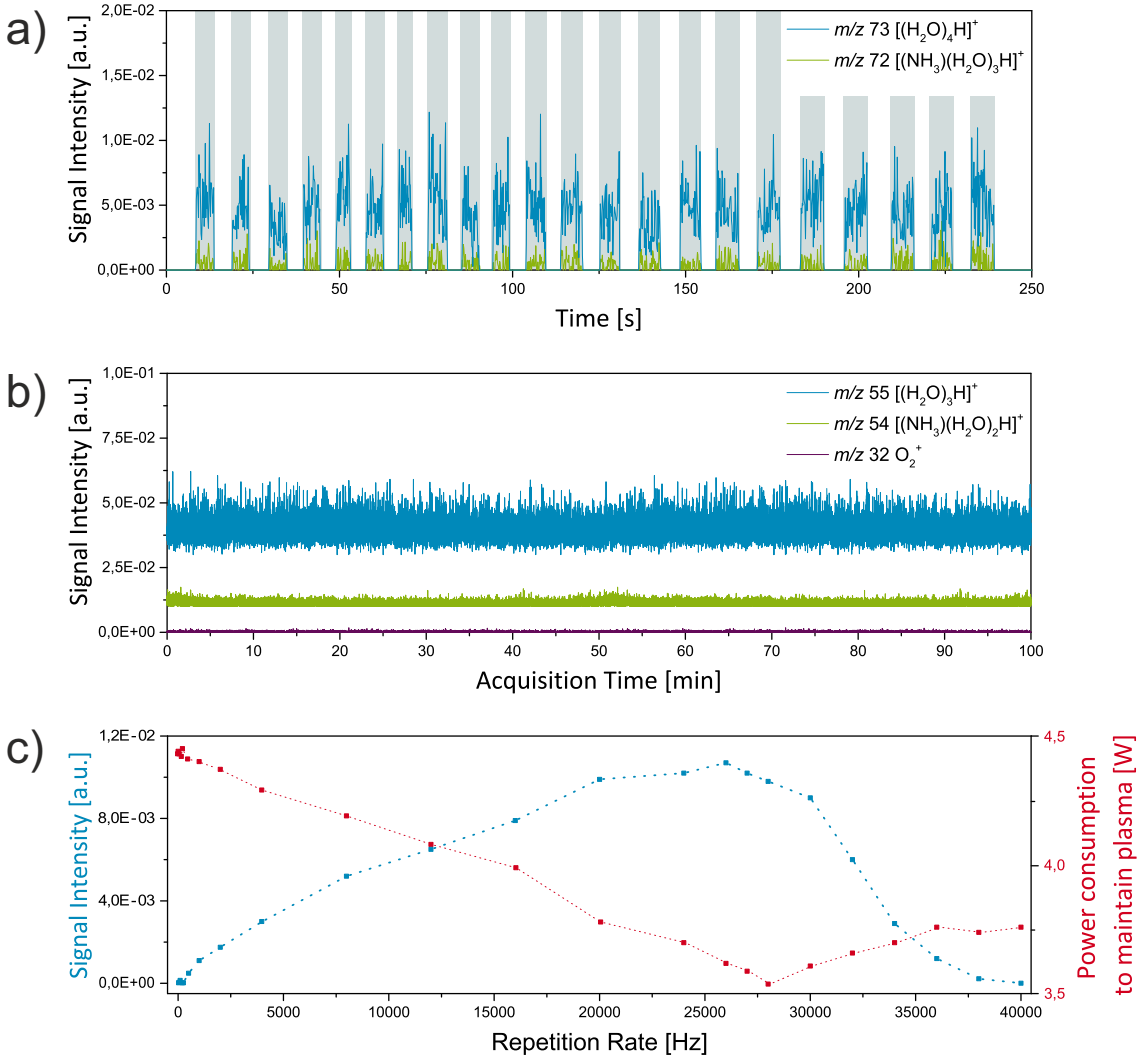

Figure 5.3: (a) Extracted ion chronograms of $[(H_2O)_4H]^+$ (blue) and $[(NH_3)(H_2O)_3H]^+$ (green) demonstrating the time-dependent ion formation of the laser-spark ion source. Grey-shaded areas correspond to the time intervals when the laser was turned on. (b) Reagent-ion signal stability over time. Extracted ion chronograms of $[(H_2O)_3H]^+$ at m/z 55 (blue), $[(NH_3)(H_2O)_2H]^+$ at m/z 54 (green), and $O_2{}^+$ at m/z 32 (purple), recorded over a timescale of 100 minutes, are shown. The plasma was ignited in the open laboratory environment. (c) Mass spectral response of $[(H_2O)_4H]^+$ (m/z 73) dependent on the repetition rate of the excitation laser (blue) and power consumed to maintain the laser-spark (red).

visual plasma appearance was found stable and exhibited the maximum signal intensity of the steady-state MS signal. In consequence, the overall ionization efficiency of analyte molecules should be the highest using these settings.

In an additional comparative study, the optical power coupled into the laser plasma was determined as the difference of the laser power measured (1) directly above and (2) directly below the airborne LIP. The obtained response can either be caused by Rayleigh scattering or light consumed to drive the plasma mainly *via* inverse Bremsstrahlung. Since the observed plasma is extremely hot (typically $T = 6\,000$–$23\,000$ K),[314] the contribution of scattering can be neglected and the measured difference in laser power can be approximated as the optical power consumed to maintain the plasma. The resulting difference between both values is plotted as the red squares in Fig. 5.3c. With an increasing repetition rate less power is coupled into the formed plasma with a minimum value found at 28 kHz. Going to higher values, the power difference increases again. At first, this result seems counterintuitive, but it merely reflects that each new laser pulse finds a volume of air still minimally excited by the previous LIP. Thus, with increasing repetition rate, *i.e.*, decreasing delay between two consecutive plasma events, the power consumed by re-igniting the plasma decreases. At 28 kHz a minimum power consumption of 3.5 W is reached. The increase in power consumption above this repetition rate has technical reasons and reflects a decrease in population inversion inside the laser gain medium due to the technical limitation of the optical pumping of the laser crystal. Thus, for stable conditions with maximum ionization efficiency, a repetition rate of 26 kHz is used.

5.3.2 Airborne Laser-Spark Mass Spectrometry of Test Compounds

A variety of representative samples was chosen to evaluate the overall performance of the laser-spark ion source, including low molecular weight compounds of different physical state, charge state, polarity, and volatility.

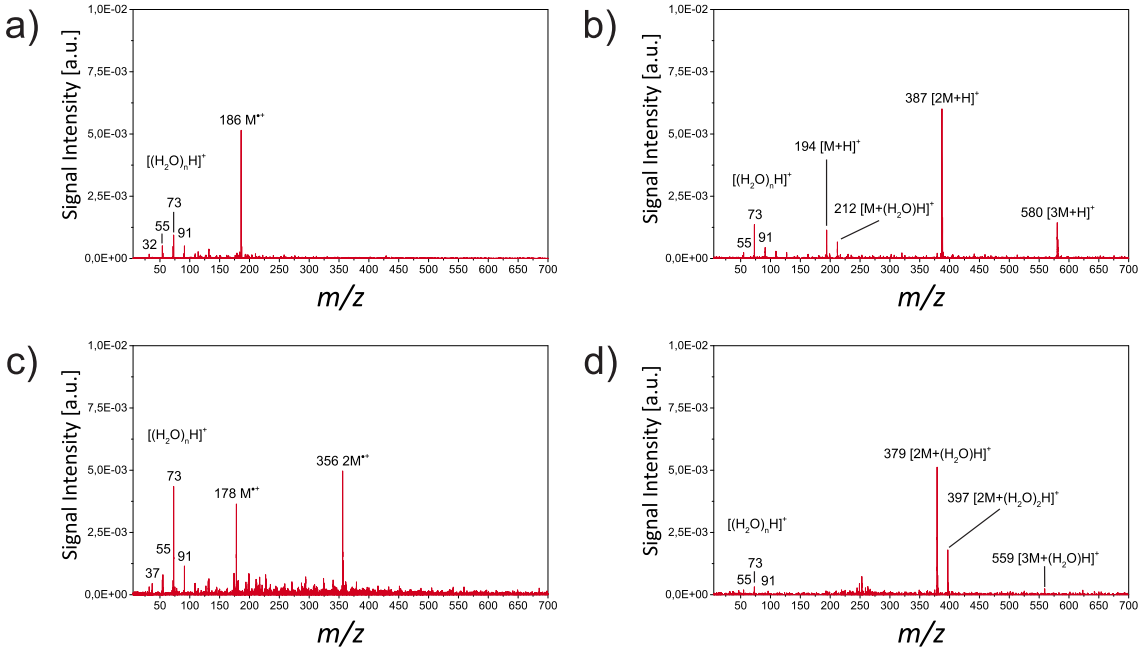

Figure 5.4: Mass spectra of solid test compounds: (a) ferrocene, (b) L-phenylalanine ethyl ester hydrochloride, (c) anthracene, and (d) D(+)-glucose.

Mass spectra of solid test compounds were obtained from ferrocene, L-phenylalanine ethyl ester hydrochloride, anthracene, and D(+)-glucose. The organometallic ferrocene has been chosen intentionally since it has been used in the previous chapters as a plasma thermometer molecule. The corresponding mass spectrum is depicted in Fig. 5.4a. A pronounced formation of the intact ferrocenium cation $M^{\cdot+}$ (m/z 186) is observed. Further signals stem from residual reactant background ions, including $O_2{}^+$ (m/z 32) and proton-bound water clusters $[(H_2O)_nH]^+$ with $n = 2$–5.

As shown in Fig. 5.4b, the singly charged protonated molecular ion $[M+H]^+$ (m/z 194), as well as the proton-bound dimer $[2M+H]^+$ (m/z 387), and trimer $[3M+H]^+$ (m/z 580) are present in the mass spectrum of L-phenylalanine ethyl ester hydrochloride. Further signals are identified as the adduct of the singly charged monomer and ubiquitous water $[M+(H_2O)H]^+$ at m/z 212. No primary fragmentation products of the intact ester are observed.

The novel ion source has been also applied for the analysis of anthracene (Fig. 5.4c). As expected for non-polar molecules, odd-electron molecular ions are observed as the most abundant species dominating the mass spectral pattern. The anthracene monomer $M^{\cdot+}$ is detected at *m/z* 178 and the dimer $2M^{\cdot+}$ at *m/z* 356. Additional signals stem from residual protonated water clusters $[(H_2O)_nH]^+$ with n = 2–5.

The capabiliy to detect sugars as demanding analytes in spectrometric experiments has been demonstrated using anhydrous D(+)-glucose (Fig. 5.4d). Upon sample introduction, the presence of omnipresent water clusters is drastically quenched. Instead, a new series of signals becomes apparent which are attributed to D(+)-glucose. The signal at *m/z* 379 is identified as $[2M+(H_2O)H]^+$, accompanied by $[2M+(H_2O)_2H]^+$ at *m/z* 397 and $[3M+(H_2O)H]^+$ at *m/z* 559.

Remarkably, the airborne laser-spark ion source behaved different than expected. Although LIPs are commonly associated with the presence of rather harsh operating conditions, for all solid test compounds studied, the recorded spectra resembled ambient mass spectra, as acquired by means of DBD ionization. In none of the cases, high-abundant atomic ions or fragmentation products were observed.

The proposed ionization scheme was also capable of performing the mass analysis of samples in its liquid state. As examples, methyl salicylate, *n*-butanol, the polymer polyethylene glycol (PEG) 200, and the N-(*tert*-butoxycarbonyl)-L-cysteine methyl ester were tested. In the case of methyl salicylate (Fig. 5.5a) the ion peaks of the proton-bound molecular ion $[M+H]^+$ (*m/z* 153) and the dimer $[2M+H]^+$ (*m/z* 305) dominate the mass spectral pattern. In addition, minor abundant signals that stem from protonated water clusters $[(H_2O)_nH]^+$ are detected below *m/z* 100.

As shown in Fig. 5.5b, the signals observed in the mass spectrum of *n*-butanol indicate the presence of an additional reaction channel for molecular ion formation. Two

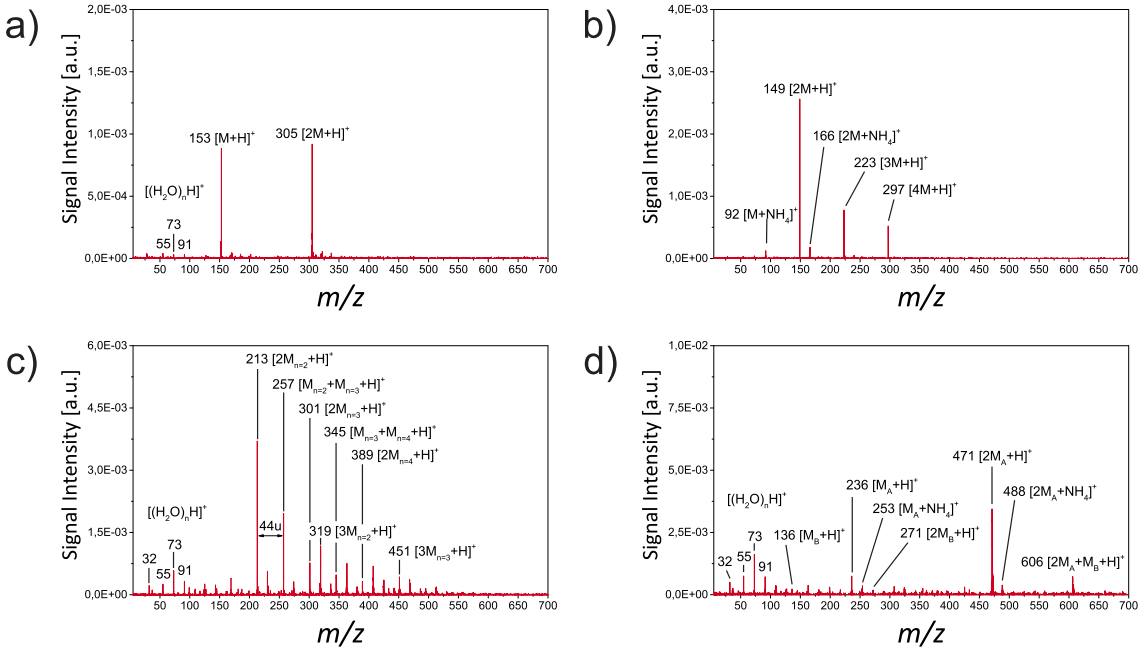

Figure 5.5: Mass spectra of liquid test compounds: (a) methyl salicylate, (b) *n*-butanol, (c) polyethylene glycol (PEG) 200, and (d) N-(*tert*-butoxycarbonyl)-L-cysteine methyl ester.

different analyte-containing signal series are detected, yielding either protonated or ammoniated molecules. As for the major part of the investigated test compounds, the formation of protonated species seems to be the preferred reaction channel, compared to the stabilization of ammonia adducts. Ion peaks indicating a single ion formation $[M+H]^+$ (m/z 75) and $[M+NH_4]^+$ (m/z 92), dimerization $[2M+H]^+$ (m/z 149) and $[2M+NH_4]^+$ (m/z 166), trimerization $[3M+H]^+$ (m/z 223) and $[3M+NH_4]^+$ (m/z 240), and formation of the tetramer $[4M+H]^+$ (m/z 297) and $[4M+NH_4]^+$ (m/z 314) are found in the recorded mass spectrum.

Ambient desorption / ionization of the polymer PEG 200 yielded the mass spectrum given in Fig. 5.5c. The recorded spectrum is mainly composed of different signal propagations, which can be identified due to the characteristic mass difference of 44 Da, representing one subunit of ethylene oxide. The labeled ion peaks are assigned to $[2M_{n=2}+H]^+$ at m/z 213, $[M_{n=2}+M_{n=3}+H]^+$ at m/z 257, $[2M_{n=3}+H]^+$ at m/z 301, $[M_{n=3}+M_{n=4}+H]^+$

at *m/z* 345, $[2M_{n=4}+H]^+$ at *m/z* 389, $[3M_{n=2}+H]^+$ at *m/z* 319, and $[3M_{n=3}+H]^+$ at *m/z* 451. Furthermore, the spectrum reveals the presence of an additional ammoniated signal series of PEG, starting with $[2M_{n=2}+NH_4]^+$ at *m/z* 230.

Fig. 5.5d depicts the obtained mass spectrum of the N-(*tert*-butoxycarbonyl)-L-cysteine methyl ester. The intact molecule is detected in form of the singly charged protonated monomer $[M_A+H]^+$ (*m/z* 236) and dimer $[2M_A+H]^+$ (*m/z* 471), as well as the corresponding ammoniated species $[M_A+NH_4]^+$ (*m/z* 253) and $[2M_A+NH_4]^+$ (*m/z* 488). Closer inspection of the residual ion peaks in lower abundance reveals the presence of the unprotected L-cysteine methyl ester $[M_B]$. These ions could be the first observed products of an occuring fragmentation process. However, when considering the fragment-free spectra observed for all the other studied molecules, they most likely originate from impurities of the initial protected amino acid. The protonated L-cysteine methyl ester is detected as the singly charged protonated monomer $[M_B+H]^+$ (*m/z* 136) and the dimer $[2M_B+H]^+$ (*m/z* 271). Further, the ion peak at *m/z* 606 can be assigned to be an adduct, formed from two BOC protected amines and one molecule of the unprotected ester $[2M_A+M_B+H]^+$.

In addition, the laser-spark ion source was also tested for the analysis of non-polar compounds, namely, toluene, *o*-xylene, anisole, and *tert*-butylbenzene (Fig. 5.6). As expected, all of these compounds revealed the same ionization behavior and preferred the formation of odd-electron molecular ions. The recorded mass spectrum of toluene exhibits the formation of the radical cation $M^{\cdot+}$ at *m/z* 92 and $2M^{\cdot+}$ at *m/z* 184, in the presence of protonated water clusters $[(H_2O)_nH]^+$. Likewise, the mass spectra obtained from *o*-xylene, anisole, and *tert*-butylbenzene show a similar ionization behavior. The molecular ion $M^{\cdot+}$ and dimer $2M^{\cdot+}$ of *o*-xylene are detected at *m/z* 106 and *m/z* 212. Anisole shows a pronounced ion formation at *m/z* 108 and *m/z* 216, whereas the analysis of *tert*-butylbenzene yields a mass spectrum comprising the molecular ion $M^{\cdot+}$ at *m/z* 134 and the dimer $2M^{\cdot+}$ at *m/z* 268.

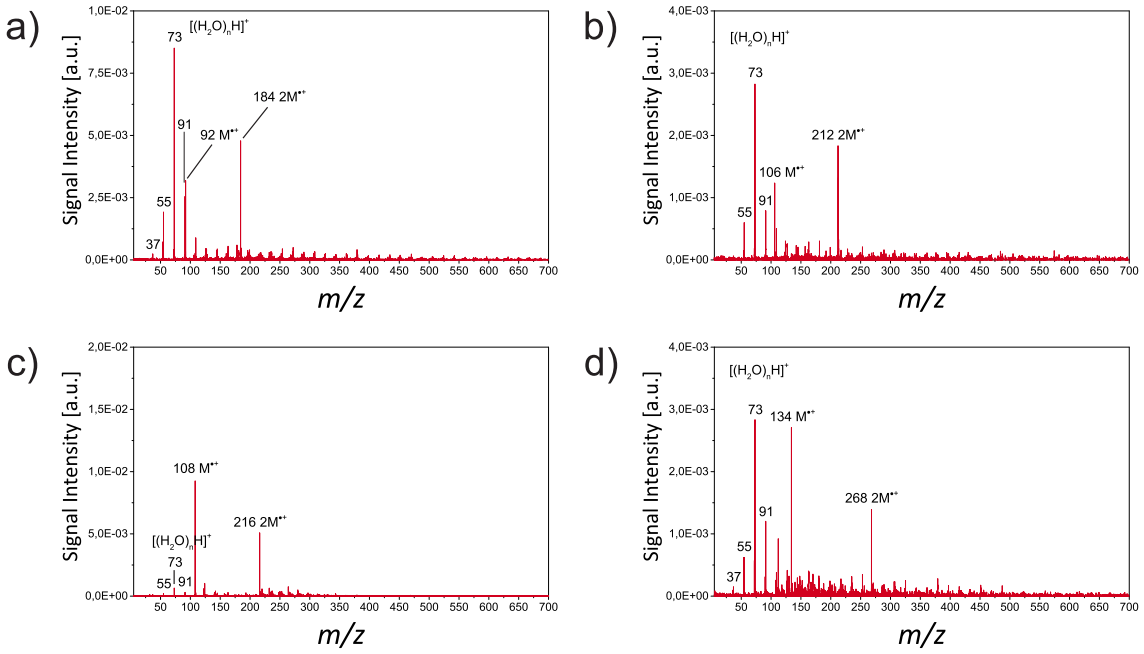

Figure 5.6: Mass spectra of nonpolar compounds: (a) toluene, (b) *o*-xylene, (c) anisole, and (d) *tert*-butylbenzene.

5.3.3 Airborne Laser-Spark Mass Spectrometry of Real Life Samples

To endorse the novel ionization technique for the purpose of true ambient analysis under more realistic conditions, a number of real life samples was examined, including over-the-counter pharmaceuticals, as well as foods and spices.

Fig. 5.7 depicts three selected mass spectra of typical anti-inflammatory drugs, including ibuprofen, paracetamol, and diclofenac sodium. For each analysis, the intact tablets were held below the LIP. By residual laser light, the sample vaporization was initiated, followed by subsequent interactions between the reagent-ions in the vicinity of the plasma and the neutral analyte molecules, being present in the gas phase. The mass spectrum of ibuprofen is depicted in Fig. 5.7a. As reported for the DBD ion source (see Chapter 3 and 4), a pronounced formation of ammonium adducts $[n\mathrm{M}{+}\mathrm{NH_4}]^+$ is observed for each of the chosen test pharmaceuticals. The ammoniated monomer and dimer of ibuprofen are $[\mathrm{M}{+}\mathrm{NH_4}]^+$ (m/z 224) and $[2\mathrm{M}{+}\mathrm{NH_4}]^+$ (m/z 430), respectively. Likewise, the inves-

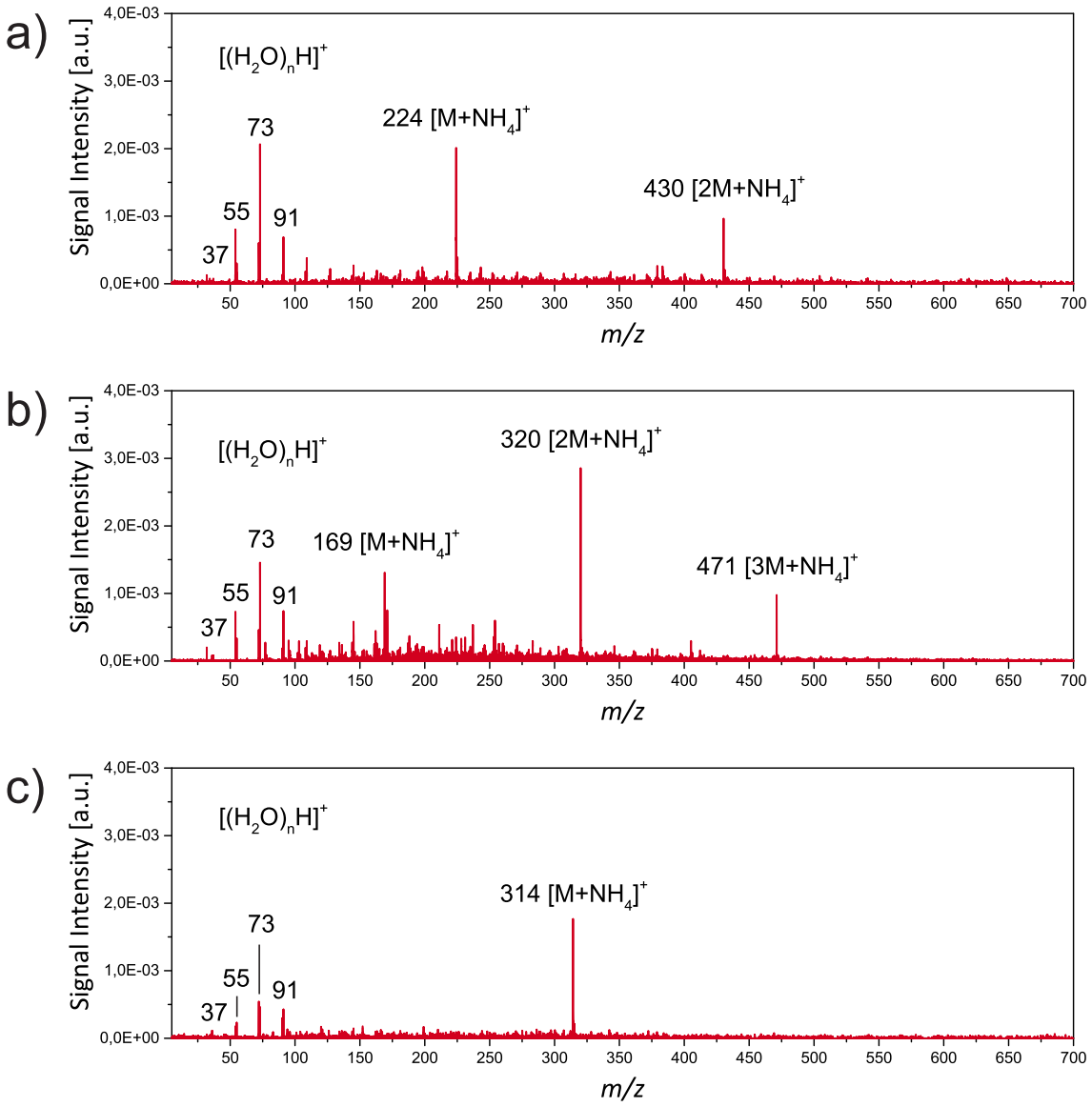

Figure 5.7: Recorded mass spectra of different over-the-counter pharmaceuticals: (a) ibuprofen, (b) paracetamol, and (c) diclofenac sodium.

tigation of paracetamol shows a similar mass spectral pattern (Fig. 5.7b), including the monomer $[M+NH_4]^+$ (*m/z* 169), dimer $[2M+NH_4]^+$ (*m/z* 320), and trimer $[3M+NH_4]^+$ (*m/z* 471). In case of the diclofenac sodium salt (Fig. 5.7c), only a single characteristic ion peak is observed, which is identified as the ammoniated monomer of the active ingredient diclofenac $[M+NH_4]^+$ (*m/z* 314).

Mass spectra obtained from lemon grass, fresh garlic slices, and apple skin are shown in Fig. 5.8. Introducing lemon grass in the sampling region yields a characteristic signal response of citral, typically found in the plant oil in ppm range (Fig. 5.8a). Citral itself is a mixture of terpenoids with the molecular formula $C_{10}H_{16}O$, including the isomers geranial and nerial and exhibits a strong lemon odor. The most abundant ion peak is assigned to be the protonated dimer $[2M+H]^+$ (*m/z* 305). Further signals in minor abundance stem from the protonated monomer $[M+H]^+$ (*m/z* 153), the hydrated monomer $[M+(H_2O)H]^+$ at *m/z* 171, and the ammoniated dimer $[2M+NH_4]^+$ (*m/z* 322).

As expected, the direct analysis of a freshly peeled garlic clove (Fig. 5.8b) immediately reveals the presence of allicin, the predominant organosulfur compound in garlic (3.2–4.8 $mg\,g^{-1}$, < 30 µmol).[317] After tissue damage occurs, the enzyme alliinase converts the alliin to allicin.[318] The predominant ions are the dimeric species of allicin $[2M+H]^+$ (*m/z* 325) and $[2M+NH_4]^+$ (*m/z* 342). Minor abundant ion peaks include the protonated monomer $[M+H]^+$ (*m/z* 163), the stabilized ammonia adduct $[M+NH_4]^+$ (*m/z* 180), and the ammoniated trimer $[3M+NH_4]^+$ (*m/z* 504). In contrast to other ambient ionization schemes, such as the PADI source, additional fragmentation processes of the target molecule allicin are not observed.[106]

As a third example, the skin of an apple was directly exposed to the laser light and the ionization was investigated by MS analysis (Fig. 5.8c). In this case, only one signal of interest can be observed at *m/z* 203, which is assigned to the sodium adduct of glucose / fructose $[M+Na]^+$.

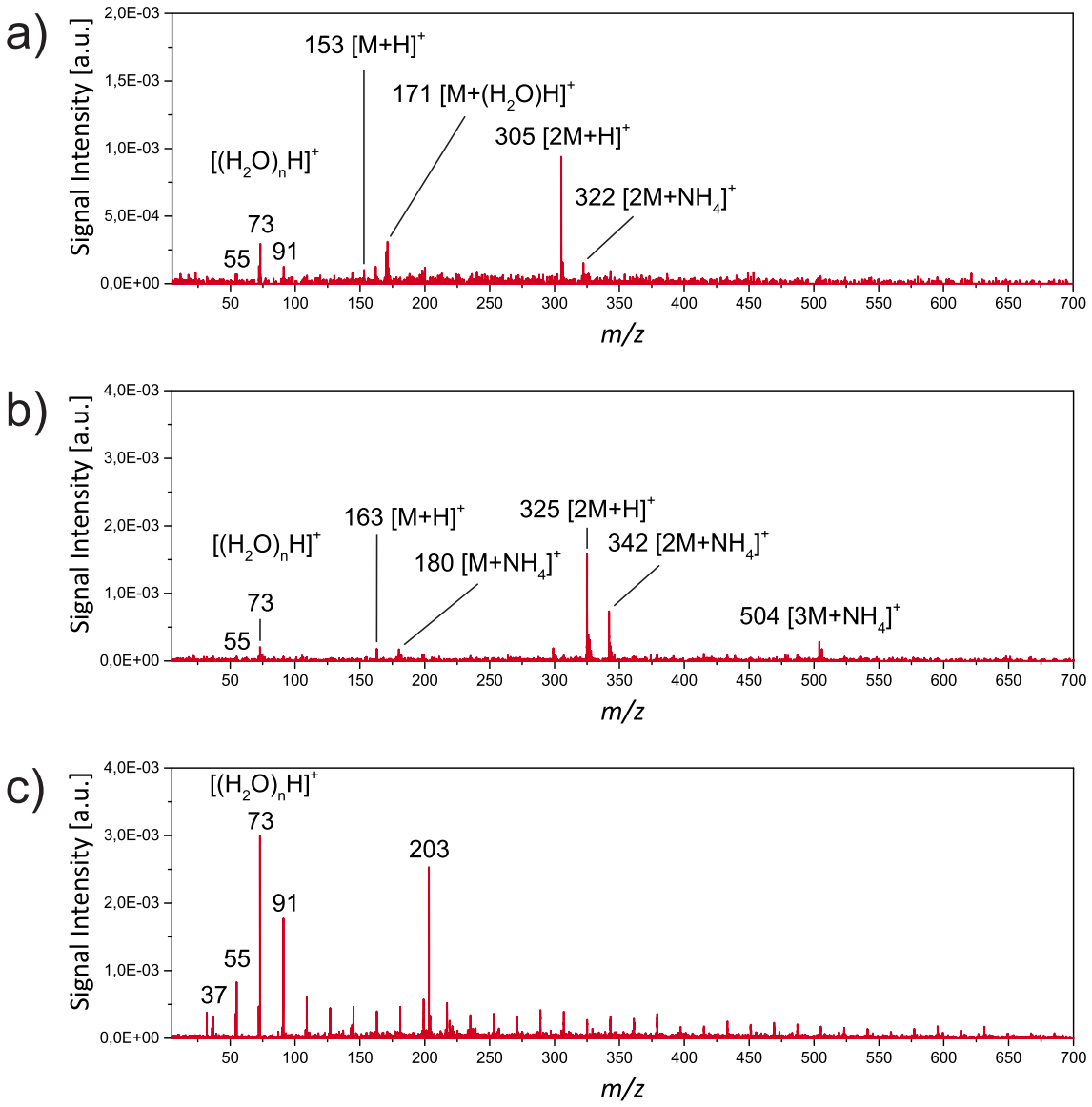

Figure 5.8: MS analysis of foods and spices: (a) mass spectrum of lemon grass, (b) mass spectrum of a fresh garlic clove, and (c) mass spectrum obtained from apple skin.

5.3.4 Possible Analyte Ionization Pathways

In the course of this feasibility study, the positive mode reagent-ion population, and a variety of test analytes representing different compound classes were studied. While the obtained results clearly demonstrate the new technique's high sensitivity for all test compounds, the exact ionization pathway becomes increasingly unclear. The low selectivity of the laser-spark technique suggests the assumption that instead of one single prevailing mechanism, a superposition of several potentially parallel ionization pathways occurs, as has been discussed for most plasma-based ambient ionization techniques.[115,119,138,142] Though each of these plasma sources operates with a different type of discharge, they all end up in generating intact molecular ions. As has been argued in the literature,[319] these findings can be attributed to the high gas density and high collision rates at atmospheric pressure, giving rise to interactions of the initial charge carriers with the gaseous constituents of the surroundings, such as O_2, N_2, H_2O, or a dopant vapor. As a result, this process not only induces a loss of excess energy *via* collisional deactivation, but also forms a subsequent generation of reactants that can be detected *via* nascent species mass spectrometry. Upon the presence of neutral analyte molecules, the observation of the following species is feasible due to the interactions with the above-mentioned reactive intermediates: $[n\mathrm{M}{+}\mathrm{H}]^+$, $[n\mathrm{M}{+}(\mathrm{H_2O})_m\mathrm{H}]^+$, $[n\mathrm{M}{+}\mathrm{NH_4}]^+$, $[n\mathrm{M}{+}(\mathrm{NH_3})(\mathrm{H_2O})_m\mathrm{H}]^+$, and $n\mathrm{M}^{\cdot+}$.

In the case of the laser-spark ionization scheme, the presented mass spectral data strongly corroborate the above-made assumption that the ionization of target molecules does not occur by a single and clearly defined mechanism. Based on the detected background and analyte ions, the following reaction pathways for the formation of positively charged analyte molecules are conceivable:

(1) Considering the cluster size distribution of $[(\mathrm{H_2O})_n\mathrm{H}]^+$ shown in Fig. 5.2a, three different reaction pathways can be derived to yield bare protonated molecules of the type $[n\mathrm{M}{+}\mathrm{H}]^+$. First, a direct proton transfer ionization is feasible, involving protonated water clusters with a high gas phase acidity, namely, $[(\mathrm{H_2O})_{n=1-3}\mathrm{H}]^+$.[23,147] Second, the

formation of $[n\mathrm{M}+\mathrm{H}]^+$ can also proceed *via* a microenvironment interaction. Here, the analyte enters a large proton-bound solvent cluster $[(\mathrm{H_2O})_{n>3}\mathrm{H}]^+$ either by a so-called ligand switching or ligand association reaction,[153,156–159] followed by an electrical field-driven collisional decomposition of the ion-bound solvent cluster further downstream in the intermediate pressure regions of the mass spectrometer.[148] A potential indicator for the presence of this intracluster protonation of analytes in parallel to cluster decomposition processes is the detection of partially hydrated $[n\mathrm{M}+(\mathrm{H_2O})_m\mathrm{H}]^+$ ions, as can be seen in Fig. 5.4. Third, a dopant-assisted proton transfer reaction has been discussed throughout the literature.[320]

(2) As has been discussed in Chapter 2, the presence of ammonia is not expected to originate from an impurity of the plasma / carrier gas or the laboratory environment. More likely, an active ammonia formation out of ambient $\mathrm{N_2}$ and $\mathrm{H_2O}$ is believed to cause the presence of ammonium hydrate clusters $[(\mathrm{NH_3})(\mathrm{H_2O})_n\mathrm{H}]^+$, serving as additional ionization agents. These species are capable of either ionizing a much narrower set of analytes *via* direct proton transfer ionization or, most likely, undergo a direct three-body ion-molecule association reaction / ligand switching process to form ion association products of the type $[n\mathrm{M}+\mathrm{NH_4}]^+$ and $[n\mathrm{M}+(\mathrm{NH_3})(\mathrm{H_2O})_m\mathrm{H}]^+$, similar to $[(\mathrm{H_2O})_n\mathrm{H}]^+$.[153,174,185] This postulation, again, brings to attention the seeming contradiction of a hot plasma and the observation of intact molecules. On one hand, the organometallic compound ferrocene does not release its central iron atom, while on the other hand the formation of ammonia out of ambient nitrogen requires the cleavage of the nitrogen triple bond.

(3) Besides these forms of ionization, alternative reaction channels are known to exist resulting in the formation of odd electron molecular ions $n\mathrm{M}^{\cdot+}$ from nonpolar molecules. Possible reaction channels that should be taken into consideration are a charge transfer ionization *via* $\mathrm{O_2}^+$, NO^+, or $\mathrm{NO_2}^+$, an electron impact ionization, a photo ionization mechanism caused by the self-emission of the plasma kernel, thermal ionization *via* adiabatic compression in a shock wave, as well as Penning ionization.

Though it is possible that these parallel ionization mechanisms are taking place simultaneously, the primary formation of the above-mentioned reactive intermediates remains unclear. The chemistry that occurs in the close vicinity of the plasma is completely decoupled from the chemistry in the transfer region of the mass spectrometer. An interpretation based solely on the terminal ion signal distribution is extremely difficult. Thus, without the investigation of the plasma characteristics by means of complementary plasma diagnostic tools, valid conclusions cannot be drawn.

5.4 Conclusion

The first use of a quasi-continuous airborne laser-spark ion source for ambient desorption / ionization mass spectrometry was demonstrated. It allows for the rapid, non-contact analysis of a variety of test compounds at ambient pressure. Its fundamental physical properties, such as the excellent spatial and temporal definition, the high electron and ion densities, the low selectivity, the low power consumption, the absence of additional solvents or a sheath gas, and the high effective cross section in maintaining the plasma, make it a promising candidate for non-targeted, high-throughput screening approaches. Moreover, due to the absence of solid or liquid electrodes, the ion source does not suffer from chemical interferences or fatigue originating from erosive burning or from electrode consumption. Over a prolonged timescale, the instrument exhibited no ionization performance loss and, thus, guarantees a maintenance-free source operation. The overall plasma maintains electro-neutrality, minimizing charge effects and accompanying long term drift of the charged particle trajectories. In the airborne plasma approach the ambient air not only serves as the plasma medium, but at the same time also slows down the laser-induced nascent ions *via* collisional cooling.

The obtained mass spectral data strongly suggest that the ionization of analyte molecules does not occur in the plasma itself, but is induced by an interaction with nascent ionic fragments, electrons, and / or far ultraviolet photons in the plasma vicinity. Experimentally,

this indirect ionization scheme was shown to be widely unspecific to the chemical nature of the analyte and hardly resulted in primary fragmentation of the studied molecules. Furthermore, the laser-spark not only tolerated the presence of high analyte concentrations, but was also found to be capable of measuring compounds in the lower ppm range. Overall, the ion source was applied for the analysis of several gaseous, liquid, and solid state test compounds, including polar and nonpolar hydrocarbons, organometallics, saccharides, low mass active ingredients of pharmaceuticals, as well as biomolecules in foodstuffs.

The comparability between the laser-spark mass spectra and those obtained by other ambient techniques strongly suggests the presence of ionization mechanisms similar to DBD or DART, most likely involving protonated water clusters and nitrogen ions as highly active ionization agents. With these ambient techniques, the laser-spark ionization also shares its upper mass limitation of detectable molecules. A rough estimate of the highest detectable mass can currently be given as $\sim$1 kDa. However, the found similarity to DART or DBD formed ion patterns does not fully explain the existing ionization pathways. Another open question lies in the absence of atomic ions or fragmentation products in the observed mass spectra. These open questions will be adressed in the following chapter.

6 Characterization of the Airborne Laser-Spark Ion Source

In the previous chapter, a quasi-continuous LIP was shown to be a promising candidate for the non-targeted analysis of different analytes via ambient desorption / ionization mass spectrometry. Throughout, intact molecular ions were readily detected. In contrast, the self-emission of the plasma, investigated within this chapter, depicts a pronounced degree of dissociation into atomic and ionic species. To understand this contradictory behavior, deeper insights into the ionization processes are needed. This chapter focuses on the detection of volatile organic compounds. The gaseous sample introduction eliminates the influence of desorption / evaporation processes, thus enabling a more direct evaluation of the underlying gas phase, fluid-dynamic, and chemical processes in and around the LIP. In the first part of this chapter, time-integrated and time-resolved optical emission spectroscopy, shadowgraph imaging, and mass spectrometry diagnostics result in a unified dynamic understanding. The results reveal the ion formation to be strongly dependent on the electronic temperature and number density inside the plasma origin. In the second part, different volatiles are studied to evaluate analytical figures of merit. Eventually, for a classification among existing ionization schemes, the results are directly compared to an APCI setup.

Based on:
Bierstedt, A.; Kersten, H.; Glaus, R.; Gornushkin, I.; Panne, U.; Riedel J. *Analytical Chemistry* **2017**, *89*, 3437–3444.

6.1 Experimental

6.1.1 Chemical Reagents

n-Butanol (99.5%) and methanol (> 99.9%) were purchased from AppliChem (Darmstadt, Germany), methyl salicylate from Sigma Aldrich (Steinheim, Germany), rhodamine B from Lambda Physik AG (Goettingen, Germany), and toluene (99.9%) from Acros Organics (Geel, Belgium). Fresh spearmint (*Mentha spicata*) and basil leafs (*Ocimum basilicum*) were bought in a local supermarket. Argon (≥ 99.999%, Linde, Berlin, Germany), helium (99.999%, Linde, Berlin, Germany), N_2 (99.999%, Air Liquide, Berlin, Germany), and compressed air (technical grade, ISO 8573-1:2010 grade 4) were used throughout the experiments as carrier or plasma gases. All chemicals were used without further purification.

6.1.2 Airborne Laser-Spark Mass Spectrometry

A schematic representation of the system used to investigate the ionization of volatiles is given in Fig. 6.1. Briefly, it comprises the laser-spark ion source, a TOF MS, and a gas phase sampling unit. The basic principle of the laser-spark ion source has been described in the preceding chapter, so merely a brief description is given here. The second harmonic output of a DPSS laser (Conqueror 3-LAMBDA, Nd:YVO_4, 532 nm, 1 Hz–500 kHz, average output power: 12 W at 50 kHz, max. pulse energy: 300 µJ / pulse, pulse width: < 10 ns, Compact Laser Solutions GmbH, Berlin, Germany) was focused through an aspheric lens (C240TME-A, $f = 8$ mm, $N_A = 0.50$, Thorlabs, Dachau, Germany) centrally in front of the atmospheric pressure interface of the EL-API-HTOF MS (TOFWERK AG, Thun, Switzerland), at a distance of 2 mm from the conical inlet. The TOF MS was operated in single reflectron geometry and positive ion mode. Unless stated otherwise, mass spectra were integrated over an acquisition time of 15 s with an extraction rate of 12.5 kHz. For further instrumental details see Fig. A-2. The excitation laser was operated at 26 kHz. To perform spatially resolved ionization yield measurements, the aspheric lens was mounted onto a translation stage (MT1, Thorlabs, Dachau, Germany) to introduce a vertical displacement along z (refer to Fig. 6.1) between the plasma and the inlet orifice.

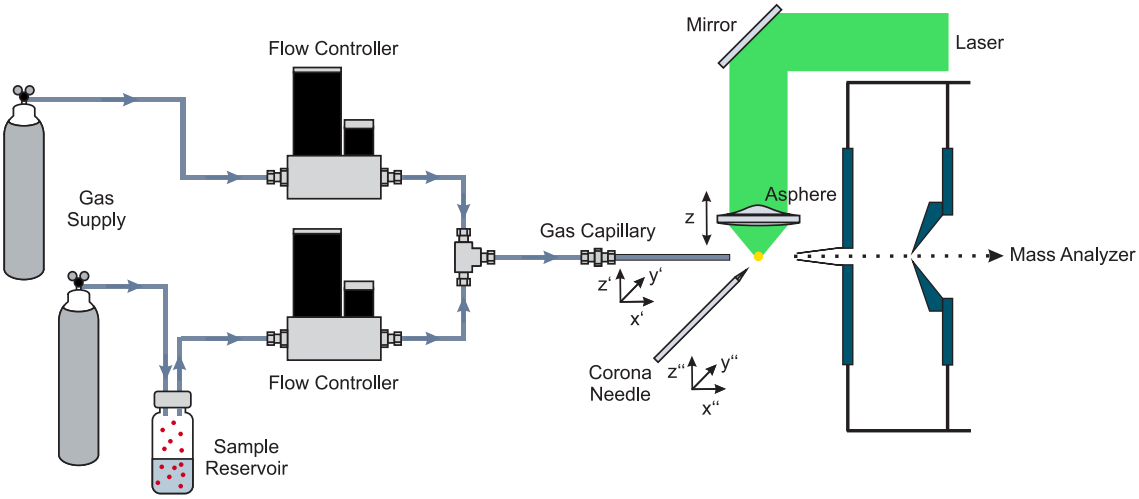

Figure 6.1: Schematic diagram of the gas phase sample generation system coupled to the airborne laser-spark setup. In addition, an APCI source is implemented for reference measurements. The arrows represent adjustable degrees of freedom for geometrical optimization of the individual components.

For direct comparison of the sensitivity, an APCI source was implemented perpendicular to the MS inlet. High-voltage was provided by a laboratory power supply (PS 350, SRS, Sunnyvale, U.S.A.), fed to the tip of a disposable cannula (0.8 mm × 120 mm, B. Braun, Melsungen, Germany). A stable corona discharge was observed using 2.5 kV (discharge current: 3 µA). The cannula was mounted on a 3D translational stage (MT3, Thorlabs, Dachau, Germany). The exact positioning along *x"*, *y"*, and *z"* was optimized before each experiment to result in maximum ion yield at the given voltage.

6.1.3 Dynamic Headspace Sampling

A carrier gas stream was fed through the headspace of a temperature controlled reservoir. The analyte-enriched outflow was adjusted by a mass flow controller (Bronkhorst High Tech B.V., Ruurlo, The Netherlands) and fed into a mixing tee, connected to a parallel bypass (constant flow: 2.0 $\mathrm{L\,min^{-1}}$, mass flow controller GFC17, Analyt-MTC GmbH, Müllheim, Germany). The resulting gas stream of adjustable analyte concentration (3–300 ppm, v / v) was fed through a borosilicate glass capillary (GB 150-8P,

o.d. 1.50 mm, i.d. 0.86 mm, Science Products GmbH, Hofheim, Germany) fixed in a 1/16 in.–1/4 in. Swagelok connector. The capillary was placed coaxially in front of the MS inlet on a 3D-translational stage (*x'*, *y'*, *z'*, M-UMR5.25, M-8UMR8.25, Newport, Irvine, U.S.A. and MT1, Thorlabs, Dachau, Germany). In subsequent experiments, the sample generation system was fed with different carrier gases and samples.

6.1.4 Optical Emission Spectroscopy

Time-integrated UV / Vis Emission Spectroscopy

Time-integrated emission spectra were acquired perpendicular to the laser beam *via* an optical fiber, placed at a distance of 5 mm from the plasma center. The other end of the fiber was connected to a Czerny-Turner spectrograph (Shamrock SR-303i-B, 1800 grooves / mm grating, ANDOR Technology Ltd., Belfast, UK). The dispersed light was detected by a CCD camera (iDus, −65 °C, ANDOR Technology Ltd., Belfast, UK). Unless stated otherwise, the entrance slit width was 150 µm and the acquisition time per spectrum was set to 1 s.

Transient UV / Vis Emission Spectroscopy

For additional time-resolved optical emission spectroscopy experiments, the plasma excitation laser was externally triggered by a digital delay generator DG645 (SRS, Sunnyvale, U.S.A.) with a repetition rate of 3 kHz. Plasma radiation was collected using a large aperture collector-collimator (CC52, F/2, ANDOR Technology Ltd., Belfast, UK) placed on a 3D translational stage (MT3, Thorlabs, Dachau, Germany) above the LIP. Light was delivered *via* an optical fiber to the entrance slit of an Echelle spectrometer (Aryelle Butterfly, LTB Lasertechnik Berlin GmbH, Berlin, Germany), equipped with an intensified CCD camera (iStar 734, −35 °C, ANDOR Technology Ltd., Belfast, UK). Gate delay and gate width adjustment and synchronization to the laser pulse were achieved by the DG645.

Time-integrated UV Emission Spectroscopy

VUV emission measurements of LIPs were performed in collaboration with the physical chemistry department of the University Wuppertal. Spectra were recorded using the ARC VM-502 vacuum monochromator system (Acton Research Corporation, Princeton Instruments, Trenton, U.S.A.), equipped with an aberration-corrected concave holographic grating (Al / MgF_2 coating, 1200 groves / mm). A homebuilt gas-tight cell was directly connected to the entrance slit of the spectrograph. To ignite the LIP inside, the laser beam was focused through an aspheric lens (A240-C, $f = 8.0$ mm, $N_A = 0.5$, Thorlabs, Dachau, Germany), which was mounted in a ceramic sleeve to adjust the position of the plasma origin relative to the entrance slit of the spectrograph.

Coherent radiation at 1064 nm was provided by a DPSS laser (Titan AC 30 MM, Nd:YAG, 100 Hz, average output power: ≤ 10 MW, pulse energy: 30 mJ / pulse, pulse width: < 5 ns, IBL Innovation Berlin Laser GmbH, Berlin, Germany). Before each set of experiments, the entire instrument was evacuated to a pressure of 2×10^{-6} mbar (TMH065, Pfeiffer Vacuum GmbH, Aßlar, Germany and Trivac D16B, Leybold GmbH, Cologne, Germany) and subsequently flushed with argon until the desired pressure level was reached. Eventually, the LIP was ignited, and the VUV radiation dispersed by the monochromator and detected by a photomultiplier tube (R928, Hamamatsu Photonics, Hamamatsu City, Japan) with a homebuilt sodium salicylate scintillator plate. Conversion of the obtained analog signal was achieved by an analog-to-digital converter (R232-ADC 16 / 24, taskit GmbH, Berlin, Germany). Spectra were recorded within the spectral range from 40–320 nm.

6.1.5 Pump-probe Shadowgraph Imaging

Temporally resolved visualization of airborne LIPs was achieved with two different experimental arrangements: (1) Laser-spark formation was induced using the same setup as for the MS experiments (DPSS laser Conqueror 3-Lambda and aspherical lens C240TME-A). For back illumination of the LIP vicinity, the laser-induced amplified spontaneous

emission of a methanolic rhodamine B solution (25 µM) was used. As excitation laser, a frequency-doubled flashlamp-pumped Nd:YAG laser (Surelite, 532 nm, pulse energy: 30 mJ / pulse, pulse width: 7 ns, Continuum, San Jose, U.S.A.) was focused by a cylindrical lens (f = 7.5 cm) into the filled quartz glass cuvette (QG 10.00 mm, Hellma Analytics, Müllheim, Germany). Both lasers were externally triggered by a DG645 digital delay generator (SRS, Sunnyvale, U.S.A.) at a repetition rate of 9 Hz. The application of argon (2.0 L min^{-1} *via* mass flow controller GFC17, Analyt-MTC GmbH, Müllheim, Germany) was mandatory for a decent visualization of the plasma. Delay times were synchronized using two photodiodes (DET10A, Thorlabs, Dachau, Germany) connected to a digital oscilloscope (TDS 2024B, Tektronix, Beaverton, U.S.A.). Photographs were acquired using an EOS 400D camera (Canon Inc., Tokyo, Japan) with an inverted SMC Pentax-M 28 mm F2.8 objective (ASAHI OPT. Co., Japan) mounted orthogonal to the propagation direction of the LIP excitation laser beam path. Detection of the incident laser light was avoided by the use of a 532 nm notch filter, introduced between the LIP and the camera. (2) For better contrast, experiments of higher energy LIP were additionally recorded. While the LIP was ignited in argon (2.0 L min^{-1}) by a flashlamp-pumped Nd:YAG laser (Surelite, 1064 nm, pulse energy: 150 mJ / pulse, pulse width: 7 ns, Continuum, San Jose, U.S.A.), the plasma vicinity was back illuminated by the visible light of a second laser (Minilite, 532 nm, pulse energy: 0.5 mJ / pulse, pulse width: 6 ns, Continuum, San Jose, U.S.A.). The latter was magnified by a 4x beam expander (BE02-05-A, Thorlabs, Dachau, Germany), passed the plasma after an adjustable temporal delay and was imaged onto the detector chip of a CCD camera (DV434-BU2, ANDOR Technology Ltd., Belfast, UK). Both lasers were synchronized by a DG535 delay generator (SRS, Sunnyvale, U.S.A.). For both arrangements, the obtained images were post-processed (background subtraction and gamma adjustment) using the ImageJ software suite.

6.2 Results and Discussion I - Plasma Characteristics

The spectrometric results shown in Chapter 5 indicate that the airborne laser-spark ion source may differ from the typical LIBS approach. The striking resemblance of the positive mode reagent-ion population, as well as the detection of non-dissociated analyte ions, suggests a similar mechanistic pathway for the formation of positively charged ions to the family of APCI-like plasma-based ionization sources, such as DBD, LTP or FAPA. The latter ion sources have been extensively characterized by means of optical emission spectroscopy,[89,115,135,176] which provided complementary information to the spectrometric data, and thus not only helped to shortlist reactants that are involved in the formation of molecular ions, but also improved their sensitivity.

For the above-named helium-driven ion sources, it is commonly accepted that the formation of protonated molecules of the type $[n\mathrm{M}+\mathrm{H}]^+$ can be briefly summarized as follows: *Via* Penning ionization with formed metastable helium atoms, and / or charge transfer reactions with $He_2{}^+$, secondary reactants are formed out of the surrounding gas phase, *e.g.*, $N_2{}^+$. The latter is regarded as the primary reaction intermediate in the well-known APCI reaction sequence (see also Chapter 2) and results in the formation of proton-bound water clusters, which potentially transfer their charge onto the neutral analyte.

Though the process of generating a laser-induced breakdown in air seems to be a simple and straightforward approach, the physics involved in the initiation of a LIP and its expansion are still under investigation.[321] Besides complex laser interactions with the gas phase, involving several simultaneously ocurring processes, such as self-focusing, self-trapping, multiphoton and cascade ionization, and inverse bremsstrahlung absorption,[322–325] especially the experimental conditions, including the excitation wavelength, pulse duration, pulse energy, the focusing conditions, and the nature of the surrounding atmosphere, drastically affect the breakdown treshold, the expansion of the laser-spark, and the involved plume chemistry.[321,326,327]

LIPs, produced during the laser-induced breakdown of gases, are known to be capable of exciting and ionizing their surrounding medium. In principle, two mechanisms potentially contribute to this process, including (1) photoexcitation and ionization by intense ultraviolet emission from the self-emision of the plasma kernel and / or (2) heating by strong shock waves, generated by the plasma kernel during its expansion into the ambient.[321] Therefore, in the first part of this Chapter, the DPSS laser-driven LIP was interrogated by using optical emission spectroscopy, shadowgraph imaging, and mass spectrometry in tandem, to elucidate the relevant excitation mechanisms that lead to the detection of intact molecular ions in ambient mass spectrometry analysis.

6.2.1 Time-integrated UV / Vis Emission Spectroscopy

Fig. 6.2a depicts the time-averaged optical emission spectrum of the airborne laser-spark ion source ignited in the open laboratory environment. The signal pattern exhibits a pronounced degree of dissociation into atomic and ionic species. Major atomic emission lines are predominantly found in the near-IR region of the electromagnetic spectrum for O I (715.6 nm, 777.4 nm, 844.5 nm) and N I (746.7 nm, 821.5 nm, 868.9 nm), accompanied by less abundant emission features originating from N II (343–593 nm) and H I (656.3 nm). In addition, progressions of weak emission lines assigned to N_2 ($C^3\Pi_u \rightarrow B^3\Pi_g$) and N_2^+ (${B^2\Sigma_u}^+ \rightarrow {X^2\Sigma_g}^+$) are detected in the spectral range between 313–434 nm and 387–428 nm, respectively. Further spectral contributions of other diatomic species, such as OH, NH or CN, are not observed.

The results shown here substantially differ from the previously recorded emission spectra of the DBD probe (refer to Chapter 2). While the higher plasma temperature can account for the presence of predominant atomic and ionic species, the unexpectedly weak contributions of molecular emission features, such as the vibronic progression of ${N_2}^+$, stand in strong contrast to the absence of atomic ions and the pronounced detection of protonated water cluster ions in the respective mass spectra. The formation of the latter reactant species is widely accepted to follow the APCI cascade mechanism.[89,115,116,119,176]

Nonetheless, it is important to keep in mind that this spectroscopic study is (1) recorded on-axis with the plasma kernel, (2) only line of sight averaged, (3) observed orthogonal to the laser-spark expansion direction, and (4) temporally and spatially integrated. Accordingly, the relatively low emission intensity of molecular bands does not directly correlate to low number densities of excited molecules. On the contrary, the significantly higher state densities of molecular species merely distribute the total number of excited molecules over a larger partition function. Despite the difference in plasma parameters, another important aspect that has not been considered by now is the fact that, typically, electrically driven plasmas use a sweep gas. Therefore, in a second set of experiments, laser-sparks were generated in directed gas-streams of compressed air, dry nitrogen, argon, and helium to provide different physical properties of expansion dynamics and plasma chemistry, considering the differences in laser absorption properties, mass density, and speciation. To visualize the effect of gas addition on the plasma performance, first, optical emission spectra were recorded.

The addition of 2.0 $\mathrm{L\,min^{-1}}$ compressed air (Fig. 6.2b) merely increases the overall brightness of the plasma by a factor of three to four, while the relative intensities of the individual emission lines remain unchanged. This increase might be caused by replenishing cold air (being the plasma medium) in the late plasma zone, before the ignition of the subsequent laser-spark. This assumption is corroborated by the observed trend that the increase in overall brightness is less pronounced for lower repetition rates. As can be expected, the addition of 2.0 $\mathrm{L\,min^{-1}}$ dry $\mathrm{N_2}$ (Fig. 6.2c) shifts the relative intensity ratio of nitrogen and oxygen originating lines. Besides this quenching, the O I lines at 715.6 nm, 777.4 nm, and 844.5 nm remain visible. They stem from atomic relaxation of oxygen with high internal term energy of 14.5 eV, 10.7 eV, and 10.9 eV, respectively, indicating that oxygen from the surrounding air must find a way into the hot plasma region. Furthermore, in contrast to the spectra shown in Fig. 6.2a and Fig. 6.2b, additional spectral features arising from OH ($\mathrm{A^2\Sigma^+ \rightarrow X^2\Pi}$) are observed in the shorter wavelength region of the spectrum at 281–285 nm and 306–309 nm.

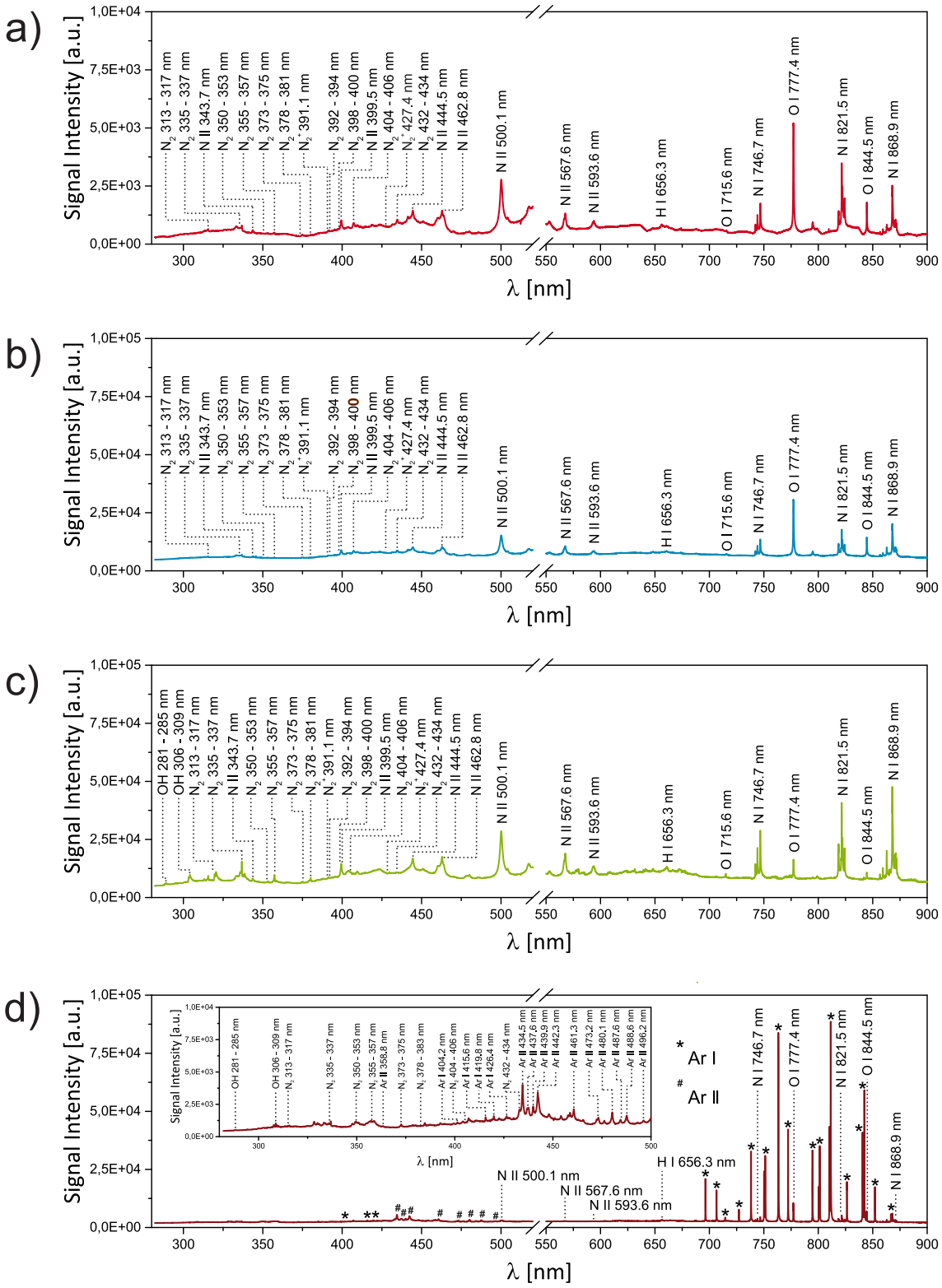

Figure 6.2: Time-integrated UV / Vis emission spectra out of ambient air (a), and upon addition of 2.0 L min^{-1} compressed air (b), dry N_2 (c), and argon (d).

Upon the addition of the noble gas argon (Fig. 6.2d), even brighter emission spectra are observed. To avoid the saturation of the CCD detector, the slit width of the spectrograph was reduced to 50 µm and the acquisition time was set to 0.01 s. The recorded emission spectrum (Fig. 6.2d) exhibits a comparable distribution of nitrogen and oxygen originating lines, between predominant atomic argon lines in the near-IR region of the electromagnetic spectrum. Moreover, as can be seen in the inset in Fig. 6.2d, weak bandheads of the second positive nitrogen system ($C^3\Pi_u \rightarrow B^3\Pi_g$) and molecular emission from OH ($A^2\Sigma^+ \rightarrow X^2\Pi$) are observed, accompanied by atomic argon emission lines (404.2 nm, 415.6 nm, 419.8 nm, 426.4 nm) and stronger ionic contributions of argon (358.8 nm, 434.5 nm, 437.6 nm, 439.9 nm, 442.3 nm, 461.3 nm, 473.2 nm, 480.1 nm, 487.6 nm, 488.6 nm, 496.2 nm). As previously observed for the argon-driven DBD ion source (see Chapter 2), emission attributed to N_2^+ ($B^2\Sigma_u{}^+ \rightarrow X^2\Sigma_g{}^+$) is not detected.

Unexpectedly, the addition of helium (results not shown) quenched the DPSS laser-driven plasma entirely. This result can be mainly attributed to the energetically high lying electronic and Rydberg states.

Parallel to the spectroscopic interrogation of the laser-spark, ambient mass spectrometry experiments were conducted to investigate the formation of reactant background ions using exactly the same experimental conditions. The recorded mass spectra out of ambient air, without replenishing the late plasma zone, as well as upon the addition of 2.0 $\mathrm{L\,min^{-1}}$ compressed air, dry nitrogen, and argon are shown in Fig. 6.3a–6.3d, respectively. As expected, the enhancement in optical brightness, depicted in Fig. 6.2, can be seen to go along with an enhanced reagent-ion formation in the complementary mass spectra. This result is especially noticeable for the formation of protonated water clusters $[(H_2O)_nH]^+$, but less pronounced for their ammoniated analogues $[(NH_3)(H_2O)_nH]^+$ and charge transfer promoting ions. Moreover, atomic ions are still absent in each of the recorded mass spectra. In fact, the only indicator for bonds being broken throughout the plasma process is the presence of NO^+ and $[(NH_3)(H_2O)_nH]^+$.

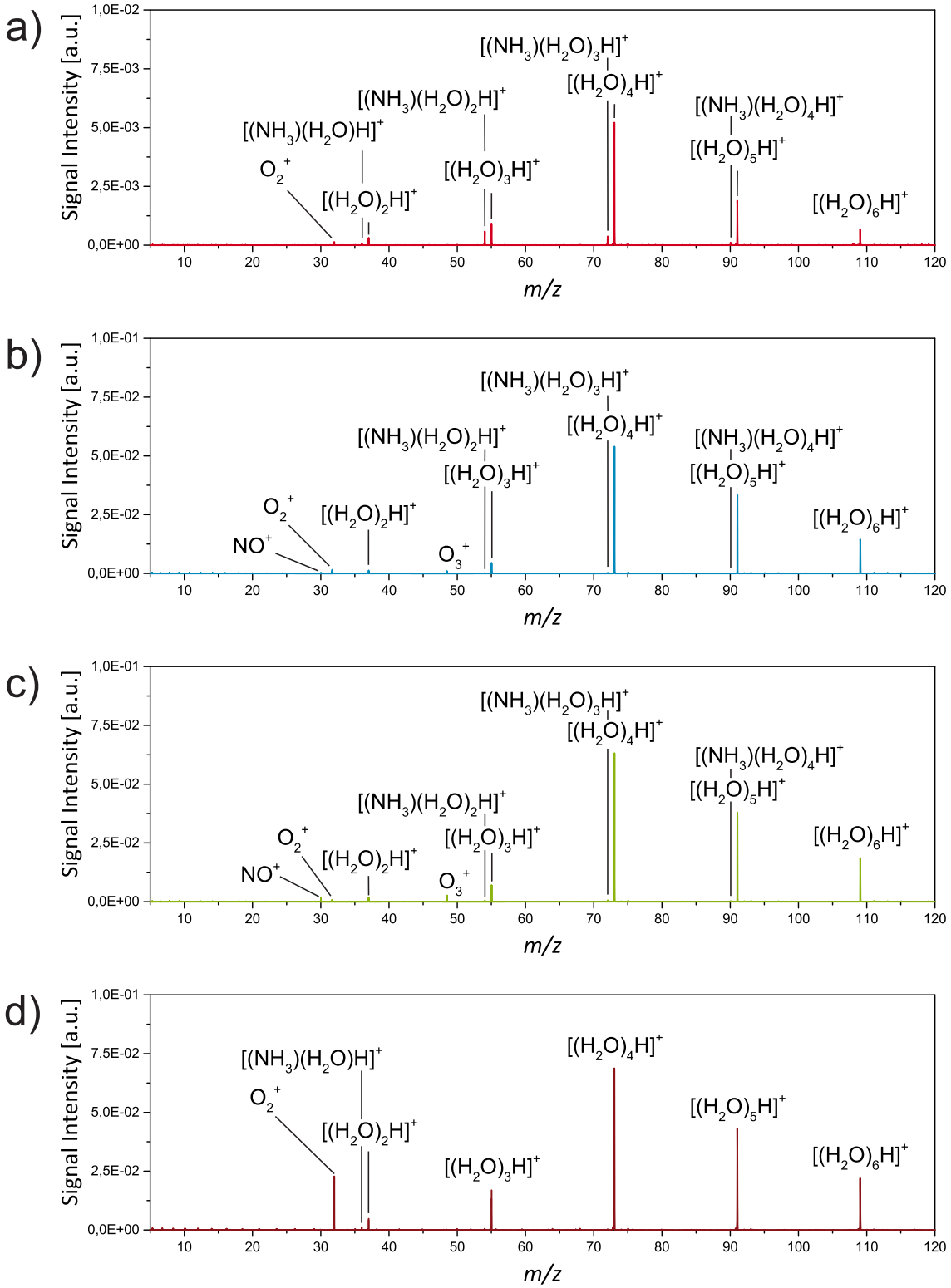

Figure 6.3: Reagent-ion background produced out of ambient air (a), and upon addition of 2.0 L min^{-1} of compressed air (b), dry N_2 (c), and argon (d).

Interestingly, in contrast to the optical brightness, the overall abundance of reagent-ions does not seem to depend strongly on the gas type itself. While the addition of argon yields plasmas of high brilliance, it does not result in the strongest signal enhancement in the observed mass spectra. Instead, considering the most abundant ion peak $[(H_2O)_4H]^+$ at m/z 73, comparable results are obtained by simply using compressed air or dry nitrogen, which is highly favorable in terms of maintenance costs, availability, and application for in-field experiments.

6.2.2 Time-integrated UV Emission Spectroscopy

LIPs emit profoundly in the ultraviolet and visible region of the electromagnetic spectrum with several contributions from ionic, atomic and molecular species. However, due to the relatively high ionization energies of molecular oxygen and nitrogen (12.1 and 15.6 eV or 102.5 nm and 79.5 nm, respectively), only photons in the VUV regime are energetic enough to cause a step-ionization or direct ionization of the surrounding atmospheric constituents. Therefore, UV emission spectra within the spectral window from 40–320 nm were recorded in collaboration with the physical chemistry department of the University Wuppertal. Owing to the strong absorption of VUV radiation by molecular oxygen,[328] the plasma ignition and subsequent observation were conducted within a homebuilt gas-tight cell flushed with argon at 1300 mbar.

The recorded emission spectrum is given in Fig. 6.4. It is primarily characterized by three different spectral features, comprising atomic, ionic, and molecular emission. Between 58–72 nm, a broad peak with a local maximum at 67.7 nm is observed. Regarding its asymmetry, the signal is expected to be the result of several superimposed emission signals, including N II at 64.8 nm, Ar II at 66.6 nm, 67.3 nm, and 67.7. nm, as well as C II at 68.7 nm. Another convoluted spectral feature becomes apparent between 108–144 nm. Most likely, this signal originates from transitions of N I at 113.4 nm, 119.3 nm, 120.1 nm, and 124.3 nm, O I at 130.1 nm, and C II at 133.6 nm. Furthermore, continuous VUV emission arises from the second continuum of Ar_2^* with a local maximum around 127 nm.[329]

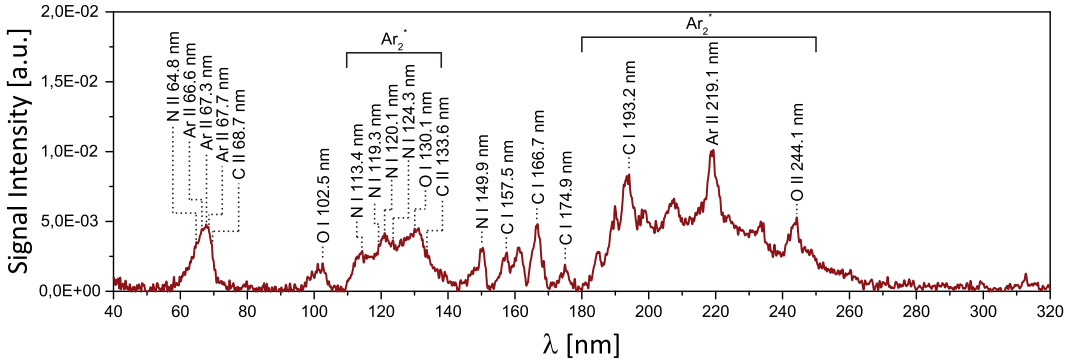

Figure 6.4: UV emission spectrum of the LIP ignited in an argon atmosphere held at 1300 mbar.

Shifted towards the red, radiation from the third continuum of Ar_2^* is observed between 180–260 nm,[330] superimposed by further emission lines assigned to C I, Ar II, and O II at 193.2 nm, 219.1 nm, and 244.1 nm, respectively. Additional spectral features originate from O I at 102.5 nm, N I at 149.9 nm, and C I at 157.5 nm, 166.7 nm and 174.9 nm. VUV radiation of these species is expected to originate from air contamination in the plasma cell. After filling the system with inert gas, at least $\approx 2 \times 10^{-6}$ mbar of air were still present inside the vacuum chamber.

The photons emitted in the investigated spectral window correspond to a number of highly energetic transitions which exceed the average ionization energy of most organic molecules and components in the adjacent gas layer of the plasma. Accordingly, an additional photochemical reaction pathway has to be considered that may also induce either a direct ionization of analyte molecules or a formation of secondary reagent-ions. Though VUV light is highly absorbed by molecular O_2 [328], and thus should be minimized under ambient conditions, it cannot be fully neglected in the close vicinity of the plasma kernel. In such a scenario, the oxygen content in air would not be enough to completely suppress the VUV contributions.

6.2.3 Transient UV / Vis Emission Spectroscopy

Since LIPs are known to be transient, the temporal evolution of the plasma is of great importance for the involved excitation mechanisms. Typically, the luminous lifetime of a plasma is characterized by the following events: Shortly after the plasma initiation, intense continuum radiation is emitted, followed by the subsequent emission of discrete narrow lines or bands of excited ions, atoms, and molecules, before plasma extinction. Since the unspecific continuum radiation abates much faster in time than the specific contributions of atomic, ionic, and molecular emission, a time-resolved series of the spectral contributions allows for a temporal tracking of the plasmas chemical equilibriums' fate.

A series of time-resolved UV / Vis emission spectra is shown in Fig. 6.5. Stepwise, the gate delay was adjusted in 100 ns steps. Gate width was set to 100 ns. Note that for this set of experiments, it was only possible to achieve meaningful spectral data upon the addition of a 2.0 $\mathrm{L\,min^{-1}}$ argon stream. This was due to the lower duty cycle, dictated by the maximum repetition rate of the multichannel plate (MCP) inside the iCCD camera. Another reason was the much higher f-number of the time-resolved Echelle spectrometer.

Considering the presented data, it becomes obvious that the total luminous lifetimes of DPSS laser-driven plasmas are much shorter (only a few hundred ns) than those from plasmas induced by conventional flashlamp-pumped lasers with 1–100 mJ or even higher pulse energies. As a consequence, a time-resolved analysis is often unpractical or nearly impossible with commonly used gated iCCD cameras.[331] LIPs initiated by high energy laser pulses exhibit characteristic plasma lifetimes in the range between $\sim$10–100 µs, involving continuum radiation at $t \lesssim 100$ ns, ionic emission at $t \lesssim 500$ ns, atomic emission at $t \lesssim$ 1–10 µs and molecular emission at $t \gtrsim 10$ µs.[332,333] In contrast, the results presented in Fig. 6.5 strongly suggest that the plamas generated by the DPSS laser are short-lived with a total plasma lifetime comparable to the duration of the laser pulse. In the present case, at the temporal delay of $\Delta t = 0$, spectral contributions from unspecific continuum radiation are almost negligible and predominant emission lines from several atomic species,

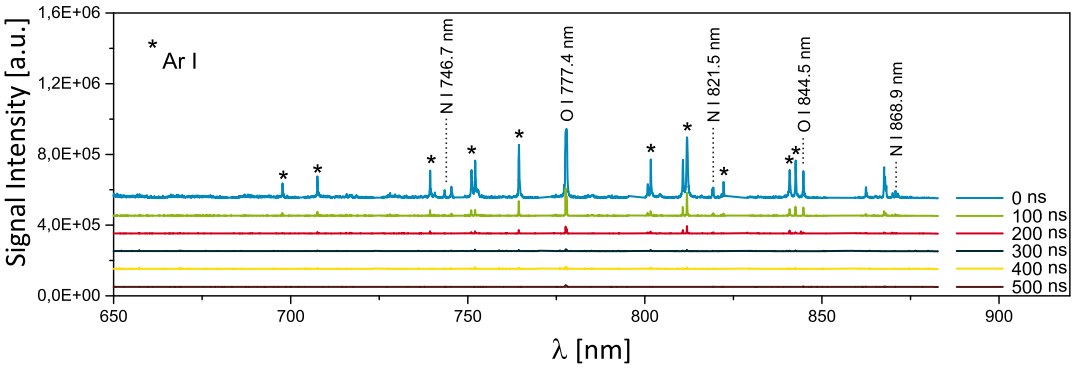

Figure 6.5: Time-gated UV / Vis emission spectra for the LIP ignited in the open laboratory environment, upon the addition of 2.0 L min^{-1} argon. Due to the weak molecular emission bands, only the near-IR region of each spectrum is shown. Given numbers denote the applied temporal delays.

including Ar I, N I and O I are already observable. These findings can be mainly attributed to the limited amount of energy available to sustain the plasma after the initial breakdown, and are in good agreement with the previous publications on laser-induced microplasmas.[268,331,334] The same fast plasma kinetics are observed for all detected emission lines. The elemental plasma radiance decreases with a determined first order rate constant of only 65 ns. Approximately 500 ns after the initial plasma ignition, hardly any emission can be observed. Unfortunately, the contribution of molecular emission lines in the studied timeframe is too weak for a meaningful time-resolved analysis. However, molecular bands are visible in the temporally integrated UV / Vis emission spectra, and their decay is known to follow much slower kinetics.[130]

6.2.4 Pump-probe Shadowgraph Imaging of the Spark Morphology

By focusing an intense laser pulse into a gaseous medium held at atmospheric pressure, the strong electromagnetic fields generated in the focal volume can cause a gas breakdown and initiate plasma formation. This process is accompanied by the formation of expanding shock waves which cause heating of the adjacent atmosphere, and thus affect the plasma dynamics. Two dominating mechanisms, including radiative and detonative heating, are discussed of being responsible for the excitation and ionization of the surrounding gaseous

medium. While radiative heating involves UV radiation and high energy photons to interact with the surrounding atmosphere, detonative heating is based on the formation and propagation of a high pressure shock front at the plasma / ambient boundary, which may be also capable of exciting and ionizing the ambient environment.[321]

For a temporal-resolved visualization of the DPSS laser-driven LIP, pump-probe shadowgraph imaging experiments were conducted to study the shock wave expansion with respect to the plasma origin. The obtained results were acquired in subsequent imaging experiments with different temporal delays t_D between the excitation laser and the back-illumination laser (pump-probe). Each image in the time sequence was recorded from independent breakdown events. In the individual experiments, the first laser ignited a plasma, while the second laser imaged the resulting shock wave at its current position. As in the time-resolved emission spectroscopy experiments, the addition of argon was found mandatory to achieve the necessary contrast.

Fig. 6.6a–6.6c represent the shock wave propagation of the DPSS laser-driven plasma, recorded at various times after the LIP generation. The optically bright part of this low-energy LIP can be seen to have a size of only 80 µm × 25 µm, which is fairly small compared to higher energy LIPs. In between the individual breakdown events, the origin of the microplasma appears to be highly stable and localized. Further, the shadowgram images exhibit the plasma kernel to be elongated in the laser propagation direction, which is due to translational absorption,[321] while the propagating shock wave reveals a top-bottom asymmetric cylindrical shape. Note that due to the very low energy of the individual LIP of merely 75 µJ (25% of the 300 µJ / pulse),[335] the images are sums of 500 individual laser pulses. Accordingly, the pulse-to-pulse fluctuations in the plasma conditions lead to an artificial broadening of the already weak shock front visualization that becomes stronger toward longer delay times (see Fig. 6.6c).

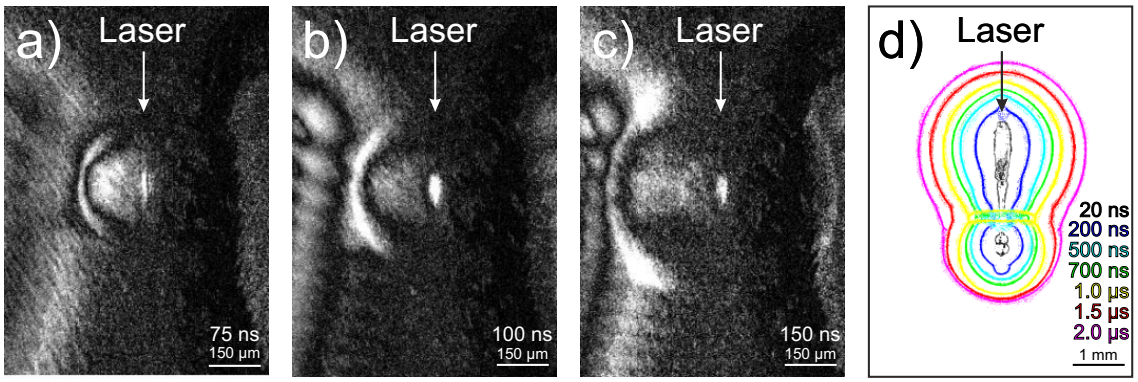

Figure 6.6: (a–c) Pump-probe stroboscopic shadowgraphs of the shock wave propagation around the microplasma, used for ambient mass spectrometry. (d) Reference measurement of a higher energy LIP. The laser beam is incident from the top side. Each image in the time sequence is recorded from independent laser breakdown events. Given numbers denote the corresponding delay times.

To visualize the effect of the teardrop shape on the shock wave morphology, a second set of experiments with higher laser power was conducted. The results are shown in Fig. 6.6d. Here, the spatially well-defined shock waves of seven subsequent experiments are superimposed in different colors in one picture. Albeit the different laser power in the two data sets, the shock wave dynamics are qualitatively comparable with the only striking difference being the absolute plasma size and time scale. At $t_D = 200$ ns an expanding pressure wave can be seen, caused by the larger refractive index of the denser wave front. The density wave travels in all directions with an initial wave front velocity of 2.100 $\mathrm{m\,s^{-1}}$. Toward longer delay times this supersonic expansion is decelerated until at $t_D = 2$ µs sonic speed is achieved. In addition, the second experiment reveals that the plasma morphology itself is time-dependent. While at early times propagating shock waves of an asymmetric cylindrical shape are observed, a transformation into a more spherical shape toward later plasma lifetimes is observed.

Recapitulating, the results obtained from the pump-probe shadowgraph imaging experiments helped to corroborate the transient nature of the DPSS laser-driven plasma and visualized the asymmetric expansion of the generated shock wave, as well as the changes in

the LIP expansion velocities. However, the initial question to which extent either radiative or detonative heating may contribute to the ionization of the adjacent gaseous medium still remains unclear. To adress this open question, recently, Harilal *et al.*[321] presented a multiple diagnostics approach. In this study, shadowgraphic and time-resolved imaging experiments were used to examine the shock generation, shock propagation, and spark self-emission morphology at different plasma lifetimes, while spatiotemporal-resolved emission spectroscopy helped to investigate the individual emission features at on- and off-kernel positions. Their results showed that shadowgraph images only partially reflect the self-emission of LIPs. Instead, emission from the plasma core is restricted closer to the focal plane, and thus the volume of the emitting region is much smaller than the volume of the explosion region. While the light emitted by the kernel profoundly exhibited unspecific broadband emission, followed by ionic and atomic emission, the off-kernel position (at 2.5 mm distance to the plasma center) showed a preferential excitation and emission in the UV region of the electromagnetic spectrum, originating from N_2 ($C^3\Pi_u \rightarrow B^3\Pi_g$) and $N_2{}^+$ (${B^2\Sigma_u}^+ \rightarrow {X^2\Sigma_g}^+$). Considering the propagation velocities of the shock wave compared to the speed of light, the results demonstrate that in case of higher energy LIPs, UV radiation from the hot kernel is solely responsible for the photo-excitation and emission of the surrounding cold medium. These results were further corroborated by modeling the shock wave expansion which provided supporting evidence that the pressure of the generated shocks is not strong enough to excite the cold off-kernel gas.

Referring to this section's introduction on the ionization mechanism of electrically driven plasmas, the spectral emission features of the off-kernel emission of LIPs correlate very well with the spectrometric detection of $[(H_2O)_nH]^+$, which is most likely formed *via* an $N_2{}^+$ involving APCI-like reaction sequence. The concentrically expanding pressure wave keeps the analyte spatially apart from the hot kernel volume by drifting it toward the outer periphery. In this colder region, the analyte gets ionized either directly by the intense UV radiation emitted by the plasma core or *via* interaction with secondary reagent-ions.

6.2.5 Time-integrated UV / Vis Emission Spectroscopy of Carbon-laden Gas Streams

According to the above said, the expanding shock front causes a unidirectional diffusion barrier which may prevent molecules outside the plasma from ever reaching the hot plasma kernel until the shock wave decays. In case of the DPSS laser-driven microplasma, this barrier is especially pronounced in the first 65 ns, *i.e.*, the lifetime of the hot plasma (see also Fig. 6.5). At the same time, this strictly outbound matter transport also causes a rarefaction inside the former plasma center. As a consequence, from the second laser pulse on, all plasma events are less intense and less bright than the first one. A replenishing with fresh gas can only occur after the plasma event is over (between two pulses in repetitive experiments), when the center is cold again. In particular, experiments with high repetition rates, *i.e.*, short time intervals between two laser pulses, should benefit from an additional directed gas flow to support the diffusive transport into the former plasma zone, as shown in Fig. 6.2 and Fig. 6.3.

The validity of this simple picture of replenshing the rarefied plasma zone is tested by recording time-integrated UV / Vis emission spectra of airborne LIPs ignited in different carbon-laden gas streams. If this externally applied gas stream entirely remains in the plasma periphery, only ionized organic molecules should be formed which cannot be observed in the optical emission spectra. On the other hand, if the carbon-laden gas stream reaches the hot plasma kernel, an atomization and recombination to CN would be expected. Therefore, 2.0 $\mathrm{L\,min^{-1}}$ pure nitrogen were fed through the headspace of a sample reservoir filled with either *n*-butanol, toluene or ferrocene. In this indirect approach, the latter organic compounds serve as a source of carbon, while the N_2 stream provides an excess of N in the plasma. These settings were chosen intentionally since the spectrometric analysis of *n*-butanol, toluene, and ferrocene, discussed in the preceding chapter, yielded exclusively intact molecular ions.

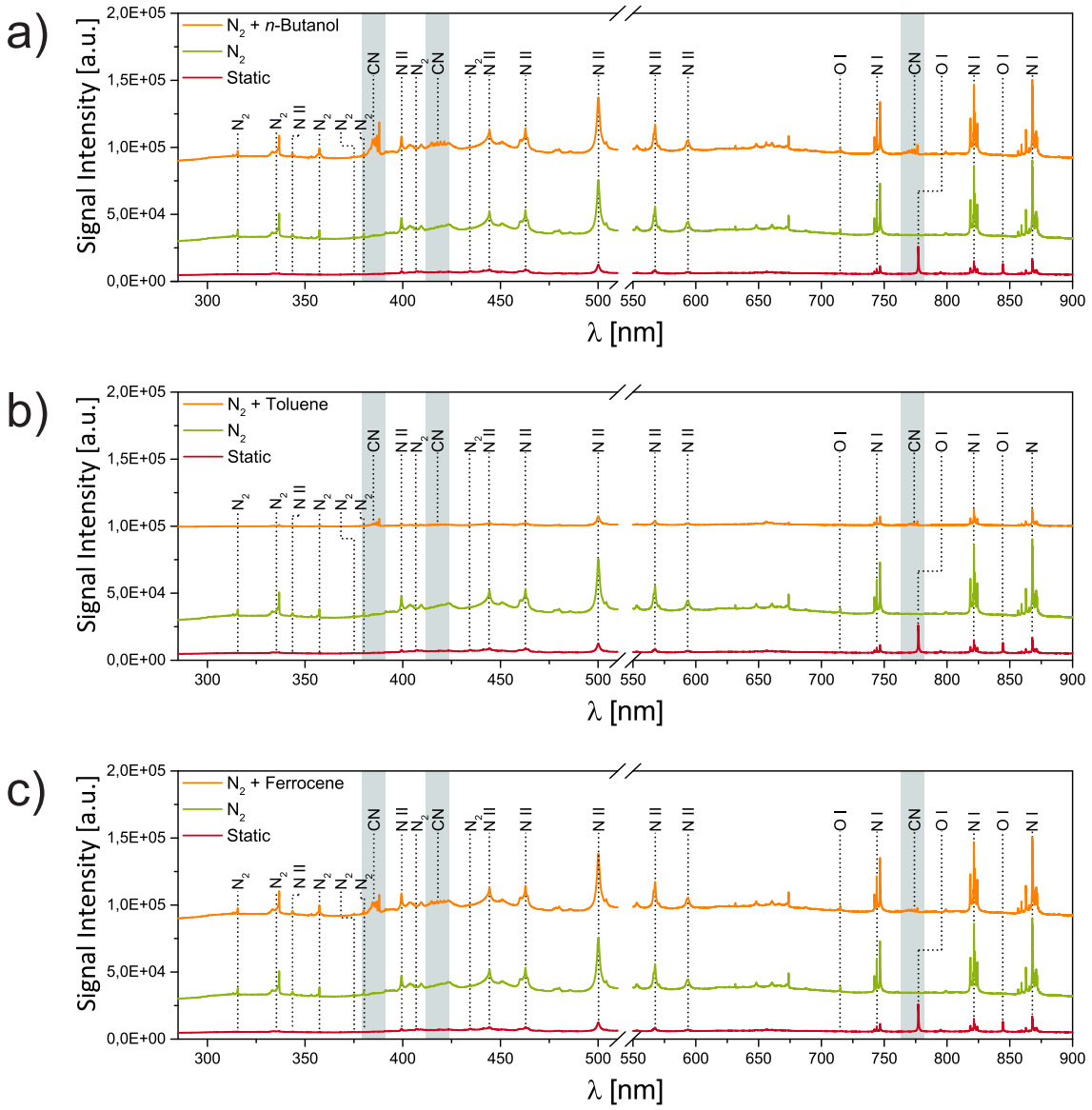

Figure 6.7: Optical emission spectra obtained from 3 different carbon-laden N_2 streams, including (a) *n*-butanol, (b) toluene, and (c) ferrocene. Spectra representing the presence of analyte in the gas stream are shown in orange. Reference measurements in a pure N_2 stream, and without an additional gas are depicted in green and red, respectively. The grey-shaded areas highlight the spectral contributions of CN.

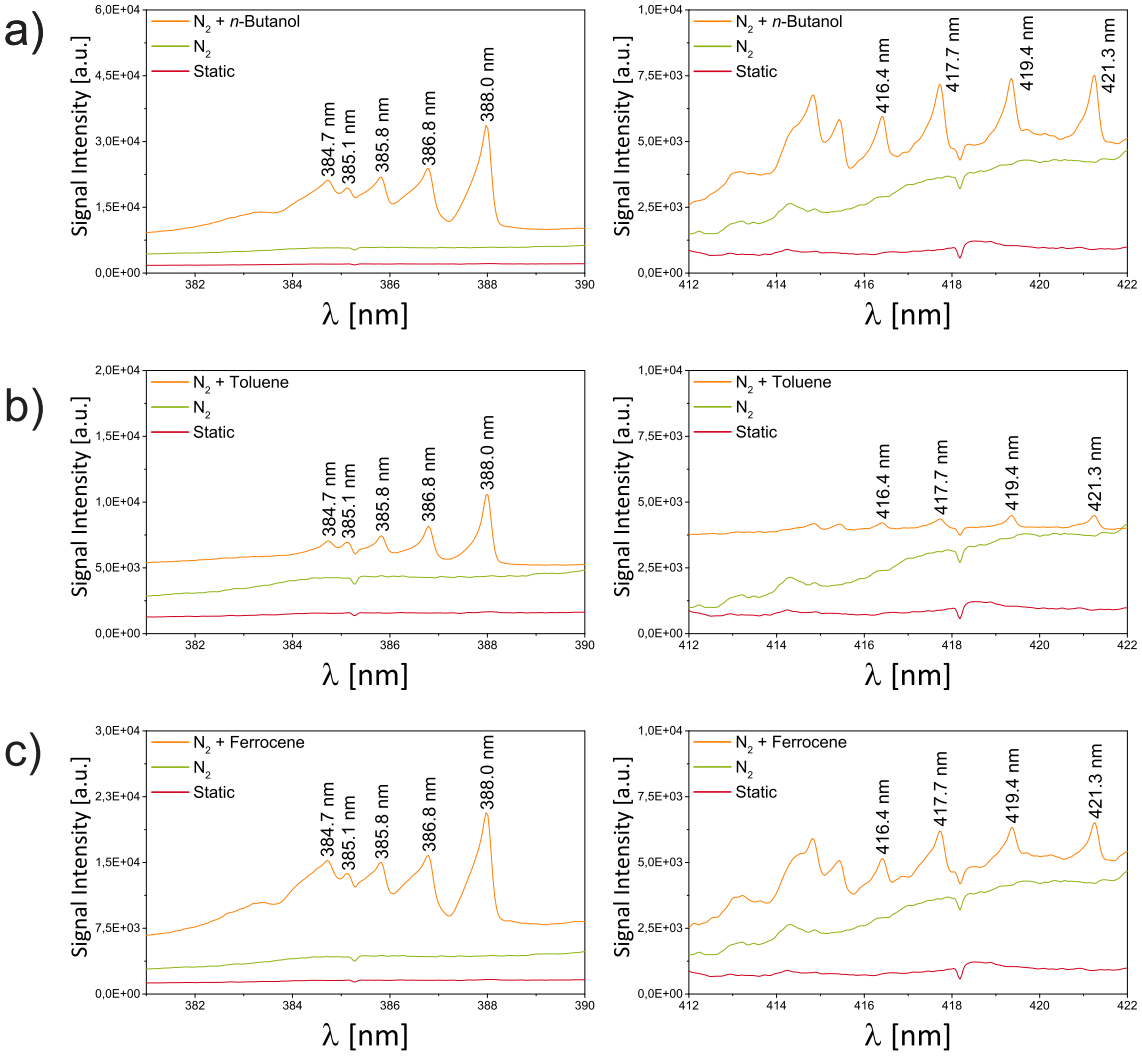

Figure 6.8: Detailed optical emission of the band progression ($\Delta v = 0$ and $\Delta v = -1$) of the violet system of CN ($B^2\Sigma^+ \rightarrow X^2\Sigma^+$) in the spectral range between 381–390 nm and 412–422 nm. The individual graphs represent the highlighted areas in Fig. 6.7.

As can be seen in Fig. 6.7, for each analyte, an ensemble of spectra was recorded to visualize the response of three individual scenarios: (1) spectral analysis of the LIP ignited in the laboratory environment, but without replenishing the former plasma center (red spectrum), (2) spectral analysis of the LIP ignited in a pure N_2 stream (green spectrum), and (3) spectral analysis of the LIP ingited in a carbon-enriched N_2 stream (orange spec-

trum). For the latter experiment, prior to each measurement, the gas stream was turned on five minutes before the optical spectrum was recorded to ensure the presence of target molecules at the plasma origin.

Scenario (1) and (2) yielded emission spectra that showed identical emission features to those discussed earlier in Section 6.2.1. For both settings, the individual spectral patterns are dominated by strong atomic and ionic emission lines of ubiquitous nitrogen and oxygen, accompanied by weaker molecular emission of N_2 ($C^3\Pi_u \rightarrow B^3\Pi_g$) and N_2^+ ($B^2\Sigma_u{}^+ \rightarrow X^2\Sigma_g{}^+$). The unassigned emission features between 600–700 nm are first order artefacts of the N_2 ($C^3\Pi_u \rightarrow B^3\Pi_g$) progression detected in the second blazing order of the spectrograph. In the case of scenario (3), the ignition of LIPs in a carbon-enriched gas stream results in the detection of additional spectral features that can be assigned to the CN violet band ($B^2\Sigma^+ \rightarrow X^2\Sigma^+$) with $\Delta v = 0$ and $\Delta v = -1$ between 381–390 nm and 412–422 nm, respectively (detailed band progressions are shown in Fig. 6.8). The highlighted area between 760–780 nm is a first order artefact of the CN progression detected in the second blazing order of the spectrograph. These results clearly indicate that an atomization of the introduced gas stream is taking place since the CN molecule has not been present initially. Instead, CN emission arises from the recombination of carbon and nitrogen atoms into electronically excited CN. However, to which extent this atomization / ionization / recombination occurs in the hot plasma kernel or the expanding shock wave cannot be elucidated. Nonetheless, compared to the applied carbon and nitrogen amount being present in the applied gas stream, the signal intensities of the CN band are comparably low and emission lines from the C_2 Swan band cannot be detected.

These findings can be rationalized by two different fundamental processes that have been discussed in the literature: (1) By examining the formation of molecular species in LIPs, Glaus *et al.*[130] observed an incomplete dissociation of carbon bonds, and thus a reduced number of atomized carbon in the plasma to form CN. (2) The LIBS experiments conducted by Hohreiter and Hahn[336] suggest a physical mechanism that selectively per-

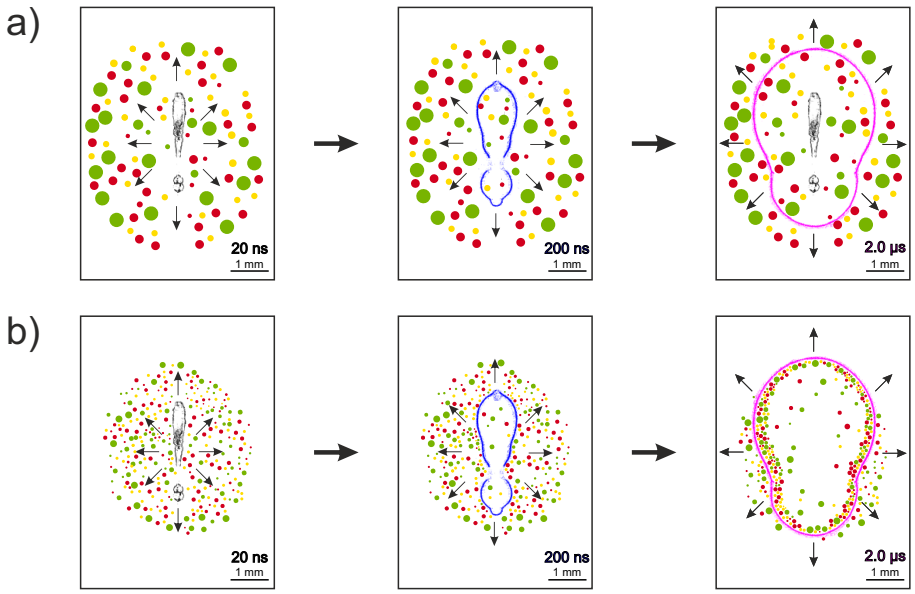

Figure 6.9: Simplified macroscopic description of the proposed interaction between the expanding shock wave and analyte species of different size and mass, adapted from Hohreiter and Hahn.[336] While larger particulates (>0.1 µm) resist the outward transport initiated by the expanding shock wave and remain in the plasma center (a), nano-scale analyte species tend to be depleted from the plasma core toward the plasma edges (b).

turbs gaseous analyte species during plasma formation and growth, thereby affecting the final amount of target species present within the LIP. This hypothesis is also based on the formation of a shock wave, which rapidly expands from the plasma origin. By performing similar experiments with carbon-laden gas streams, they observed that analytes at the molecular level tend to be selectively swept out of the plasma core toward the plasma edges, where the temperature and electron densities are significantly lower. In contrast, analytes at the particular scale are less affected by the drag forces and remain in the plasma center (Fig. 6.9). In the present context, both explanations substantiate the above-mentioned coexistence of two spatially separated ionization channels: (1) inside the plasma, a thermal ionization including atomization occurs, while (2) in the colder vicinity of the plasma, intact molecules are ionized photochemically. The ratio between these two channels is determined by the matter transport between the two zones, which is ultimately governed by the detonative density wave.

6.2.6 Conclusion I

The implementation of a low energy DPSS laser-driven microplasma as an ionization source for ambient MS applications resulted in the formation of intact molecular ions without visible fragmentation. In contrast, the investigation of the temporally integrated optical plasma emission depicted a pronounced degree of dissociation into atomic and ionic species. This contradiction could be rationalized by the transient behavior of the LIP. The pulsed character of the plasma led to the formation of shock waves, which concentrically expanded around the hot plasma core, as observed *via* the shadowgraph imaging experiments. In addition, time-resolved spectroscopy revealed very short absolute plasma lifetimes. Though the microplasma approach exhibited high temperatures sufficient to break apart molecules into atoms, those high temperatures only exist for a small fraction of the absolute lifecycle of the plasma. In consequence, the possible interaction time between the analyte and the hot plasma gets relatively short. During this timeframe, the diffusion of target molecules into the plasma is prevented by a pressure wave gradient that selectively sweeps the molecules toward the plasma edges. At these off-kernel positions, where temperatures and electron densities are significantly lower, the analyte gets ionized either directly by the intense UV radiation emitted by the hot plasma core or *via* interaction with secondary reagent-ions. Furthermore, the presence of shock waves causes a rarefaction inside the plasma center, which could be verified by the enhancing effect of a directed gas stream toward the plasma center. In this way, a micrometer-sized, hot, and dense plasma can be used as a well-defined ion source, providing high ionization yields with relatively low specificity toward the analytes polarity or ionization energy.

6.3 Results and Discussion II - Analytical Performance

In the first part of this chapter, the beneficial influence of leading a plasma gas into the LIP was observed. Both the self-emission of the plasma and the reagent-ion population were found to be drastically enhanced. In order to qualify the viability of the gas-supported microplasma for future mass spectrometry applications, in the second part of this chapter, this gas flow dependence is systematically studied, including both the gas type and the applied flow rate. Afterwards, flow-dependent ionization yields of selected target compounds are determined, followed by an evaluation of the analytical performance, and a classification of the current setup among existing atmospheric pressure ionization schemes.

6.3.1 Gas Flow Dependence

Prior to the analysis of selected target compounds, the role of the volumetric flow of a directed gas stream on the generation of secondary reactants was investigated (Fig. 6.10). Therefore, the plasma origin was fixed centrally in front of the MS inlet and positive mode reagent-ion spectra were recorded while compressed air, dry nitrogen or argon were streamed through the plasma region at variable defined flow rates.

For all three scenarios, the acquired blank spectra showed a comparable signal pattern to those depicted in Fig. 6.3. The spectra were dominated by a progression of protonated water cluster ions $[(H_2O)_nH]^+$ and minor abundant ammoniated cluster ions of the type $[(NH_3)(H_2O)_nH]^+$. Charge transfer carriers, including O_2^+, NO^+, and NO_2^+ were observed to different extents, depending on the applied plasma gas. Independent of the gas type and the applied flow rate, the overall cluster size distribution of $[(H_2O)_nH]^+$ remained unchanged, with $n = 4$ being the most abundant signal. Again, it should be noted that the observed higher mass clusters do not reflect the cluster composition outside the vacuum region of the mass spectrometer, but are most likely formed in the expansion zone of the conical inlet. If at all, a thermally equilibrated population of proton-bound water clusters at atmospheric pressure comprises very rarely more than nine ligands.[148] In the

presented setup, no heating, declustering potential or collision zone exists downstream the inlet, whereas on other vacuum transfer systems the partition of unreactive higher mass clusters would be less (as shown in Fig. 5.2).

Going into more detail, a direct comparison of the individual spectrometric responses indicates that for each of the applied plasma gases a gain in detected ion current was observed toward higher flow rates. As can be seen, this increase is especially pronounced for the protonated water cluster ions. At moderate flow rates, starting around 0.3 $\mathrm{L\,min^{-1}}$, the signal increase follows a linear behavior, until at approximately 1.0 $\mathrm{L\,min^{-1}}$, the signal enhancement levels off, with roughly two orders of magnitude higher signal intensity. The overall extent of the signal increase was not found to depend on the gas type. However, in case of the noble gas argon (see Fig. 6.10c), the use of higher flow rates (> 1.2 $\mathrm{L\,min^{-1}}$) results in a significant decrease of the extracted signal intensity of $[(H_2O)_2H]^+$.

This drop in signal intensity might be caused by a pronounced change in the gas phase composition (increasing argon concentration, supplanting atmospheric constituents), and thus an augmented population of the long-lived metastable states of argon. As has been discussed for the Ar-DBD (see Chapter 2), the excitation into these Rydberg states acts as an energy sink. The low-lying energetic states of $Ar_m{}^*$ do not carry enough energy to sufficiently ionize N_2, O_2, or H_2O. Accordingly, the generation of protonated water clusters as potential chemical ionization reagents is hindered, which results in a completely different excited state chemistry.[124,169] Nonetheless, in case of the present setup, the formation of $[(H_2O)_nH]^+$ was not completely quenched upon the use of a higher argon flux. This result is most likely due to the following reasons: (1) the difference in ion source geometry. In contrast to most electrically driven plasmas in which the gaseous breakdown is initiated in an enclosed discharge cell, the airborne laser-spark is operated in the open laboratory environment. Thus, still a substantial amount of atmospheric constituents should be present in the close plasma vicinity to form $[(H_2O)_nH]^+$.

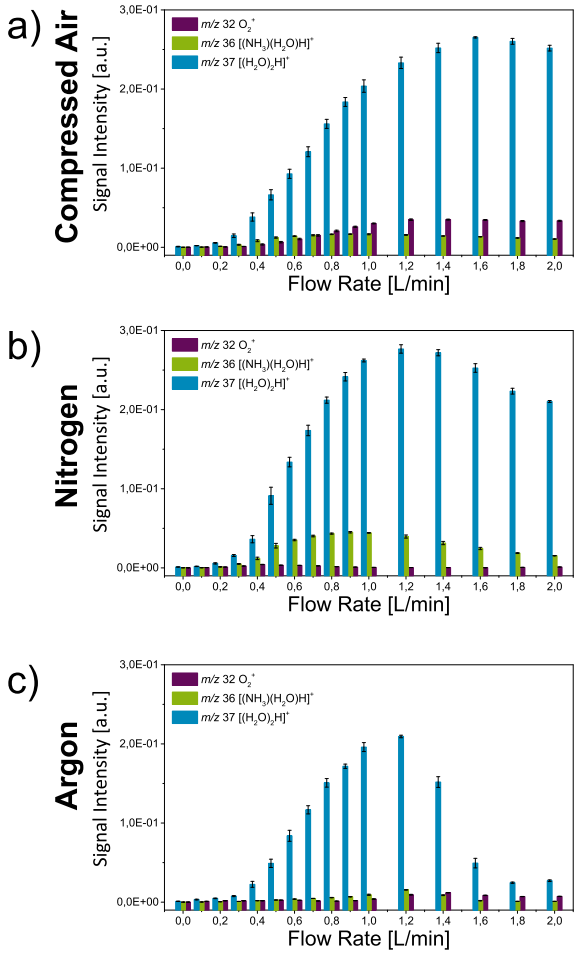

Figure 6.10: Flow-dependent reagent-ion formation of the airborne laser-spark ion source including the precursor ions O_2^+ at m/z 32, the ammonium water cluster $[(NH_3)(H_2O)H]^+$ at m/z 36, and the proton-bound water dimer $[(H_2O)_2H]^+$ at m/z 37. To replenish the former plasma zone either (a) compressed air, (b) dry nitrogen, or (c) argon were applied. Each data point depicts the sum of 400 subsequent mass spectra, acquired over 60 s.

(2) Despite the absence of N_2^+, electronically excited Ar and the highly energetic argon dimer provide enough energy to directly ionize H_2O. The presence of both species has been confirmed in the previous spectroscopic characterization experiments, however, their exact quantity has not been determined.

In contrast, the absolute increase of the hydrated ammonia cluster ion $[(NH_3)(H_2O)H]^+$ and the charge transfer carrier $O_2{}^+$ are much weaker, but can be found to peak around the same flow value. As can be expected, the addition of compressed air yielded in a more pronounced formation of $O_2{}^+$ than $[(NH_3)(H_2O)H]^+$ toward higher flow rates, while in case of dry nitrogen these signals behaved vice versa. These findings correlate well with the emission spectra shown in Fig. 6.2 and, again, provide supporting evidence for an *in-situ* formation of NH_3 out of the surrounding ubiquitous N_2 and H_2O.

Next, an analogous set of experiments was conducted in which the introduced plasma gases were laden *via* dynamic headspace sampling with the target compounds *n*-butanol and toluene. Both analytes exhibit compound-specific chemical properties, which are reflected in their ionization behavior. As has been shown in Chapter 5, the laser-spark mass spectra of *n*-butanol are dominated by two different analyte-containing signal progressions yielding major abundant ion peaks for $[n\mathrm{M}{+}\mathrm{H}]^+$ and minor abundant association products of the type $[n\mathrm{M}{+}\mathrm{NH_4}]^+$. In contrast, the MS analysis of toluene exhibited a preferred formation of odd-electron molecular ions $n\mathrm{M}^{\cdot+}$. The results of these measurements are summarized in Fig. 6.11, which compares the individual spectrometric performance of the various plasma gases as a function of the gas flow rate. Note the given magnification factors that were applied for visualization purposes only.

Upon the introduction of an analyte-enriched gas stream, charge transfer reactions can be followed between the reagent-ions and the neutral analyte molecules. As a consequence, a strong decrease of the initial charge carriers, accompanied by an increase of the respective analyte signal, occurs. In consistency with the above-said, for the polar test compound *n*-butanol, a proton transfer ionization is observed as the preferred reaction channel. An increasing flow rate of all tested plasma gases results in an increment of the $[n\mathrm{M}{+}\mathrm{H}]^+$ abundance. However, a closer inspection of the individual spectrometric responses as well indicates these species to respond to the addition of moist compressed air stronger than on dry nitrogen and argon. Similar trends are observed for the formation

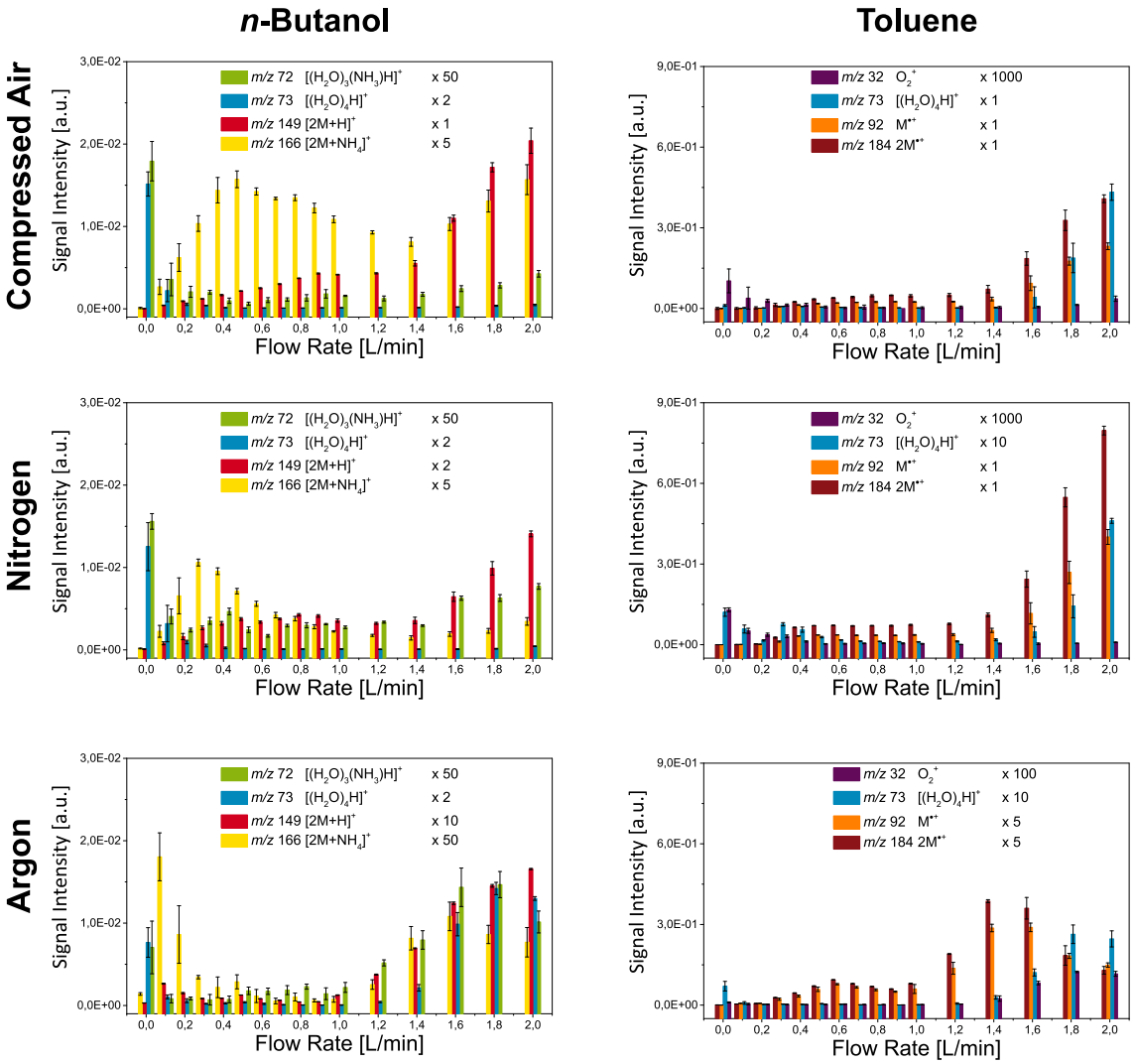

Figure 6.11: Flow-dependent ionization yields of *n*-butanol and toluene. Different carrier gases, including compressed air, dry N_2, and argon were used. Each data point depicts the sum of 400 subsequent mass spectra, acquired over 60 s. Magnification factors are arbitrary and for visualization purposes only.

of the minor abundant association products of the type $[n\mathrm{M}{+}\mathrm{NH_4}]^+$. Since the generation of ammonia is proposed out of atmospheric N_2 and H_2O, the application of compressed air or N_2 exhibited higher signal intensities for the respective species than argon. Another particularly striking feature is the fact that the butanol-containing ion clusters exhibit a bimodal distribution upon the addition of compressed air and N_2. When increasing the

gas flow, a local maximum below 1 L min^{-1} becomes apparent, followed by the global increase toward higher flux. In between these two maxima, an increasing gas flow correlates to either a stagnation (see *m/z* 149 $[2M+H]^+$) or even a temporary decrease in ion signal (see *m/z* 166 $[2M+NH_4]^+$). The exact reason for this behavior remains unclear since none of the depicted ion channels can be seen to compensate for this decrease. At first sight, this effect correlates well with the decrease in humidity along the tested plasma gases. However, without further supporting evidence valid conclusions cannot be drawn.

In case of toluene, the formation of odd-electron molecular ions $nM^{\cdot+}$ exhibits a similar flow dependence and increases in the presence of an additional gas stream. Out of this set of experiments, the total enhancement was found to be the strongest upon the addition of dry N_2, followed by compressed air and argon. The most likely mechanisms for the observed formation of $nM^{\cdot+}$ are charge transfer ionization, photoionization, and electron impact ionization. All of the above are feasible due to the higher number density of excited species when a gas stream is applied, the enhanced self-emission of the hot plasma core with wavelengths short enough for single-photon ionization, and the high density of free electrons. Another outcome of the toluene screening experiments can be derived when comparing the individual extracted signal intensities of $[(H_2O)_4H]^+$ shown on the left and on the right column of Fig. 6.11. Depending on the presence of atmospheric H_2O, the formation of the radical cation dimer of toluene goes along with a rise in signal intensity for $[(H_2O)_nH]^+$. This process is commonly exploited in dopant-assisted atmospheric pressure photoionization (APPI)[337] and can be rationalized by a cascade of complex closely coupled reactions and equilibria that result in the formation of an ion-bound cluster between primary toluene ions and the matrix compound water. The latter cluster species are known to undergo extremely fast intracluster chemistry, followed by a decomposition of the initial cluster network to the corresponding neutral radical and a protonated water cluster.[338] Accordingly, the results indicate that it could be also useful to add a dopant in future MS experiments to enhance the ionization efficiency and selectivity of the laser-spark ionization scheme, as observed in dopant-assisted APPI.[337]

The observed signal increase for both test compounds is mainly attributed to a growing analyte concentration in the gas phase, in combination with an observed increase of the earlier formed reactive charge carriers. An augmentation merely by an improved fluid-dynamic guiding into the inlet is unlikely, given the reactive species velocities derived from Fig. 6.6. To further rule out the relative gas velocity toward the MS inlet as the main cause for the signal increase, in an additional experiment the streaming gas capillary was aligned perpendicular to the atmospheric pressure interface. This change in geometry merely resulted in a signal decrease of factor two. In comparison, the acquired overall signal intensities by axial streaming were found to result in a two orders of magnitude increase. The most plausible reason is, therefore, the replenishing of the plasma volume, prior rarefied by the preceding plasma. Out of economic considerations, its hampered availability on in-field campaigns, and the lesser pronounced ion signal enhancement, in the following experiments argon was discarded as plasma gas.

6.3.2 Geometrical Alignment

In the first part of this chapter, the shadowgraphy imaging experiments revealed that, similar to higher energy LIPs, an asymmetric elongation of the DPSS laser-driven plasma, antiparallel to the direction of the laser beam, occurs. Recall its small dimensions of only 80 µm × 25 µm, the positioning of the microplasma relative to the inlet orifice should affect the total number of available reagent-ions, and as a consequence the ionization efficiency of the laser-spark ionization scheme. To map the reagent-ion distribution around the plasma, spatially resolved MS profiles were recorded (a) without a replenishing gas stream (referred to as static), (b) upon the addition of 2.0 $\mathrm{L\,min^{-1}}$ compressed air, and (c) 2.0 $\mathrm{L\,min^{-1}}$ dry N_2. The results are shown in Fig. 6.12. Mass spectra were recorded at different lens displacements along the z direction, to scan the plasma position with respect to the axis, defined by the gas support nozzle and the MS inlet orifice (refer to Fig. 6.1). Step size was 250 µm. Positive numbers correspond to the LIP being above the gas flow axis and negative values to the LIP below the gas flow axis, respectively. Each data point depicts the sum of 400 consecutive mass spectra, acquired over 60 s.

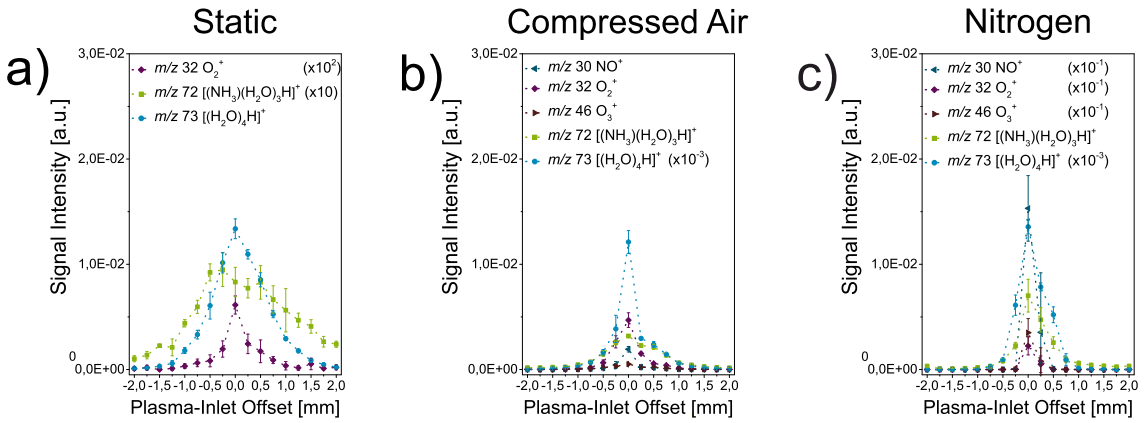

Figure 6.12: Lateral distribution of reagent-ions around the laser-driven microplasma. The LIP was ignited in ambient air, (a) without a replenishing gas stream (referred to as static), (b) upon addition of 2.0 L min^{-1} compressed air, and (c) 2.0 L min^{-1} dry N_2. Note the applied magnification factors.

For all experimental arrangements, the extracted reagent-ion profiles can be seen to follow a peak distribution, with a maximum signal response at the plasma / inlet offset of 0.0 mm. However, the individual profiles exhibit different slopes and shapes, suggesting different species lifetimes and reactivities. These results can be seen to be much more pronounced for the static LIP experiment (Fig. 6.12a), which will be briefly discussed in the following: Among the depicted ion traces, the profile for *m/z* 72, representing the hydrated ammonia cluster $[(NH_3)(H_2O)_3H]^+$, exhibits the broadest ion signal distribution along the entire investigated area and develops the same top-bottom asymmetry that has been observed earlier in the shock wave visualization experiments. Full width at half maximum for the green profile is $\approx$2.5 mm. Toward smaller displacements, the ion peaks associated with $[(H_2O)_nH]^+$ experience a strong increase in signal intensity and become the most abundant reagent-ion species. Full width at half maximum for the $[(H_2O)_4H]^+$ profile, plotted in blue, is $\approx$1.0 mm. In contrast, relevant signal intensities for the charge transfer promoting ion $O_2{}^+$ are only detected in an area of $\pm$250 µm around the inlet orifice of the mass analyzer. At the given conditions, the decreasing widths suggest the proton / charge transfer reactivity to descend according $O_2{}^+ > [(H_2O)_nH]^+ > [(NH_3)(H_2O)_nH]^+$. On top of that, the investigated lateral reagent-ion distribution reveals the dimensions of the

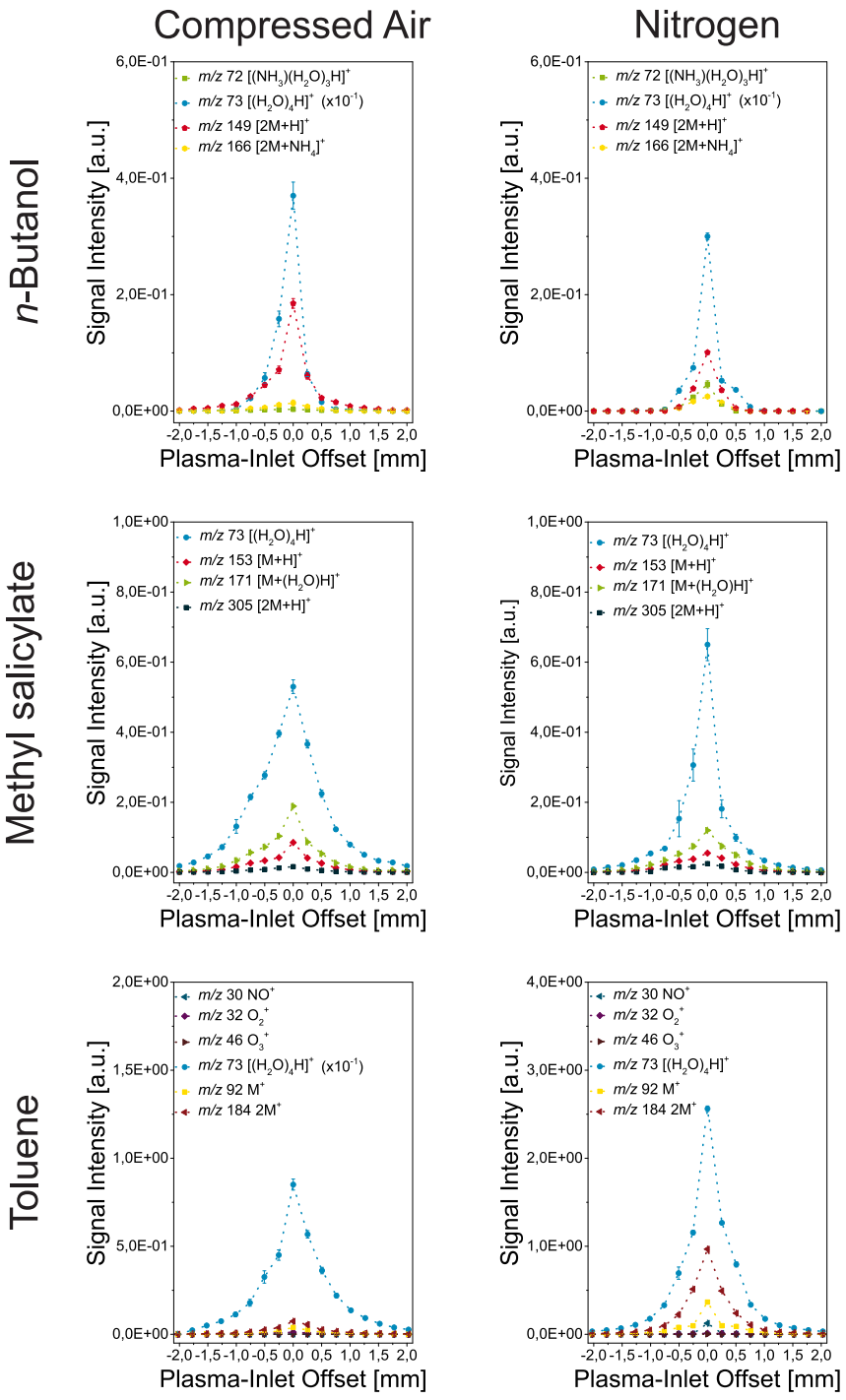

Figure 6.13: Spatially resolved ionization yields of *n*-butanol, methyl salicylate, and toluene (10 ppm, v / v, respectively). The analyte was carried off *via* dynamic headspace sampling. As the carrier gas either 2.0 L min^{-1} compressed air or dry N_2 were used. Note the applied magnification factors.

plasma affected zone. The scale of the bright plasma and the width of the O_2^+ signal distribution deviate by factor three, which is reasonable considering the solid angle between the plasma itself and the MS inlet.

Comparing the lateral ion distributions of the static setup and the application of gas streams, a similar trend is observed, regarding the maximum signal response. Despite the already discussed signal enhancement, the most striking difference is the narrowing of the $[(NH_3)(H_2O)_3H]^+$ and $[(H_2O)_4H]^+$ profiles, that appears to be most likely flow determined. Moreover, a direct comparison between the compressed air-assisted and nitrogen-assisted LIP exhibits a much higher presence of charge-transfer promoting ions, namely, NO^+, O_2^+, and O_3^+, when pure nitrogen is streamed toward the LIP origin. To clarify, whether the spatial distribution of reagent-ions also reflects in the ion traces of analyte molecules, *n*-butanol, toluene, and methyl salicylate were introduced into the gas stream to cover a preferably broad range of different analyte ion formation pathways. In addition to the already discussed portfolio of analyte ions, the formation of hydrated analyte ions of the type $[n\mathrm{M}+(H_2O)_nH]^+$ is readily observed upon the introduction of methyl salicylate. The spatially resolved ion yields can be seen in Fig. 6.13 to strongly resemble the reagent-ion profiles depicted in Fig. 6.12.

6.3.3 Reproducibility

Besides the capability of generating ions in a non-selective and highly efficient fashion, the reproducibility of signal intensity is a major criterion for any successful analytical application of the new ion source. While some forms of ionization, such as classical *in vacuo* EI, already exhibit a well controlled reproducibility that allows data to be matched to reference libraries or samples,[339] most atmospheric pressure ionization techniques have yet to achieve such level of reproducibility.[340] The variability in signal is partially caused by the individual ionization processes themselves, because of competetive ionization and ion suppression effects.[341–344] However, even for samples that are analyzed in a mode in which these effects should be negligible, spectral differences between consecutive experi-

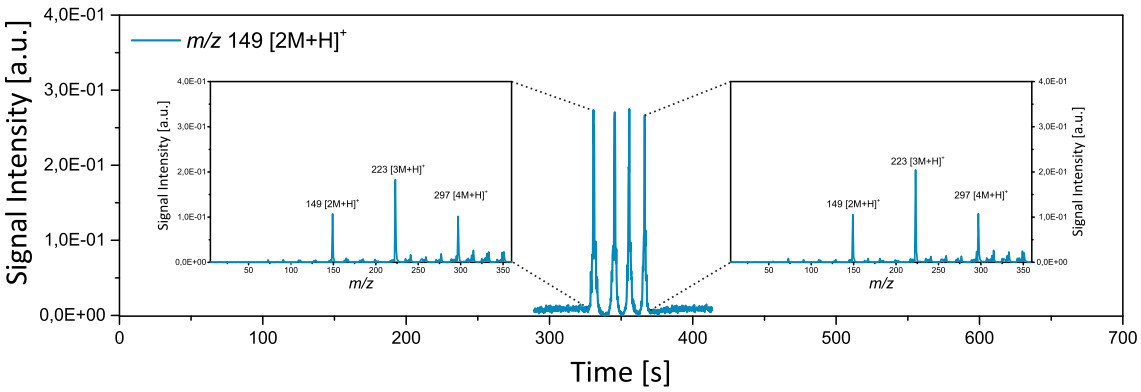

Figure 6.14: Extracted ion chronogram of the protonated *n*-butanol dimer $[2M+H]^+$ (*m/z* 149) obtained from consecutive injections of *n*-butanol (10 ppm, v / v). Compressed air (2.0 L min^{-1}) was used as the carrier gas. Each inset depicts corresponding mass spectrum of a single injection of sample.

ments are still observed.[345] This leads to the conclusion that also instrument-dependent factors have equally profound effects on the recorded spectral data. By directly comparing the classical ionization schemes and atmospheric pressure analysis, the most striking difference is that the formation of ions is not taking place in the same environment than that in which they are detected. Accordingly, ambient mass spectrometry analysis always requires the ion packages to travel through an atmospheric pressure interface in which they successively pass mutltiple ion optical elements, drastically affecting the intrinsic ion transmission characteristics.

To evaluate the reproducibility of the presented experimental setup (dynamic headspace sampling in combination with airborne laser-spark mass spectrometry), headspace aliquots of *n*-butanol were introduced consecutively into the plasma vicinity at the same mass flow. Fig. 6.14 depicts the extracted ion signal for the protonated dimer $[2M+H]^+$ at *m/z* 149. Further, integrated mass spectra corresponding each to a single injection of sample (10 ppm, v / v) are shown in the insets of Fig. 6.14. The depicted ion profile was obtained during the geometrical alignment, by changing the position of the gas capillary relative to the position of the laser-spark and the MS inlet orifice. Since only the gas capillary was moved by a motorized translational stage back and forth along axis y' (refer

to Fig. 6.1) while the LIP was constantly switched on, the recorded ion profile strongly resembles those depicted in Fig. 6.13. The descriptive statistics of the height of intensity show that the spectrometric analysis is highly repeatable, namely, the mean of four replicate injections is 0.271 with the standard deviation $\sigma = 0.003$.

6.3.4 Qualitative Comparison of APCI and LIP

In Chapter 5, the laser-spark ion source has been shown to be a promising candidate for the rapid, contactless analysis of a variety of test compounds and real life samples at ambient pressure. However, a validation of the novel ionization scheme, such as a direct comparison with an established and well-known atmospheric pressure ionization technique, has not been reported by now. Out of all plasma-based ionization schemes, APCI was chosen here, due to its equivalent localized, spot-sized point-of-charge origin. Even in dimensionality, the tip of the APCI emitter can be compared to the laser-induced microplasma. Because the two ionization sources were coupled to the same sample introduction system and mass spectrometer, their analytical performance could be directly compared. For this validation study, spearmint (*M. spicata*) and basil (*O. basilicum*) were chosen as target samples, while compressed air was used as the plasma / carrier gas. The latter was enriched with analyte-specific volatiles *via* dynamic headspace sampling. The corresponding mass spectra are depicted in Fig. 6.15.

As can be seen, the introduction of spearmint leafs results in similar mass spectra for the APCI and the LIP ionization scheme. A progression of (*R*)-(-)-carvone containing ion peaks of the type $[n\mathrm{M}+\mathrm{H}]^+$ with $n = 1$–3 is observed at *m/z* 151, 301, and 451, respectively. The signals at *m/z* 169, 187, and 205 represent the attachment of water molecules to (*R*)-(-)-carvone, yielding the association products $[\mathrm{M}+(\mathrm{H_2O})_n+\mathrm{H}]^+$. Below *m/z* 100, residual protonated water cluster ions $[(\mathrm{H_2O})_n\mathrm{H}]^+$ with $n = 2$–5 are present.

The spectrometric analysis of basil results in a progression of $[n\mathrm{M}+\mathrm{H}]^+$ with $n = 1$–3 of linalool / 1.8-cineol at *m/z* 155, 309, and 463, accompanied by less abundant water

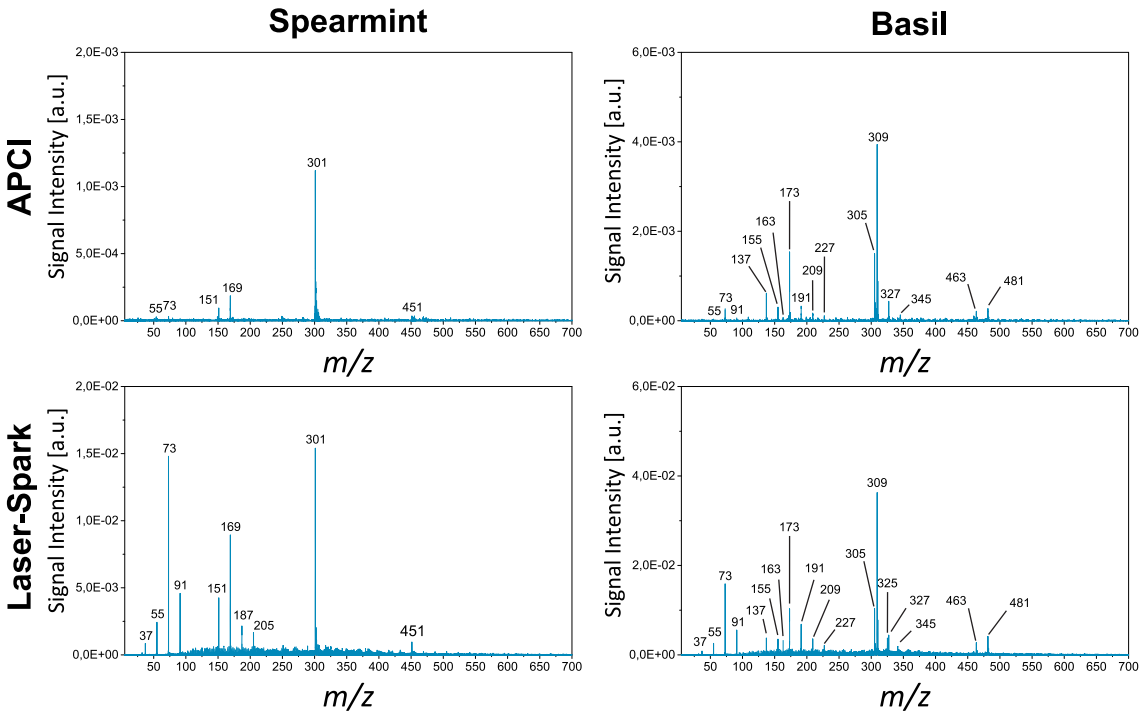

Figure 6.15: Mass spectra of spearmint and basil leafs analyzed either *via* APCI or the laser-spark ionization scheme.

adducts at m/z 173, 191, 209, 227, 327, 345, and 481. Further signals are assigned to $[M+H]^+$ and $[2M+H]^+$ of limonene at m/z 137 and m/z 273, $[M+H]^+$ and $[2M+H]^+$ of methyl cinnamate at m/z 163 and m/z 325, and $[2M+H]^+$ of citral at m/z 305. Again, the laser-spark spectrum shows a substantial amount of residual proton-bound water cluster ions up to m/z 100, compared to APCI.

Both ionization sources are based on gas phase ionization processes, creating ions at atmospheric pressure. For both target samples, the individual mass spectra were dominated by the presence of protonated molecular ions, while severe fragmentation or degradation products could not be identified. As a consequence, the laser-spark ionization scheme can be referred to as comparably soft ionization source under the given experimental conditions. Throughout, the obtained laser-spark spectra exhibited a series of ion peaks with intensities that are found to be roughly one order of magnitude higher than those for

APCI. Furthermore, these spectra still showed a substantial amount of secondary ionization agents. Their detection suggests that the initial number of reagent-ions produced by the LIP approach was much higher than with the well-established APCI ion source.

6.3.5 Quantitative Analysis of Methyl Salicylate

While the comparison study provided a direct evaluation of the laser-spark ionization scheme, still additional absolute numbers are desirable to examine its ability for quantitative analysis. Therefore, headspace samples of methyl salicylate of different concentrations were measured, without any supplemental heating of the sample reservoir. The recorded mass spectra were analyzed and a calibration curve ($y = 0.0114\,x$ - 0.046), shown in Fig. 6.16, was plotted revealing a limit of detection of 4 ppm (v / v) for methyl salicylate. This number might appear relatively large at first, but at this early stage of instrumental development, the overall performance is still limited regarding the vacuum transfer, declustering, and desolvation steps. Along the investigated concentration range, the calibration curve was found to follow a linear trend. Until now, this linearity is limited to a small concentration range above which a higher number of analyte clusters were detected with the used EL-API-HTOF MS. In the future, this number will be beneficially affected by the use of additional declustering approaches.

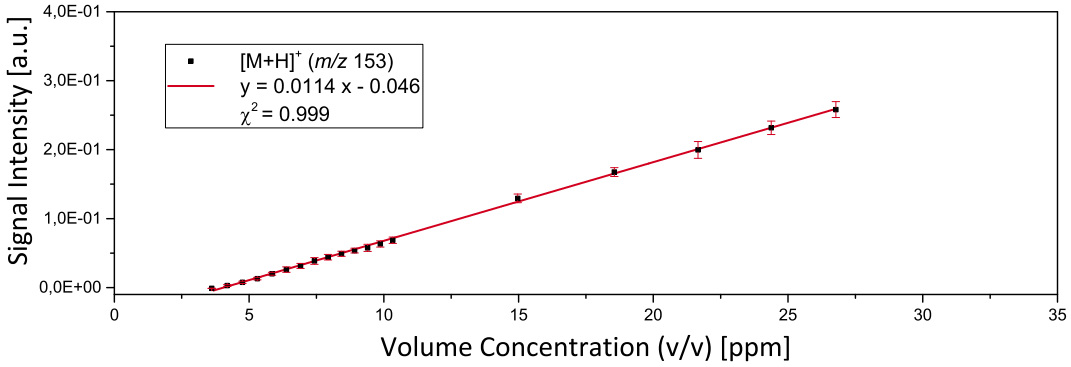

Figure 6.16: Mass spectral response of the proton-bound methyl salicylate monomer $[M+H]^+$ (m/z 153) as a function of different gas phase concentrations.

6.3.6 Conclusion II

In the second part of Chapter 6, a mass spectrometric method for the sensitive and rapid detection of gaseous samples was evaluated using the gas-assisted laser-spark ionization scheme. In contrast to the previous experimental arangement that solely employed an ambient desorption / ionization mechanism, instrumental improvements were achieved by implementing a gas phase sampling unit. The latter allowed for a simple analysis of volatile target compounds and real life samples *via* the dynamic headspace sampling technique. Spectrometric comparison experiments with various plasma gases, including compressed air, dry nitrogen, and argon, were conducted and corroborated the transient plasma behavior observed in the first part of this chapter. With an increasing gas flux, each scenario yielded a significant increase in the measured ion current, which could be mainly attributed to an accelerated reorganization of the former plasma zone, being dictated by the high repetition rate of the DPSS laser. Both the relative signal intensities of the positive mode reagent-ion population and the abundance of analyte-containing ions were found to be increased by at least one order of magnitude, compared to the "static" experiments described in Chapter 5. In terms of sensitivity, the noble gas argon exhibited the lesser pronounced ion signal enhancement for both polar and nonpolar analytes. Consequently, out of economic considerations and its hampered availability on in-field campaigns, argon was discarded as plasma gas, and compressed air was determined to be the plasma gas of choice. To further improve the sensitivity of the experimental arrangement, the positioning of the MS inlet, the microplasma, and the gas capillary relative to each other was optimized based on the maximum signal response. It was found that the system operates best in a collinear arrangement. As for the reproducibility, the spectrometric analysis of replicate injections of *n*-butanol demonstrated the system to have negligible statistical variance. The limit of detection for methyl salicylate was found to be in the lower ppm range. Eventually, due to its highly localized character, the microplasma source was directly compared to the APCI ionization scheme and showed a superior performance, resulting in an order of magnitude higher signal intensity.

7 Confinement and Enhancement of an Airborne Atmospheric Laser-Induced Plasma by an Ultrasonic Acoustic Resonator

Throughout the last decade, a growing interest has focused on the development of novel plasma-based spectrochemical sources which come with a reduced operational overhead compared to the well-established ICP. Among the broad number of promising techniques, the portfolio of plasma sources can be roughly categorized to be either electrically-driven or laser-induced. Following the latter approach, a DPSS laser-driven microplasma has been introduced that can be used either for the spectroscopic or spectrometric detection. As has been shown in Chapter 6, dynamic matter transport builds up, yielding a rarefied density regime in the plasma core, surrounded by an area of compressed matter. This rarefaction leads to a decrease in plasma intensity and analyte number density, both of which are detrimental for analytical purposes. Since the repetitive ignition of LIPs is a transient process, a restoration of the former gaseous medium by other dynamically equilibrated diffusion processes would be favorable. This chapter examines the effect of an acoustic standing wave inside an ultrasonic resonator on the performance of the airborne LIP.

Based on:
Bierstedt, A.; Panne, U.; Riedel J. *Journal of Analytical Atomic Spectrometry* **2018**, *33*, 135–140.

7.1 Introduction

Over the last three decades, plasma-based spectrochemical analysis almost entirely relied on ICP coupled to either spectroscopic or spectrometric detection. Particularly when coupled with mass spectrometry, ICP is rightly recognized as a powerful tool for multielement trace analysis of most nowadays samples, with the elements of interest being present at the ppb to ppt levels. While its analytical utility has been continuously enhanced through better source control and vastly improved detection instrumentation,[346] the basic construction of these devices has not seen major appreciable changes in more than 30 years that resulted in commercial acceptance.[347,348] Instead, improvements in sensitivity, and to a lesser extent in selectivity, have been predominantly achieved by the use of additional extraction and chromatographic techniques that provide analyte preconcentration and matrix removal / modification.[349]

Besides the vast advantages of ICP, namely, the high stability with respect to the plasma temperature and electron number density, the technique is not without shortcomings. Both plasma gas (> 15 L min^{-1} Ar) and power consumption (> 1 kW) are high and along with the need for vacuum equipment effectively tie conventional ICP instruments to the laboratory.[350] Different from standard ICP instrumentation, most fields of analytical science have already experienced an evolution toward platforms with a smaller footprint. Typical features include a lower sample consumption, lower solvent consumption (if needed at all), lower gas flux, and reduced power consumption.[351] These efforts not only result in a reduction of operational costs, enhanced sample throughput, and efficiency, but also yield in miniaturized instrumentation that can be made transportable. Thus, access to in-field campaigns is granted. Miniaturization of ICP has been proposed, however, resonance conditions of the radial frequency make the coil diameter scale with the plasma pressure. As a consequence, down-scaled plasma torches can only be operated in reduced argon pressure.[352] On top of that, ionization difficulties and problems with spectral and matrix interferences warranted the investigation of alternative plasma sources.[353]

Accordingly, there has been a great deal of interest to develop competitive spectrochemical sources that come with a lower operational overhead.[354] To satisfy these needs, a plethora of low-power, electrically-driven plasma devices have been reported by now. Among these, DART,[36] DBD / LTP,[104,105] FAPA,[133] and others[45] have been extensively used as desorption / ionization sources or served as reactive agent generators for ambient (molecular) mass spectrometry, whereas microwave plasmas, capacitively coupled plasmas, and atmospheric pressure glow discharges are typically reported in the literature for elemental MS analysis.[353,355] Beyond the specialized case of microdischarges,[356] basically only two other designs have been described for the analysis of characteristic photon emission: the electrolyte cathode discharge[114] and the liquid sampling atmospheric pressure glow discharge (APGD).[357]

All the above-mentioned devices share the common denominator of an operation at atmospheric pressure. The latter comes with several benefits (such as simplifying and shortening the analytical procedure, minimization of sample preparation, high sample throughput, analysis of samples in its native state), though admittedly at the cost of reduced sensitivity / selectivity at many instances. Best obtained limits of detection for these techniques range from the ppm to the lower ppb level. Thus, several research groups have initiated work to steadily improve their analytical performance. Over the years, parameters that were found to play a crucial role for electrically driven discharges include the identity of the discharge gas, the gas flux, the discharge current, the source geometry, the electrode configuration, as well as the overall sampling conditions (positioning, angles, distances).[117,358,359] Recently, these efforts culminated in the development of tunable devices, both based on the operation principle of an APGD. While the tunable FAPA ion source by Badal *et al.*[142] has been applied for ambient molecular mass spectrometry, the APGD of Marcus and co-workers[354] shows a remarkable analytical versatility since analytes can be determined either spectroscopically or spectrometrically with different sampling regimes, comprising a liquid phase sample introduction, a laser ablation coupling, or an ambient desorption / ionization mechanism.

Another likely promising technique has been introduced in this work, utilizing an airborne laser-driven microplasma which can be either directly analyzed by means of OES, also known under the term LIBS,[360,361] or ambient MS (see also Chapter 5 and 6). Instead of using a conventional low repetition rate flashlamp-pumped laser, this setup employs a current state-of-the-art DPSS laser. Its main improvements over traditional flashlamp-pumped systems, namely, the higher repetition rates (and thus higher duty cycles), as well as the improved power conversion efficiency, allow for the ignition of an airborne LIP at a repetition rate of 26 kHz with an optical power of ≈ 3.6 W, corresponding to an overall electrical power consumption of < 50 W.

To LIPs this brings several obvious advantages which directly result from the repetition rate and the accompanying better event statistics.[268] There is, however, an upper limit for this statistical improvement, as for ever-higher rates, the relaxation processes between individual laser pulses start to fall short. A closer inspection reveals that above a threshold repetition rate the pulsed character of the plasma introduces a dynamic equilibrium governed by shockwaves, in which the plasma region is depleted of reactive plasma gas. Within the tens of microseconds in between two subsequent plasma events, the gas pushed outside the plasma origin cannot be replenished and from the second laser pulse on, all plasma events are less intense and less bright than the first one. Upon application of a directed gas stream, it could be shown that this matter rarefaction can be compensated for by restoring the gaseous medium in the central plasma zone. However, the application of a continuous gas stream was also found to introduce a wash-out effect of the analyte concentration inside the plasma region[336] and upon higher gas fluxes of room temperature gas even to quench the plasma.

Despite the addition of a plasma gas, several other strategies have been reported within the LIBS community to alleviate the lack of sensitivity and repeatability in LIP-based analysis,[352] which are at least partially introduced by the transient nature of the plasma, the sampling process itself, and the plasma temperature.[362] Among these approaches,

technically expensive solutions, such as double-pulse LIBS[363], multiple pulse laser excitation,[352] and resonantly enhanced LIBS,[361] have become the most popular ways of accomplishing this task. Further cost-effective and more simple methods of plasma conditioning that are not directly related to the excitation laser include the manipulation of the gas atmosphere (gas composition and pressure),[364] the use of secondary ionization sources to prolong the lifetime of the plasma,[211,311,362] or the use of confinement strategies (such as spatial and magnetic confinement).[352]

Since the repetitive ignition of LIPs is a transient process in a dynamic equilibrium, a restoration of the former gaseous medium by another dynamically equilibrated diffusion process would be favorable. Such dynamic pressure equilibria at frequencies near the repetition rate of the DPSS laser (several kHz) exist inside acoustic resonators. In contrast to a steady flow of gas, a standing wave results in little or no net gas transport over large distances. Instead, the convective flux inside the acoustic resonator gets accelerated ensuring an effective short range matter exchange. In recent years, acoustic resonators have experienced a renaissance in contactless microfluidic applications[365–368] and the technique is well understood and even commercially available. In this chapter, the effect of an acoustic standing wave inside an ultrasonic resonator on the performance of an airborne LIP is tested and the beneficial influence of such an acoustic field is demonstrated for (1) an overall increase of sensitivity and (2) an effective discrimination between the signal contribution of a directionally introduced sample and the ubiquitous, diffusion-controlled background gas.

7.2 Experimental

7.2.1 Laser-Induced Plasma

By analogy with the experimental arrangements presented in Chapter 5 and 6, 532 nm laser light generated by a 26 kHz pulsed DPSS laser (Conqueror 3-LAMBDA, Nd:YVO_4, average output power: 12 W at 50 kHz, max. pulse energy: 300 µJ / pulse, pulse width: < 10 ns, Compact Laser Solutions GmbH, Berlin, Germany) was directed *via* consecutive Nd:YAG laser mirrors (NB1-K13, Thorlabs, Dachau, Germany) on an aspheric lens with a short focal length of $f = 8$ mm and a high numerical aperture of $N_A = 0.50$ (C240TME-A, Thorlabs, Dachau, Germany). Both the short focal length, as well as the large numerical aperture result in a tight focus, *i.e.*, large photon density, which was found necessary to ignite the airborne microplasma. The latter was ignited either in an external experimental arangement for spectroscopic measurements or in front of the atmospheric pressure interface of the EL-API-HTOF MS, as described in the last two chapters.

7.2.2 Standing Wave Acoustic Field Generation and Characterization

All experiments were performed using a homebuilt ultrasonic trap.[369] Up to now, this device has been used exclusively for the acoustic levitation and subsequent contactless analysis of small sample volumes.[370–372] Briefly, it consists of a USK 800 sandwich piezo transducer driven by the 200 W output signal of a MWI-400 high frequency generator at 41 kHz (MTH-Maschinenbau Technologie Herrde, Henstedt-Ulzburg, Germany), a tapered doubly coned titanium sonotrode ending in a radiating plate, and a concave shaped reflector. The sonotrode and reflector were assembled in a single axis setup and adjusted for maximum sound pressure to a resonant distance of 5 / 2 wavelengths (≈ 21 mm). Previous results indicate the resonator to be operated under acoustic saturation conditions. In contrast to levitation experiments, here, the trap axis was aligned parallel to the table top. Eventually, this setup was placed on an optical breadboard equipped with a 3D translational stage (3 × PT1/M, Thorlabs, Dachau, Germany) allowing for individual positioning between the acoustic field and the operated LIP. Visualization of the fast

pressure dynamics was performed by scanning laser Doppler vibrometry (PSV-500-3D Scanning Vibrometer, Polytec GmbH, Berlin branch, Germany).

7.2.3 Spectral Recording

The beneficient effects of acoustic confinement were evaluated by a spectral recording of the plasma species. Therefore, temporally integrated optical emission spectra, covering the wavelength range between 280–920 nm, were recorded. The experimental arrangement used is presented in Fig. 7.1. The LIP was ignited inside the gap between the sonotrode and the reflector. Single emission spectra were collected orthogonally to the beam path *via* an optical fiber placed at a distance of 10 mm above the plasma center. The other end of the optical fiber was connected to a Czerny-Turner spectrograph (Shamrock SR-303i-B, 1800 grooves / mm grating, ANDOR Technology Ltd., Belfast, UK) coupled to a CCD camera (iDus, −65 °C, ANDOR Technology Ltd., Belfast, UK). The entrance slit width was 150 µm and the acquisition time per spectrum was set to 0.1 s.

In a second set of experiments, the position of the LIP was kept constant, while the position of the acoustic field was varied in space. Thus, a spatially resolved interrogation was achieved by conducting two individual line scans: one along the propagation of the emitted soundwave and one orthogonally to this axis. Each 250 µm a fingerprint spectrum of the plasma radiation, covering a reduced wavelength range between 700–900 nm, was recorded to investigate the influence of the standing wave in the acoustic field on the emission of the plasma. Eventually, to mimic an analyte introduction, the line scan experiment along the propagation axis was repeated using the LIP ignited in a gentle argon ($\geq$ 99.999%, Linde, Berlin, Germany) stream. The latter was controlled by a mass flow controller (GFC17, Analyt-MTC GmbH, Müllheim, Germany) and fed from below through a 90° bent stainless steel capillary (i.d. 150 µm, length: 100 mm) fixed in a 1/16 in.–1/4 in. Swagelok connector. The argon flow rate was set to 0.1 L min^{-1}. Due to a strong increase in brightness, the acquisition time was reduced to 0.01 s and the entrance slit width of the spectrograph adjusted to 50 µm.

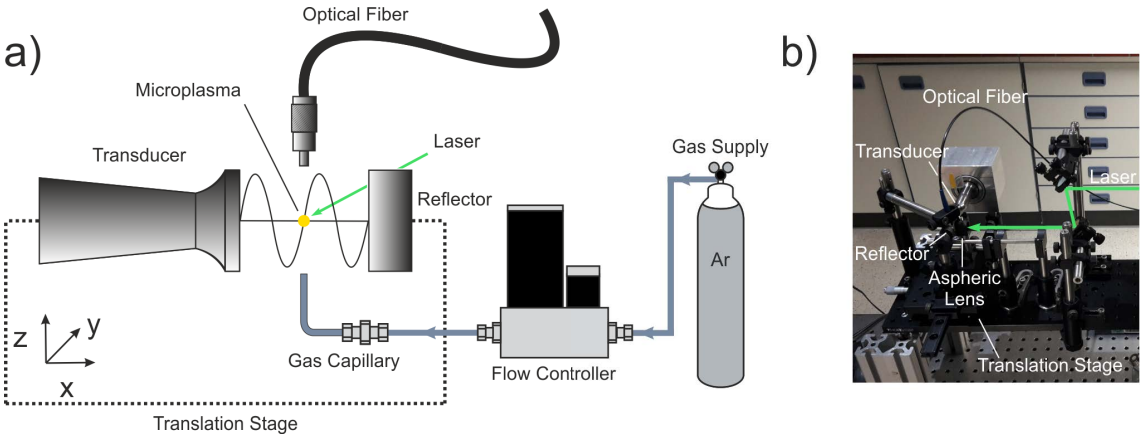

Figure 7.1: Experimental arrangement for spectroscopic measurements including the acoustic cavity, a 90° bent gas capillary to introduce the analyte, the LIP, and acquisition optics. (a) Schematic representation. (b) Top-view photograph of the real setup. The entire acoustic resonator comprising the driver, sonotrode, and reflector, at a fixed resonant distance, was mounted on a 3D translational stage and could be displaced with respect to the other fixed components.

7.2.4 Mass Spectrometry Interrogation

The number density of reagent-ions per volume is a critical parameter that determines the ionization efficiency, and thus the overall sensitivity of ambient mass spectrometry applications. To examine the effects of acoustic modulation on the positive mode reagent-ion population of the laser-spark ion source, the acoustic resonator unit was implemented into the experimental setup utilized in the preceding chapter.

A schematic representation and side-view photograph of the real setup are given in Fig. 7.2. Reagent-ion background spectra were recorded at different positions of the acoustic field with respect to the fixed LIP origin, gas capillary outlet, and MS inlet. All experiments were carried out with a customized atmospheric pressure coupled TOF MS (EL-API-HTOF MS, Tofwerk AG, Thun, Switzerland). The instrument was operated in single reflectron geometry using the positive ion mode. Integrated mass spectra were recorded with an acquisition time of 5 s and an extraction rate of 12.5 kHz. For further instrumental details see also Fig. A-2.

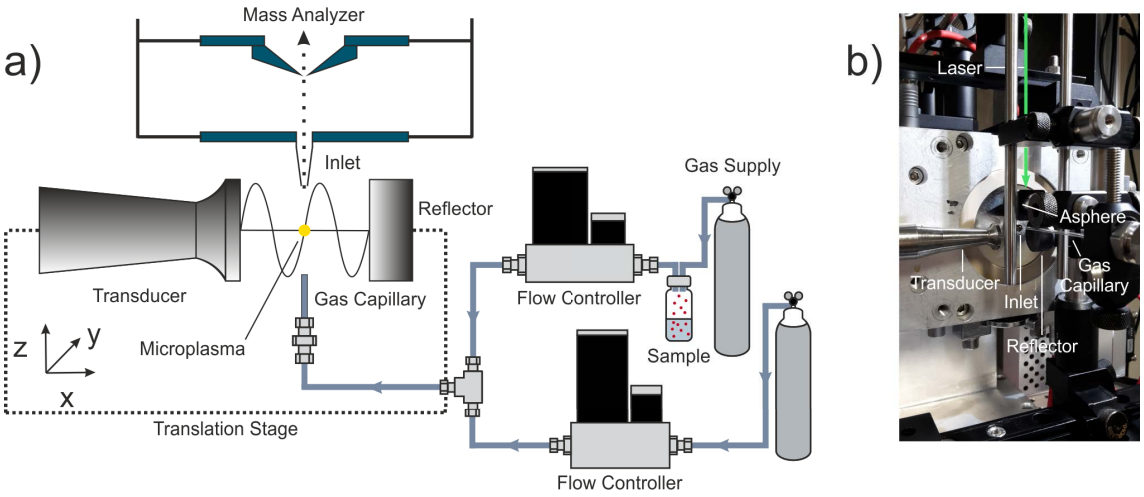

Figure 7.2: Experimental setup for spectrometric measurements comprising the acoustic cavity, a capillary coupled to a gas phase sampling system, the LIP, and a TOF MS with an atmospheric pressure interface. (a) Schematic representation. (b) Side-view photograph of the real setup. The acoustic resonator was mounted on a 3D translational stage and could be displaced with respect to the other fixed components.

7.3 Results and Discussion

7.3.1 Pressure Field Diagnostics

Constructive interference conditions inside the acoustic resonator are greatest when the reflector opposes the sonotrode at a distance of several integer half wavelengths. These resonant conditions result in the capability of acoustic levitation, since at given acoustic pressure the pressure gradient inside the sound field overcompensates for the gravity. Consequently, an optimal geometry was first verified by stable levitation of a 5 µL water droplet at the central pressure minimum. Maintaining the same geometry, the sound pressure distribution between the sonotrode and the reflector was mapped by 3D laser Doppler vibrometry. Fig. 7.3 shows a top-view photograph of the trap containing the levitated water droplet (a) and without the droplet, but superimposed with a false-color representation of the pressure field at the respective half periods of one ultrasonic cycle applied to the piezo unit of the acoustic trap in (b) and (c), respectively. The pressure distribution can be seen to develop antinodes (*i.e.*, points of maximum displacement) of

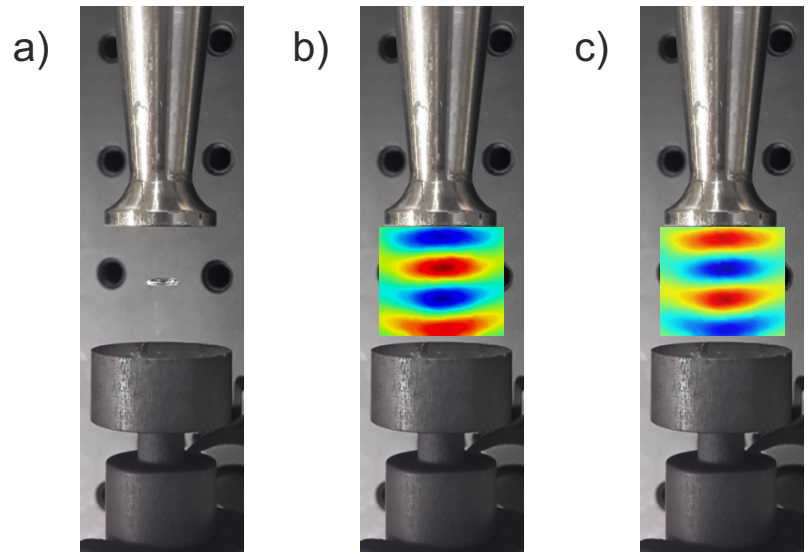

Figure 7.3: (a) Top-view photograph of the acoustic trap containing a levitated water droplet of 5 µL volume. (b and c) Visualized sound pressure distribution between the transducer (top) and the reflector (bottom) of the levitation device *via* Laser Doppler vibrometry. The pressure maps are represented in false color. Green indicates equilibrium pressure, whereas red and blue areas depict zones of acoustically induced compression or rarefaction.

high local pressure (red and blue), intersected by pressure nodes (zones of no displacement) at the unaltered pressure of the surroundings (green). These pressure maps nicely resemble earlier simulated and recorded sound field distributions inside the used resonator.[369]

7.3.2 Optical Emission Spectra of Airborne LIP

In a first set of spectroscopic experiments, the laser-induced microplasma was ignited directly in the open laboratory gas phase, while the optical emission was spectrally analyzed. The result is shown in Fig. 7.4a.

The spectrum can be seen to exhibit predominant atomic emission lines originating from O I (777.4 nm, 844.5 nm), N I (746.7 nm, 821.5 nm, 868.9 nm), and H I (656.3 nm), transitions of N II (444.5 nm, 462.8 nm, 500.1 nm) and progressions of weak emission lines assigned to N_2 ($C^3\Pi_u \rightarrow B^3\Pi_g$) and N_2^+ ($B^2\Sigma_u^+ \rightarrow X^2\Sigma_g^+$) in the spectral range

between 313–434 nm and 391–427 nm, respectively. As discussed in Chapter 6, the effect of a predominating rarefaction inside the plasma center was observable when slightly replacing the exact plasma position to a fresh volume of air by moving the alignment mirrors. Whenever a new spot was exposed to the laser focus, a series of brighter and louder plasmas was observed, rapidly followed by a relaxation to the previous conditions.

This situation changed upon the addition of a directed steady gas flow toward the plasma origin. In this case, 0.1 $\mathrm{L\,min^{-1}}$ argon was applied to the LIP, resulting in a stable enhancement of the optical brightness. This enhancement also reflected in the volume of the audible acoustic shock emitted by each LIP. Argon was chosen because it results in a speed of sound similar to air while being spectrally distinguishable. In contrast to LIBS experiments at higher laser fluences,[373] the introduction of helium effectively quenched the microplasma formation. This finding can be rationalized by the population of the non-ionic high energy metastable Rydberg states of helium.

A closer inspection of the corresponding emission spectrum (Fig. 7.4b) revealed that this increase in brilliance affects the entire spectrum. A direct comparison between Fig. 7.4a and 7.4b displays that in accordance with a roughly fivefold increase in signal intensity almost no change in the relative peak intensities occurs. The most striking difference consists of spectral contributions associated with atomic or ionic argon (labelled with the superscripts * or $^\#$ in the spectrum, respectively). In other words, a restoration of the rarefied plasma region with argon results in a larger number of excited air species. The subtle change in relative intensities between N and O lines indicates a comparable plasma temperature. These results can be rationalized by effective energy dissipation inside the plasma. The lowest electronically excited state in argon ($^2\mathrm{P}_{3/2}$) has a term energy of 11.6 eV, only slightly exceeding the ^{4}S term of oxygen at 10.8 eV, responsible for the strongest visible emission line at 777.4 nm, while all observed argon transitions in Fig. 7.4b can be assigned to include at least the second lowest $^2\mathrm{P}_{3/2}$ state at 13.1 eV, justifying the existence of the strong N I line at 821.5 nm (11.9 eV) and the population of ionic species,

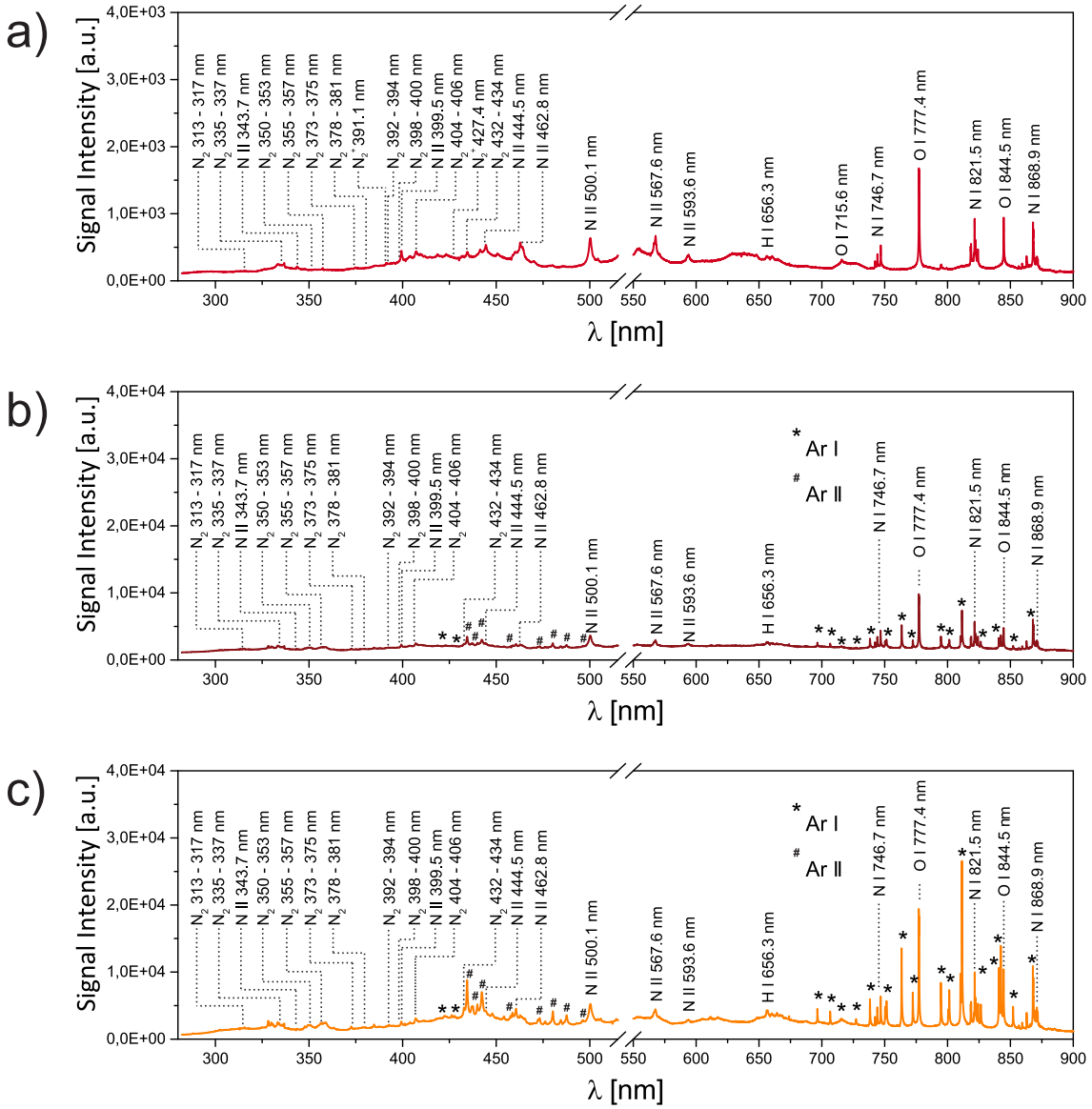

Figure 7.4: LIP emission spectra acquired (a) in the open laboratory atmosphere, and (b) upon addition of 0.1 L min^{-1} argon for compensation of the rarefaction effect inside the plasma center without applied acoustic field. (c) Recorded emission spectrum of the LIP ignited inside the acoustic field and addition of 0.1 L min^{-1} argon. Note the break in the x-axis to cut off the excitation laser wavelength.

but also explaining the absence of $N_2{}^+$ ($B^2\Sigma_u{}^+ \rightarrow X^2\Sigma_g{}^+$), given its higher ionization energy of 15.6 eV. Further, the progression of molecular nitrogen N_2 ($C^3\Pi_u \rightarrow B^3\Pi_g$; upper term energy 11.1 eV) apparently also got excited. N_2 can take up energy *via* different pathways, either as electronic energy yielding in stable highly excited dimers or as vibrational / rotational energy, eventually leading to dissociation (bond energy: 9.8 eV). Since the N / N_2 ratio appears to remain unaltered, the addition of argon more likely results in an electronic energy transfer rather than an increase in inelastic scattering with excitation of dissociative vibrational states.

Fig. 7.4c depicts the spectral emission of the LIP in the presence of the additional acoustic field. The ultrasonic resonator was aligned in a way that the LIP spatially coincided with the central pressure node. On top of an additional threefold enhancement in absolute signal intensity, now the pattern of relative intensities also changes. While upon constant argon addition, but without applied acoustic pressure, the oxygen transition at 777.4 nm results in the most dominant peak, within the sound field the highest spectral intensity can be assigned to the Ar I doublet around 811.4 nm. Obviously, the enhancement goes along with a change in the number densities of the three atomic species N, O and Ar. Two effects can potentially cause the first observation of overall higher brilliance: (1) The presence of the acoustic field induces a higher number density in the pressure antinodes (refer to Fig. 7.3). (2) Both the pressure gradient and the acoustically induced particle velocity yield in a higher convective matter exchange inside the resonator. In consequence, the two effects result in a static (1) or dynamic (2) increase in the local density of excitable matter inside the laser focus. Since the laser matter / interaction eventually forms the plasma, both effects would result in the observed behavior. The relative enrichment of argon signal contribution to the spectrum, however, supports the dynamic model.

For an unambiguous differentiation between the separate contributions of a static or a dynamic enhancement, the 3D sound field was mapped by several individual LIP-OES experiments. The lateral distance between two subsequently recorded optical spectra was

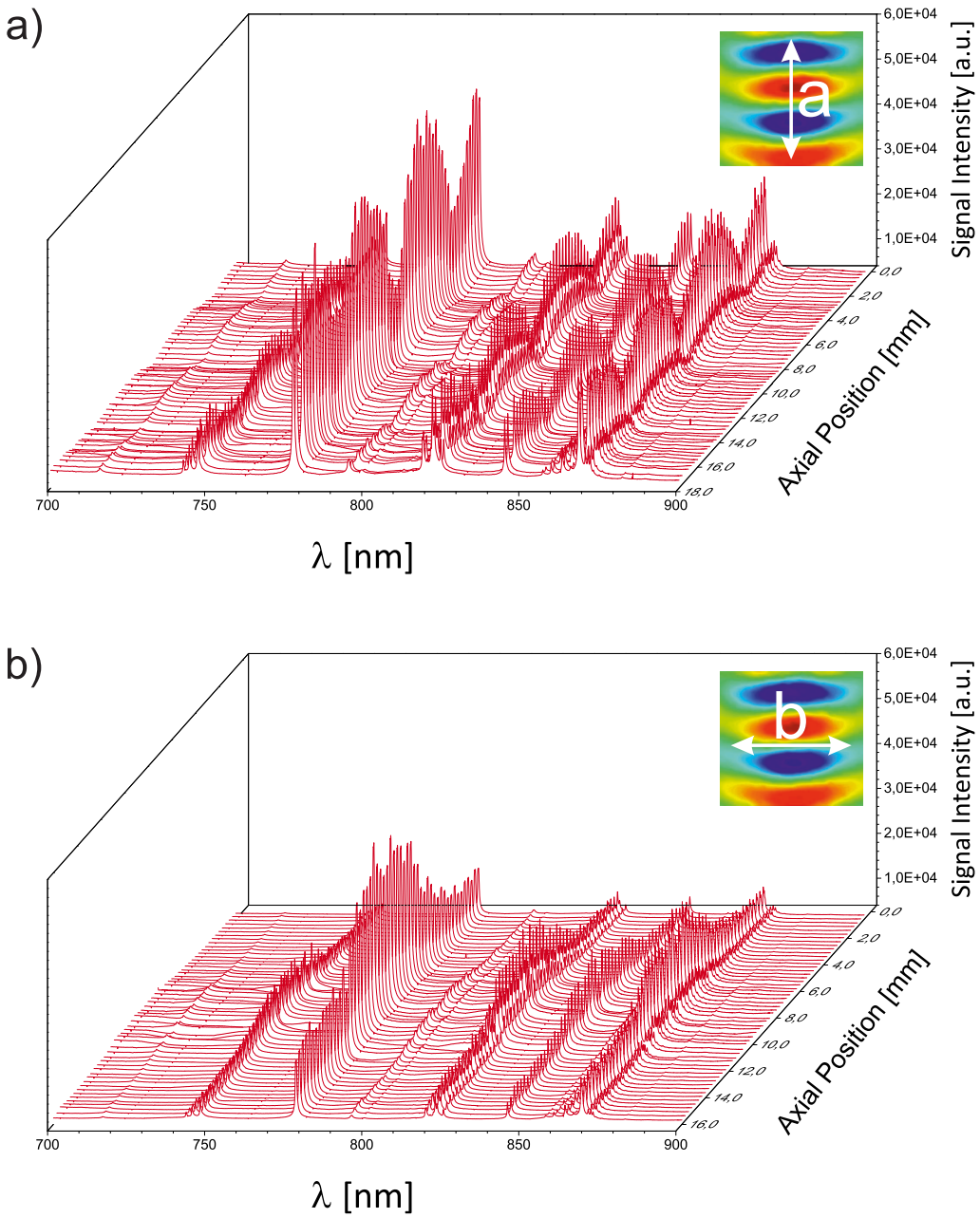

Figure 7.5: Spectrally resolved emission of the LIP inside the acoustic field screened along the two principal axes of the acoustic resonator. The integral sound fields and the respective line scans of the mapping experiment are given in each subfigure.

chosen to be 250 µm. This high resolution is possible due to the small dimension of the LIP (shown in the preceding chapter to be 80 µm × 25 µm). First, the acoustic resonator was mapped without any additional gas stream. The resulting 3D map is represented by two central cuts through the pressure field along its principal axes in Fig. 7.5. As can be seen in Fig. 7.4, the highest informational content regarding the respective N / O / Ar atomic concentrations is found in the fingerprint region between 700–900 nm.

Fig. 7.5a depicts the near-IR region of the optical spectrum along the resonator's axis of circular symmetry *a* and Fig. 7.5b along the orthogonal axis *b*. For clarity, the integral sound fields and the respective paths of the mapping experiments are depicted in an inset inside the respective subfigure. In addition, the corresponding full spectra covering the wavelength range between 280–920 nm are attached in Fig.A-7 and A-8, respectively. Following this path, the intensity of the individual emission spectra in Fig. 7.5a increases along the acoustic pressure (indicated in false color in the inset). Throughout this undulating intensity distribution, the relative intensities do not change. The same trend is observed for the orthogonal case in Fig. 7.5b. Here, similar to the pressure, the signal intensity peaks at the center and monotonically decreases toward the periphery. As a consequence, for the spectral intensity of ubiquitous static gases (as the atmospheric background signal), the static enhancement effect is responsible. The signal scales with the equilibrated pressure distribution of the standing wave. In an analytical experiment, the positions of the pressure nodes could therefore be used for an effective background suppression. The quenching of the surrounding gas is likley to stem from the overall elevated pressure within the resonator. The latter originates from the superimposed contribution of higher order pressure terms arising from acoustic saturation. The saturated conditions are corroborated by a power dependent set of individual spectral recordings shown in Fig. A-9.

In contrast to the surrounding atmospheric gases, the introduction of the analyte is typically localized and directed. This analyte could be an analyte-enriched headspace vapor, a particle-laden gas stream[374], or a sample ablated by a plasma ignited in the

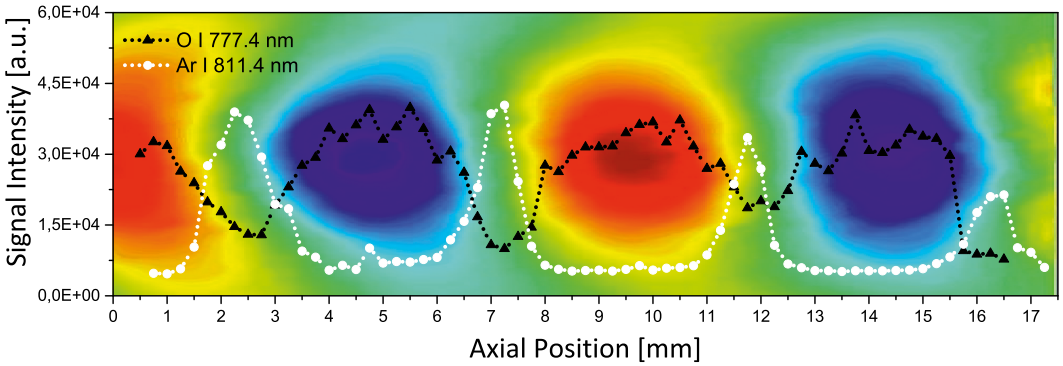

Figure 7.6: Overlay of the local pressure inside the acoustic resonator and the optical emission peak intensity along the central line scan *a*. For the color code of the false color representation of the pressure field refer to Fig. 7.3. The OES signal of O I at 777.4 nm representing the atmospheric background and the emission line at 811.4 nm of the model analyte argon are presented in black and white, respectively.

close vicinity of the sample surface. The latter geometry was proposed for the suppression of matrix effects in LIBS experiments by De Giacomo *et al.*[375] In this fashion, ablated matter would be produced in the relatively cold outer perimeter of the plasma and would need to propagate upstream to reach the high plasma core.[130] The same holds true for all suggested sample introduction schemes. To mimic either of these sample introduction geometries, in a follow-up experiment argon was used as the model analyte. Similar to the above-mentioned sampling scenarios, the argon flow was fixed with respect to the focusing lens position. Accordingly, it was always injected from the same point of origin relative to the LIP. Using this setup, a lateral line scan along the resonator was conducted, by analogy with the scan depicted in Fig. 7.5a. The resulting distributions of the peak intensity of the O I spectral line at 777.4 nm and the Ar I line at 811.4 nm are plotted against the distance from the radiating plate toward the acoustic reflector. The resulting distributions are depicted in Fig. 7.6. For a better orientation, the pressure map is superimposed onto the figure. The oxygen line resembles the above discussed behaviour of a background gas, statically trapped inside the pressure antinodes with local minima at the pressure node positions. The extrinsically applied and inwardly directed argon, on the other hand, preferentially flows toward the low pressure regions avoiding areas of already elevated

pressure. This local concentration leads to a fivefold increase of Ar spectral intensity. Since argon in this experiment represents the analyte, at these positions inside the resonator the acoustic confinement yields an increase in the signal-to-background ration of factor > 20. This drastic enhancement well justifies the relatively little additional instrumental effort.

7.3.3 Airborne Laser Spark Mass Spectrometry in Acoustic Fields

Thus far, it has been shown that the approach of igniting a laser-driven microplasma in the central pressure minimum of an ultrasonic acoustic resonator yielded in a fourfold optical signal enhancement, while at the same time background contributions were successfully suppressed. In accordance with the results shown in the last chapter, this increase in optical brightness may also result in a higher abundance of reagent-ions, which is critical to the ionization efficiency in complementary laser-spark mass spectrometry experiments. In order to investigate this hypothesis, the entire acoustic resonator unit was removed from the setup for spectral recordings and implemented into the MS experiment described in Chapter 6. By again exploiting the acoustic resonators' capability for noncontact object handling, for the first proof of principle, the central pressure minimum of the resonant acoustic field was positioned directly in the focus of the aspheric lens while being on-axis with the atmospheric pressure inlet and the exit of the gas capillary (see also Fig. 7.2). In this way, an optimal spatial overlap between the acoustic standing wave inside the ultrasonic resonator, the laser-induced microplasma, the gas phase sampling unit, and the MS inlet was granted.

Fig. 7.7 displays the intermediate positive mode ion signal responses for the laser-spark ion source operated (a) in the open laboratory environment and without repleneshing the late plasma zone, (b) upon the addition of 0.1 $\mathrm{L\,min^{-1}}$ argon, and (c) in the presence of the resonant acoustic field and addition of 0.1 $\mathrm{L\,min^{-1}}$ argon. As expected, throughout the individual scenarios the increase in optical brightness can be seen to go alongside a stepwise enhancement of detected reagent-ion signal. By comparing the most abundant ion peak in the laser-spark mass spectra $[(H_2O)_4H]^+$ at m/z 73, a roughly twofold higher

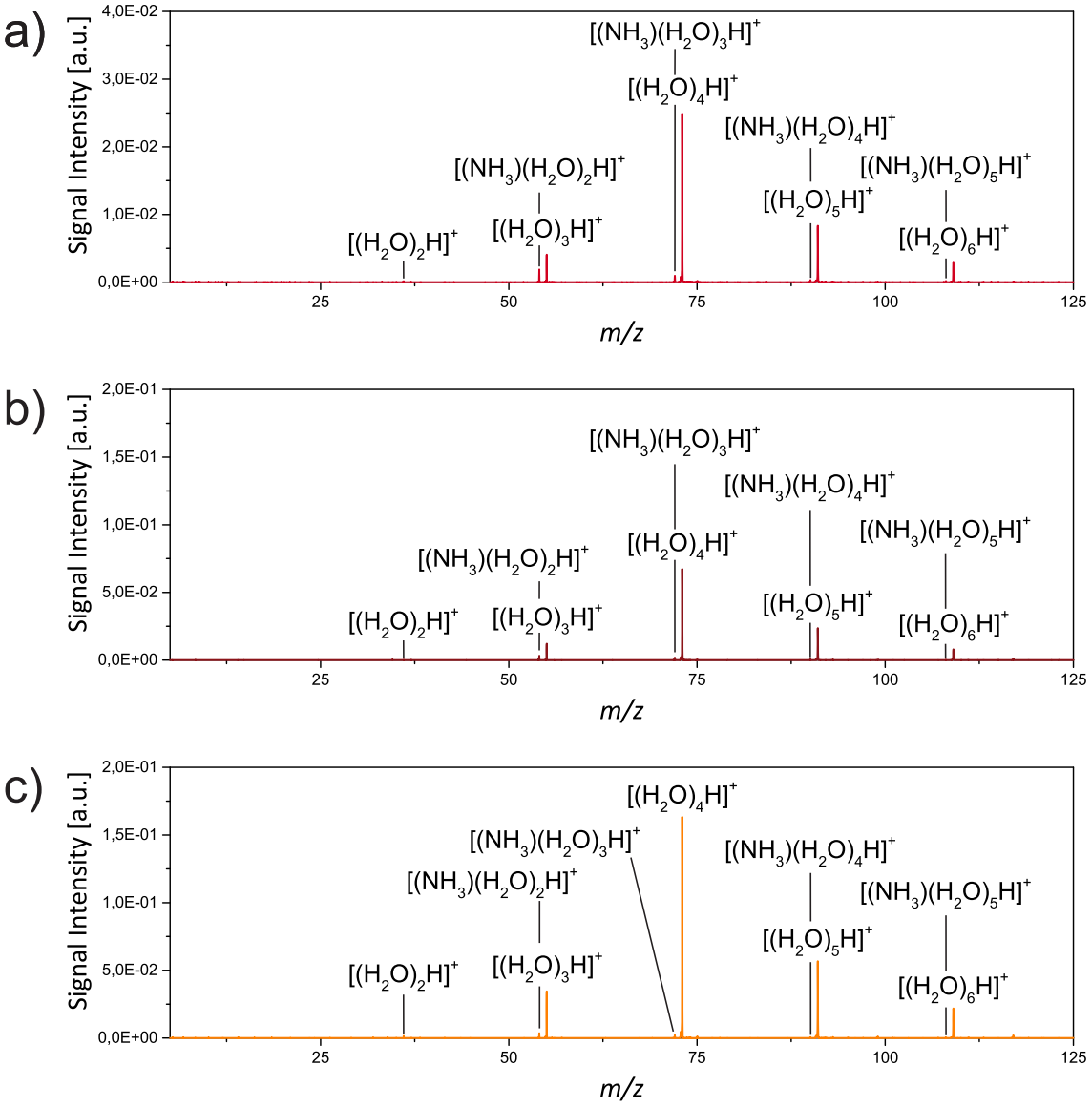

Figure 7.7: Positive mode reagent-ion background spectra for the laser-spark ion source operated in (a) the open laboratory atmosphere, and (b) upon addition of 0.1 L min^{-1} argon. The mass spectrum shown in (c) was obtained in the presence of the acoustic field and addition of 0.1 L min^{-1} argon.

signal is observed when solely applying a gentle stream of argon to alleviate the rarefaction of the former plasma center. In the presence of the resonant acoustic field, the ion signal intensity experiences an additional doubling. In contrast to the experiments shown in Chapter 6, these enhancement factors hold true for each reactant in the mass spectra, including the high-abundant proton-bound water cluster ions, as well as the minor abundant hydrated ammonium cluster ions and charge transfer promoting species. In reverse, these results imply that the presence of the resonant acoustic field does not induce a change in the overall gas composition, but the rapid alteration of the acoustic pressure contributes positively to the diffusion process toward the rarefied plasma center *via* the presence of localized pressure maxima.

In a follow-up experiment, a series of positive mode reagent-ion spectra was recorded along the resonators axis of circular symmetry a, similar to the spectroscopic line scan shown in Fig. 7.6. For this spatially resolved spectrometric interrogation, the lateral resolution between two subsequently acquired spectra was chosen to be 500 µm. To ensure comparable operational conditions, an argon flow of 0.1 $\mathrm{L\,min^{-1}}$ was applied. Out of this data set, the signal intensity of the base peak $[(H_2O)_4H]^+$ and the TIC were exemplarily plotted in dependence of the distance from the radiating plate toward the opposing reflector. The resulting distributions are shown in Fig. 7.8. As can be seen, a strongly localized and equidistant enhancement of the reagent-ion signal by a factor of four becomes readily apparent which coincides well with the pressure nodes at unaltered pressure of the surroundings. In contrast, at areas of elevated pressure, the overall signal level of the reagent-ion spectrum decreases to values that are typically obtained when the laser-spark ion source is operated without any additional enhancement or confinement strategies. In consequence, this second experiment not only confirmed the above-made hypothesis of an acoustic field-induced reagent-ion signal enhancement, but also suggests the use of an acoustic resonator for an effective spatially confined sample introduction, in which the high local pressure antinodes function as a fluid dynamic diffusion barrier.

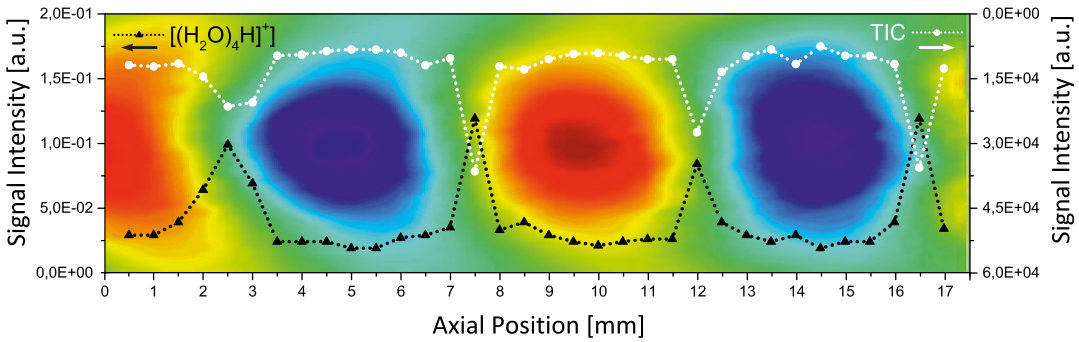

Figure 7.8: Overlay of the local pressure inside the acoustic resonator and the signal intensity of $[(H_2O)_4H]^+$ along the resonators axis of circular symmetry *a*. The measured TIC is plotted in white. Note the inverted scalebar on the right. For the color code of the false color representation of the pressure field refer to Fig. 7.3.

7.4 Conclusion

The results discussed throughout this chapter demonstrate that ambient gas phase molecules (static gas) and model analyte introduced by a directional flux (directed gas) respond differently on an applied resonant acoustic field. The standing pressure wave inside the acoustic resonator primarily acts on the static gas by forming a periodic progression of subsequent pressure nodes and antinodes. Consequently, the general concept of an isotropic pressure distribution along all dimensions in any open system is no longer valid. Given the small footprint and the contactless character of the utilized laser plasma probe, a spatially resolved interrogation of the oxygen concentration along this pressure transient could be performed. Since the absolute number density of oxygen molecules resembles the local concentration (the partial pressures of air are constant) multiplied by the absolute pressure, the trace of oxygen-related emission signal resembles this periodic sequence in absolute pressure.

Upon analyte (directed gas) addition, now the pressure antinodes (*i.e.*, the local regions of elevated pressure) act as localized barriers. According to the Navier-Stokes equations, a compressible fluid will preferentially flow along ∇p toward the nodes where pressure is minimal. This behavior leads to an additional anisotropy in gas composition. Now, not

only the pressure is unevenly distributed, but also the relative concentrations at different positions inside the resonator become spatially dependent. In terms of the directed gas, the partial pressure now has a maximum at the same regions where the absolute pressure exhibits minima. This directly translates to the finding that the model analyte argon can be detected with a twentyfold higher signal-to-background intensity in the presence of a resonant acoustic field.

The presented results show how underlying physical processes can be exploited to increase the analytical performance. This study was based on the main findings of the previous two chapters, that (1) the microplasma intensity depends on the local pressure, (2) the local element and elemental ion number density inside the plasma reflects the local concentration of the respective element in the gas phase (partial pressure), and (3) the local ion partial pressure convoluted with the local analyte concentration results in local gas phase analyte ion concentration. The demonstration of a selective enhancement in wanted elemental emission signal of the model analyte (argon) along with a synergetic suppression of unwanted signal contribution originating from ubiquitous background (oxygen) is a two-sided result. On one hand it shows vast potential for future sampling applications, on the other it concurrently corroborates the above mentioned empirical assumptions. The coincidence of the regions of highest model analyte signal in OES experiments with the best signal-to-background values for mass spectrometric reagent-ion species detection further substantiates the ion formation pathways discussed in Chapter 2. Accordingly, this chapter not only introduces a strategy for systematic sampling, but also attests a deep understanding of the matter transport properties within both the acoustic resonator and the plasma.

8 Concluding Overview

Throughout this thesis, the unique characteristics of current state-of-the-art DPSS lasers were shown to be the determining factors for the superior performance of existing analytical techniques and the development of novel analytical applications. When compared to conventional flashlamp-pumped solid-state laser systems, the advantages of the DPSS laser can be loosely categorized into infrastructural and physical benefits. In terms of the infrastructural benefits, the superior power conversion and the smaller footprint of the DPSS laser directly reflect in an enhanced compatibility, as required in hyphenated setups and portable solutions. At the same time, the longer lifetime of the pump-unit, as well as the monolithic design make them robust and ideal candidates for remote sensing applications and the use in harsh environments. More important, however, are the physical benefits that derive from these technical assets, namely, the reduced beam parameter product, the improvement in pulse-to-pulse fluctuations, and the higher repetition rate. The first allows the output of the DPSS laser to be focused onto a smaller spot, resulting in higher photon densities and a better spatial resolution in laser-based imaging experiments, while the latter two directly translate into excellent robustness and more flexible duty cycles.

Regarding laser ablation post-ionization ambient mass spectrometry, the DPSS laser was successfully used to achieve a phase transition of sample matter from the condensed phase to the gaseous phase, which was then post-ionized *via* a versatile, matrix-free, and fast DBD ion source. Based on the better spatial resolution of the focused laser spot and the higher repetition rate, an efficient laser ablation leading to clearly detectable ion

patterns could be established within fractions of a second, at a lateral resolution of several 10 µm. This combination bears the potential to overcome today's intrinsic limitations of laser-based imaging techniques. The demand posed by the ever-higher number of interrogated pixels, *i.e.*, the increased acquisition time, can be compensated by the higher repetition rates of DPSS lasers. As a result, the overall analysis time to arrive at a full image can be kept on a convenient level. Hence, although no actual ion images were recorded, this study establishes the basis for future high-speed, high-resolution ambient mass spectrometry imaging.

The successful interfacing of laser ablation post-ionization ambient mass spectrometry and Raman spectroscopy into a single analytical instrument could also be only achieved due to the unique features of the utilized DPSS laser. Its high repetition rate greatly improves the duty cycle of the laser pulse pattern, when compared to conventional flashlamp-pumped solid-state lasers. Accordingly, the laser systems used throughout this thesis were capable of generating laser pulses at repetition rates up to the order of hundreds of kHz, significantly minimizing the optical downtime. The resulting flexibility in the duty cycle allowed for the use of pulsed lasers as excitation sources for Raman spectroscopy, as an example for scattering techniques in which the response is only detectable throughout the temporal excitation window. While at first these results might seem counterintuitive, the application of DPSS lasers offers additional advantages. The most crucial one involves the much higher photon densities, which enable access to nonlinear optic phenomena. The latter lead to the generation of resonantly tunable excitation light, which translates to an increased sensitivity, since the Raman scattering cross section varies inversely with the forth power of the excitation laser wavelength. By combining these two beneficial features, the designed combination of orthogonal analytical techniques showed a superior performance, when compared to each standalone technique. As a consequence, a powerful analytical instrument was constructed that could be utilized for the biunique identification of analyte compounds in a single run, which otherwise would be unattainable.

The third topic of this thesis, that emerged from the exploitation of the characteristic DPSS laser features, comprises the development of a generally new quasi-continuous airborne LIP for ambient ionization. Since the optical densities of the individual DPSS laser pulses can be very high, above a certain value, they are sufficient to induce the breakdown of the dielectric properties of the surrounding gaseous medium, resulting in the formation of an airborne LIP. In principle, the same is possible using conventional flashlamp-pumped solid-state lasers. However, the DPSS-based laser system offers two decisive advantages: The first is an improved stability in terms of pulse-to-pulse fluctuations in the laser beam energy, leading to comparable and temporally stable laser-sparks. The second is, yet again, the higher repetition rate, which allows to increase the rate of subsequent plasma events, until a quasi-continuous airborne LIP is achieved. The latter, on its own, was shown to pave the path to a plethora of optional applications in analytical chemistry.

Its usefulness was demonstrated by employing the quasi-continuous airborne LIP for the qualitative, non-selective, rapid, and contactless MS analysis under ambient conditions. Analytes were determined with different sampling regimes, comprising either an ambient desorption / ionization mechanism or a gas phase sample introduction. In that way, intact molecular ions were detected out of a variety of gaseous, liquid and solid phase samples. The explanation for this behavior was proposed *via* a comprehensive plasma diagnostics approach in the form of a straightforward fluid-dynamical model. The results not only provide a more detailed look inside the incorporated ionization processes and the mass transport, but also explain the surprisingly low fragment-ion content and the absence of atomic species in the recorded mass spectra.

Given the beam quality factor close to unity, which results in the ability to focus the output of DPSS lasers in a small volume, the LIP was produced in microscopic spatial dimensions. Thus, a laterally resolved imaging interrogation of the surroundings was possible *via* optical emission spectroscopy. Based on this measurement capability, a novel handling strategy for ambient spectroscopic and mass spectrometric instruments was intro-

duced, exploiting the transient pressure dynamics inside an ultrasonic acoustic resonator. The presented laboratory-based proof of concepts suggest that the proposed experimental designs could be utilized for in-field analytics, where ultimately another set of DPSS laser-specific features would come into play, namely, their compactness, portability, robustness, ease of maintenance, and ease of operation.

In summary, all conducted studies represent shining examples, attesting DPSS lasers a bright future in instrumental analytics.

Bibliography

[1] Peuser, P.; Schmitt, N. P. In *Diodengepumpte Festkörperlaser*; Herziger, G., Weber, H., Eds.; Springer: Berlin, Heidelberg, 1995; pp 1–10.

[2] Maiman, T. H. *Nature* **1960**, *187*, 493–494.

[3] Singh, S. C.; Zeng, H.; Guo, C.; Cai, W. *Nanomaterials: Processing and Characterization with Lasers*; Wiley-VCH Verlag GmbH & Co. KGaA: Weinheim, 2012; pp 1–34.

[4] Huber, G.; Kränkel, C.; Petermann, K. *Journal of the Optical Society of America B* **2010**, *27*, B93–B105.

[5] Bowman, S. R. *Optical Engineering* **2012**, *52*, 021012.

[6] Kück, S. *Applied Physics B: Lasers and Optics* **2001**, *72*, 515–562.

[7] Davarcioglu, B. *International Archive of Applied Sciences and Technology* **2010**, *2*, 1–12.

[8] Zellmer, H.; Tünnermann, A. In *Lasers and Current Optical Techniques in Biology*; Palumbo, G., Pratesi, R., Hader, D.-P., Jori, G., Eds.; The Royal Society of Chemistry: London, 2004; pp 97–104.

[9] Grechin, S. G.; Nikolaev, P. P. *Quantum Electronics* **2009**, *39*, 1–17.

[10] Newman, R. *Journal of Applied Physics* **1963**, *34*, 437.

[11] Byer, R. L. *Science* **1988**, *239*, 742–747.

[12] Keyes, R. J.; Quist, T. M. *Applied Physics Letters* **1964**, *4*, 50–52.

[13] Danielmeyer, H. G.; Ostermayer, F. W. *Journal of Applied Physics* **1972**, *43*, 2911–2913.

[14] Hughes, D. W.; Barr, J. R. M. *Journal of Physics D: Applied Physics* **1992**, *25*, 563–586.

[15] Fan, T. Y. *The Lincoln Laboratory Journal* **1990**, *3*, 413–426.

[16] Giesen, A.; Hügel, H.; Voss, A.; Wittig, K.; Brauch, U.; Opower, H. *Applied Physics B: Lasers and Optics* **1994**, *58*, 365–372.

[17] Berger, J.; Hoffman, N. J.; Smith, J. J.; Welch, D. F.; Streifer, W.; Radecki, D.; Scifres, D. R. *Optics Letters* **1988**, *13*, 306–308.

[18] Thomson, J. *Philosophical Magazine Series 6* **1912**, *24*, 209–253.

[19] Longevialle, P. *Advances in Mass Spectrometry: Volume 11B*; Heyden & Son Limited: London, 1985; p 1153.

[20] Dempster, A. J. *Physical Review* **1918**, *11*, 316–325.

[21] Munson, M. S. B.; Field, F. H. *Journal of The American Chemical Society* **1966**, *88*, 2621–2630.

[22] Knewstubb, P. F.; Sugden, T. M. *Proceedings of the Royal Society of London A: Mathematical, Physical and Engineering Sciences* **1960**, *255*, 520–537.

[23] Shahin, M. M. *The Journal of Chemical Physics* **1966**, *45*, 2600–2605.

[24] Paul, W.; Reinhard, H. P.; von Zahn, U. *Zeitschrift für Physik* **1958**, *152*, 143–182.

[25] Horning, E. C.; Horning, M. G.; Carroll, D. I.; Dzidic, I.; Stillwell, R. N. *Analytical Chemistry* **1973**, *45*, 936–943.

[26] Carroll, D. I.; Dzidic, I.; Stillwell, R. N.; Haegele, K. D.; Horning, E. C. *Analytical Chemistry* **1975**, *47*, 2369–2373.

[27] Horning, E. C.; Carroll, D. I.; Dzidic, I.; Haegele, K. D.; Horning, M. G.; Stillwell, R. N. *Journal of Chromatography A* **1974**, *99*, 13–21.

[28] Fenn, J. B.; Mann, M.; Meng, C. K.; Wong, S. F.; Whitehouse, C. M. *Science* **1989**, *246*, 64–71.

[29] Dole, M.; Mack, L. L.; Hines, R. L.; Mobley, R. C.; Ferguson, L. D.; Alice, M. B. *The Journal of Chemical Physics* **1968**, *49*, 2240–2249.

[30] Mack, L. L.; Kralik, P.; Rheude, A.; Dole, M. *The Journal of Chemical Physics* **1970**, *52*, 4977–4986.

[31] Karas, M.; Bachmann, D.; Hillenkamp, F. *Analytical Chemistry* **1985**, *57*, 2935–2939.

[32] Tanaka, K.; Waki, H.; Ido, Y.; Akita, S.; Yoshida, Y.; Yoshida, T.; Matsuo, T. *Rapid Communications in Mass Spectrometry* **1988**, *2*, 151–153.

[33] Laiko, V. V.; Baldwin, M. A.; Burlingame, A. L. *Analytical Chemistry* **2000**, *72*, 652–657.

[34] Alberici, R. M.; Simas, R. C.; Sanvido, G. B.; Romão, W.; Lalli, P. M.; Benassi, M.; Cunha, I. B. S.; Eberlin, M. N. *Analytical and Bioanalytical Chemistry* **2010**, *398*, 265–294.

[35] Takats, Z.; Wiseman, J. M.; Gologan, B.; Cooks, R. G. *Science* **2004**, *306*, 471–473.

[36] Cody, R. B.; Laramée, J. A.; Durst, H. D. *Analytical Chemistry* **2005**, *77*, 2297–2302.

[37] Cooks, R. G.; Ouyang, Z.; Takats, Z.; Wiseman, J. M. *Science* **2006**, *311*, 1566–1570.

[38] Venter, A.; Nefliu, M.; Cooks, R. G. *TrAC Trends in Analytical Chemistry* **2008**, *27*, 284–290.

[39] Nemes, P.; Vertes, A. *TrAC - Trends in Analytical Chemistry* **2012**, *34*, 22–33.

[40] Takáts, Z.; Wiseman, J. M.; Cooks, R. G. *Journal of Mass Spectrometry* **2005**, *40*, 1261–1275.

[41] Cotte-Rodríguez, I.; Takáts, Z.; Talaty, N.; Chen, H.; Cooks, R. G. *Analytical Chemistry* **2005**, *77*, 6755–6764.

[42] Takáts, Z.; Cotte-Rodriguez, I.; Talaty, N.; Chen, H.; Cooks, R. G. *Chemical Communications* **2005**, 1950–1952.

[43] Cody, R. B. In *Applied electrospray mass spectrometry: Practical Spectroscopy Series Volume 32*; Pramanik, B. N., Ganguly, A. K., Gross, M. L., Eds.; Marcel Dekker, Inc.: New York, 2002; pp 1–104.

[44] Monge, M. E.; Harris, G. A.; Dwivedi, P.; Fernández, F. M. *Chemical Reviews* **2013**, *113*, 2269–2308.

[45] Ding, X.; Duan, Y. *Mass Spectrometry Reviews* **2015**, *34*, 449–473.

[46] Li, L.-P.; Feng, B.-S.; Yang, J.-W.; Chang, C.-L.; Bai, Y.; Liu, H.-W. *Analyst* **2013**, *138*, 3097–3103.

[47] Correa, D. N.; Santos, J. M.; Eberlin, L. S.; Eberlin, M. N.; Teunissen, S. F. *Analytical Chemistry* **2016**, *88*, 2515–2526.

[48] Wiley, J. S.; Shelley, J. T.; Cooks, R. G. *Analytical Chemistry* **2013**, *85*, 6545–6552.

[49] Mulligan, C. C.; Talaty, N.; Cooks, R. G. *Chemical Communications* **2006**, 1709–1711.

[50] Monge, M. E.; Fernandez, F. M. In *Ambient Ionization Mass Spectrometry (New Developments in Mass Spectrometry)*; Domin, M., Cody, R., Eds.; The Royal Society of Chemistry: London, 2015; pp 1–22.

[51] Chen, H.; Gamez, G.; Zenobi, R. *Journal of The American Society for Mass Spectrometry* **2009**, *20*, 1947–1963.

[52] Harris, G. A.; Galhena, A. S.; Fern, F. M. *Analytical Chemistry* **2011**, *83*, 4508–4538.

[53] Van Berkel, G. J.; Pasilis, S. P.; Ovchinnikova, O. *Journal of Mass Spectrometry* **2008**, *43*, 1161–1180.

[54] Huang, M. Z.; Cheng, S. C.; Cho, Y. T.; Shiea, J. *Analytica Chimica Acta* **2011**, *702*, 1–15.

[55] Javanshad, R.; Venter, A. R. *Analytical Methods* **2017**, *9*, 4896–4907.

[56] Raman, C. V.; Krishnan, K. S. *Nature* **1928**, *121*, 501–502.

[57] Landsberg, G.; Mandelstam, L. *Die Naturwissenschaften* **1928**, *16*, 557–558.

[58] Smekal, A. *Die Naturwissenschaften* **1923**, *11*, 873–875.

[59] Larkin, P. *Infrared and Raman spectroscopy, Principles and Spectral Interpretation*; Elsevier: Waltham, MA, 2011.

[60] Ferraro, J. R.; Nakamoto, K.; Brown, C. W. *Introductory Raman Spectroscopy*, 2nd ed.; Elsevier: Waltham, MA, 2003.

[61] Kneipp, K.; Kneipp, H.; Itzkan, I.; Dasari, R. R.; Feld, M. S. *Chemical Reviews* **1999**, *99*, 2957–2976.

[62] Long, D. A. *The Raman effect: a unified treatment of the theory of Raman scattering by molecules.*; John Wiley & Sons Ltd: Chichester, 2002.

[63] Fan, F.; Feng, Z.; Li, C. *Chemical Society Reviews* **2010**, *39*, 4794–4801.

[64] Rassat, S. D.; Davis, E. J. *Applied Spectroscopy* **1994**, *48*, 1498–1505.

[65] Robert, B. *Photosynthesis Research* **2009**, *101*, 147–155.

[66] Fleischmann, M.; Hendra, P. J.; McQuillan, A. J. *Chemical Physics Letters* **1974**, *26*, 163–166.

[67] Petry, R.; Schmitt, M.; Popp, J. *Chemphyschem: a European journal of chemical physics and physical chemistry* **2003**, *4*, 14–30.

[68] Kneipp, K.; Wang, Y.; Kneipp, H.; Perelman, L. T.; Itzkan, I.; Dasari, R. R.; Feld, M. S. *Physical Review Letters* **1997**, *78*, 1667–1670.

[69] Kneipp, J.; Kneipp, H.; Kneipp, K. *Chemical Society Reviews* **2008**, *37*, 1052–1060.

[70] Asher, S. A.; Johnson, C. R. *Science* **1984**, *225*, 311–313.

[71] Asher, S. A. *Analytical Chemistry* **1993**, *65*.

[72] Bowie, B. T.; Chase, D. B.; Griffiths, P. R. *Applied Spectroscopy* **2000**, *54*, 200A–207A.

[73] IUPAC, In *IUPAC. Compendium of Chemical Terminology*, 2nd ed.; Mc Naught, A., Wilkinson, A., Eds.; Blackwell Scientific Publications: Oxford (1997). XML online corrected version: http://goldbook.iupac.org (2006-) created by Nic, M.; Jirat, J.; Kosata, B.; updates compiled by Jenkins, A. ISBN 0-9678550-9-8. https://doi.org/10.1351/goldbook.

[74] Langmuir, I. *Proceedings of the National Academy of Sciences* **1928**, *14*, 627–637.

[75] Bogaerts, A.; Neyts, E.; Gijbels, R.; Van der Mullen, J. *Spectrochimica Acta Part B: Atomic Spectroscopy* **2002**, *57*, 609–658.

[76] Britun, N.; Minea, T.; Konstantinidis, S.; Snyders, R. *Journal of Physics D: Applied Physics* **2014**, *47*, 224001.

[77] Amorim, J.; Baravian, G.; Jolly, J. *Journal of Physics D: Applied Physics* **2000**, *33*, R51.

[78] Heywood, M. S.; Taylor, N.; Farnsworth, P. B. *Analytical Chemistry* **2011**, *83*, 6493–6499.

[79] Miles, R. B.; Lempert, W. R.; Forkey, J. N. *Measurement Science and Technology* **2001**, *12*, R33.

[80] Chen, S. Y.; Maksimchuk, A.; Umstadter, D. *Nature* **1998**, *396*, 653–655.

[81] Villagran-Muniz, M.; Sobral, H.; Camps, E. *IEEE Transactions on Plasma Science* **2001**, *29*, 613–616.

[82] Bak, M. S.; Wermer, L.; Im, S.-k. *Journal of Physics D: Applied Physics* **2015**, *48*, 485203.

[83] Langmuir, I. *Physical Review* **1929**, *33*, 954–989.

[84] Fantz, U. *Plasma Sources Science and Technology* **2006**, *15*, 137–147.

[85] Fraunhofer, J. *Annalen der Physik* **1817**, *56*, 264–313.

[86] Ellis, W. C.; Spencer, R. L.; Reininger, C.; Farnsworth, P. B. *J. Anal. At. Spectrom.* **2017**, *32*, 2407–2415.

[87] Wagner, H.-E.; Brandenburg, R.; Kozlov, K.; Sonnenfeld, a.; Michel, P.; Behnke, J. *Vacuum* **2003**, *71*, 417–436.

[88] Shelley, J. T.; Stindt, A.; Riedel, J.; Engelhard, C. *Journal of Analytical Atomic Spectrometry* **2014**, *29*, 359–366.

[89] Bierstedt, A.; Panne, U.; Rurack, K.; Riedel, J. *Journal of Analytical Atomic Spectrometry* **2015**, *30*, 2496–2506.

[90] van Dijk, J.; Kroesen, G. M. W.; Bogaerts, A. *Journal of Physics D: Applied Physics* **2009**, *42*, 190301.

[91] von Siemens, E. W. *Poggendorfs Annalen der Physik und Chemie* **1857**, *102*, 66–122.

[92] Park, G. Y.; Park, S. J.; Choi, M. Y.; Koo, I. G.; Byun, J. H.; Hong, J. W.; Sim, J. Y.; Collins, G. J.; Lee, J. K. *Plasma Sources Science and Technology* **2012**, *21*, 043001.

[93] Tendero, C.; Tixier, C.; Tristant, P.; Desmaison, J.; Leprince, P. *Spectrochimica Acta Part B: Atomic Spectroscopy* **2006**, *61*, 2–30.

[94] Laroussi, M. *IEEE Transactions on Plasma Science* **2002**, *30*, 1409–1415.

[95] Kogelschatz, U. *Plasma Physics and Controlled Fusion* **2004**, *46*, B63.

[96] Kogelschatz, U. *Plasma Chemistry and Plasma Processing* **2003**, *23*, 1–46.

[97] Liu, S.; Yu, Y.-L.; Wang, J.-H. *Journal of Analytical Atomic Spectrometry* **2017**, *32*, 2118–2126.

[98] Yu, Y.; Du, Z.; Chen, M.; Wang, J. *Angewandte Chemie International Edition* **2008**, *47*, 7909–7912.

[99] Meyer, C.; Müller, S.; Gurevich, E. L.; Franzke, J. *Analyst* **2011**, *136*, 2427–2440.

[100] Guo, C.; Tang, F.; Chen, J.; Wang, X.; Zhang, S.; Zhang, X. *Analytical and Bioanalytical Chemistry* **2014**, *407*, 2345–2364.

[101] Brandt, S.; Klute, F. D.; Schütz, A.; Franzke, J. *Analytica Chimica Acta* **2017**, *951*, 16–31.

[102] Martínez-Jarquín, S.; Winkler, R. *TrAC Trends in Analytical Chemistry* **2017**, *89*, 133–145.

[103] Chen, J.; Tang, F.; Guo, C.; Zhang, S.; Zhang, X. *Analytical Methods* **2017**, DOI: 10.1039/C7AY00965H.

[104] Na, N.; Zhao, M.; Zhang, S.; Yang, C.; Zhang, X. *Journal of The American Society for Mass Spectrometry* **2007**, *18*, 1859–1862.

[105] Harper, J. D.; Charipar, N. A.; Mulligan, C. C.; Zhang, X.; Cooks, R. G.; Ouyang, Z. *Analytical Chemistry* **2008**, *80*, 9097–9104.

[106] Ratcliffe, L. V.; Rutten, F. J. M.; Barrett, D. A.; Whitmore, T.; Seymour, D.; Greenwood, C.; Aranda-Gonzalvo, Y.; Robinson, S.; McCoustra, M. *Analytical Chemistry* **2007**, *79*, 6094–6101.

[107] Chen, L. C.; Hashimoto, Y.; Furuya, H.; Takekawa, K.; Kubota, T.; Hiraoka, K. *Rapid Communications in Mass Spectrometry* **2009**, *23*, 333–339.

[108] Chen, L. C.; Yu, Z.; Furuya, H.; Hashimoto, Y.; Takekawa, K.; Suzuki, H.; Ariyada, O.; Hiraoka, K. *Journal of Mass Spectrometry* **2010**, *45*, 861–869.

[109] Chen, L. C.; Yu, Z.; Hiraoka, K. *Analytical Methods* **2010**, *2*, 897–900.

[110] Hiraoka, K.; Ninomiya, S.; Chen, L. C.; Iwama, T.; Mandal, M. K.; Suzuki, H.; Ariyada, O.; Furuya, H.; Takekawa, K. *Analyst* **2011**, *136*, 1210–1215.

[111] Almasian, M. R.; Yang, C.; Xing, Z.; Zhang, S.; Zhang, X. *Rapid Communications in Mass Spectrometry* **2010**, *24*, 742–748.

[112] Albert, A.; Shelley, J. T.; Engelhard, C. *Analytical and Bioanalytical Chemistry* **2014**, *406*, 6111–6127.

[113] Martínez-Jarquín, S.; Winkler, R. *Rapid Communications in Mass Spectrometry* **2013**, *27*, 629–634.

[114] Cserfalvi, T.; Mezei, P. *Journal of Analytical Atomic Spectrometry* **1994**, *9*, 345–349.

[115] Chan, G. C.-Y.; Shelley, J. T.; Wiley, J. S.; Engelhard, C.; Jackson, A. U.; Cooks, R. G.; Hieftje, G. M. *Analytical Chemistry* **2011**, *83*, 3675–3686.

[116] Olenici-Craciunescu, S. B.; Michels, A.; Meyer, C.; Heming, R.; Tombrink, S.; Vautz, W.; Franzke, J. *Spectrochimica Acta Part B: Atomic Spectroscopy* **2009**, *64*, 1253–1258.

[117] Albert, A.; Engelhard, C. *Spectrochimica Acta Part B: Atomic Spectroscopy* **2015**, *105*, 109–115.

[118] Meiners, A.; Leck, M.; Abel, B. *Review of Scientific Instruments* **2010**, *81*, 113507.

[119] Chan, G. C.-Y.; Shelley, J. T.; Jackson, A. U.; Wiley, J. S.; Engelhard, C.; Cooks, R. G.; Hieftje, G. M. *Journal of Analytical Atomic Spectrometry* **2011**, *26*, 1434–1444.

[120] Olenici-Craciunescu, S. B.; Müller, S.; Michels, A.; Horvatic, V.; Vadla, C.; Franzke, J. *Spectrochimica Acta Part B: Atomic Spectroscopy* **2011**, *66*, 268–273.

[121] Lu, X.; Laroussi, M. *Journal of Applied Physics* **2005**, *98*, 023301.

[122] Abdul-Majeed, W. S.; Parada, J. H. L.; Zimmerman, W. B. *Analytical and Bioanalytical Chemistry* **2011**, *401*, 2713–2722.

[123] Wright, J. P.; Heywood, M. S.; Thurston, G. K.; Farnsworth, P. B. *Journal of The American Society for Mass Spectrometry* **2013**, *24*, 335–340.

[124] Meyer, C.; Müller, S.; Gilbert-Lopez, B.; Franzke, J. *Analytical and Bioanalytical Chemistry* **2013**, *405*, 4729–4735.

[125] Müller, S.; Krähling, T.; Veza, D.; Horvatic, V.; Vadla, C.; Franzke, J. *Spectrochimica Acta Part B: Atomic Spectroscopy* **2013**, *85*, 104–111.

[126] Klute, F. D.; Michels, A.; Schütz, A.; Vadla, C.; Horvatic, V.; Franzke, J. *Analytical Chemistry* **2016**, *88*, 4701–4705.

[127] Schütz, A.; Klute, F. D.; Brandt, S.; Liedtke, S.; Jestel, G.; Franzke, J. *Analytical Chemistry* **2016**, *88*, 5538–5541.

[128] Junninen, H.; Ehn, M.; Petäjä,; Luosujärvi, L.; Kotiaho, T.; Kostiainen, R.; Rohner, U.; Gonin, M.; Fuhrer, K.; Kulmala, M.; Worsnop, D. R. *Atmospheric Measurement Techniques* **2010**, *3*, 1039–1053.

[129] Bertram, T. H.; Kimmel, J. R.; Crisp, T. A.; Ryder, O. S.; Yatavelli, R. L. N.; Thornton, J. A.; Cubison, M. J.; Gonin, M.; Worsnop, D. R. *Atmospheric Measurement Techniques* **2011**, *4*, 1471–1479.

[130] Glaus, R.; Riedel, J.; Gornushkin, I. *Analytical Chemistry* **2015**, *87*, 10131–10137.

[131] Lu, X.; Laroussi, M. *Journal of Applied Physics* **2006**, *100*, 1–6.

[132] Xiong, Q.; Lu, X.; Liu, J.; Xian, Y.; Xiong, Z.; Zou, F.; Zou, C.; Gong, W.; Hu, J.; Chen, K.; Pei, X.; Jiang, Z.; Pan, Y. *Journal of Applied Physics* **2009**, *106*, 83302.

[133] Andrade, F. J.; Shelley, J. T.; Wetzel, W. C.; Webb, M. R.; Gamez, G.; Ray, S. J.; Hieftje, G. M. *Analytical Chemistry* **2008**, *80*, 2646–2653.

[134] Good, A.; Durden, D. A.; Kebarle, P. *The Journal of Chemical Physics* **1970**, *52*, 212–221.

[135] Shelley, J. T.; Chan, G. C.-Y.; Hieftje, G. M. *Journal of The American Society for Mass Spectrometry* **2012**, *23*, 407–417.

[136] Urabe, K.; Sakai, O.; Tachibana, K. *Journal of Physics D: Applied Physics* **2011**, *44*, 115203.

[137] Reininger, C.; Woodfield, K.; Keelor, J. D.; Kaylor, A.; Fernández, F. M.; Farnsworth, P. B. *Spectrochimica Acta Part B: Atomic Spectroscopy* **2014**, *100*, 98–104.

[138] Cody, R. B. *Analytical Chemistry* **2009**, *81*, 1101–1107.

[139] Newsome, G. A.; Ackerman, L. K.; Johnson, K. J. *Analytical Chemistry* **2014**, *86*, 11977–11980.

[140] McKay, K.; Salter, T. L.; Bowfield, A.; Walsh, J. L.; Gilmore, I. S.; Bradley, J. W. *Journal of The American Society for Mass Spectrometry* **2014**, *25*, 1528–1537.

[141] Martens, T.; Mihailova, D.; van Dijk, J.; Bogaerts, A. *Analytical Chemistry* **2009**, *81*, 9096–9108.

[142] Badal, S. P.; Michalak, S. D.; Chan, G. C.-Y.; You, Y.; Shelley, J. T. *Analytical Chemistry* **2016**, *88*, 3494–3503.

[143] Shelley, J. T.; Wiley, J. S.; Chan, G. C. Y.; Schilling, G. D.; Ray, S. J.; Hieftje, G. M. *Journal of The American Society for Mass Spectrometry* **2009**, *20*, 837–844.

[144] Andrade, F. J.; Shelley, J. T.; Wetzel, W. C.; Webb, M. R.; Gamez, G.; Ray, S. J.; Hieftje, G. M. *Analytical Chemistry* **2008**, *80*, 2654–2663.

[145] National Institute of Standards and Technology (NIST); Gaithersburg MD, U.S.A., 2018. `https://www.nist.gov/srd`.

[146] Dzidic, I.; Carroll, D. I.; Stillwell, R. N.; Horning, E. C. *Analytical Chemistry* **1976**, *48*, 1763–1768.

[147] Sunner, J.; Nicol, G.; Kebarle, P. *Analytical Chemistry* **1988**, *60*, 1300–1307.

[148] Klee, S.; Albrecht, S.; Derpmann, V.; Kersten, H.; Benter, T. *Analytical and Bioanalytical Chemistry* **2013**, *405*, 6933–6951.

[149] Searcy, J. Q.; Fenn, J. B. *The Journal of Chemical Physics* **1974**, *61*, 5282–5288.

[150] Searcy, J. Q. *The Journal of Chemical Physics* **1975**, *63*, 4114–4119.

[151] Yang, X.; Castleman, A. W. *Journal of The American Chemical Society* **1989**, *111*, 6845–6846.

[152] Symonds, J. M.; Galhena, A. S.; Fernández, F. M.; Orlando, T. M. *Analytical Chemistry* **2010**, *82*, 621–627.

[153] Blake, R. S.; Monks, P. S.; Ellis, A. M. *Chemical Reviews* **2009**, *109*, 861–896.

[154] Kawai, Y.; Yamaguchi, S.; Okada, Y.; Takeuchi, K.; Yamauchi, Y.; Ozawa, S.; Nakai, H. *Chemical Physics Letters* **2003**, *377*, 69–73.

[155] Kawai, Y.; Yamaguchi, S.; Okada, Y.; Takeuchi, K. *Journal of the Mass Spectrometry Society of Japan* **2004**, *52*, 271–276.

[156] Viggiano, A. A.; Dale, F.; Paulson, J. F. *The Journal of Chemical Physics* **1988**, *88*, 2469–2477.

[157] Midey, A. J.; Williams, S.; Arnold, S. T.; Viggiano, A. A. *The Journal of Physical Chemistry A* **2002**, *106*, 11726–11738.

[158] Adams, N. G.; Bohme, D. K.; Dunkin, D. B.; Fehsenfeld, F. C.; Ferguson, E. E. *The Journal of Chemical Physics* **1970**, *52*, 3133–3140.

[159] Liang, C. W.; Lee, Y. T.; Chen, C. H.; Wang, Y. S. *International Journal of Mass Spectrometry* **2010**, *291*, 61–66.

[160] Klee, S.; Brockhaus, A.; Wißdorf, W.; Thinius, M.; Hartmann, N.; Benter, T. *Rapid Communications in Mass Spectrometry* **2015**, *29*, 143–154.

[161] Barnett, R. N.; Landman, U. *The Journal of Physical Chemistry A* **1997**, *101*, 164–169.

[162] Mizuse, K.; Kuo, J.-L.; Fujii, A. *Chemical Science* **2011**, *2*, 868–876.

[163] Tachikawa, H.; Takada, T. *RSC Advances* **2014**, *5*, 6945–6953.

[164] Li, D.; Tian, Y.-H.; Zhao, Z.; Li, W.; Duan, Y. *Journal of Mass Spectrometry* **2015**, *50*, 388–395.

[165] Fujii, T.; Iwase, K.; Selvin, P. C. *International Journal of Mass Spectrometry* **2002**, *216*, 169–175.

[166] Bernier, M. C.; Alberici, R. M.; Keelor, J. D.; Dwivedi, P.; Zambrzycki, S. C.; Wallace, W. T.; Gazda, D. B.; Limero, T. F.; Symonds, J. M.; Orlando, T. M.; Macatangay, A.; Fernández, F. M. *Journal of The American Society for Mass Spectrometry* **2016**, *27*, 1203–1210.

[167] Brewer, L. E.; McGregor, W. K. *Physics of Fluids* **1962**, *5*, 1485–1486.

[168] Baldwin, K. *Contemporary Physics* **2005**, *46*, 105–120.

[169] Dane, A. J.; Cody, R. B. *Analyst* **2010**, *135*, 696–699.

[170] Yang, H.; Wan, D.; Song, F.; Liu, Z.; Liu, S. *Analytical Chemistry* **2013**, *85*, 1305–1309.

[171] Cody, R. B.; Dane, A. J. *Rapid Communications in Mass Spectrometry* **2016**, *30*, 1181–1189.

[172] Pérez, J. J.; Harris, G. A.; Chipuk, J. E.; Brodbelt, J. S.; Green, M. D.; Hampton, C. Y.; Fernández, F. M. *Analyst* **2010**, *135*, 712–719.

[173] Norman, M.; Hansel, A.; Wisthaler, A. *International Journal of Mass Spectrometry* **2007**, *265*, 382–387.

[174] Blake, R. S.; Wyche, K. P.; Ellis, A. M.; Monks, P. S. *International Journal of Mass Spectrometry* **2006**, *254*, 85–93.

[175] Salter, T. L.; Gilmore, I. S.; Bowfield, A.; Olabanji, O. T.; Bradley, J. W. *Analytical Chemistry* **2013**, *85*, 1675–1682.

[176] Andrade, F. J.; Wetzel, W. C.; Chan, G. C.-Y.; Webb, M. R.; Gamez, G.; Ray, S. J.; Hieftje, G. M. *Journal of Analytical Atomic Spectrometry* **2006**, *21*, 1175–1184.

[177] Yu, Y.; Du, Z.; Chen, M.; Wang, J. *Angewandte Chemie International Edition* **2008**, *47*, 7909–7912.

[178] Kratzer, J.; Mester, Z.; Sturgeon, R. E. *Spectrochimica Acta Part B: Atomic Spectroscopy* **2011**, *66*, 594–603.

[179] Kuklya, A.; Engelhard, C.; Kerpen, K.; Telgheder, U. *Journal of Analytical Atomic Spectrometry* **2016**, *31*, 1574–1581.

[180] Zhu, Z.; Chan, G. C.-Y.; Ray, S. J.; Zhang, X.; Hieftje, G. M. *Analytical Chemistry* **2008**, *80*, 8622–8627.

[181] Massines, F.; Ségur, P.; Gherardi, N.; Khamphan, C.; Ricard, A. *Surface and Coatings Technology* **2003**, *174–175*, 8–14.

[182] Paris, P.; Aints, M.; Laan, M.; Valk, F. *Journal of Physics D: Applied Physics* **2004**, *37*, 1179–1184.

[183] Paris, P.; Aints, M.; Valk, F.; Plank, T.; Haljaste, A.; Kozlov, K. V.; Wagner, H.-E. *Journal of Physics D: Applied Physics* **2005**, *38*, 3894–3899.

[184] A. Qayyum, S. Z. *Journal of Applied Physics* **2005**, *98*, 103303.

[185] Lindinger, W.; Hansel, A.; Jordan, A. *International Journal of Mass Spectrometry and Ion Processes* **1998**, *173*, 191–241.

[186] Macha, S. F.; McCarley, T. D.; Limbach, P. A. *Analytica Chimica Acta* **1999**, *397*, 235–245.

[187] Vons, V.; Creyghton, Y.; Schmidt-Ott, A. *Journal of Nanoparticle Research* **2006**, *8*, 721–728.

[188] Sugimura, N.; Furuya, A.; Yatsu, T.; Igarashi, Y.; Aoyama, R.; Izutani, C.; Yamamoto, Y.; Shibue, T. *European Journal of Mass Spectrometry* **2017**, *23*, 4–10.

[189] Haddad, R.; Sparrapan, R.; Eberlin, M. N. *Rapid Communications in Mass Spectrometry* **2006**, *20*, 2901–2905.

[190] Haapala, M.; Pól, J.; Saarela, V.; Arvola, V.; Kotiaho, T.; Ketola, R. A.; Franssila, S.; Kauppila, T. J.; Kostiainen, R. *Analytical Chemistry* **2007**, *79*, 7867–7872.

[191] Gilbert-López, B.; Schilling, M.; Ahlmann, N.; Michels, A.; Hayen, H.; Molina-Díaz, A.; García-Reyes, J. F.; Franzke, J. *Analytical Chemistry* **2013**, *85*, 3174–3182.

[192] Cheng, S.-C.; Shiea, C.; Huang, Y.-L.; Wang, C.-H.; Cho, Y.-T.; Shiea, J. *Analytical Methods* **2017**, *9*, 4924–4935.

[193] Conzemius, R. J.; Capellen, J. M. *International Journal of Mass Spectrometry and Ion Physics* **1980**, *34*, 197–271.

[194] Trim, P. J.; Djidja, M.-C.; Atkinson, S. J.; Oakes, K.; Cole, L. M.; Anderson, D. M. G.; Hart, P. J.; Francese, S.; Clench, M. R. *Analytical and Bioanalytical Chemistry* **2010**, *397*, 3409–3419.

[195] Becker, J. S.; Dietze, H. J. *Fresenius' Journal of Analytical Chemistry* **1992**, *344*, 69–86.

[196] Wu, C.; Dill, A. L.; Eberlin, L. S.; Cooks, R. G.; Ifa, D. R. *Mass Spectrometry Reviews* **2013**, *32*, 218–243.

[197] Kiss, A.; Hopfgartner, G. *Methods* **2016**, *104*, 142–153.

[198] Hillenkamp, F.; Unsöld, E.; Kaufmann, R.; Nitsche, R. *Applied Physics* **1975**, *8*, 341–348.

[199] Herzog, R. F. K.; Viehböck, F. P. *Physical Review* **1949**, *76*, 855–856.

[200] Heeren, R. M. A.; McDonnell, L. A.; Amstalden, E.; Luxembourg, S. L.; Altelaar, A. F. M.; Piersma, S. R. *Applied Surface Science* **2006**, *252*, 6827–6835.

[201] Maldonado-Torres, M.; López-Hernández, J. F.; Jiménez-Sandoval, P.; Winkler, R. *Journal of Proteomics* **2014**, *102*, 60–65.

[202] Morlock, G.; Ueda, Y. *Journal of Chromatography A* **2007**, *1143*, 243–251.

[203] Liu, Y.; Ma, X.; Lin, Z.; He, M.; Han, G.; Yang, C.; Xing, Z.; Zhang, S.; Zhang, X. *Angewandte Chemie International Edition* **2010**, *49*, 4435–4437.

[204] Laskin, J.; Heath, B. S.; Roach, P. J.; Cazares, L.; Semmes, O. J. *Analytical Chemistry* **2012**, *84*, 141–148.

[205] Kolaitis, L.; Lubman, D. M. *Analytical Chemistry* **1986**, *58*, 2137–2142.

[206] Coon, J. J.; McHale, K. J.; Harrison, W. W. *Rapid Communications in Mass Spectrometry* **2002**, *16*, 681–685.

[207] Nemes, P.; Vertes, A. *Analytical Chemistry* **2007**, *79*, 8098–8106.

[208] Shelley, J. T.; Ray, S. J.; Hieftje, G. M. *Analytical Chemistry* **2008**, *80*, 8308–8313.

[209] Galhena, A. S.; Harris, G. A.; Nyadong, L.; Murray, K. K.; Fernandez, F. M. *Analytical Chemistry* **2010**, *82*, 2178–2181.

[210] Vaikkinen, A.; Shrestha, B.; Kauppila, T. J.; Vertes, A.; Kostiainen, R. *Analytical Chemistry* **2012**, *84*, 1630–1636.

[211] Lu, Y.; Zhou, Y. S.; Qiu, W.; Huang, X.; Gao, Y.; Liu, L.; Lei, Y. T.; Zhang, T. C.; Jiang, L.; Silvain, J. F.; Lu, Y. F. *Journal of Analytical Atomic Spectrometry* **2015**, *30*, 1663–1667.

[212] Keelor, J. D.; Farnsworth, P. B.; Weber, A. L.; Abbott-Lyon, H.; Fernandez, F. M. *Journal of The American Society for Mass Spectrometry* **2016**, 1–11.

[213] Pento, A. V.; Nikiforov, S. M.; Simanovsky, Y. O.; Grechnikov, A. A.; Alimpiev, S. S. *Quantum Electronics* **2013**, *43*, 55–59.

[214] Albert, A.; Engelhard, C. *Analytical Chemistry* **2012**, *84*, 10657–10664.

[215] Prentice, B. M.; Chumbley, C. W.; Caprioli, R. M. *Journal of Mass Spectrometry* **2015**, *50*, 703–710.

[216] Moskovets, E.; Preisler, J.; Chen, H. S.; Rejtar, T.; Andreev, V.; Karger, B. L. *Analytical Chemistry* **2006**, *78*, 912–919.

[217] Loboda, A. V.; Krutchinsky, A. N.; Bromirski, M.; Ens, W.; Standing, K. G. *Rapid Communications in Mass Spectrometry* **2000**, *14*, 1047–1057.

[218] Spraggins, J. M.; Caprioli, R. M. *Journal of The American Society for Mass Spectrometry* **2011**, *22*, 1022–1031.

[219] Morrisette, E.; Goldberg, T. *NASA Technical Papers* **1978**, *1207*, 1–37.

[220] Bajic, S. Electrospray and atmospheric pressure chemical ionization mass spectrometer and ion source, 1995. `https://www.google.com/patents/DE19652021A1?cl=de`.

[221] Bruins, A. P. *Mass Spectrometry Reviews* **1991**, *10*, 53–77.

[222] Lin, B.; Sunner, J. *Journal of The American Society for Mass Spectrometry* **1994**, *5*, 873–885.

[223] Whitehouse, C. M.; Dreyer, R. N.; Yamashita, M.; Fenn, J. B. *Analytical Chemistry* **1985**, *57*, 675–679.

[224] Geromanos, S.; Freckleton, G.; Tempst, P. *Analytical Chemistry* **2000**, *72*, 777–790.

[225] El-Faramawy, A.; Siu, K. W. M.; Thomson, B. A. *Journal of The American Society for Mass Spectrometry* **2005**, *16*, 1702–1707.

[226] Schneider, B. B.; Javaheri, H.; Covey, T. R. *Rapid Communications in Mass Spectrometry* **2006**, *20*, 1538–1544.

[227] Wißdorf, W.; Müller, D.; Brachthäuser, Y.; Langner, M.; Derpmann, V.; Klopotowski, S.; Polaczek, C.; Kersten, H.; Brockmann, K.; Benter, T. *Journal of The American Society for Mass Spectrometry* **2016**, *27*, 1550–1563.

[228] Fomina, N. S.; Kretinina, A. V.; Masyukevich, S. V.; Bulovich, S. V.; Lapushkin, M. N.; Gall, L. N.; Gall, N. R. *Journal of Analytical Chemistry* **2013**, *68*, 1151–1157.

[229] Page, J. S.; Kelly, R. T.; Tang, K.; Smith, R. D. *Journal of The American Society for Mass Spectrometry* **2007**, *18*, 1582–1590.

[230] Page, J. S.; Marginean, I.; Baker, E. S.; Kelly, R. T.; Tang, K.; Smith, R. D. *Journal of The American Society for Mass Spectrometry* **2009**, *20*, 2265–2272.

[231] Pritchard, P. J. *Fox and McDonald's Introduction to Fluid Mechanics*, 8th ed.; John Wiley & Sons, Inc.: Hoboken, 2011.

[232] Krutchinsky, A. N.; Padovan, J. C.; Cohen, H.; Chait, B. T. *Journal of The American Society for Mass Spectrometry* **2015**, *26*, 649–658.

[233] Krutchinsky, A. N.; Padovan, J. C.; Cohen, H.; Chait, B. T. *Journal of The American Society for Mass Spectrometry* **2015**, *26*, 659–667.

[234] Kantrowitz, A.; Grey, J. *Review of Scientific Instruments* **1951**, *22*, 328–332.

[235] Yamashita, M.; Fenn, J. B. *The Journal of Physical Chemistry* **1984**, *88*, 4451–4459.

[236] Wang, X.; Kruis, F. E.; McMurry, P. H. *Aerosol Science and Technology* **2005**, *39*, 611–623.

[237] Wang, X.; Gidwani, A.; Girshick, S. L.; McMurry, P. H. *Aerosol Science and Technology* **2005**, *39*, 624–636.

[238] Bi, X.-X.; Ganguly, B.; Huffman, G. P.; Huggins, F. E.; Endo, M.; Eklund, P. C. *Journal of Materials Research* **1993**, *8*, 1666–1674.

[239] Heszler, P.; Elihn, K.; Boman, M.; Carlsson, J.-O. *Applied Physics A* **2000**, *70*, 613–616.

[240] Zhang, A.; Sun, H.; Wang, P.; Han, Y.; Wang, X. *The Analyst* **2012**, *137*, 293–300.

[241] Giannossa, L. C.; Acquaviva, M.; De Benedetto, G. E.; Acquafredda, P.; Laviano, R.; Mangone, A. *Analytical Methods* **2014**, *6*, 3490–3499.

[242] Ingo, G. M.; Angelini, E.; de Caro, T.; Bultrini, G. *Applied Physics A* **2004**, *79*, 171–176.

[243] Liang, Y.-Z.; Xie, P.; Chan, K. *Journal of Chromatography B* **2004**, *812*, 53–70.

[244] Ermer, J.; Vogel, M. *Biomedical Chromatography* **2000**, *14*, 373–383.

[245] Shafer, K. H.; Lucas, S. V.; Jakobsen, R. J. *Journal of Chromatographic Science* **1979**, *17*, 464–470.

[246] Hirschfeld, T. *Analytical Chemistry* **1980**, *52*, 297A–312A.

[247] Gohlke, R. S. *Analytical Chemistry* **1959**, *31*, 535–541.

[248] Hites, R. A. *Analytical Chemistry* **2016**, *88*, 6955–6961.

[249] Nafie, L. A. *Journal of Raman Spectroscopy* **2016**, *47*, 1548–1565.

[250] Köhler, M.; MacHill, S.; Salzer, R.; Krafft, C. *Analytical and Bioanalytical Chemistry* **2009**, *393*, 1513–1520.

[251] Bocklitz, T. W.; Crecelius, A. C.; Matthäus, C.; Tarcea, N.; von Eggeling, F.; Schmitt, M.; Schubert, U. S.; Popp, J. *Analytical Chemistry* **2013**, *85*, 10829–10834.

[252] Ahlf, D. R.; Masyuko, R. N.; Hummon, A. B.; Bohn, P. W. *The Analyst* **2014**, *139*, 4578–4585.

[253] Jadoul, L.; Malherbe, C.; Calligaris, D.; Longuespée, R.; Gilbert, B.; Eppe, G.; De Pauw, E. *European Journal of Lipid Science and Technology* **2014**, *116*, 1080–1086.

[254] Nevin, A.; Melia, J. L.; Osticioli, I.; Gautier, G.; Colombini, M. P. *Journal of Cultural Heritage* **2008**, *9*, 154–161.

[255] Heudt, L.; Debois, D.; Zimmerman, T. A.; Köhler, L.; Bano, F.; Partouche, F.; Duwez, A. S.; Gilbert, B.; De Pauw, E. *Forensic Science International* **2012**, *219*, 64–75.

[256] Belu, A.; Mahoney, C.; Wormuth, K. *Journal of Controlled Release* **2008**, *126*, 111–121.

[257] Li, Z.; Chu, L.-Q.; Sweedler, J. V.; Bohn, P. W. *Analytical Chemistry* **2010**, *82*, 2608–2611.

[258] Williams, C. T.; Takoudis, C. G.; Weaver, M. J. *The Journal of Physical Chemistry B* **1998**, *102*, 406–416.

[259] Williams, C. T.; Chan, H. Y. H.; Tolia, A. A.; Weaver, M. J.; Takoudis, C. G. *Industrial & Engineering Chemistry Research* **1998**, *37*, 2307–2315.

[260] Nijhuis, T. A. X.; Tinnemans, S. J.; Visser, T.; Weckhuysen, B. M. *Physical Chemistry Chemical Physics* **2003**, *5*, 4361–4365.

[261] Valero-Pedraza, M. J.; Gascón, V.; Carreón, M. A.; Leardini, F.; Ares, J. R.; Martín, Á.; Sánchez-Sánchez, M.; Banãres, M. A. *Microporous and Mesoporous Materials* **2016**, *226*, 454–465.

[262] Sutin, B. M. Dual-spectroscopy detection apparatus and method. 2014; `https://www.google.com/patents/US20140104597`.

[263] Ma, X.; Ouyang, Z. *TrAC Trends in Analytical Chemistry* **2016**, *85*, 10–19.

[264] Meher, A. K.; Chen, Y.-C. *Analytical Chemistry* **2016**, *88*, 9151–9157.

[265] Liu, J.; Wang, H.; Manicke, N. E.; Lin, J.-M.; Cooks, R. G.; Ouyang, Z. *Analytical Chemistry* **2010**, *82*, 2463–2471.

[266] Bierstedt, A.; Stindt, A.; Warschat, C.; Panne, U.; Riedel, J. *European Journal of Mass Spectrometry* **2014**, *20*, 367–374.

[267] Bierstedt, A.; Riedel, J. *Methods* **2016**, *104*, 3–10.

[268] Hoehse, M.; Gornushkin, I.; Merk, S.; Panne, U. *Journal of Analytical Atomic Spectrometry* **2011**, *26*, 414–424.

[269] Pein, B. C.; Sun, Y.; Dlott, D. D. *The Journal of Physical Chemistry B* **2013**, *117*, 10898–10904.

[270] Lippincott, E. R.; Nelson, R. D. *Spectrochimica Acta* **1958**, *10*, 307–329.

[271] Long, T. V.; Huege, F. R. *Chemical Communications* **1968**, *20*, 1239–1241.

[272] Bodenheimer, J.; Loewenthal, E.; Low, W. *Chemical Physics Letters* **1969**, *3*, 715–716.

[273] Koenig, L.; Angood, a. C. *Journal of Polymer Science* **1970**, *8*, 1787–1796.

[274] Miyazawa, T.; Fukushima, K.; Ideguchi, Y. *The Journal of Chemical Physics* **1962**, *37*, 2764–2776.

[275] Miyazawa, T.; Ideguchi, Y.; Fukushima, K. *Journal of Polymer Science* **1962**, *62*, 146–147.

[276] Samuel, A. Z.; Umapathy, S. *Polymer Journal* **2014**, *46*, 330–336.

[277] Vueba, M.; Pina, M.; Batista de Carvalho, L. *Journal of Pharmaceutical Sciences* **2008**, *97*, 845–859.

[278] Jubert, A.; Legarto, M. L.; Massa, N. E.; Tévez, L. L.; Okulik, N. B. *Journal of Molecular Structure* **2006**, *783*, 34–51.

[279] Rossi, B.; Verrocchio, P.; Viliani, G.; Mancini, I.; Guella, G.; Rigo, E.; Scarduelli, G.; Mariotto, G. *Journal of Raman Spectroscopy* **2009**, *40*, 453–458.

[280] Ferrer, I.; Thurman, E. M. *Analytical Chemistry* **2005**, *77*, 3394–3400.

[281] Zayed, M. A.; Hawash, M. F.; Fahmey, M. A.; El-Gizouli, A. M. M. *Journal of Thermal Analysis and Calorimetry* **2012**, *108*, 315–322.

[282] Wallace, J. L. *British Journal of Pharmacology* **2004**, *143*, 1–2.

[283] Manov, I.; Motanis, H.; Frumin, I.; Iancu, T. C. *Acta Pharmacologica Sinica* **2006**, *27*, 259–272.

[284] Kyriakides, M.; Maitre, L.; Stamper, B. D.; Mohar, I.; Kavanagh, T. J.; Foster, J.; Wilson, I. D.; Holmes, E.; Nelson, S. D.; Coen, M. *Archives of Toxicology* **2016**, *90*, 3073–3085.

[285] Howell, B. A.; Siler, S. Q.; Watkins, P. B. *Toxicology Letters* **2014**, *226*, 163–172.

[286] Stein, S. E. In *NIST Chemistry WebBook, NIST Standard Reference Database Number 69*; Linstrom, P. J., Mallard, W. G., Eds.; National Institute of Standards and Technology: Gaithersburg MD, U.S.A., 2017.

[287] Amado, A. M.; Azevedo, C.; Ribeiro-Claro, P. J. *Spectrochimica Acta Part A: Molecular and Biomolecular Spectroscopy* **2017**, *183*, 431–438.

[288] McGregor, L.; Rychkov, D. A.; Coster, P. L.; Day, S.; Drebushchak, V. A.; Achkasov, A. F.; Nichol, G. S.; Pulham, C. R.; Boldyreva, E. V. *CrystEngComm* **2015**, *17*, 6183–6192.

[289] Agnew, L. R.; McGlone, T.; Wheatcroft, H. P.; Robertson, A.; Parsons, A. R.; Wilson, C. C. *Crystal Growth and Design* **2017**, *17*, 2418–2427.

[290] Hannay, N. B. *Review of Scientific Instruments* **1954**, *25*, 644–648.

[291] Honig, R. E.; Woolston, J. R. *Applied Physics Letters* **1963**, *2*, 138–139.

[292] Honig, R. E. *Applied Physics Letters* **1963**, *3*, 8–11.

[293] Berkowitz, J.; Chupka, W. A. *The Journal of Chemical Physics* **1964**, *40*, 2735–2736.

[294] Lincoln, K. A. *Analytical Chemistry* **1965**, *37*, 541–543.

[295] Fenner, N. C.; Daly, N. R. *Review of Scientific Instruments* **1966**, *37*, 1068–1070.

[296] Fenner, N. C.; Daly, N. R. *Journal of Materials Science* **1968**, *3*, 259–261.

[297] Vastola, F. J.; Mumma, R. O.; Pirone, A. J. *Organic Mass Spectrometry* **1970**, *3*, 101–104.

[298] Posthumus, M. A.; Kistemaker, P. G.; Meuzelaar, H. L. C.; de Brauw, M. C. *Analytical Chemistry* **1978**, *50*, 985–991.

[299] Ban, V. S.; Knox, B. E. *International Journal of Mass Spectrometry and Ion Physics* **1969**, *3*, 131–141.

[300] Yu, Q.; Chen, L.; Huang, R.; Hang, W.; Huang, B.; Hang, W.; He, J. *TrAC Trends in Analytical Chemistry* **2009**, *28*, 1174–1185.

[301] Milán, M.; Laserna, J. J. *Spectrochimica Acta Part B: Atomic Spectroscopy* **2001**, *56*, 275–288.

[302] Dingle, T.; Griffiths, B. W.; Ruckman, J. C. *Vacuum* **1981**, *31*, 571–577.

[303] Herrmann, A.; Leutwyler, S.; Schumacher, E.; Wöste, L. *Chemical Physics Letters* **1977**, *52*, 418–425.

[304] Boesl, U.; Neusser, H. J.; Schlag, E. W. *Zeitschrift für Naturforschung A* **1978**, *33*, 1546–1548.

[305] Zandee, L.; Bernstein, R. B.; Lichtin, D. A. *The Journal of Chemical Physics* **1978**, *69*, 3427–3429.

[306] Trim, P. J.; Snel, M. F. *Methods* **2016**, *104*, 127–141.

[307] Michael, S. M.; Chien, B. M.; Lubman, D. M. *Analytical Chemistry* **1993**, *65*, 2614–2620.

[308] Russo, R. E.; Klunder, G. L.; Grant, P.; Andresen, B. D. *Applied Physics A* **1999**, *69*, S895–S897.

[309] Dawson, J. H. J.; Guilhaus, M. *Rapid Communications in Mass Spectrometry* **1989**, *3*, 155–159.

[310] Fricker, M. B.; Günther, D. In *Recent Advances in Laser Ablation ICP-MS for Archaeology*; Dussubieux, L., Golitko, M., Gratuze, B., Eds.; Springer: Berlin, Heidelberg, 2016; pp 1–19.

[311] He, X. N.; Xie, Z. Q.; Gao, Y.; Hu, W.; Guo, L. B.; Jiang, L.; Lu, Y. F. *Spectrochimica Acta Part B: Atomic Spectroscopy* **2012**, *67*, 64–73.

[312] Moshkunov, K. A.; Alimpiev, S. S.; Grechnikov, A. A.; Nikifirov, S. M.; Pento, A. V.; Simanovsky, Y. O. *Journal of Physics: Conference Series* **2014**, *558*, 012012.

[313] Noll, R. *Laser-Induced Breakdown Spectroscopy: Fundamentals and Applications*; Springer: Berlin Heidelberg, 2012.

[314] Panne, U. In *Laser in Environmental and Life Sciences: Modern Analytical Methods*; Hering, P., Lay, J. P., Stry, S., Eds.; Springer: Berlin, Heidelberg, 2004; pp 99–123.

[315] Huang, M.; Marshall, K. A.; Hieftje, G. M. *Analytical Chemistry* **1986**, *58*, 207–210.

[316] Martens, T.; Bogaerts, A.; Brok, W. J. M.; van der Mullen, J. J. a. M. *Journal of Analytical Atomic Spectrometry* **2007**, *22*, 1033–1042.

[317] Rybak, M. E.; Calvey, E. M.; Harnly, J. M. *Journal of Agricultural and Food Chemistry* **2004**, *52*, 682–687.

[318] Block, E.; Dane, A. J.; Thomas, S.; Cody, R. B. *Journal of Agricultural and Food Chemistry* **2010**, *58*, 4617–4625.

[319] Klee, S.; Derpmann, V.; Wißdorf, W.; Klopotowski, S.; Kersten, H.; Brockmann, K. J.; Benter, T.; Albrecht, S.; Bruins, A. P.; Dousty, F.; Kauppila, T. J.; Kostiainen, R.; O'Brien, R.; Robb, D. B.; Syage, J. A. *Journal of The American Society for Mass Spectrometry* **2014**, *25*, 1310–1321.

[320] Kauppila, T. J.; Syage, J. A.; Benter, T. *Mass Spectrometry Reviews* **2017**, *36*, 423–449.

[321] Harilal, S. S.; Skrodzki, P. J.; Miloshevsky, A.; Brumfield, B. E.; Phillips, M. C. *Physics of Plasmas* **2017**, *24*, 1–16.

[322] Thiyagarajan, M.; Scharer, J. *Journal of Applied Physics* **2008**, *104*, 013303.

[323] Yalçin, b.; Crosley, D. R.; Smith, G. P.; Faris, G. W. *Applied Physics B: Lasers and Optics* **1999**, *68*, 121–130.

[324] Glumac, N. G.; Elliott, G. S.; Boguszko, M. *AIAA Journal* **2005**, *43*, 1984–1994.

[325] Nedanovska, E.; Nersisyan, G.; Morgan, T. J.; Hüwel, L.; Murakami, T.; Lewis, C. L. S.; Riley, D.; Graham, W. G. *Journal of Applied Physics* **2015**, *117*, 013302.

[326] Simeonsson, J. B.; Miziolek, A. W. *Applied Physics B Laser and Optics* **1994**, *59*, 1–9.

[327] Tambay, R.; Thareja, R. K. *Journal of Applied Physics* **1991**, *70*, 2890–2892.

[328] Watanabe, K.; Inn, E. C. Y.; Zelikoff, M. *The Journal of Chemical Physics* **1953**, *21*, 1026–1030.

[329] Millet, P.; Birot, A.; Brunet, H.; Dijolis, H.; Galy, J.; Salamero, Y. *Journal of Physics B: Atomic and Molecular Physics* **1982**, *15*, 2935–2944.

[330] Krötz, W.; Ulrich, A.; Busch, B.; Ribitzki, G.; Wieser, J. *Physical Review A* **1991**, *43*, 6089–6094.

[331] Gornushkin, I. B.; Amponsah-Manager, K.; Smith, B. W.; Omenetto, N.; Winefordner, J. D. *Applied Spectroscopy* **2004**, *58*, 762–769.

[332] Skrodzki, P. J.; Shah, N. P.; Taylor, N.; Hartig, K. C.; LaHaye, N. L.; Brumfield, B. E.; Jovanovic, I.; Phillips, M. C.; Harilal, S. S. *Spectrochimica Acta Part B: Atomic Spectroscopy* **2016**, *125*, 112–119.

[333] Hartig, K. C.; Harilal, S. S.; Phillips, M. C.; Brumfield, B. E.; Jovanovic, I. *Optics Express* **2017**, *25*, 11477–11490.

[334] Rieger, G. W.; Taschuk, M.; Tsui, Y. Y.; Fedosejevs, R. *Spectrochimica Acta Part B: Atomic Spectroscopy* **2003**, *58*, 497–510.

[335] Bierstedt, A.; Riedel, J. *European Journal of Mass Spectrometry* **2016**, *22*, 105–114.

[336] Hohreiter, V.; Hahn, D. W. *Analytical Chemistry* **2005**, *77*, 1118–1124.

[337] Kauppila, T. J.; Kersten, H.; Benter, T. *Journal of The American Society for Mass Spectrometry* **2014**, *25*, 1870–1881.

[338] Li, S.; Bernstein, E. R. *The Journal of Chemical Physics* **1992**, *97*, 792–803.

[339] Ausloos, P.; Clifton, C. L.; Lias, S. G.; Mikaya, A. I.; Stein, S. E.; Tchekhovskoi, D. V.; Sparkman, O. D.; Zaikin, V.; Zhu, D. *Journal of The American Society for Mass Spectrometry* **1999**, *10*, 287–299.

[340] Bogusz, M. J.; Maier, R.-D.; Krüger, K. D.; Webb, K. S.; Romeril, J.; Miller, M. L. *Journal of Chromatography A* **1999**, *844*, 409–418.

[341] Annesley, T. M. *Clinical Chemistry* **2003**, *49*, 1041–1044.

[342] Gosetti, F.; Mazzucco, E.; Zampieri, D.; Gennaro, M. C. *Journal of Chromatography A* **2010**, *1217*, 3929–3937.

[343] Trufelli, H.; Palma, P.; Famiglini, G.; Cappiello, A. *Mass Spectrometry Reviews* **2011**, *30*, 491–509.

[344] Furey, A.; Moriarty, M.; Bane, V.; Kinsella, B.; Lehane, M. *Talanta* **2013**, *115*, 104–122.

[345] Lecchi, P.; Zhao, J.; Wiggins, W. S.; Chen, T. H.; Yip, P. F.; Mansfield, B. C.; Peltier, J. M. *Journal of The American Society for Mass Spectrometry* **2009**, *20*, 398–410.

[346] Hieftje, G. M. *Spectrochimica Acta Part B: Atomic Spectroscopy* **1992**, *47*, 3–25.

[347] Broekaert, J. A. C.; Siemens, V. *Spectrochimica Acta Part B: Atomic Spectroscopy* **2004**, *59*, 1823–1839.

[348] Marcus, R. K.; Quarles, C. D.; Barinaga, C. J.; Carado, A. J.; Koppenaal, D. W. *Analytical Chemistry* **2011**, *83*, 2425–2429.

[349] Pröfrock, D.; Prange, A. *Applied Spectroscopy* **2012**, *66*, 843–868.

[350] Webb, M. R.; Andrade, F. J.; Hieftje, G. M. *Journal of Analytical Atomic Spectrometry* **2007**, *22*, 766–774.

[351] Jakubowski, N.; Dorka, R.; Steers, E.; Tempez, A. *Journal of Analytical Atomic Spectrometry* **2007**, *22*, 722–735.

[352] Galbács, G. *Analytical and Bioanalytical Chemistry* **2015**, *407*, 7537–7562.

[353] Sheppard, B. S.; Caruso, J. A. *Journal of Analytical Atomic Spectrometry* **1994**, *9*, 145–149.

[354] Marcus, R. K.; Manard, B. T.; Quarles, C. D. *Journal of Analytical Atomic Spectrometry* **2017**, *32*, 704–716.

[355] Franzke, J.; Kunze, K.; Miclea, M.; Niemax, K. *Journal of Analytical Atomic Spectrometry* **2003**, *18*, 802–807.

[356] Gianchandani, Y. B.; Wright, S. A.; Eun, C. K.; Wilson, C. G.; Mitra, B. *Analytical and Bioanalytical Chemistry* **2009**, *395*, 559–575.

[357] Marcus, R. K.; Davis, W. C. *Analytical Chemistry* **2001**, *73*, 2903–2910.

[358] Orejas, J.; Pfeuffer, K. P.; Ray, S. J.; Pisonero, J.; Sanz-Medel, A.; Hieftje, G. M. *Analytical and Bioanalytical Chemistry* **2014**, *406*, 7511–7521.

[359] Manard, B. T.; Gonzalez, J. J.; Sarkar, A.; Dong, M.; Chirinos, J.; Mao, X.; Russo, R. E.; Marcus, R. K. *Spectrochimica Acta Part B: Atomic Spectroscopy* **2014**, *94-95*, 39–47.

[360] Hahn, D. W.; Omenetto, N. *Applied Spectroscopy* **2010**, *64*, 335–366.

[361] Hahn, D. W.; Omenetto, N. *Applied Spectroscopy* **2012**, *66*, 347–419.

[362] Pedarnig, J. D.; Heitz, J.; Ionita, E. R.; Dinescu, G.; Praher, B.; Viskup, R. *Applied Surface Science* **2011**, *257*, 5452–5455.

[363] Babushok, V. I.; DeLucia, F. C.; Gottfried, J. L.; Munson, C. A.; Miziolek, A. W. *Spectrochimica Acta Part B: Atomic Spectroscopy* **2006**, *61*, 999–1014.

[364] Effenberger, A. J.; Scott, J. R. *Sensors* **2010**, *10*, 4907–4925.

[365] Santesson, S.; Nilsson, S. *Analytical and Bioanalytical Chemistry* **2004**, *378*, 1704–1709.

[366] Foresti, D.; Nabavi, M.; Klingauf, M.; Ferrari, A.; Poulikakos, D. *Proceedings of the National Academy of Sciences* **2013**, *110*, 12549–12554.

[367] Marzo, A.; Seah, S. A.; Drinkwater, B. W.; Sahoo, D. R.; Long, B.; Subramanian, S. *Nature Communications* **2015**, *6*, 8661.

[368] Marzo, A.; Barnes, A.; Drinkwater, B. W. *Review of Scientific Instruments* **2017**, *88*, 085105.

[369] Stindt, A.; Andrade, M. A. B.; Albrecht, M.; Adamowski, J. C.; Panne, U.; Riedel, J. *Review of Scientific Instruments* **2014**, *85*, 015110.

[370] Stindt, A.; Albrecht, M.; Panne, U.; Riedel, J. *Analytical and Bioanalytical Chemistry* **2013**, *405*, 7005–7010.

[371] Warschat, C.; Stindt, A.; Panne, U.; Riedel, J. *Analytical Chemistry* **2015**, *87*, 8323–8327.

[372] Warschat, C.; Riedel, J. *Review of Scientific Instruments* **2017**, *88*, 105108.

[373] Henry, C. A.; Diwakar, P. K.; Hahn, D. W. *Spectrochimica Acta Part B: Atomic Spectroscopy* **2007**, *62*, 1390–1398.

[374] Diwakar, P. K.; Loper, K. H.; Matiaske, A.-M.; Hahn, D. W. *Journal of Analytical Atomic Spectrometry* **2012**, *27*, 1110–1119.

[375] De Giacomo, A.; De Pascale, O. *Thin Solid Films* **2004**, *453-454*, 328–333.

[376] DeCarlo, P. F.; Kimmel, J. R.; Trimborn, A.; Northway, M. J.; Jayne, J. T.; Aiken, A. C.; Gonin, M.; Fuhrer, K.; Horvath, T.; Docherty, K. S.; Worsnop, D. R.; Jimenez, J. L. *Analytical Chemistry* **2006**, *78*, 8281–8289.

Appendix

EL-API-HTOF MS - Capillary Inlet

A detailed schematic of the EL-API-HTOF MS (TOFWERK AG, Thun, Switzerland) is shown in Fig. A-1. This prototype was initially designed for an ICP coupling, but modified for molecular mass spectrometry applications, afterwards. The instrument consists of four differentially pumped stages (**S 1**–**S 4**), equipped with an assembly of different ion guiding and focusing optics.

To ensure that the vacuum system can cope with the higher first-stage pressure, the original pumping ensemble is backed up with a Varian TriScroll 600 (Varian Inc. Vacuum Technologies, Lexington, U.S.A.) in the first differential pumping stage (**S 1**) and a Uno 30M rotary vane pump (Pfeiffer Vacuum GmbH, Aßlar, Germany) as the forepump for a three-stage Flow 270 3P turbomolecular pump (1000 Hz, Pfeiffer Vacuum GmbH, Aßlar, Germany). Due to the higher gas load of the helium-driven DBD, an additional turbomolecular drag pump (TMH-065, Pfeiffer Vacuum GmbH, Aßlar, Germany) is installed in the second pumping stage (**S 2**) to withdraw excessive gas and solvent vapor.

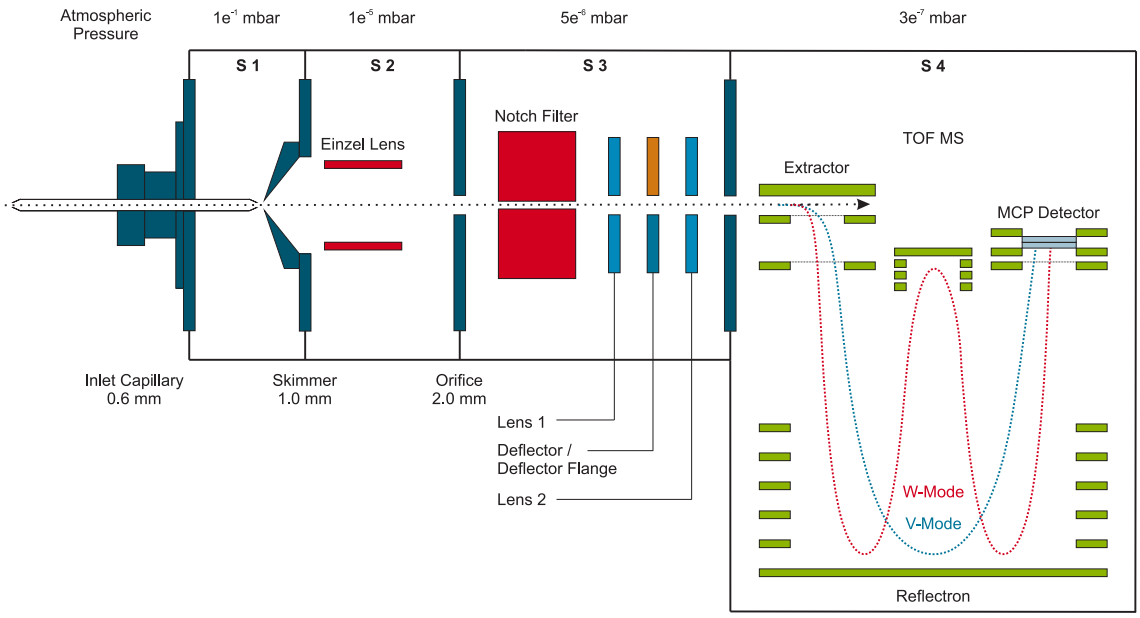

Figure A-1: Schematic of the EL-API-HTOF MS equipped with an inlet capillary.

The initial pressure reduction is achieved by a 150 mm long resistive glass capillary (o.d. 6.5 mm, i.d. 0.6 mm, Photonis, Sturbridge, U.S.A.), fixed in a KF40 pinch screw connection (VACOM, Jena, Germany). No external heating is applied to the capillary. Application of a declustering potential is possible, however, highest signal intensities are achieved, when the electrode is floating between the neighboring potential fields. Due to the large pressure difference between the capillary entrance and exit, the gas pressure drops to a few hundred mbar along the capillary passage. Thus, the gas flow drags ions into the vacuum region and accelerates them to trans-sonic conditions, followed by an expansion from the capillary end into the first differential pumping stage (**S 1**). A center portion of this primary beam of gas and ions is subsampled through an electrically biased skimmer (i.d. 1.0 mm) into the second stage of differential pumping (**S 2**). The latter houses a cylindrical einzel lens, which directs the ion beam onto an orifice / notch filter (not in use) assembly, installed in the third differential pumping stage (**S 3**). Eventually, the ion beam is directed and accelerated by a series of DC optics into an orthogonal extraction, reflectron TOF mass analyzer (**S 4**).

The latter is arranged in a double-reflectron-geometry that can be used to create either a single-reflectron or a triple-reflectron flight path, referred to as V- and W-mode, respectively. The V-mode represents a standard reflectron configuration in which the ions follow a trajectory from the extraction region into the reflectron and back to the MCP detector (effective ion path length L = 1.3 m).[376] In W-mode, ions exiting the reflectron are directed into a hard mirror, which focuses them back into the reflectron for a second pass, before traveling to the MCP detector. Thus, a longer effective ion path length of L = 2.9 m can be achieved.[376] While the mass resolving power of the TOF MS increases over a longer flight path, at the same time, a rise in the lateral broadening of the ions limits the total number of ions that strike the detector. Therefore, the V-mode is higher in sensitivity, whereas the W-mode offers higher mass resolution.

EL-API-HTOF MS - Conical Skimmer Inlet

Further progress regarding an enhanced sampling efficiency proofed that the use of a conical sampling orifice resulted in a shorter temporal response and an increased ion transmission (see Chapter 3). Therefore, the former inlet capillary was exchanged by a custom-made conical skimmer inlet.

For its design, a metal plate with a central orifice of 0.3 mm in diameter was extended by a commercially available airbrush nozzle (Harder & Steenbeck, Norderstedt, Germany). At the inlet toward atmospheric pressure, the inner diameter of this skimmer is 150 µm and increases linearly to 4.0 mm toward the vacuum system of the mass spectrometer, at a total length of 15.0 mm. The inlet is held at room temperature. Application of a declustering potential is possible, however, highest signal response is obtained, when the electrode is floating between the neighboring potential fields.

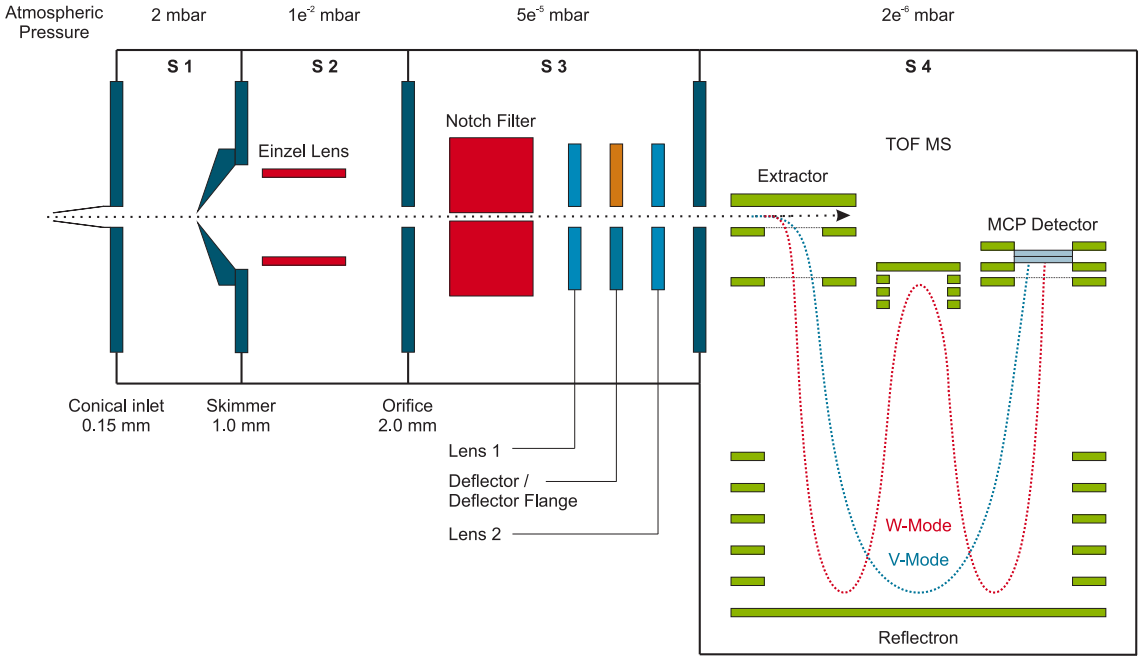

Figure A-2: Schematic of the EL-API-HTOF MS equipped with a conical skimmer.

Except the primary sample introduction, the main structure of the instrument is of the same design as in the above-described configuration. Briefly, ions are sequentially guided through four stages of differentially pumping (**S 1**–**S 4**), comprising a skimmer (i.d. 1.0 mm) / einzel lens assembly, followed by an orifice (i.d. 2.0 mm) / notch filter combination, before being focused and accelerated by a series of DC optics into the orthogonal extraction, reflectron TOF MS. The latter can be operated at high sensitivity (V-mode) or high mass resolution (W-mode). Throughout all experiments, the notch filter was not in use.

To maintain a stable vacuum in the drift region of the mass analyzer, a dry scroll vacuum pump (Varian TriScroll 600, Varian Inc. Vacuum Technologies, Lexington, U.S.A.) is installed in the first pumping stage (**S 1**) and a rotary vane pump (Uno 30M, Pfeiffer Vacuum GmbH, Aßlar, Germany) serves as the forepump for a Flow 270 3P turbomolecular pump (700 Hz, Pfeiffer Vacuum GmbH, Aßlar, Germany). Due to the smaller diameter of the new inlet, the stress of the vacuum system is drastically reduced and makes the application of an additional turbomolecular pump in the second pumping stage (**S 2**) redundant.

Q-API-HTOF MS

Another custom-designed version of the API-HTOF MS (TOFWERK AG, Thun, Switzerland), similar to the one described in References [128] and [129], was used for the additional spectrometric analysis of nascent plasma species. It comprises a system of four differentially pumped stages (**S 1**–**S 4**), but different ion guiding and focusing optics (see Fig. A-3).

Ions are sampled through a homebuilt, extended inlet orifice (i.d. 0.5 mm, length: 34.0 mm, aluminum, floating, non-heated) into a short, segmented radio frequency (RF)-only quadrupole (**S 1**), having tunable frequency and amplitude. This quadrupole permits the creation of an electric field for the effective collisional dissociation of weakly-bound cluster species, while simultaneously directing, focusing, and cooling the expansive ion beam. [129]

Subsequently, the ion beam exits this dissociation chamber through an electrically biased skimmer orifice (i.d. 1 mm) into a second RF-only quadrupole in pumping stage **S 2**. The ion beam is then directed into the third stage of differential pumping (**S 3**), housing a series of DC optics that, eventually, focus and accelerate the ions into an orthogonal extraction, reflectron TOF mass analyzer (**S 4**). As for the previous instrument, the system can be operated in two different modes: the V-mode, offering high sensitivity, or the W-mode, resulting in a higher mass resolution.

The high vacuum for the HTOF MS is generated by a three-stage SplitFlow 270 3P turbomolecular pump (Pfeiffer Vacuum GmbH, Aßlar, Germany), combined with a MD1 VARIO-SP diaphragm pump (Vacuubrand GmbH + CO KG, Wertheim, Germany) as the forepump, and a dry scroll vacuum pump (Varian TriScroll 600, Varian Inc. Vacuum Technologies, Lexington, U.S.A.), installed in the first pumping stage (**S 1**).

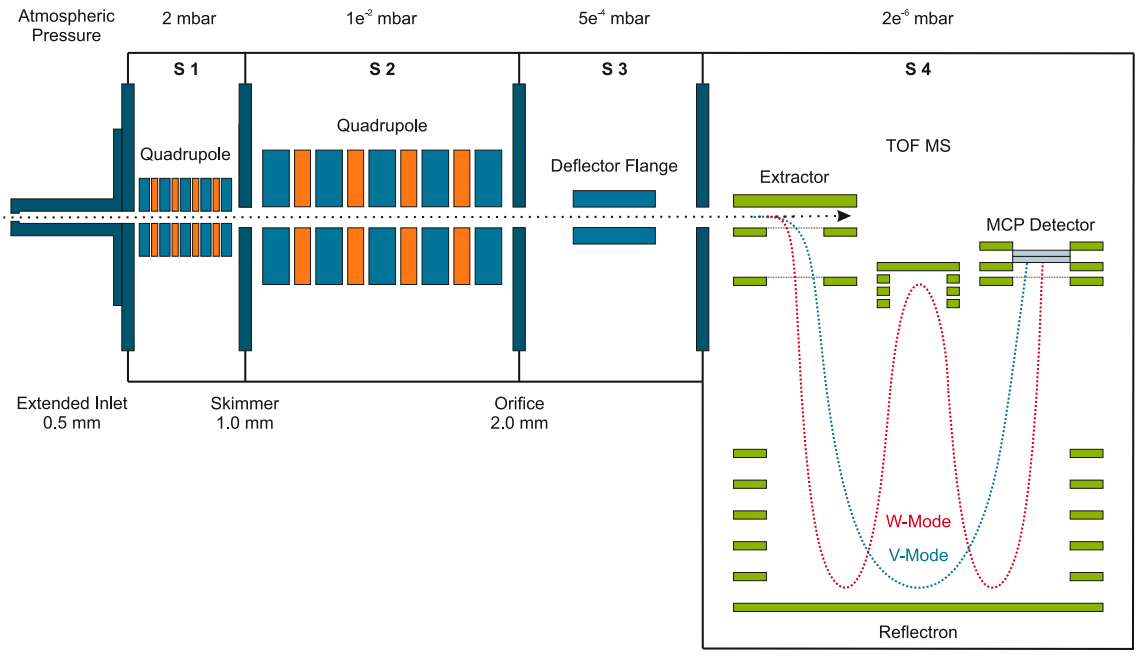

Figure A-3: Schematic of the Q-API-HTOF MS equipped with an extended inlet.

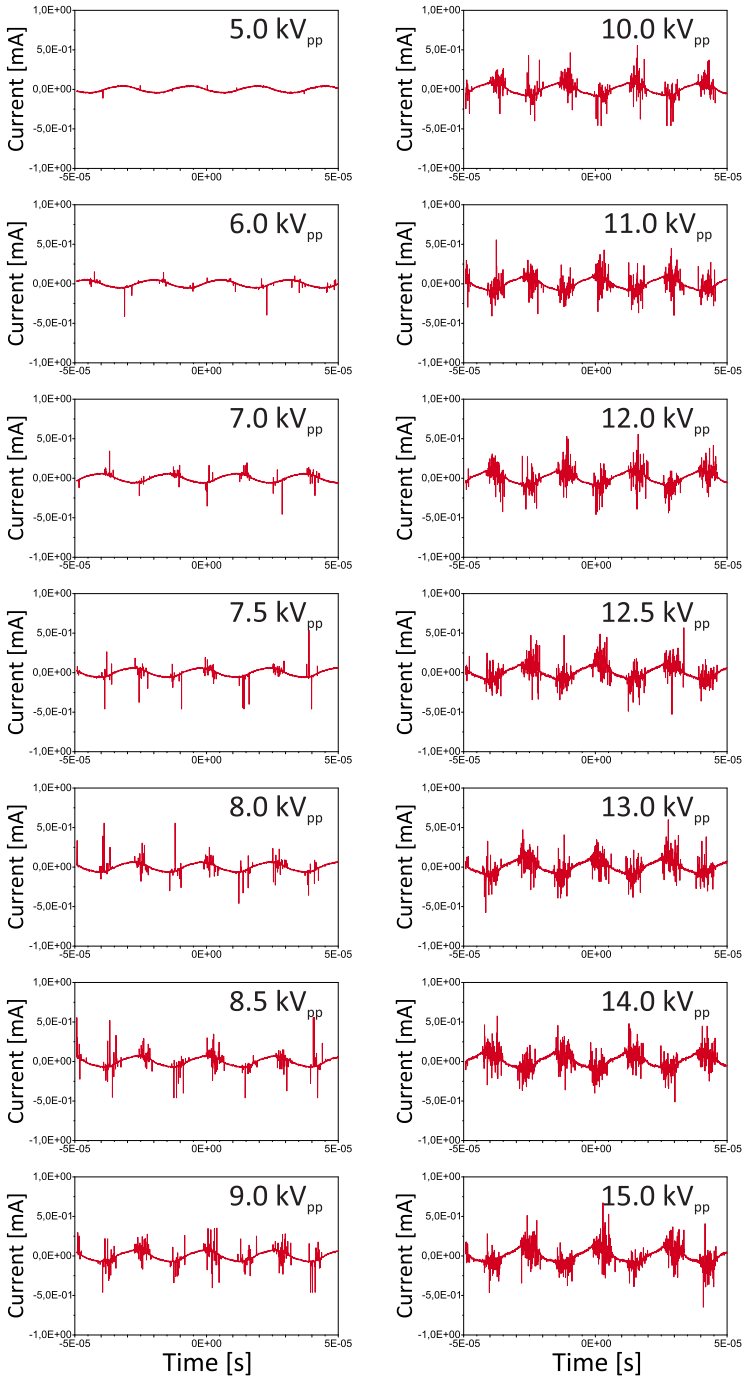

Figure A-4: Recorded current / voltage profiles for the DBD ion source operated with helium and varying input voltages.

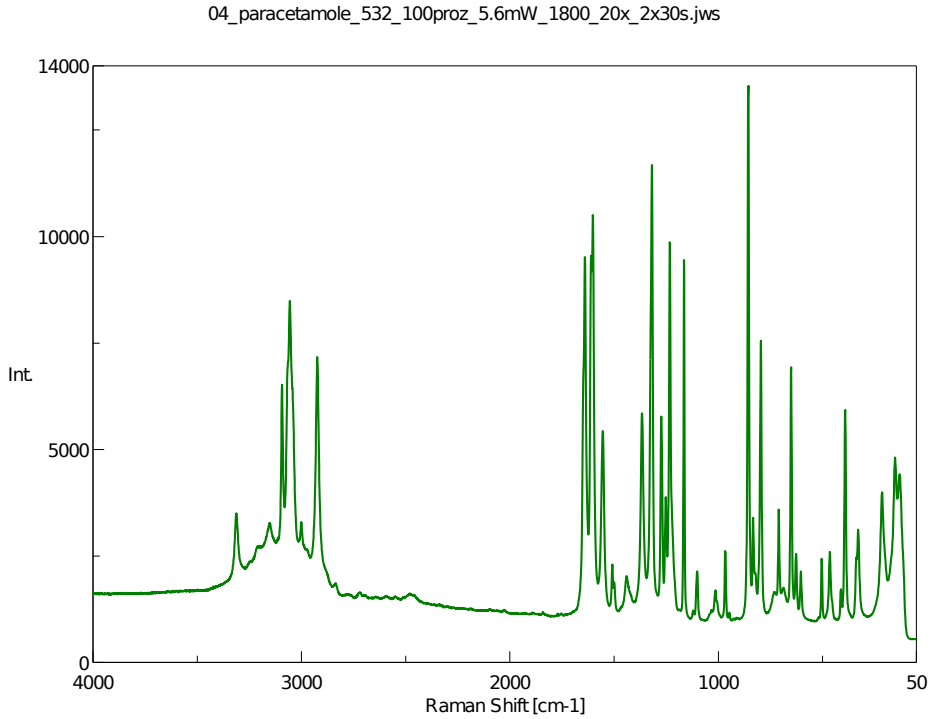

04_paracetamole_532_100proz_5.6mW_1800_20x_2x30s.jws

[Comments]
Sample name
Comment
User
Division
Company SALSA Photonics Application Lab

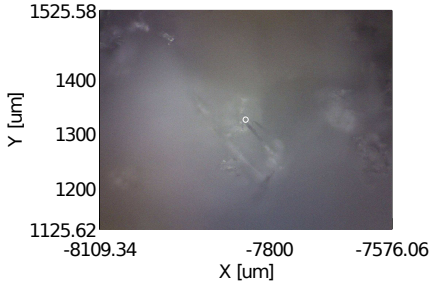

[Detailed Information]
Creation date 10/20/2017 12:18 PM

Data array type Non-linear data array
Horizontal axis Raman Shift [cm-1]
Vertical axis Int.
Start 48.7682 cm-1
End 4000.38 cm-1
Data points 3920

[Measurement Information]
Model Name NRS 4100
Serial Number A002761822

Measurement Date 10/20/2017 12:15 PM

Exposure	30 sec
Accumulation	2
Center wavenumber	1096.44 cm-1
Z position	20478.6 um
Binning Upper	70
Binning Lower	129
Valid Channel	1 - 1650
CCD	DR32400_FI
Laser wavelength	532.07 nm
Monochromator	Single
Grating	1800 l/mm
Slit	50 x 8000 um
Rejection filter	532.1 nm
Resolution	3.67 cm-1, 1.18 cm-1/pixel
Objective lens	MPLN 20 x
BS/DM	BS 30/70
Laser power	5.6 mW
Attenuator	100%
Cosmic ray reduction	On
CCD temperature	-61.0 C
Shift	-10.00 cm-1

Figure A-5: Raman spectrum of pure paracetamol measured with a JASCO NRS-4100 dispersive Raman spectrometer at the SALSA Photonics Application Lab.

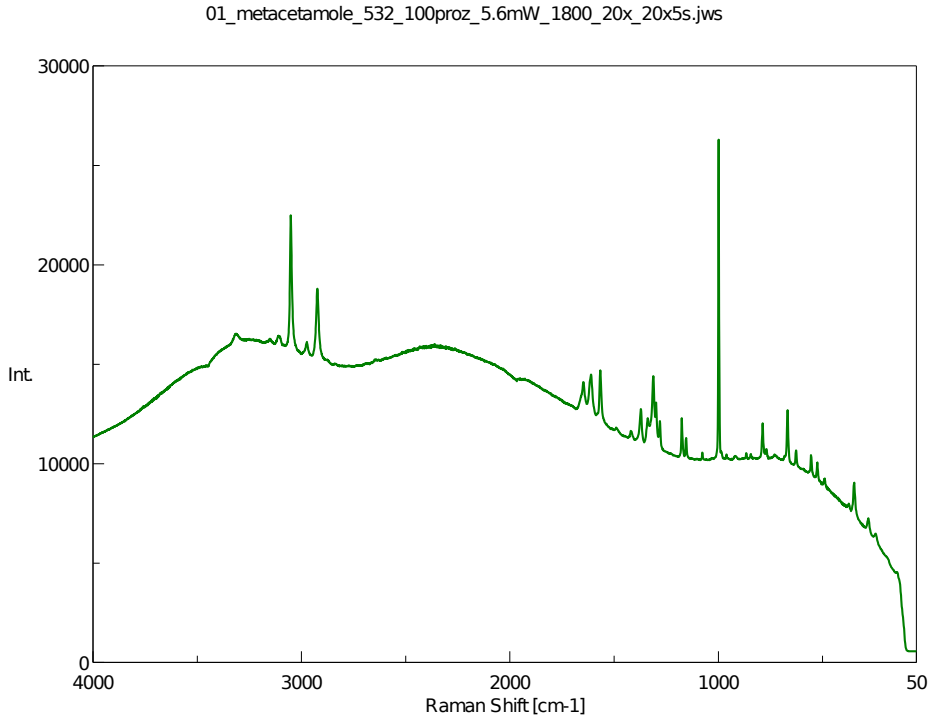

01_metacetamole_532_100proz_5.6mW_1800_20x_20x5s.jws

[Comments]
Sample name
Comment
User
Division
Company SALSA Photonics Application Lab

[Detailed Information]
Creation date 10/20/2017 11:48 AM

Data array type Non-linear data array
Horizontal axis Raman Shift [cm-1]
Vertical axis Int.
Start 48.7682 cm-1
End 4000.38 cm-1
Data points 3920

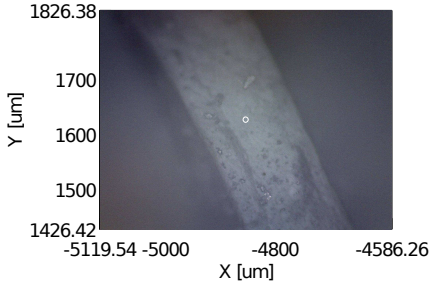

[Measurement Information]
Model Name NRS 4100
Serial Number A002761822

Measurement Date 10/20/2017 11:39 AM

Exposure	5 sec
Accumulation	20
Center wavenumber	1096.44 cm-1
Z position	20516.5 um
Binning Upper	70
Binning Lower	129
Valid Channel	1 - 1650
CCD	DR32400_FI
Laser wavelength	532.07 nm
Monochromator	Single
Grating	1800 l/mm
Slit	50 x 8000 um
Rejection filter	532.1 nm
Resolution	3.67 cm-1, 1.18 cm-1/pixel
Objective lens	MPLN 20 x
BS/DM	BS 30/70
Laser power	5.6 mW
Attenuator	100%
Cosmic ray reduction	On
CCD temperature	-61.0 C
Shift	-10.00 cm-1

Figure A-6: Raman spectrum of pure metacetamol measured with a JASCO NRS-4100 dispersive Raman spectrometer at the SALSA Photonics Application Lab.

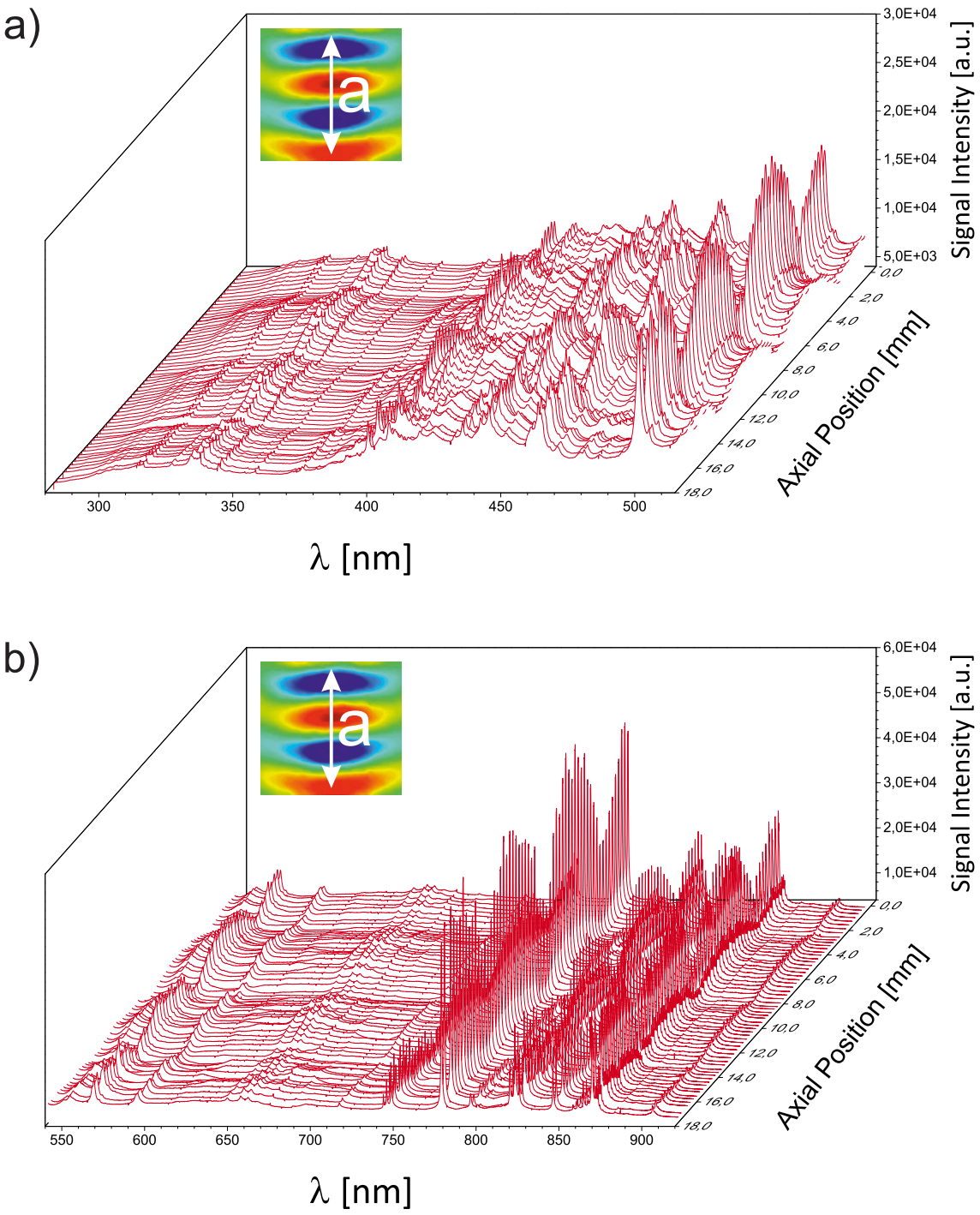

Figure A-7: Detailed spatially resolved interrogation of the acoustic field along the principal axis *a*, covering the spectral wavelength between (a) 280–515 nm and (b) 540–920 nm. Each 250 µm, a full spectrum of the plasma radiation was recorded to visualize the effect of the standing wave in the acoustic field on the plasma emission. The given inset depicts the integral sound field and the respective line scan.

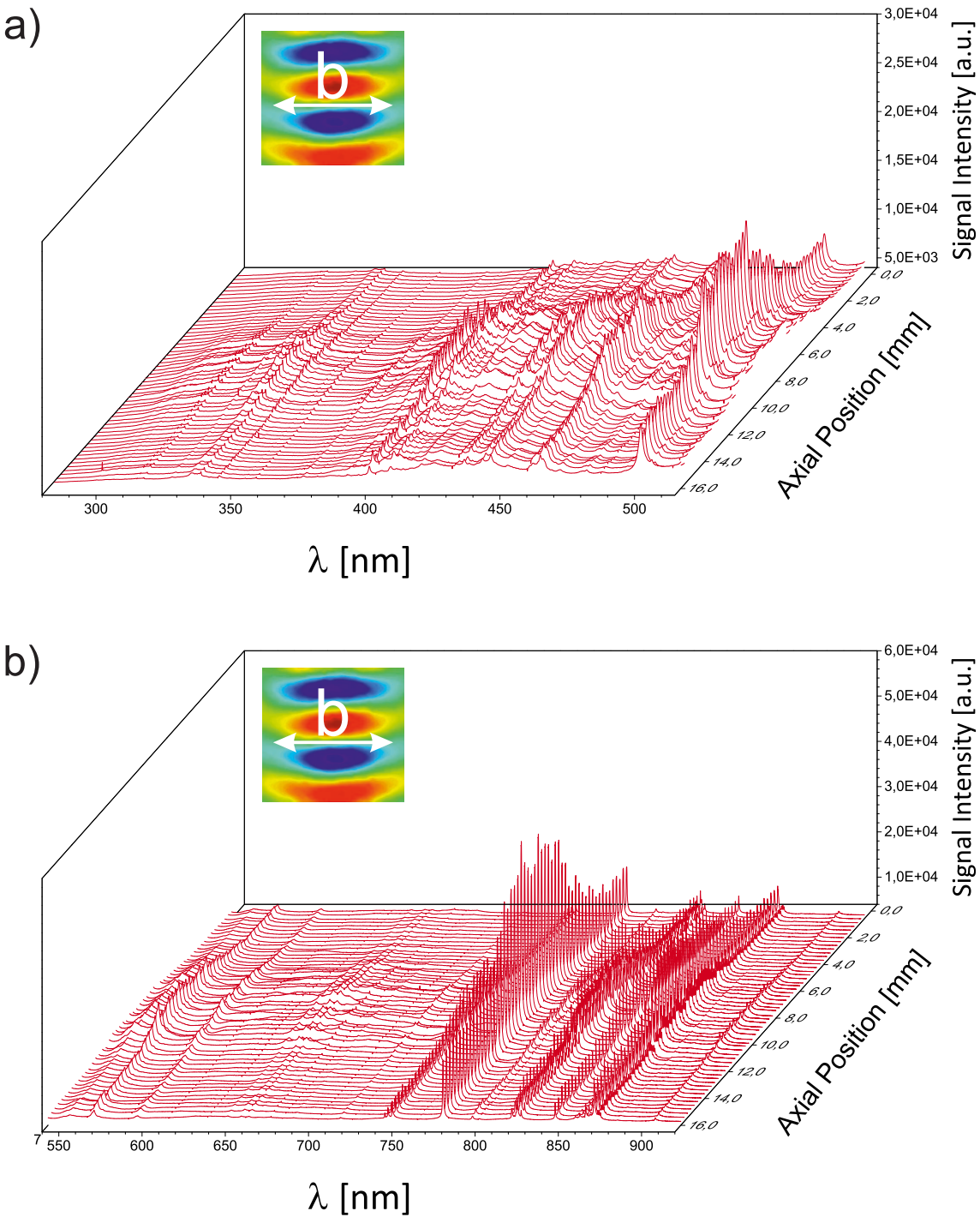

Figure A-8: Detailed spatially resolved interrogation of the acoustic field along the principal axis b, covering the spectral wavelength between (a) 280–515 nm and (b) 540–920 nm. Each 250 µm, a full spectrum of the plasma radiation was recorded to visualize the effect of the standing wave in the acoustic field on the plasma emission. The given inset depicts the integral sound field and the respective line scan.

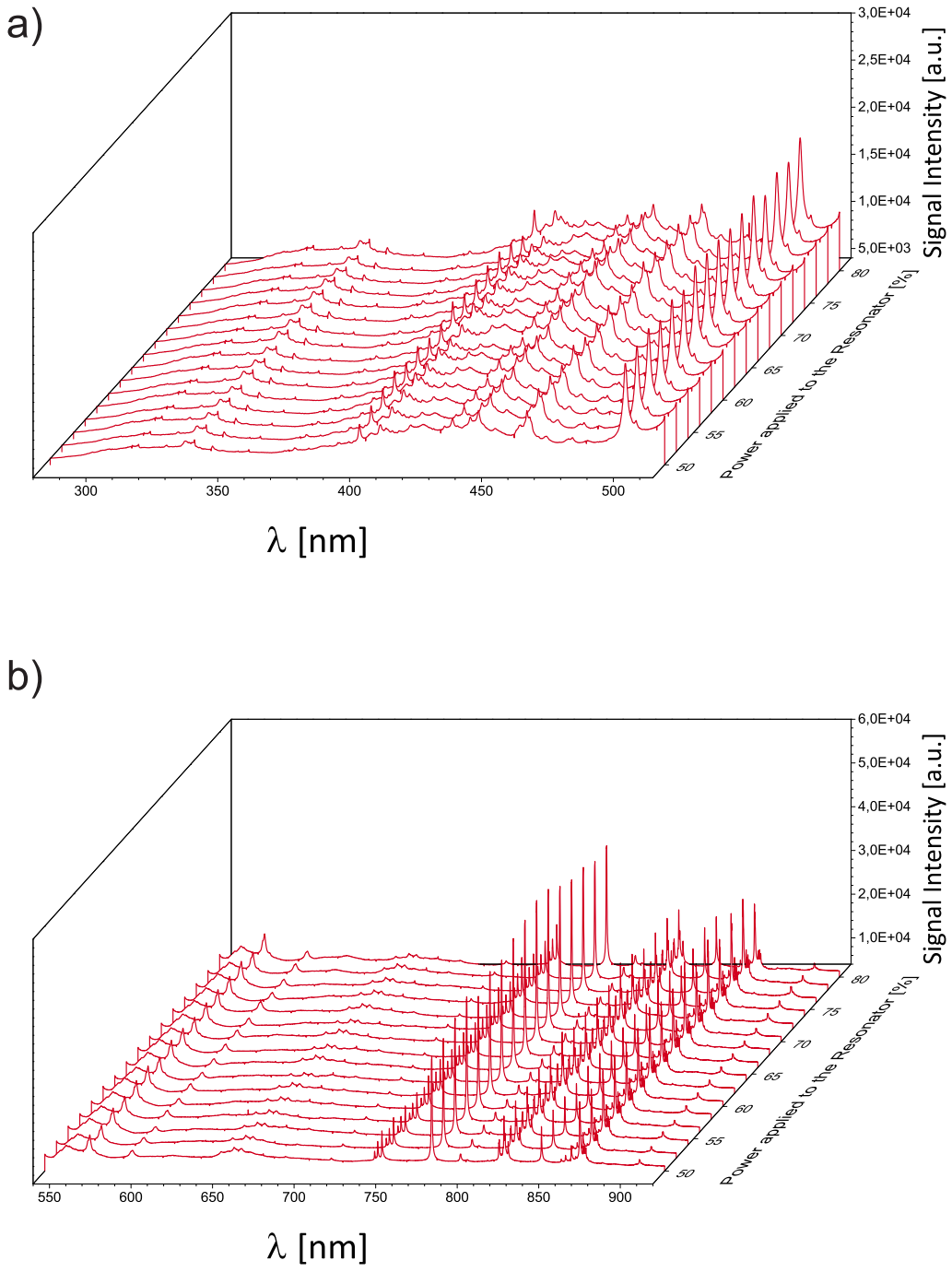

Figure A-9: Power dependence on the spectral response of the LIP ignited in the central pressure minimum, covering the spectral wavelength between (a) 280–515 nm and (b) 540–920 nm. The spectra do not change with respect to the applied power to the ultrasonic transducer, which corroborates acoustic saturation.

Publications

Articles

Bierstedt, A.; Panne, U.; Riedel, J. Confinement and enhancement of an airborne atmospheric laser-induced plasma by an ultrasonic acoustic resonator, *Journal of Analytical Atomic Spectrometry* **2018**, *33*, 135–140.

Bierstedt, A.; Kersten, H.; Glaus, R.; Gornushkin, I.; Panne, U.; Riedel, J. Characterization of an airborne laser-spark ion source for ambient mass spectrometry, *Analytical Chemistry* **2017**, *89*, 3437–3444.

Bierstedt, A.; Riedel, J. Airborne laser-spark for ambient desorption/ionization, *European Journal of Mass Spectrometry* **2016**, *22*, 105–114.

Bierstedt, A.; Riedel, J. High-repetition rate laser ablation coupled to dielectric barrier discharge postionization for ambient mass spectrometry, *Methods* **2016**, *104*, 3–10.

Bierstedt, A.; Panne, U.; Rurack, K.; Riedel, J. Characterization of two modes in a dielectric barrier discharge probe by optical emission spectroscopy and time-of-flight-mass spectrometry, *Journal of Analytical Atomic Spectrometry* **2015**, *30*, 2496–2506.

Bierstedt, A.; Stindt, A.; Warschat, C.; Panne, U.; Riedel, J. High repetition rate atmospheric pressure MALDI in combination with liquid matrices, *European Journal of Mass Spectrometry* **2014**, *20*, 367–374.

Stindt, A.; Warschat, C.; Bierstedt, A.; Panne, U.; Riedel, J. Characterisation of an inexpensive sonic spray ionisation source using laser induced fluorescence imaging and mass spectrometry, *European Journal of Mass Spectrometry* **2014**, *20*, 21–29.

Patents

Bierstedt, A.; Riedel, J. Analysevorrichtung für gasförmige Proben und Verfahren zum Nachweis von Analyten in einem Gas, Patent Nr. 10 2016 113 771.5.

Presentations

Bierstedt, Riedel, J. Airborne laser spark ionization, 2^{nd} International Conference on Ionization Principles in Organic and Inorganic Mass Spectrometry, 16.10. – 18.10.2017, Menorca, Spain.
Bierstedt, Riedel, J. Airborne laser spark ionization, SciX 2017, 08.10. – 13.10.2017, Reno, NV, U.S.A.
Bierstedt, A.; Bräkling, S.; Rieger, J.; Kersten, H.; Glaus, R.; Gornushkin, I.; Riedel, J. Development and characterization of an airborne laser-spark ion source for ambient desorption / ionization mass spectrometry, 21^{st} International Mass Spectrometry Conference, 20.08. – 26.08.2016, Toronto, ON, Canada.
Bierstedt, A.; Panne, U.; Riedel, J. Development of a new versatile instrument combining laser ablation mass spectrometry and laser emission spectroscopy, 63^{rd} ASMS Conference on Mass Spectrometry and Allied Topics, 31.05. – 04.06.2015, St. Louis, MO, U.S.A.
Bierstedt, A.; Riedel, J.; Panne, U. Elucidation of reagent-ion formation in a versatile low-temperature plasma probe combining emission spectroscopy and ambient time-of-flight mass spectrometry, 4^{th} Berliner Chemie Symposium, 09.04.2015, Berlin, Germany.
Bierstedt, A.; Riedel, J.; Panne, U. Characterization of a versatile low-temperature plasma torch by optical emission spectroscopy and time-of-flight mass spectrometry, 48^{th} Annual Meeting of the DGMS, 01.03. – 04.03.2015, Wuppertal, Germany.
Bierstedt, A.; Riedel, J. Combination of Raman spectroscopy and laser ablation mass spectrometry, Doktorandenseminar des DAAS - Spektroskopie und Spurenanalytik 2014, 22.09. – 24.09.2014, Münster, Germany.
Riedel, J.; Stindt, A.; Warschat, C.; Bierstedt, A.; Panne, U. Levitated droplets in mass spectometry, SciX 2013, 30.09. – 04.10.2013, Milwaukee, WI, U.S.A.
Kadenkin, A.; Geisler, S.; Florek, S.; Bierstedt, A.; Gornushkin, I.; Riedel, J.; Panne, U. Laser induced breakdown spectroscopy with the use of fast diode pumped solid state laser, Doktorandenseminar des DAAS - Spektroskopie und Spurenanalytik 2013, 09.07. – 11.07.2012, Mainz, Germany.
Kadenkin, A.; Bierstedt, A.; Panne, U.; Riedel, J.; Gornushkin, I.; Florek, S.; Geisler, S. Laser induced breakdown spectroscopy with the use of fast diode pumped solid state laser, EUROANALYSIS 16, 11.09. – 15.09.2011, Belgrad, Serbia.

Posters

Bierstedt, A.; Riedel, J. Improving the performance of the laser-spark ion source for the detection of volatile organic compounds under ambient conditions, 50^{th} Annual Meeting of the DGMS, 05.03. – 08.03.2015, Kiel, Germany.

Bierstedt, A.; Kersten, H.; Glaus, R.; Gornushkin, I.; Riedel, J. Development of a laser induced plasma ion source for ambient mass spectrometry, 5^{th} Berliner Chemie Symposium, 12.04.2016, Berlin, Germany.

Bierstedt, A.; Kersten, H.; Glaus, R.; Gornushkin, I.; Riedel, J. Laser induced plasma ion source coupled to ambient mass spectrometry, 49^{th} Annual Meeting of the DGMS, 28.02. – 02.03.2016, Hamburg, Germany.

Bierstedt, A.; Warschat, C.; Michalik-Onichimowska, A.; Riedel, J.; Rurack, K. Laser Desorption strategies for ambient molecular mass spectrometry, Adlershofer Forschungsforum 2015, 11.11.2015, Berlin, Germany.

Warschat, C.; Stindt, A.; Bierstedt, A.; Panne, U.; Riedel, J. Near-IR laser induced desorption sampling of acoustically levitated liquids, 4^{th} Berliner Chemie Symposium, 09.04.2015, Berlin, Germany.

Warschat, C.; Stindt, A.; Bierstedt, A.; Panne, U.; Riedel, J. Near-IR laser induced desorption sampling of acoustically levitated liquids, 48^{th} Annual Meeting of the DGMS, 01.03. – 04.03.2015, Wuppertal, Germany.

Bierstedt, A.; Riedel, J.; Panne, U. Combination of laser spectroscopy and laser ablation mass spectrometry, 20^{th} International Mass Spectrometry Conference, 24.09. – 29.09.2014, Geneva, Switzerland.

Warschat, C.; Stindt, A.; Bierstedt, A.; Panne, U.; Riedel, J. Charakterisierung einer Sonic Spray Ionisationsquelle mittels Laserinduzierter Fluoreszenz, 47^{th} Annual Meeting of the DGMS, 02.03. – 05.03.2014, Frankfurt am Main, Germany.

Bierstedt, A.; Stindt, A.; Warschat, C.; Riedel, J.; Panne, U. High repetitation rate AP-MALDI in combination with liquid matrices, 47^{th} Annual Meeting of the DGMS, 02.03. – 05.03.2014, Frankfurt am Main, Germany.

Bierstedt, A.; Stindt, A.; Warschat, C.; Riedel, J.; Panne, U. Ionische Flüssigkeiten als Matrices für die AP-MALDI MS, 46^{th} Annual Meeting of the DGMS, 10.03. – 13.03.2013, Berlin, Germany.

Gornushkin, I.; Kadenkin, A.; Bierstedt, A.; Panne, U.; Riedel, J.; Florek, S.; Geisler, S. Novel low cost compact Echelle spectrograph for laser induced breakdown spectroscopy with a diode pumped solid state laser, Colloquium Spectroscopicum Internationale XXXVII, 28.08. – 02.09.2011, Rio de Janeiro, Brazil.

Acknowledgements

This thesis would not have been possible without the exceptional guidance and assistance of numerous people. I am grateful to all of those with whom I have had the pleasure to work during this and other related projects. The following people deserve special mention:

- ... my doctoral supervisor, Ulrich Panne, for offering me the possibility to work on the topic of laser-based instrumental analytics. His support and strategic advice over the last four years, as well as the excellent working atmosphere at BAM facilitated my research, which is invaluable.
- ... my second supervisor, Jens Riedel, who taught me to think, act, and write as a successful scientist does. His passion, ambition, and curiosity to approach scientific problems has been always contagious and motivational. I highly appreciate his contributions of time and ideas to make my PhD experience so productive and stimulating. I will always remember the joy I felt when our "friday afternoon experiments" succeeded. Most of them paved the way for this thesis.
- ... the other members of my graduate commitee, Michael W. Linscheid, Ilko Bald, Kannan Balasubramanian, and Kallol Ray. Reviewing a PhD thesis takes time and effort. I am grateful to them for that.
- ... my amazing colleagues and friends of the "Rocket Science" lab. Thank you to Arne, Carsten, and Ola for having so much fun, even when times were the roughest.
- ... the talented LIBS guys; in particular, Ardian, Igor, Reto, and Sasha.
- ... everyone at BAM, who helped along in a way or another, especially Axel, Anka, Basti, Christoph, Jule, Konny, Thomas, Sabine, Steffi, and Yves.
- ... our collaboration partners at the University Wuppertal.
- ... my family and friends for continuously encouraging me throughout this experience. And finally, to Rosi, I am eternally grateful for your support, understanding, and patience throughout the past four years.

Thank you!

Statement of Authorship

I declare that I am the sole author of this thesis. It was prepared specifically for the degree Dr. rer. nat. while under supervision at the Humboldt-Universität zu Berlin. If any of my work contained within this thesis has been published prior to submission, I have obtained the necessary permission to reproduce and include it. I have not applied for a doctor's degree in the doctoral subject elsewhere and do not hold a corresponding doctor's degree. Further, I have fully acknowledged and referenced the ideas and work of others, whether published or unpublished, in my thesis. No other sources and tools than those listed in the bibligraphy and identified as references were used. I have taken due note of the Faculty of Mathmatics and Natural Sciences PhD Regulations, published in the Official Gazette of the Humboldt-Universität zu Berlin no. 126 / 214 on 18/11/2014.

Berlin, 05.03.2018
Andreas Bierstedt